

Technische Universität München

Fakultät für Chemie

Lehrstuhl für Fest – Körper NMR Spektroskopie

Dynamic Aspects of the Human Eye Lens Molecular Chaperones alphaA- and alphaB- Crystallin studied by NMR Spectroscopy

Maria Stavropoulou

Vollständiger Abdruck der von der Fakultät für Chemie der Technischen Universität München zur Erlangung des akademischen Grades

Doktors der Naturwissenschaften (Dr. rer. nat.)

genehmigten Dissertation.

Vorsitzender:

Prof. Dr. Johannes Buchner

Prüfer der Dissertation:

1. Prof. Dr. Bernd Reif
2. Prof. Dr. Sevil Weinkauff

Die Dissertation wurde am 31.08.2017 bei der Technischen Universität München eingereicht und durch die Fakultät für Chemie am 09.11.2017 angenommen.

Technische Universität München

Fakultät für Chemie

Lehrstuhl für Fest – Körper NMR Spektroskopie

**Dynamic Aspects of the Human Eye Lens
Molecular Chaperones alphaA- and alphaB-
crystallin studied by NMR Spectroscopy**

Maria Stavropoulou

Author's Declaration

This thesis is submitted in line with the regulations of the Technical University of Munich in partial fulfilment of the degree of *Doctor rerum naturalium* (Dr. rer. nat.). This thesis does not contain any material published by another person except where due reference is made in text. The experimental work described in this thesis is original work and has not been submitted for a degree or diploma at any other university.

September 2017
Maria Stavropoulou

Zusammenfassung

Kleine Hitzeschockproteine, einschließlich beider alpha-Kristallin-Gene der menschlichen Augenlinse, alphaA- und alphaB-Kristallin, spielen eine wichtige Rolle bei der Proteinhomeostase, weil ihre ATP-unabhängige Chaperon-Aktivität eine unkontrollierte Proteinaggregation verhindert. alphaA und alphaB haben ~58% Sequenzhomologie und bilden heterogene und hochdynamische oligomere Ensembles bis zu einem Molekulargewicht von 1 MDa. Ihre monomere Untereinheit setzt sich aus der zentralen alpha-Kristallin-Domäne (AKD) und den flankierenden N- und C-terminalen Regionen (NTR bzw. CTR) zusammen. Die CTR beherbergt ein hochkonserviertes IXI-Motiv, das wesentlich ist für die Oligomerisierung. alphaA kommt am häufigsten in der Augenlinse vor. Im Gegensatz dazu wird alphaB ubiquitär in mehreren Geweben exprimiert. Hier zeigen wir unter Verwendung moderner NMR-Spektroskopie, dass der alphaB-Komplex aus asymmetrischen Bausteinen zusammengesetzt ist, und dass alphaB durch seine inhärente strukturelle Plastizität mit einer breiten Palette von strukturell unterschiedlichen Klienten interagiert. Interaktionsstudien mittels Immunogold markierter und negativ kontrastierter Proben bestätigten, dass alphaB das Fibrillen bildende AlzheimerAβ40-Peptid vorzugsweise an seinen Kanten bindet, während die Bindung eines amorph aggregierenden Klienten durch den partiell unstrukturierten NTR erfolgt. Darüber hinaus deuten Phosphorylierungs-imitierende alphaB-Mutanten darauf hin, dass Phosphorylierung zu einer Verminderung des Molekulargewichts führt. Obwohl die CTR von α-Kristallinen hochflexibel, unstrukturiert und Lösungsmittel zugänglich ist, zeigen CTRs hochaufgelöste Lösungs-NMR-Spektren. In der vorliegenden Arbeit führen wir NMR-Untersuchungen über die Konformation und Dynamik des ungeordneten CTR des menschlichen alphaA Proteins durch, das zwei natürlich vorkommende Cysteine enthält, die für seine Redox-Empfindlichkeit verantwortlich sind. Wir haben das Rückgrat von ¹⁵N, ¹³C-markiertem alphaA, sowie die Seitenketten, zugeordnet und beobachteten mehrere zusätzliche NMR-Signale für Reste in der Nähe von Prolin 160, 167 und 171. Wir stellten fest, dass alle detektierten Konformere unstrukturiert sind und die zusätzlichen Resonanzen aus der *cis-trans*-Peptidyl-Prolyl-Isomerisierung um die I159-P160 (IPV-Motiv), K166-P167 und A170-P171 Peptidbindungen entstehen. Die Population der *cis*-P160, *cis*-P167 und *cis*-P171 Konformation beträgt bei physiologischen Temperaturen etwa 6%, 15% bzw. 5%, und die *cis*-P160 Konformation zeigt insbesondere eine Tendenz zur Ausbildung einer beta-Strang-Konformation. Zusammengefasst zeigen diese Daten eine potentielle Rolle für die *cis-trans*-Prolin-Isomerisierung bei der Regulierung der Oligomerisierung von kleinen Hitzeschockproteinen. Weiterhin haben wir paramagnetische Relaxationsverstärkungs-Experimente durchgeführt, durch die wir bestätigen konnten, dass sich ein geringer Anteil von ca. 15-20% des CTR von alphaA in einem Domänen austauschzustand befindet, und dass sowohl transiente inter- als auch intramolekulare Wechselwirkungen mit benachbarten Oligomeren ausgebildet werden können. ¹⁵N Relaxationsexperimente zeigten auch, dass die oxidierte Form von alphaA geringfügig flexibler ist als die reduzierte Form, und dass im Allgemeinen alphaA, reduziert oder oxidiert, im Vergleich zu alphaB, in ihrer CTR dynamischer zu sein scheint. Unsere Untersuchungen wurden schließlich erweitert durch biochemische und NMR Daten über ein verkürztes Konstrukt des menschlichen alphaA Proteins, die zeigen, dass die Gesamtgröße von alphaA_{ox(62-166)} im Vergleich zu alphaA_{red(62-166)} erhöht ist und höhermolekulare oligomere Ensembles gebildet werden, die in einem tetrameren Zustand zu sein scheinen, entsprechend eines Molekulargewichts von 80 kDa, wohingegen alphaA_{red(62-166)} womöglich nur als Dimer vorliegt.

Summary

Small heat shock proteins (sHsps), including the two alpha-crystallin genes of the human eye lens, alphaA- and alphaB-crystallin, play an important role in protein homeostasis, because their ATP-independent chaperone activity inhibits uncontrolled protein aggregation. alphaA and alphaB have ~58% sequence homology and they form heterogeneous and highly dynamic oligomeric ensembles of molecular weights up to 1 MDa. Their monomeric subunit is organized into the central alpha-crystallin domain (ACD) and the flanking N- and C-terminal regions (NTR and CTR), respectively. The CTR harbours a highly conserved IXI-motif important for oligomerization. alphaA is mostly predominant in the eye lens. By contrast, alphaB is ubiquitously expressed in several tissues. Here, by using state-of-the-art NMR spectroscopy, we show that the alphaB complex is assembled from asymmetric building blocks and suggest that alphaB with its structural plasticity interacts with a wide range of structurally variable clients. Interaction studies using immunogold-labeling negative stained samples demonstrated that alphaB binds the fibril-forming Alzheimer's disease Abeta40 peptide preferentially to its edges and an amorphously aggregating client by the partially disordered NTR. Phosphorylation-mimicking alphaB mutants suggest that the protein upon phosphorylation yields a decreased molecular weight. Although, the CTR of alpha-crystallins is highly flexible, unstructured and solvent accessible, CTRs give rise to well-resolved solution-state NMR spectra. Here, we report solution-state NMR investigations of the conformation and dynamics of the disordered CTR of human alphaA, which contains two naturally occurring cysteines responsible for its redox sensitivity. We assigned the backbone of ^{15}N , ^{13}C -labeled alphaA, as well as the side chains, and observed multiple additional NMR signals for residues in the vicinity of prolines 160, 167 and 171. We determined that, while all observed forms are highly disordered, the extra resonances arise from the cis-trans peptidyl-prolyl isomerization about the I159-P160 (IPV motif), K166-P167 and A170-P171 peptide bonds. The cis-P160, cis-P167 and cis-P171 are populated to 6%, 15% and 5%, respectively, at physiological temperatures and cis-P160 in particular shows a tendency to adopt beta-strand conformations. These findings indicate a potential role for cis-trans proline isomerization in regulating the oligomerization of sHsps. We further carried out paramagnetic relaxation enhancement experiments, where we could confirm that a small amount of ca. 15-20% of the CTR of alphaA is in a domain swapping state, and that it can form both, transient inter- and intra-molecular interactions with neighbouring oligomers. ^{15}N relaxation experiments showed that the oxidized form of alphaA is slightly more flexible than the reduced, and in total, alphaA, reduced or oxidized, appears to be more dynamic in its CTR compared to alphaB. Our investigations were finally extended by biochemical and NMR data on the truncated construct of human alphaA, which showed that the overall size of alphaAox(62-166) is increased compared to alphaAred(62-166), and it forms higher molecular weight oligomeric ensembles that appear to be in a tetrameric state, corresponding to a molecular weight of 80 kDa, while alphaAred(62-166) seems to be only dimeric.

,έν οἶδα, ὅτι οὐδέν οἶδα‘

Σωκράτης

,I know that I know nothing‘

Socrates

Acknowledgement

The completion of my dissertation and subsequent PhD has been a long journey. Many have questioned whether I would finish my dissertation, as they have doubted my commitment to it. I, on the other hand, except for losing confidence so many times, except for computers crashing and experiments not working, I needed to work as much as possible, and however the pure frustration in general, I knew I'd complete my PhD. I just had to do it in my own time and on my own terms. At any rate, I have finished, but I could not have succeeded without the invaluable support, patience and guidance of several people. In one way or another, each one individually contributed, so it is to them that I owe my deepest gratitude.

Since my first day in TUM, I have been given the opportunity by **Prof. Bernd Reif** to work in his group and evolve as a research scientist during the past five years. Therefore, my utmost gratitude goes to my enthusiastic supervisor and mentor, Bernd. My PhD has been a great experience and I thank Bernd wholeheartedly, not only for his academic support, motivation and patience, but also for giving me freedom to pursue various projects without objection. I am heartily thankful for his trust, supervision and help in every step I was about to take. He has never judged nor pushed, when he knew I needed to juggle priorities, and always replied with laughter to my sense of humor. He was always there smiling and advising me, always for my own good.

I would also like to express my gratitude to **Prof. Sevil Weinkauff**, our collaborator and member of my examining committee, for giving me the chance to join the α A project. Her flexibility in scheduling, gentle encouragement and relaxed demeanor made for a good working relationship and the impetus for me to finish. She was continually there to help and advise me with pleasure when needed, always in a team and adventurous spirit with regard to research, but also life. We've laughed together and she's also been kind, when I needed to cry. Sevil thanks for everything!

Of course, how can I forget one of the Profis on α -crystallins, **Prof. Johannes Buchner**. I really appreciate it for being part of my examination committee and also of my thesis throughout the years of my PhD, guiding me with scientific ideas and input. I am also really grateful to **Dr. Martin Haselbeck** and **Dr. Katrin Back**, our collaborators, who helped me especially in the lab work and my dear colleague **Dr. Christoph Kaiser** with whom I shared a lot of funny stories, except science that made our work run even more smoothly. Their academic support, input and personal cheering are greatly appreciated.

Special thanks go to all members of the **Reif group**, my office and lab mates, who have contributed immensely to my personal and professional time at TUM. Thanks for the fruitful hints, as well as for humorous private discussions. Thank you to those who helped the project as graduate students, **Pamina Kazman** and **Sarah Meinhold**. Both of you did a great job and I wish you all the best in your future plans in science.

Next, I owe my deepest gratitude to my colleague **Dr. Sam Asami**, for his patience and unselfish, but also unfailing support from the first day we met. Sami has played the part of teacher, friend, confidant, conscience, humorist etc. etc. He has always been a tremendous help no matter the task or circumstance. He has been tough on me, but also supportive and caring. We laughed, fought and cried together. However, Sam's guidance, constant feedback and excitement in regard to science kept me also motivated. For all these reasons and many, many more, S, I am eternally grateful. Thanks a lot for the precious moments we shared along the way. You shall be remembered as a warm and friendly heart and one of the few who assisted

me in completing my doctoral degree. I wish you lots of happiness and success in your work and private life, and you know that my house will always have an open door for you and your beloved ones!

I would also like to thank **all of my friends** who supported me in writing, and incited me to strive towards my goal. I am sincerely grateful for the memories we have shared and those we have yet to create. In particular, I would like to thank **Konstantina** for the hours we spent on the phone, while writing my thesis. She was always there to listen to my complaints and stories.

Though, no acknowledgments would be complete without giving thanks to **my family**. Words cannot express how grateful I am to **my mother, Vasiliki** and **my father, Anastasios** for all of the sacrifices that made on my behalf, and that they never complained that I only managed to see them a few days per year the last five years. You have taught me a lot about hard work and self-respect, about persistence and about how to be independent. Mom, especially, was a great role model of resilience, strength and character. Both have always expressed how proud they are of me and how much they love me. I too am proud of them and love them to the most. I am grateful for them both and for the ‘smart genes’ they passed on to me. Your prayer for me was what sustained me thus far. Thank you for supporting me for everything, and especially I can’t thank you enough for encouraging me throughout this experience by cheering me up every day.

Last, but not least, I would like to express appreciation to my future **husband, Yannis**, who spent sleepless nights with, and was always my support in the moments when there was no one to answer my queries. Yannis has unconditionally loved me during my good and bad times and he is the only person who can appreciate my quiriness and sense of humor. These past several years have not been an easy ride, both academically and personally. At the same time, he has also given me so many happy and beautiful memories throughout this journey. We have laughed and cried, traveled and played, built and settled, planned and discussed our lives. I truly thank him for sticking by my side, even when I was irritable and depressed. There are no words to convey how much I love him. The past years, I feel that we both learned a lot about life and strengthened our commitment and determination to each other, and to live life to the fullest.

My parents and Yannis, as my biggest fans and supporters, are the most important people in my world and I dedicate this thesis to them. Σας αγαπώ πολύ και σας ευχαριστώ! Φασολάκι μας σε περιμένουμε!

Financial support for this study was provided by **SFB1035** and I am grateful to both excellent graduate schools, **TUM – Graduate School** and **GRK1721**, which gave me the chance to participate in international scientific conferences and different soft skills courses.

Maria Stavropoulou

Table of Contents

Author's Declaration	iii
Zusammenfassung	iv
Summary	v
Acknowledgement	vii
Table of Contents	9
List of Figures	13
List of Tables	15
Abbreviations	16
1. Introduction	17
1.1. Protein Homeostasis and Folding	17
1.2. Molecular Chaperones	18
1.3. Heat Shock Proteins and Stress Response	21
1.4. Small Heat Shock Proteins	22
1.5. The α-crystallins: Structural Organization of Primary Sequence	25
1.6. Structure and Function of αB-Crystallin	27
1.6.1. The Role of Post-translational Modifications on α B-Crystallin	31
1.6.1.1. Phosphorylation of α B	31
1.6.1.2. Other Post-translational Modifications	33
1.6.2. Disease-related Mutations in the α B-Crystallin Sequence	33
1.7. Structure and Function of αA-Crystallin	35
1.7.1. The Role of Post-translational Modifications on α A-Crystallin	37
1.7.1.1. Phosphorylation of α A	37
1.7.1.2. Other Post-translational Modifications	38
1.7.2. Disease-related Mutations in the α A-Crystallin Sequence	38
1.8. Alzheimer's Disease	38
1.8.1. The A β Amyloid Peptide	39
1.8.2. The Structure of A β Amyloid Fibrils	40
1.8.3. The Role of α B-Crystallin in Alzheimer's Disease	42
1.9. Nuclear Magnetic Resonance Spectroscopy in Structural Biology	42
1.9.1. The Basic Principles of NMR	43
1.9.2. Chemical Shift	45
1.9.3. Protein Dynamics in NMR	47
1.9.3.1. Paramagnetic Relaxation Enhancement (PRE)	47
1.9.3.2. Relaxation	48
1.9.4. Diffusion-Ordered NMR Spectroscopy (DOSY)	49
1.9.5. Assignment Experiments in Solution-state NMR	50
1.9.6. Investigation of Large Biomolecules by NMR	50
1.9.6.1. Solid-state NMR Spectroscopy	51
1.9.6.2. Magic-Angle Spinning (MAS)	52

1.9.6.3. Proton-Driven Spin Diffusion (PDSD) Experiments	53
2. Aim of the Study.....	54
3. Materials and Methods	55
3.1. Materials.....	55
3.1.1. Chemicals.....	55
3.1.2. Equipment and Software.....	55
3.1.3. Bacterial Strains, Plasmids and Primers.....	55
3.1.4. Cell Growth Media.....	56
3.1.5. Buffer Solutions.....	57
3.2. Methods.....	58
3.2.1. Molecular Biology and Microbiological Methods.....	58
3.2.1.1. Plasmid Purification	58
3.2.1.2. Preparation of Competent Cells.....	58
3.2.1.3. Polymerase Chain Reaction and Site-directed Mutagenesis.....	58
3.2.1.4. Transformation of <i>E. coli</i> Cells.....	59
3.2.1.5. Glycerol Stocks.....	59
3.2.1.6. Agarose Gel Electrophoresis	59
3.2.1.7. Determination of DNA Concentration	60
3.2.1.8. Recombinant Protein Expression.....	60
3.2.1.8.1. Unlabeled Protein	60
3.2.1.8.2. ¹⁵ N or ¹³ C, ¹⁵ N Enrichment in Proteins	60
3.2.1.8.3. ² H, ¹³ C, ¹⁵ N and ILV - Labeling.....	61
3.2.1.9. Cell Harvest and Storage.....	61
3.2.2. Biochemical Methods and Sample Preparation.....	61
3.2.2.1. Cell Lysis	61
3.2.2.2. Purification of α -Crystallins.....	62
3.2.2.2.1. Anion-Exchange Chromatography (AEC).....	62
3.2.2.2.1.1. Weak Anion-Exchange Chromatography.....	62
3.2.2.2.1.2. Strong Anion-Exchange Chromatography.....	62
3.2.2.2.2. Size Exclusion Chromatography (SEC)	63
3.2.2.2.3. Strong Anion-Exchange Chromatography II	63
3.2.2.2.4. Strong Anion-Exchange Chromatography with Urea (uAEC)	63
3.2.2.2.5. Hydrophobic Interaction Chromatography (HIC).....	64
3.2.2.2.6. Analytical Size Exclusion Chromatography (aSEC).....	64
3.2.2.2.7. Ni – NTA Purification of α B-6E.....	64
3.2.2.3. Dialysis	65
3.2.2.4. SDS-PAGE Electrophoresis	65
3.2.2.5. Determination of Protein Concentration	65
3.2.2.6. Concentration of protein Samples by Ultrafiltration	65
3.2.2.7. Storage of Protein Samples.....	66
3.2.2.8. Mass Spectroscopy.....	66

3.2.2.9.	Monitoring Degradation.....	66
3.2.2.10.	Limited Proteolysis.....	66
3.2.2.11.	Analytical Ultracentrifugation (AUC).....	66
3.2.2.12.	PEGylation Reaction of the Full-length α B-Crystallin.....	67
3.2.2.13.	Purification of Recombinant A β ₄₀ Amyloid Peptide.....	67
3.2.2.14.	Tricine-SDS-PAGE Electrophoresis.....	67
3.2.2.15.	Transmission Electron Microscopy (TEM).....	68
3.2.2.15.1.	Preparation of A β ₄₀ Fibrils.....	68
3.2.2.15.2.	Negative Staining.....	68
3.2.2.15.3.	Immunoelectron Microscopy.....	68
3.2.3.	NMR Spectroscopy.....	69
3.2.4.	Solution-state NMR Spectroscopy.....	69
3.2.4.1.	Sample Preparation.....	69
3.2.4.2.	Peak Integration and Chemical Shift Perturbation (CSP).....	69
3.2.4.3.	DOSY Experiments.....	70
3.2.4.4.	Resonance Assignment Experiments.....	70
3.2.4.5.	Secondary Structure Prediction.....	71
3.2.4.6.	Titration Experiments.....	71
3.2.4.7.	NMR Relaxation Analysis.....	71
3.2.4.8.	Paramagnetic Relaxation Enhancement.....	71
3.2.4.9.	¹ H ^N R ₁ Relaxation Rates.....	72
3.2.4.10.	Methyl-TROSY Experiments.....	72
3.2.4.11.	¹³ C, ¹³ C NOESY-type Experiments in Solution – state NMR.....	73
3.2.5.	Magic-Angle Spinning in Solid – state NMR Spectroscopy.....	73
3.2.5.1.	Sample Preparation – Packing of Rotors.....	73
3.2.5.2.	¹³ C, ¹³ C-Correlation PDSO Experiments.....	74
4.	Results.....	75
4.1.	Growth Curves of A β ₄₀ , α B-WT, α B-6E and α A-WT in Different Media.....	75
4.2.	Expression and Purification of A β ₄₀	76
4.3.	Expression and Purification of α B-WT and α B- Δ NTD.....	77
4.4.	Expression and Purification of α B-6E with and without Urea.....	81
4.5.	Expression and Purification of the C-terminal His-tagged α B-6E.....	84
4.6.	Expression and Purification of α B-6D.....	89
4.6.1.	Monitoring Degradation of α B-6D at Room Temperature.....	95
4.6.2.	Limited Proteolysis of α B-6D with α -chymotrypsin.....	96
4.6.2.1.	Comparing the Stability of α B-6D and α B-WT.....	96
4.6.2.2.	Influence of Lysozyme on Proteolytic Digestion of α B-6D.....	97
4.6.3.	Analytical Ultracentrifugation (AUC) of the Phospho-mimicking Mutants.....	98
4.6.4.	¹ H DOSY Experiments of the Phospho-mimicking Mutants.....	98
4.7.	Interaction Studies in Solution-state NMR.....	99
4.7.1.	Binding Interactions of A β ₄₀ with α B-WT.....	99

4.7.2. Binding Interactions of A β ₄₀ with α B-WT and Cu ²⁺	102
4.7.3. Binding Interactions of A β ₄₀ with α B-6E.....	104
4.8. αB uses Different Interfaces to Capture an Amorphous and an Amyloid Client.....	105
4.9. PEGylation of wild-type αB-Crystallin.....	107
4.10. αA-crystallin: NMR Study of the Dynamic Part of a Redox-sensitive sHsp.....	109
4.10.1. Biochemical Studies on the Reduced and Oxidized state of α A.....	109
4.10.2. Backbone and Side-chain Assignments of the wild-type α A.....	111
4.10.3. Interactions of α A- with α B-crystallin in Solution-state NMR.....	114
4.10.4. Paramagnetic Relaxation Enhancement Experiments of α A.....	116
4.10.5. Chemical Shift Perturbation Calculations for reduced and oxidized.....	119
4.10.6. NMR Relaxation Analysis of α A _{red} , α A _{ox} and α B.....	122
4.11. Solid – state NMR PDS spectra of αB-WT and αA-WT.....	127
4.12. ¹³C, ¹³C – Correlation Spectra of αA and αB in Solution-state NMR.....	129
4.13. Solution-state NMR Investigations of the Truncated αA Construct.....	130
4.14. Prolines Isomerization of the C-terminal Region of αA.....	134
5. Discussion.....	142
5.1. The Effect of Phosphorylation on α B Structure and Chaperone Function.....	142
5.2. The Interaction of A β ₄₀ with α B and the Cu(II) Metal Ion.....	144
5.3. The Interaction of α B-Crystallin with Different Clients.....	144
5.4. Dynamic Fluctuations of the C-terminal Region of the Human α A.....	146
5.5. <i>Cis-trans</i> Proline Isomerization in the CTR of α A.....	147
5.6. Possible Roles for <i>Cis-trans</i> Proline Isomerization in the Cells.....	148
5.7. The Polydispersity of the Human α A-crystallin.....	149
6. Conclusion and Future Remarks.....	151
7. Appendix.....	153
8. References.....	158
9. Curriculum Vitae.....	168
10. List of Publications.....	169

List of Figures

Fig. 1.1. Schematic illustration of the funnel-shaped free-energy surface of protein folding.....	17
Fig. 1.2. Molecular and cellular mechanisms to maintain native protein structure.....	18
Fig. 1.3. Organization of chaperone pathways in the cytosol.....	19
Fig. 1.4. Molecular chaperones mechanisms.....	20
Fig. 1.5. Schematic overview of the number of representatives of the sHsp family in different organisms.....	23
Fig. 1.6. Primary sequence alignment of members of the human sHsp family.....	24
Fig. 1.7. Domain Organization of α -crystallins.....	26
Fig. 1.8. Side view of the hexameric ring formed by three asymmetric dimers.....	26
Fig. 1.9. Subunit assembly of α B-crystallin.....	27
Fig. 1.10. Three-dimensional model of the α B-crystallin 24-mer.....	28
Fig. 1.11. Three-dimensional reconstructions of α B-crystallin oligomers and their distribution using EM and IM-MS.....	29
Fig. 1.12. Structural information of the α B assembly.....	30
Fig. 1.13. Domain organization of human α B.....	32
Fig. 1.14. Phosphomimicking mutants of α B.....	33
Fig. 1.15. Homology model of human α B monomer.....	34
Fig. 1.16. α A and α B oligomers.....	35
Fig. 1.17. Domain organization of α A-crystallin.....	36
Fig. 1.18. Crystal structures of truncated α A-crystallin.....	37
Fig. 1.19. Alzheimer's Disease.....	39
Fig. 1.20. Metabolic processing of the transmembrane protein APP by the endoproteases α -, β - and γ -secretase.....	39
Fig. 1.21. Levels of molecular structure within an amyloid fibril.....	40
Fig. 1.22. The 3D structure of $A\beta_{(1-42)}$ solved by solid-state NMR.....	41
Fig. 1.23. Application of a magnetic field to a randomly oriented bar magnet.....	45
Fig. 1.24. A nucleus of spin 1/2 in a magnetic field B_0 is represented.....	45
Fig. 1.25. NMR signal.....	46
Fig. 1.26. Functional Relevant Time Scales of Protein Dynamics.....	47
Fig. 1.27. Three types of PRE.....	48
Fig. 1.28. Relaxation of magnetization vectors after a 90° pulse.....	49
Fig. 1.29. Effect of a magnetic field gradient pulse.....	50
Fig. 1.30. Representation of the principle of MAS in solid-state NMR.....	52
Fig. 3.1. MAS rotor filing tool for ultracentrifuges.....	73
Fig. 4.1. Generalized bacterial growth curve showing the phases in the growth of bacterial cultures.....	75
Fig. 4.2. Growth curves.....	76
Fig. 4.3. Expression and purification of $A\beta_{40}$	77
Fig. 4.4. Representative protein purification of human α B-WT.....	78
Fig. 4.5. Representative protein purification of the α B- δ NTD mutant.....	79
Fig. 4.6. 1H , ^{15}N HSQC spectra of the δ NTD mutant.....	80
Fig. 4.7. Solution - state NMR spectra recorded at 300 K and 500 MHz.....	81
Fig. 4.8. Test Expression of the α B-6E mutant.....	82

Fig. 4.9. Representative protein purification of the α B-6E mutant.....	83
Fig. 4.10. Comparison of the analytical SEC run of α B-WT and α B-6E.....	84
Fig. 4.11. Representative expression and protein purification of the α B-6E-C-term-histag mutant.....	85
Fig. 4.12. Solution-state NMR ^1H , ^{15}N SOFAST HMQC spectra at 300 K and 900 MHz.....	86
Fig. 4.13. Overlay comparison of α B-6E, α B-WT and α B-10m.....	87
Fig. 4.14. Transmission electron microscopy of the α B-6E mutant.....	88
Fig. 4.15. SAXS and CD data of α B-6E.....	89
Fig. 4.16. Representative expression SDS-PAGE gels.....	89
Fig. 4.17. Purification of unlabeled α B-6D.....	90
Fig. 4.18. Analytical size exclusion chromatography of unlabeled α B-6D.....	91
Fig. 4.19. Purification approaches with different AEC columns.....	92
Fig. 4.20. Precipitation of α B-6D and subsequent phenyl column approaches.....	93
Fig. 4.21. Overlay of ^1H , ^{15}N HSQC spectra of α B-6D and α B-WT in phosphate buffer.....	94
Fig. 4.22. SDS gel of the degradation of unlabeled α B-6D at room temperature.....	95
Fig. 4.23. SDS gel of α B-6D and α B-WT after limited proteolysis with α -chymotrypsin.....	96
Fig. 4.24. SDS gels of lysozyme (Lyso), α B-6D, as well as α B-wt and α B-6D with lysozyme after proteolytic degradation with α -chymotrypsin.....	97
Fig. 4.25. Sedimentation velocity AUC analysis of α B-wt, α B-6E and α B-6D.....	98
Fig. 4.26. DOSY correlation curves of ^{15}N -labeled α B-WT, α B-6D and α B-6E in phosphate buffer.....	99
Fig. 4.27. α B-Mediated Inhibition of $\text{A}\beta_{40}$ Fibril Formation <i>in vitro</i>	100
Fig. 4.28. ^1H , ^{15}N chemical shift perturbations (CSPs) of $\text{A}\beta_{40}$ upon α B-WT binding.....	101
Fig. 4.29. ^1H , ^{15}N chemical shift perturbations (CSPs) of $\text{A}\beta_{40}$ upon pH titration.....	101
Fig. 4.30. Quantification of $\text{A}\beta_{40}$ titrations with $\text{Cu}(\text{Gly})_2$	103
Fig. 4.31. ^1H , ^{15}N chemical shift perturbations (CSPs) of $\text{A}\beta_{40}$ upon α B-6E binding.....	104
Fig. 4.32. Model of α B-mediated inhibition of amorphous and amyloid aggregation.....	105
Fig. 4.33. Representative immunoelectron microscopy images of $\text{A}\beta_{40}$ fibrils in the presence α B.....	106
Fig. 4.34. PEGylation of α B-crystallin.....	108
Fig. 4.35. Biochemical experiments comparing reduced and oxidized α A.....	110
Fig. 4.36. Assignment of the backbone resonances of the human wild-type α A- and α B-crystallin in solution.....	111
Fig. 4.37. HNCA and CBCA(CO)NH strip plots.....	112
Fig. 4.38. Side chain assignments of the human wild-type α A-crystallin in solution.....	113
Fig. 4.39. Carbon chemical shifts and secondary structure prediction for the C-terminal domain of α A-crystallin plotted as a function of residue number.....	114
Fig. 4.40. Hetero-oligomers of labeled- α A and unlabeled- α B in solution-state NMR.....	115
Fig. 4.41. Intramolecular versus intermolecular CTD-ACD interactions, using spin labeling and reduced α A.....	116
Fig. 4.42. Absolute intensities of the PRE samples.....	117
Fig. 4.43. Intramolecular versus intermolecular CTD-ACD interactions, using spin labeling and oxidized α A.....	118
Fig. 4.44. Chemical Shift Perturbation Mapping of $\alpha\text{A}_{\text{red}}$ and $\alpha\text{A}_{\text{ox}}$	120
Fig. 4.45. $\alpha\text{A}_{\text{ox}}$ measured at 300 K and 318 K.....	121
Fig. 4.46. $\alpha\text{A}_{\text{red}}$ measured at 300 K and 318 K.....	122
Fig. 4.47. ^{15}N relaxation analysis performed at 300 K and 500 MHz.....	124

Fig. 4.48. ^{15}N relaxation analysis performed at 300 K and 950 MHz.....	125
Fig. 4.49. T_1 and $T_{1\rho}$ intensity curves versus the recovery delay.....	126
Fig. 4.50. 2D NCA spectra of the human αA -crystallin recorded at 0°C and 750 MHz.....	127
Fig. 4.51. MAS NMR on (A) αB (black) and αA (red) oligomers in solution.....	128
Fig. 4.52. Overlay of the aliphatic region of ^{13}C , ^{15}N (A) αB - and (B) αA -crystallin in solid- (black) and solution-state (red) NMR.....	129
Fig. 4.53. ^{13}C , ^{13}C NOESY solution-state NMR spectra of the aliphatic region of ^{13}C , ^{15}N αB -crystallin (A) protonated and (B) deuterated.....	130
Fig. 4.54. HPLC and DOSY analysis of the wild-type and truncated αA	131
Fig. 4.55. Reduced versus oxidized truncated αA	132
Fig. 4.56. Truncated αA versus αB -WT and truncated αB	133
Fig. 4.57. The disordered C-terminal region of αA -crystallin contains an abundance of charged and proline residues.....	134
Fig. 4.58. <i>Cis-trans</i> proline isomerization in αA - and αB -crystallin.....	135
Fig. 4.59. Diffusion attenuation profiles.....	136
Fig. 4.60. Schematic depicting the propensity for X-Pro peptide bonds to form either <i>trans</i> - or <i>cis</i> -proline conformations.....	137
Fig. 4.61. 2D strip plots from 3D NMR spectra that were used to assign the <i>cis</i> - and <i>trans</i> -Pro conformations of the αA -crystallin C-terminal region.....	138
Fig. 4.62. <i>Cis-trans</i> isomerization of αA reduced and oxidized.....	139
Fig. 4.63. Comparison of backbone motions for the <i>cis</i> - and <i>trans</i> -Pro conformations in the C-terminal region of αA -crystallin.....	140
Fig. 5.1. Copper binding site between the β -sheets 5 and 6+7 in the ACD of αB -crystallin.....	144

List of Tables

Table 1.1. Overview of the human small heat shock proteins expression in cells and tissues.....	25
Table 1.2. Known disease-related mutations of αA - and αB -crystallin in humans.....	34
Table 1.3. Sequential homology of αA - and αB -crystallin for different representatives of Chordata.....	36
Table 1.4. Properties of selected common nuclei.....	44
Table 3.1. Recipes for bacterial growth media and their composition.....	56
Table 3.2. Buffer solutions used in this work and their respective composition are listed below.....	57
Table 3.3. The PCR reactions were prepared in the following scheme in a total volume of 50 μl	59
Table 3.4. Composition of SDS gels.....	65
Table 3.5. Composition of Tricine-SDS gels.....	68
Table 3.6. NMR experiments performed for αA -WT assignment.....	70

Abbreviations

2D/3D	two dimensional, three dimensional
ACD	alpha crystallin domain
AD	Alzheimer's Disease
ADP	adenosine diphosphate
AEC	anion-exchange chromatography
APP	amyloid precursor protein
aSEC	analytical size exclusion chromatography
ATP	adenosine triphosphate
A β ₄₀	amyloid β -peptide
CSA	chemical shift anisotropy
CSI	chemical shift index
CSP	chemical shift perturbation
CTD	C-terminal domain
CTE	c-terminal extension
CTR	C-terminal region
D ₂ O	deuterium oxide
DMSO	dimethyl sulfoxide
DNA	deoxyribo-nuclein-acid
DOSY	diffusion-ordered NMR spectroscopy
<i>E. coli</i>	<i>Escherichia coli</i>
EDTA	ethylenediaminetetraacetic acid
EM	electron microscopy
FID	free induction decay
FROSTY	Freezing rotational diffusion of protein solutions at low temperature and high viscosity
hetNOE	heteronuclear nuclear overhauser effect
HMQC	heteronuclear multiple quantum coherence
HSP	heat-shock protein
HSQC	heteronuclear single quantum coherence
IPTG	isopropyl b-D-1-thiogalactopyranoside
LB	Luria-bertani
MAS	magic-angle spinning
NMR	nuclear magnetic resonance
NOE	nuclear overhauser effect
NTD	N-terminal domain
NTR	N-terminal region
O/N	overnight
PBS	phosphate buffered saline
PCR	polymerase chain reaction
PDS	proton-driven spin diffusion
PEG	polyethylene glycol
pI	isoelectric point
SAXS	small-angle X-ray Scattering
SDS	sodium dodecylsulfate
SEC	size exclusion chromatography
sHsps	Small heat shock proteins
TROSY	transverse relaxation optimized spectroscopy
WT	wild-type
α A	α A-crystallin
α B	α B-crystallin

Standard chemical and physical abbreviations are not listed.

1. Introduction

1.1. Protein Homeostasis and Folding

The ability of organisms to detect, respond, adapt and defend any environmental stressors, was obtained during evolution and it is a fundamental capability of the living cells that grow and reproduce (Badyaev *et al.* 2005). Mammalian cells typically express more than 20,000 different proteins with varying structure and function (Kim *et al.* 2013). Proteins are the chief actors within the cells and are essential constituents of all organisms as they participate in every biological process. Cells count on specific mechanisms that regulate protein homeostasis to maintain a stable and functional proteome as it plays a very important role to the health of the cell and to all the cellular processes ensuring proper protein synthesis, folding, translocation and clearance (Hartl *et al.* 2011; Morimoto *et al.* 2009). The process that proteins need to follow in order to adopt their native, three-dimensional structure from the synthesized polypeptide chain is termed protein folding (Dobson and Karplus 1999). However, the huge number of possible conformations of a polypeptide chain makes protein folding a complex process and coordinated interactions must be performed in order for the process to succeed. For this reason the development of energy landscapes allows the folding reaction to be described and visualized in a meaningful manner (Dinner *et al.* 2000). The energetic component of this process is depicted by funnel-shaped energy surfaces. From the unfolded state, represented at the top of the funnel, proteins fold along multiple, parallel downhill routes to the native state, which is thermodynamically more stable (Fig. 1.1). Although much of the information required for the folding of polypeptide chains into functional native conformations is encoded in the primary sequence, in the cellular environment that controls the stability and function of newly synthesized proteins, proteins are at great risk of misfolding and aggregation (Hartl *et al.* 2011). As mentioned, many parallel paths down the funnel might overlap and this can trap the proteins in these intermediate, misfolded or aggregated states (Fig. 1.1, Udgaonkar 2008). Aggregation is a concentration dependent process and is greatly enhanced in the highly viscous and crowded environment of the cytosol (300-400g/l) (Ellis and Minton 2006; Zimmerman and Trach 1991), which results in excluded volume effects that substantially favors the intermolecular interactions between folding intermediates (Ellis and Minton 2006; Ellis 1996).

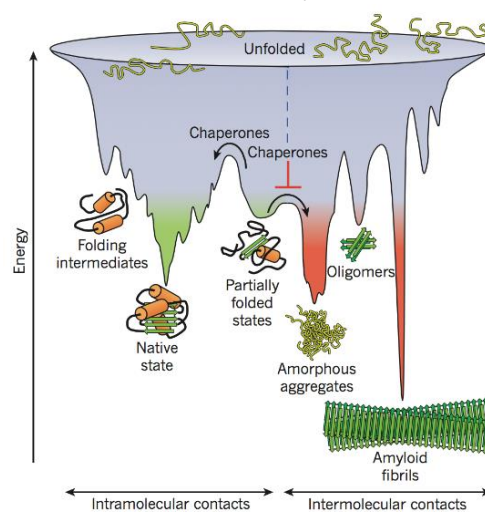


Fig. 1.1. Schematic illustration of the funnel-shaped free-energy surface of protein folding, while moving to their native state (green). Potential overlap of the free-energy landscape with that of intermolecular aggregation, arises the formation of amorphous aggregates, pre-fibrillar oligomeric states or amyloid fibrils (red). Adapted from Hartl *et al.* 2011.

In order for the cells to avoid these dangers, they developed various strategies to prevent aggregation and promote efficient folding, including molecular chaperones and the ubiquitin-dependent proteasome, which assist newly synthesized proteins to ensure their fold correctly or their degradation, and transport machineries and autophagic activities that help to localize and degrade proteins as necessary (**Fig. 1.2**) (Diaz-Villanueva *et al.* 2015; Morimoto *et al.* 2012; Hartl *et al.* 2011). Stress and aging, however, such as heat shock, oxidants, and metabolic or chronic stress, can unbalance this proteostasis network, thus increasing the risk of cellular pathology and disease. Most challenging diseases to be affected by the malfunctionality of the proteostasis machinery are diseases like Alzheimer's disease (AD), Parkinson's disease (PD), amyotrophic lateral sclerosis (ALS), Huntington's disease (HD), metabolic diseases and cancer. Each of the mentioned diseases has its own clinical and/or aging profile, but all of them share the fact that the expression of one or more aggregation-prone proteins can be causative for the disease (Morimoto *et al.* 2009). Protein misfolding should be a well-studied field in order to get to know a protein's nature, therefore, the understanding of these molecular mechanisms is a keystone for the development of pharmacological treatments of diseases associated to this (Diaz-Villanueva *et al.* 2015). In this study the main focus will rely on the mechanism of action of molecular chaperones and especially on small heat shock proteins (sHsps).

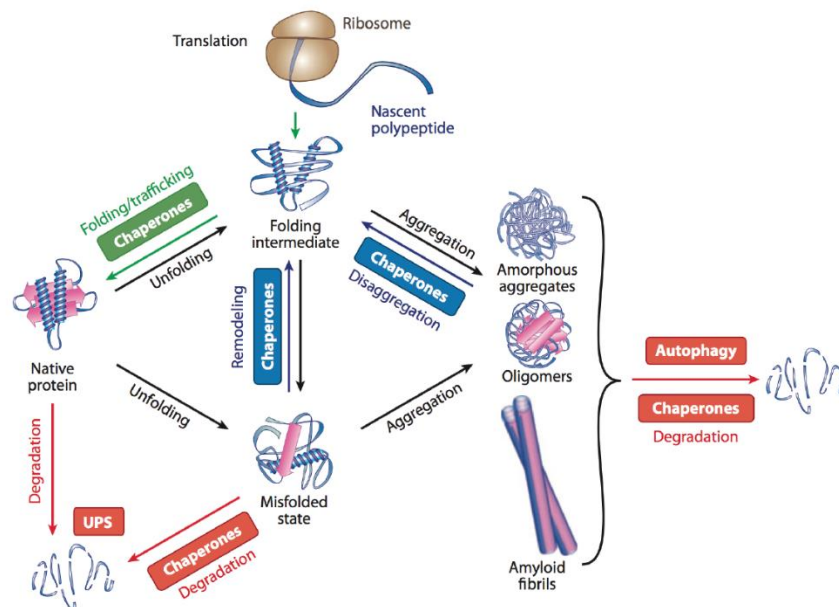


Fig. 1.2. Molecular and cellular mechanisms to maintain native protein structure. Adapted from Kim *et al.* 2013.

1.2. Molecular Chaperones

Protein folding, maintenance of proteome integrity and proteostasis require the assistance of a complex network of molecular chaperones (Hendrick and Hartl 1995). The investigation of chaperones has a long history (Ellis 1996). Molecular chaperones were firstly introduced in the literature to describe the ability of a nuclear protein to prevent the aggregation of folded histone proteins with DNA during the assembly of nucleosomes (Laskey *et al.* 1978). Later, in 1987, the term was extended to describe proteins that mediated the post-translational assembly of protein complexes (Ellis 1987) both in prokaryotic and eukaryotic cells (Hemmingsen *et al.* 1988), and the ATP-dependent protein folding was additionally shown *in vitro* (Goloubinoff *et al.* 1989).

Proteins with complex structures and high molecular weights during folding, may expose hydrophobic residues and regions of the polypeptide backbone that are not normally exposed to solvent, when the correct conformation is achieved. This makes them susceptible to non-native interactions that lead to aggregation and misfolding (Ellis and Minton 2006; Dobson and Karplus 1999). This is where the molecular chaperones play a key role to prevent protein aggregation. However, the molecular chaperone network functions are diverse during protein quality control, including procedures like protein unfolding and disaggregation and targeting terminally misfolded proteins for proteolytic degradation (Kim *et al.* 2013).

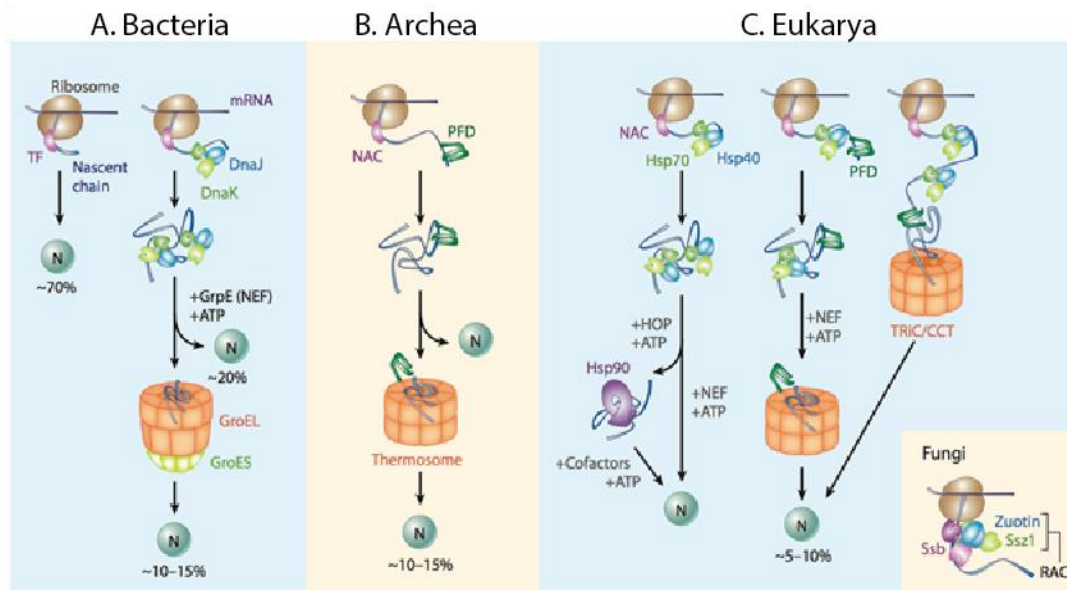


Fig. 1.3. Organization of chaperone pathways in the cytosol. In bacteria (a), archaea (b), and eukarya (c). Protein folding may start co-translationally and finish post-translationally upon chain release from the ribosome or after transfer to downstream chaperones. Adapted from Kim *et al.* 2013.

Molecular chaperones are found in the cytosol and the endoplasmic reticulum (ER) (Hartl 2002). The cytosolic pathways are highly conserved in all domains of life (bacteria, archaea and eukarya) and presented in Fig. 1.3. Chaperone involvement begins as newly synthesized proteins exit the ribosome, where there is an increased tendency to aggregate at this stage, due to exposure of non-native features, and the close proximity of nascent polypeptides of the same type at the polyribosome complex (Hartl 2002). In this phase ribosome-binding chaperones interact with the nascent polypeptide chain, followed by a second set of chaperones with no direct affinity for the ribosome, i.e. the classical Hsp70 system (Kim *et al.* 2013). After release from the ribosome, small proteins usually do not require additional modifications, in contrast to larger polypeptide chains that might require the help of Hsp70 chaperone family to fold correctly as an additional post-translational modification (Sharp and Workmann 2006; Hartl 2002).

Molecular chaperones are classified into several families according to the molecular weight of their monomers, although most of them exist as oligomers and since all members of this protein class are up-regulated in response to cellular stress, e.g. elevated temperatures, they are also known as heat-shock proteins (HSPs) (Hartl *et al.* 2011; Schlesinger 1990). The main families are usually divided into Hsp100, Hsp90, Hsp70, Hsp60 (also known as chaperonins), Hsp40 and small heat shock proteins (sHsps) (Budner 1996) and their mechanisms are illustrated in Fig. 1.4. Their molecular weights are in the range of 12-43 kDa (Vabulas *et al.* 2010). There is no homology between the different families of chaperones, however,

proteins from the same class often show sequence homology, and are functionally and structurally related (Walter and Buchner 2002). Chaperones can be further differentiated by their mode of action to the client protein. The ATP-dependent ones are termed as ‘foldases’ and they are directly involved in protein folding, while the ATP-independent are known as ‘holdases’ and they can recognize and stabilize partially folded proteins, preventing their aggregation and presenting client proteins to foldases (Bosl *et al.* 2006; Slepnev *et al.* 2002; Hartl 1996). These two types of chaperones are outlined separately in the next chapters with a focus on the sHsp family.

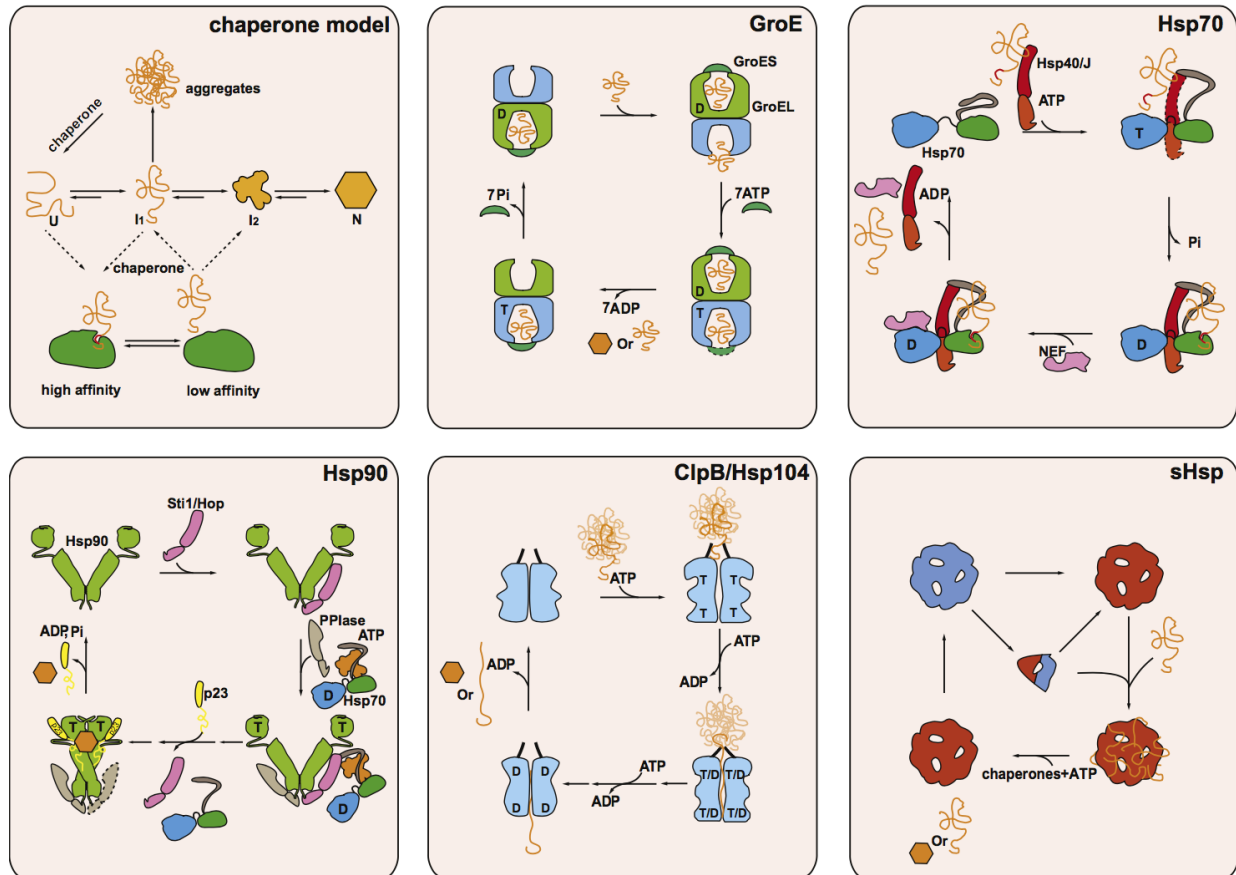


Fig. 1.4. Molecular chaperones mechanisms.

Chaperone model: Proteins fold via increasingly structured intermediates (I_1 , I_2) from the unfolded state (U) to the folded state (N), a process that under heat shock conditions can be reversed. Molecular chaperones bind proteins in non-native conformations. The shift from the high-affinity binding state to the low-affinity release state is often triggered by ATP binding and hydrolysis.

GroE: The GroE machinery in bacteria, mitochondria, and chloroplasts consists of two identical rings that enclose a central cavity each. Non-native protein is bound by the apical domains of the rings, and upon binding of ATP and the co-chaperone GroES, the protein is encapsulated and released into the cavity. ATP hydrolysis in one ring results in the release of GroES and substrate protein from the opposite ring. During encapsulation the protein may fold partially or completely, depending on the characteristics of the respective substrate protein.

Hsp70: The Hsp70 system comprises two co-chaperones: an activating protein (Hsp40/J-protein) and a nucleotide exchange factor (NEF). The activating protein can bind the non-native protein and deliver it to Hsp70. It forms a complex with Hsp70 and stimulates its ATPase activity. Hsp70 binds a stretch of seven amino acids in the substrate protein. The NEF will induce the exchange of nucleotide. The substrate protein is released presumably in a non-native form.

Hsp90: Hsp70 delivers the substrates to Hsp90. More than a dozen co-chaperones of Hsp90 exist in eukaryotes. One of them, Sti1/Hop, binds both Hsp70 and Hsp90 and at the same time inhibits Hsp90s ATPase (in yeast). In this complex, which also contains an additional PPIase co-chaperone, the substrate protein is transferred from Hsp70 to Hsp90. Sti1/Hop is released once Hsp90 binds nucleotide and a further co-chaperone, p23. The protein in complex with Hsp90 is bound and released as a structured intermediate (I_2).

ClpB/Hsp104: In bacteria and yeast, ClpB/Hsp104 is able to dissolve aggregates by actively pulling proteins through a central channel of the hexameric structure. During passage through the chaperone complex, the substrate protein is unfolded. Refolding can occur upon release, and, to some extent, it can also occur in cooperation with other chaperones.

sHsps: sHsps are oligomeric complexes that are often activated by heat or modifications. Many are believed to dissociate into smaller oligomers to become active. sHsps can bind many non-native proteins per complex. Release requires cooperation with other ATP-dependent chaperones such as Hsp70. Reproduced with permission from Elsevier (Richter et al. 2010).

1.3. Heat Shock Proteins and Stress Response

HSPs are a well-studied “stress response” of all organisms when subjected to rapid changes in their environment. Changes in the expression of the HSPs are controlled by a set of transcription factors referred to as heat shock factors (HSFs) (Bukau et al. 2006; Haslbeck et al. 2005; Hartl et al. 2002; Santoro et al. 2000). The first observation of the heat shock response was the discovery of heat-induced chromosomal puffings on the *Drosophila busckii* salivary gland chromosomes (Ritossa 1962). Later it was observed that heat shock treatment led to the synthesis of new proteins that were similar in different tissues of *Drosophila melanogaster*, while the levels of other proteins were reduced (Tissieres et al. 1974). The optimum temperature range of HSP induction varies within species. For example, for birds and mammals the optimum temperature is around 40–50 °C, for *Drosophila* 35–37 °C, for yeast 33–35 °C and for plants 35–40 °C. However, it has been found that the induction temperature can vary between different cell types of a single organism and between individual HSPs from even one cell type (Burdon 1986). In addition to increased temperatures, other insults also result in increased HSP expression, such as exposure of cells to various metals, amino acid analogues, hypoxia, and a large number of agents/treatments, which result in reduced ATP levels. HSPs or stress proteins are synthesized in cells grown under normal conditions and their expression increases (i.e. is induced) after metabolic stress (Tkáčová and Angelovičová 2012). In addition to their critical role in proteostasis, HSPs are implicated in human disease. Various medical conditions including fever, ischemia, hemodynamic overload or neurological injuries are well-known activators of HSPs *in vivo*. In infectious diseases, HSPs present within different pathogens are known to be major targets of our immune system and that’s why the study of them is very important (Macario et al. 2005).

HSP70 is one of the most conserved and stress-inducible proteins known to date (Hartl et al. 2011), with ~60% phylogenetic similarity between microbes and mammals (Bardwell et al. 1984). The ATP-dependent reaction cycle of HSP70 is regulated by chaperones of the HSP40 (also known as DnaJ) family and NEFs (Nucleotide Exchange Factors) (Mayer et al. 2010; Kampinga et al. 2010). HSP70 binding and release is achieved by an allosteric coupling between a conserved amino-terminal ATPase domain with a carboxy-terminal peptide-binding domain, the latter consisting of a β -sandwich subdomain and a α -helical lid segment (Mayer et al. 2010). During this reaction, hydrolysis of ATP to ADP is strongly accelerated by HSP40, leading to a stable peptide binding. HSP40 also interacts directly with unfolded polypeptides and can recruit HSP70 to protein substrates (Kampinga et al. 2010). After ATP hydrolysis, a nucleotide-exchange factor binds to the HSP70 ATPase domain and catalyses ADP–ATP exchange, resulting in substrate release (Sharma et al. 2010).

Chaperonins are large double-ring complexes of around 800–900 kDa that function by globally enclosing substrate proteins up to ~60 kDa for folding (Hartl et al. 2011). Chaperonins consist of two groups. Group I involves HSP60 (eukaryotes) and GroEL (bacteria). These proteins have seven-membered rings in bacteria, mitochondria and chloroplasts, and functionally cooperate with HSP10 proteins (GroES in bacteria). GroEL interacts with at least 250 different cytosolic proteins (Raineri et al. 2010; Kerner et al. 2005). The misfolded proteins are encapsulated in the apical domains of GroEL, binding to its hydrophobic amino-acid residues in the centre of the ring. GroES binding is ATP regulated and GroEL gets negatively charged in its inner wall, while the client protein is bound to it. The encapsulated protein is free to fold,

during ATP hydrolysis in the GroES-bound ring and it is subsequently released after GroES dissociation and rebound to GroEL for final refolding attempts (Hartl *et al.* 2009; Xu *et al.* 1997). The group II chaperonins, i.e. thermosome (archaea) and TRiC (eukaryotic cytosol), usually have eight-membered rings and they are independent of HSP10 factors (Munoz *et al.* 2011; Douglas *et al.* 2011; Frydman *et al.* 2001). The apical domains of these proteins, compared to the GroEL system, contain finger-like protrusions, which act as an iris-like, built-in lid and replace the function of GroES. TRiC reaction cycle is much slower than that of GroEL and TRiC interacts with approximately 10% of the newly synthesized cytosolic proteins, such as actin and tubulins (Munoz *et al.* 2011).

HSP90 is the most abundant of the HSPs. It functions downstream of HSP70 and exhibits some selectivity for a distinct set of “client” proteins. Most notably, HSP90 interacts with a variety of protein kinases and transcription factors important for growth and development. Additionally, it cooperates with several regulators and co-chaperones (Taipale *et al.* 2010; McClellan *et al.* 2007). HSP90 functions as a dimer of subunits that are assembled by their C-terminal domains and it undergoes an ATP-driven reaction cycle that is accompanied by structural rearrangements (Mayer *et al.* 2010). After ATP hydrolysis, the HSP90 monomers separate N-terminally and until the release of the client protein, various co-factors regulate the cycle like CDC37, HOP, AHA1 and p53, each one playing a different role. However, how HSP90 recruits different types of substrate protein with the help of various co-chaperones remains enigmatic. HSP90 though, has several substrate-interaction regions, and its binding strength is influenced by the structural flexibility of the substrate (Wandinger *et al.* 2008).

1.4. Small Heat Shock Proteins

Small heat shock proteins (sHsps) are a widespread and diverse class of molecular chaperones. Their monomer molecular weight varies from 12 to 43 kDa, but the most predominant number of representatives is in the range of about 20 kDa (Haslbeck *et al.* 2005; Narberhaus 2002). sHsps are often considered as non-essential chaperones, as under optimal conditions for the cell, most bacteria produce either no or negligible amounts of sHsps and only under stress conditions there is an increase at mRNA and protein level observed (Narberhaus 2002). They were first discovered in *Drosophila melanogaster* in 1974 together with other HSPs, like HSP70s and HSP40s, as proteins with small molecular mass that become activated rapidly in response to heat shock (Tissieres *et al.* 1974). Members of the sHsp family have been found throughout all kingdoms (Fig. 5A) with an exception of some pathogenic bacteria such as *Mycoplasma genitalium* and *Helicobacter pylori* (Kappe *et al.* 2002; Narberhaus 2002). In general, from bacteria (except Rhizobia) to higher eukaryotes there is a substantial increase in the number of sHsps per organism observed (*Mycobacterium tuberculosis*: 1, *Escherichia coli*: 2, *Drosophila melanogaster*: 4, *Homo sapiens*: 10, *Arabidopsis thaliana*: 19). This expansion is not yet clear, but the diversification must have occurred during differentiation in certain sHsps for functional reasons. Proteins belonging to the sHsp family are conserved and might be diverse in sequence and size, however, they share some common features, which distinguish them as a protein family, including: (i) a conserved α -crystallin domain of around 90 residues, (ii) formation of large oligomers with dynamic quaternary structure, and (iii) induction of chaperone activity by stress in suppressing protein aggregation and misfolding (Haslbeck *et al.* 2005).

The sHsps constitute the ‘first line of defense’ in terms of cellular stress. In fact, the cellular concentration of many sHsps is strongly increased in response to a variety of stresses, but they can also function constitutively in many organisms and tissues (Basha *et al.* 2012; Haslbeck *et al.* 2005; Narberhaus 2002). They were shown to act as ATP-independent molecular chaperones. Once activated, they function as holdases by partially binding exposed hydrophobic patches on non-native protein conformations and

through those actions prevent misfolded proteins from clumping together and forming aggregates (Horwitz 1992). When non-stress conditions resume, bound client proteins are released for refolding assisted by foldases (HSP40-HSP70 and HSP100) (**Fig. 1.5B**) (Haslbeck *et al.* 2005; Hoffmann *et al.* 2004). Generally, molecular chaperones exist in two states: an inactive (or low) and an active (or high) substrate affinity state (Haslbeck *et al.* 2005), and upon ATP binding and hydrolysis the transition between the two states can be triggered (Hartl 1996). In contrast, in sHsps, ATP has no direct role in the regulation of their chaperone activity and the equilibrium between these two models is controlled in a temperature-dependent manner. Upon heat-shock, the equilibrium is shifted to the high affinity state, where the active oligomer binds to the non-native substrate protein to form a stable sHsp-substrate complex that allows the prevention of irreversible substrate aggregation. Here then, together with the ATP-dependent chaperone families such as HSP70-HSP40 or HSP100, follows the release of the active substrate from the complex into its functional state for the cell. HSP70-HSP40 or HSP100 (has been identified only in bacteria, fungi and plants) can act directly on protein aggregation, however, the presence of sHsps increases the efficiency of the process (Haslbeck *et al.* 2005).

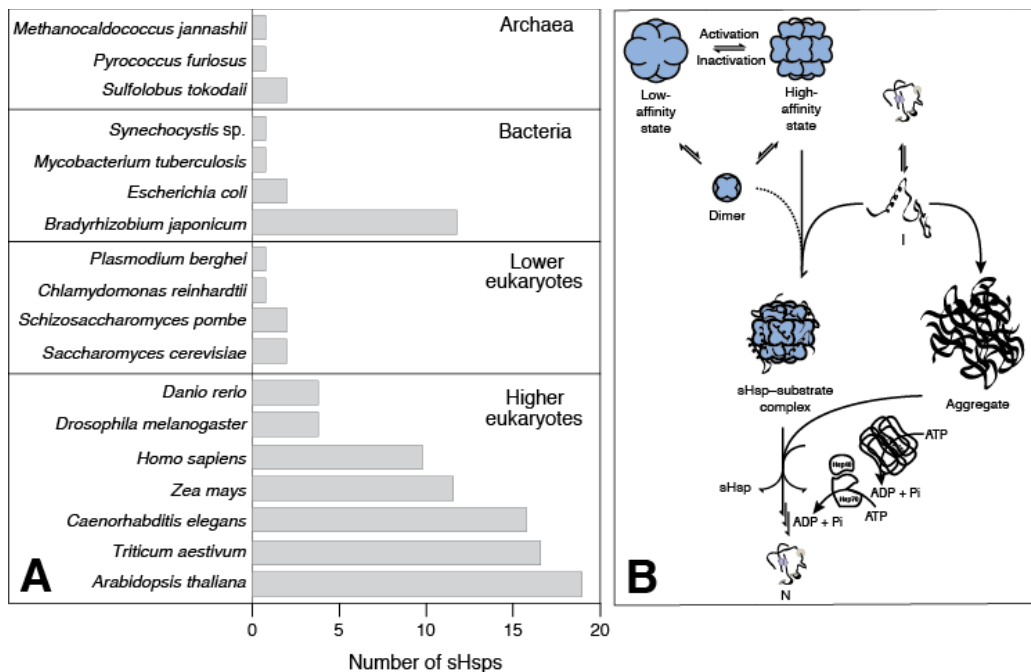


Fig. 1.5. (A) Schematic overview of the number of representatives of the sHsp family in different organisms. (B) The anti-aggregation property of sHsps. The multimeric assemblies of sHSPs are highly dynamic and exchange subunits rapidly. Upon cellular stress, the activated state can bind non-native proteins that otherwise would undergo irreversible aggregation. The non-native protein is stabilized within the highly soluble client-sHsp-complex and is directed to the ATP-dependent refolding machineries, e.g. HSP40/HSP70 and HSP100. Adapted from Haslbeck *et al.* 2005.

The universal occurrence of sHsps might be indicative of an early phylogenetic origin of this protein family (Basha *et al.* 2012; Haslbeck *et al.* 2005). Based on the results of the Human Genome Project, there are ten different sHsps specified in humans (HSPB1-HSPB10) (Gray *et al.* 2016; Kappe *et al.* 2003) (**Table 1.1**), each characterized by the presence of a conserved α -crystallin domain of about 100 residues. The primary sequence alignment of all ten human sHsps is presented in **Fig. 1.6**. The most representative sHsps are α A- and α B-crystallin, while little is known about the cellular function and regulation of the rest of the human sHsps. The human sHsps can be divided into two groups: the ubiquitous ones and the ones, whose expression and localization are restricted to distinct tissues (**Table 1.1**).

involved in forming disulfide-linked dimers is shown in cyan. The site of point mutations and an inversion mutation of the N-terminal region of α B (residues 54-60) are highlighted in yellow. Sequences were aligned using ClustalW multiple sequence alignment software as suggested by Thompson *et al.* 1994.

Table 1.1 | Overview of the human small heat shock proteins expression in cells and tissues. Currently accepted nomenclature from the HUGO Human Genome Nomenclature Database (<http://www.gene.ucl.ac.uk/cgi-bin/nomenclature/searchgenes.pl>) (Gray *et al.* 2016). The ten different human sHsp members are depicted along with their synonyms, mass, number of residues, specifications of localization and associated diseases.

HUGO	Synonyms	Mass (kDa)	Number of residues	Localization	Diseases
HSPB1	HSP27	22.3	205	Ubiquitous	Neuropathy, Cancer, Ischemia
HSPB2	MKBP	20.2	182	Heart and muscle	Myopathy, Ischemia
HSPB3	HSPL27	17.0	150	Heart and muscle	
HSPB4	CRYAA	19.9	173	Eye lens	Cataract
HSPB5	CRYAB	20.2	175	Ubiquitous	Neuropathy, Myopathy, Cancer, Ischemia, Cataract
HSPB6	HSP20	17.1	160	Ubiquitous	Neuropathy, Ischemia
HSPB7	cvHSP	18.6	170	Heart and muscle	Cardiomyopathy
HSPB8	HSP22	21.6	196	Ubiquitous	Neuropathy, Ischemia, Cancer
HSPB9	CT51	17.5	159	Testis	Cancer
HSPB10	ODF1	28.4	250	Testis	

1.5. The α -Crystallins: Structural Organization of Primary Sequence

The most widely studied family member, α -crystallin (Horwitz 1992), is a major constituent of the human eye lens, where the protein concentration may reach up to 450 mg per ml (Horwitz 2003). Initially, the isolation of these proteins proved to be intriguing, as these proteins were isolated as a large water-soluble highly dynamic oligomeric ensembles with a mass range from 200 kDa to > 1 MDa (Ecroyd and Carver 2008; MacRae 2000; Haley *et al.* 1998), like in the case of α A-crystallin (α A) and α B-crystallin (α B) (Horwitz 2003). The two α -crystallin genes in the mammalian eye lenses, α A and α B have amino acid sequence homology of about 58% and make up approximately one-third of the protein content of the eye lens (Tikhomirova *et al.* 2017; Horwitz *et al.* 1999; van der Ouderaa *et al.* 1974). Evidence that α -crystallin is essential for lens transparency and prevents protein aggregation *in vivo* comes from α A-crystallin-knockout mice, which develop severe cataracts at an early age (Horwitz 2003; Brady *et al.* 1997).

A characteristic that all sHsps share is the common structural organization. sHsps are organized into three regions: a conserved and central α -crystallin domain (ACD) flanked by a variable N-terminal and C-terminal domain (NTD and CTD, respectively) (Fig. 6) (Kriehuber *et al.* 2010; van Montfort *et al.* 2001; Kim *et al.* 1998). Dimerization of the ACD forms the basic building block of higher-order assemblies, which are established by intermolecular linkage via the terminal anchors. The sHsps exchange subunits (primarily dimers) in a constant manner (Stengel *et al.* 2010). The polydispersity of the α -crystallins is abolished by extensive deletion (~50%) of the N- and C-terminal domains (Laganowsky *et al.* 2010; Bagneris *et al.* 2009). Due to this subunit exchange, except for homo-oligomers, also hetero-oligomers may form, at higher temperatures (50°C), in compartments with different types of α -crystallins, as in the case of the eye lens, where α A performs its function in a hetero-oligomer complex with α B in a 3 to 1 ratio of α A to α B (Srinivas *et al.* 2010; Ghahghaei *et al.* 2009; Posner *et al.* 2008; Horwitz 2003).

The ACD has a sequence of around 90 residues and is the most important criterion for the integration of proteins in the α -crystallin family (Kappe *et al.* 2010). The sequential homology, however, varies from 20% to 60%, depending on the phylogenetic relationship (Kriehuber *et al.* 2010). Multiple sequence alignments

revealed that only a few amino acids are conserved, despite this structural organization (de Jong *et al.* 1998). The one is part of the sequence motif A-x-x-x-n-G-v of the ACD, which is the most significant indicator for this domain, and two further consensus motifs can be found: F-x-R-x-x-x-L, also in ACD, as well as an IXI motif in the CTD (Fig. 1.7). The average length of the ACD is around 161 amino acids, corresponding to about 18 kDa as shown by bioinformatics studies (Kriehuber *et al.* 2010).

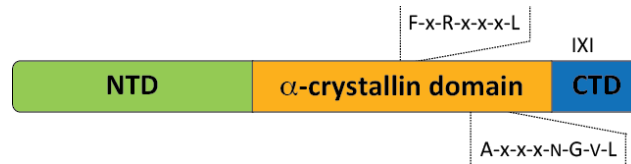


Fig. 1.7. Domain Organization of α -crystallins. The central α -crystallin domain (a) is shown in orange. The flanking Nterminal domain (NTD) and C-terminal domain (CTD) are depicted in green and blue, respectively. The approximate locations of consensus sequences are indicated by dotted lines. The figure was designed using Adobe Illustrator CS6.

The NTD is highly variable both in sequence and length. Therefore, the NTD is more responsible for the sequence variation of different α -crystallins within an organism. The average length of the NTD is about 56 residues, but it can range from 24 residues in HSP12 protein in *C. elegans* up to 247 residues in *S. cerevisiae* HSP42 (Haslbeck *et al.* 2005). In addition, the aromatic amino acids Trp and especially Phe, as well as Pro residues are overrepresented in the NTD (Kriehuber *et al.* 2010). The N-terminal regions are only partially resolved in the available crystal structures, suggesting increased flexibility (van Montfort *et al.* 2001; Van Montfort *et al.* 2001) and most of the post-translational sites for modifications are located within this region (Peschek *et al.* 2013; MacCoss *et al.* 2002).

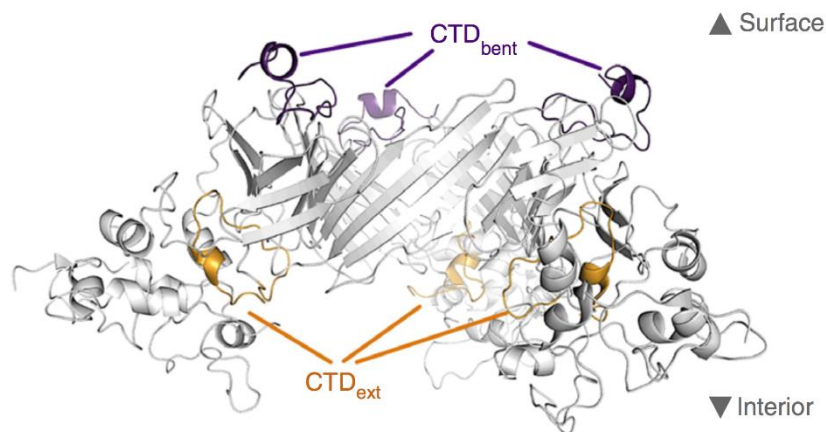


Fig. 1.8. Side view of the hexameric ring formed by three asymmetric dimers (Braun *et al.* 2011). CTD_{ext} (gold) is involved in interactions with NTD_{ext}, whereas CTD_{bent} (purple) is fairly solvent accessible. Reproduced with permission from the Nature Publishing Group (Mainz *et al.* 2015).

The C-terminal domain (also referred to as C-terminal extension), like the NTD, varies considerably in sequence. The CTD has an average length of 10 residues and does not exceed typically 20 - 25 amino acids. However, in some sHsp family members, i.e. human HSP20, the CTD is missing completely. The CTD harbors also the highly conserved, among sHsps, IXI/V-motif, in which the X is typically a proline residue (Garrido *et al.* 2012; de Jong *et al.* 1993) and can be critical for chaperone activity (Morris *et al.* 2008; Treweek *et al.* 2007; Fernando and Heikkila 2000; Kamei *et al.* 2000; Lindner *et al.* 1998) and for the stabilization of the high molecular oligomers (Basha *et al.* 2012; Hilton *et al.* 2013a; Jehle *et al.* 2010; Treweek *et al.* 2007; White *et al.* 2006; van Montfort *et al.* 2001a). Existing studies suggest that the whole

C-terminal region is flexible (Narberhaus *et al.* 2002; van Montfort *et al.* 2001; Van Montfort *et al.* 2001; Kim *et al.* 1998) (Fig. 1.8) (Mainz *et al.* 2015). Charged and polar amino acids are overrepresented in the C-terminal extension, while aliphatic and aromatic residues are underrepresented (Kriehuber *et al.* 2010). Although the α -crystallin domain is necessary for dimer formation, thus it assembles the basic building block, both flanking regions promote the formation of higher-order structures.

1.6. Structure and Function of α B – Crystallin

α B-crystallin, also called HSPB5, is a ubiquitous sHsp of 175 amino acid residues found on chromosome 11 (Ngo *et al.* 1989; Quax-Jeuken *et al.* 1985) and each monomeric subunit is 20 kDa. α B is strongly induced in response to a variety of cellular stresses and certain pathological states (Sun and MacRae 2005; Bloemendal *et al.* 2004; Clark and Muchowski 2000; Horwitz 1992). Its function is to maintain the transparency and high refractive index of the eye lens (Delaye and Tardieu 1983), thereby counteracting cataract formation and visual impairment (Bloemendal *et al.* 2004). α B-mouse knockout studies revealed that the presence of α B is not necessary for normal lens development (Brady *et al.* 2001). However, a surprising finding was the decreased life span of the knockout mice compared to the wild-type mice with the α B gene. Knockout mice lost weight, developed degenerative osteoarthritis and died prematurely (Brady *et al.* 2001). An additional finding from Andley *et al.* (2001), found that cells lacking the α B gene had a tendency to hyperproliferate.

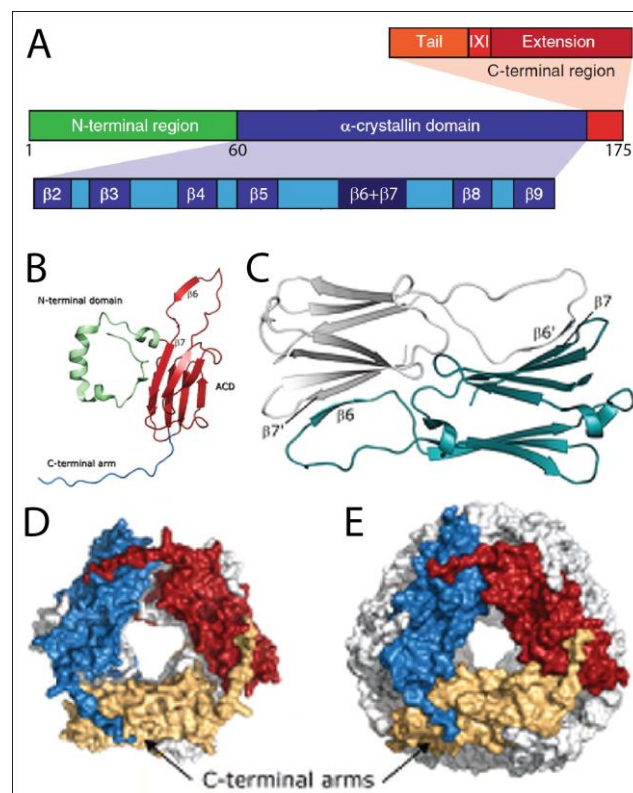


Fig. 1.9. Subunit assembly of α B-crystallin. (A) The domain organization of α B is illustrated. The ACD is composed of eight β -strands (Stengel *et al.* 2010). The C-terminal region is split into two parts, referred to here as the “tail” and “extension”, separated by an IXI motif. The N-terminal region by contrast has no obvious subdivisions. Modified from Hilton *et al.* 2012. (B) Crystal structure of wheat HSP16.9 illustrating the topology of the monomeric subunit. The conserved ACD (red) adopts an immunoglobulin-like fold with two anti-parallel β -sheets forming a β -sandwich structure. The ACD is flanked by variable N- (green) and C-terminal sequences (blue), which accomplish the higher-order assembly. (C)

Dimerization of the ACD via the strands $\beta 6$ and $\beta 7$ forms the building block of oligomeric assemblies. The two monomers of wheat HSP16.9 are colored in cyan and grey, respectively. Adapted from van Montfort *et al.* 2001. **(D)** The 12-mer assembly of wheat HSP16.9 is shown with three dimeric building blocks colored in red, blue and yellow. Modified from van Montfort *et al.* 2001. Two hexameric rings with three-fold symmetry arrange in a double-disk fashion. **(E)** For comparison, HSP16.5 of *Methanococcus jannashii* is depicted. Adapted from Kim *et al.* 1998. Three dimeric building blocks are highlighted in red, blue and yellow, respectively. Four of such hexameric rings are arranged with tetrahedral geometry in the 24-mer. The C-terminal anchors interact with neighboring monomers and thereby stabilize the complex.

Besides this specific lenticular function, the biological role of human αB is manifold as αB was also shown to interact with a wide range of substrate proteins that either aggregate amorphously or form amyloid fibril structures (Cox *et al.* 2016; Mainz *et al.* 2015; Kulig and Ecroyd, 2012; Ahmad *et al.* 2008; Nakamoto *et al.* 2007; Narayanan *et al.* 2006; Rekas *et al.* 2004; Horwitz 1992). Therefore, αB functions constitutively in multiple cell types, as it is expressed in several other tissues except the eye lens, such as the lung, kidney, brain, cardiac and skeletal muscles (Kato *et al.* 1991; Iwaki *et al.* 1990) and it is involved in neurodegenerative diseases like Parkinson's or Alzheimer's disease, in multiple sclerosis, cardiomyopathy or cancer (Steinman 2009; Sun and MacRae 2005; Vicart *et al.* 1998).

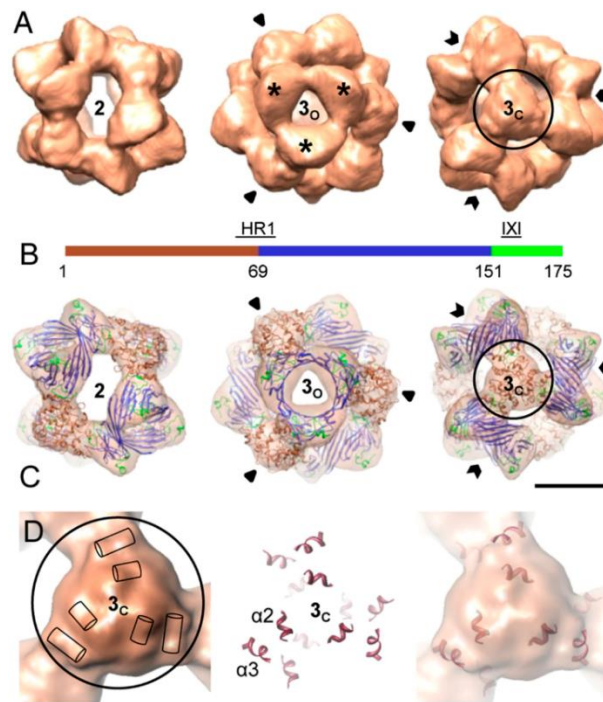


Fig. 1.10. Three-dimensional model of the αB -crystallin 24-mer. **(A)** Surface representations of the cryo-EM density map viewed along a two- (Left) and a threefold symmetry axis intercepting the area harboring a "window" (3_o , open arrows) (Center), and mass accumulation (3_c , closed arrows) (Right). Mass-rich domes surrounding 3_o are highlighted by stars. **(B)** Domain organization of human αB -crystallin: N-terminal domain (residues 1–68) (brown), ACD (residues 69–150) (blue), C-terminal region (residues 151–175) (lime green). The heterogeneous region 1 (HR1) and the IXI motif are indicated. **(C)** Views of the oligomer with the docked hybrid model of αB -crystallin 24-mer in a ribbon representation is superimposed. Ribbon color coding same as in B. **(D)** Close-up view of the density map at the area 3_c (Left). The positions of the rod-like densities are schematically indicated by cylinders. Surface near helices in the pseudoatomic model (Center) superimposed on the cryo-EM density map (Right). Copyright from the National Academy of Sciences (Braun *et al.* 2011).

The α -crystallin domain of αB is flanked by the variable N- and C-terminal regions, while the CTD is divided into the tail, the IXI-motif region and the C-terminal extension (Fig. 1.9A). Structural studies of αB have been difficult, as the protein forms polydisperse oligomers (Jehle *et al.* 2011) of different sizes, which are too heterogeneous to crystallize for X-ray diffraction studies and too large to yield reasonable linewidths in conventional solution NMR (Baldwin *et al.* 2011a; Aquilina *et al.* 2003; Horwitz 1992). Crystal structures

of sHsps have been determined firstly for HSP16.9 from wheat and HSP16.5 from *Methanococcus jannashii*, revealing 12-mer and 24-mer assemblies, respectively as presented in **Fig. 1.9** (van Montfort et al. 2001; Kim et al. 1998). These oligomers have an average mass of about 650 kDa with particles composed of 10 monomers up to more than 30 as assessed by analytical-SEC (Aquilina et al. 2003). Oligomers may exchange dimers (after activation) and therefore grow and shrink in size. The polydispersity of α B is attributed to the equilibrium between associated and dissociated forms of these building blocks. Numerous studies have suggested that this dissociated (monomeric and/or dimeric) form of sHsps is believed to be the ‘chaperone-active’ unit (Hochberg et al. 2014; Baldwin et al. 2011b). However, it has not been conclusively shown that the dimer is solely responsible for chaperone activity. Thus, more work is needed to explore the structure-function relationship of α B.

Despite the size limitation in solution NMR approaches, solution NMR has been used in examining truncated forms (Jehle et al. 2009) or regions of marked flexibility (Carver et al. 1992). Furthermore, large oligomeric species have been studied by solid-state NMR (Mainz et al. 2012; Jehle et al. 2011; Jehle et al. 2010) or via selective labeling of amino acids in methyl transverse relaxation optimised spectroscopy (TROSY) solution NMR (Baldwin et al. 2011c) and electron paramagnetic resonance (EPR) approaches (Alexander et al. 2008; Koteiche et al. 1999; McHaourab et al. 1997). All different strategies provide information, ensemble-averaged onto the monomer level, so in order to translate this onto the quaternary structure, studies such as solid-state NMR (Jehle et al. 2009), electron microscopy (EM) (pdb ID: 2YGD) (Braun et al. 2011; Jehle et al. 2011; Baldwin et al. 2011a), small-angle X-ray scattering (SAXS) (Jehle et al. 2011; Jehle et al. 2010) and ion-mobility spectrometry (IM-MS) (Baldwin et al. 2011a) have been combined, and all report on the oligomeric form of α B.

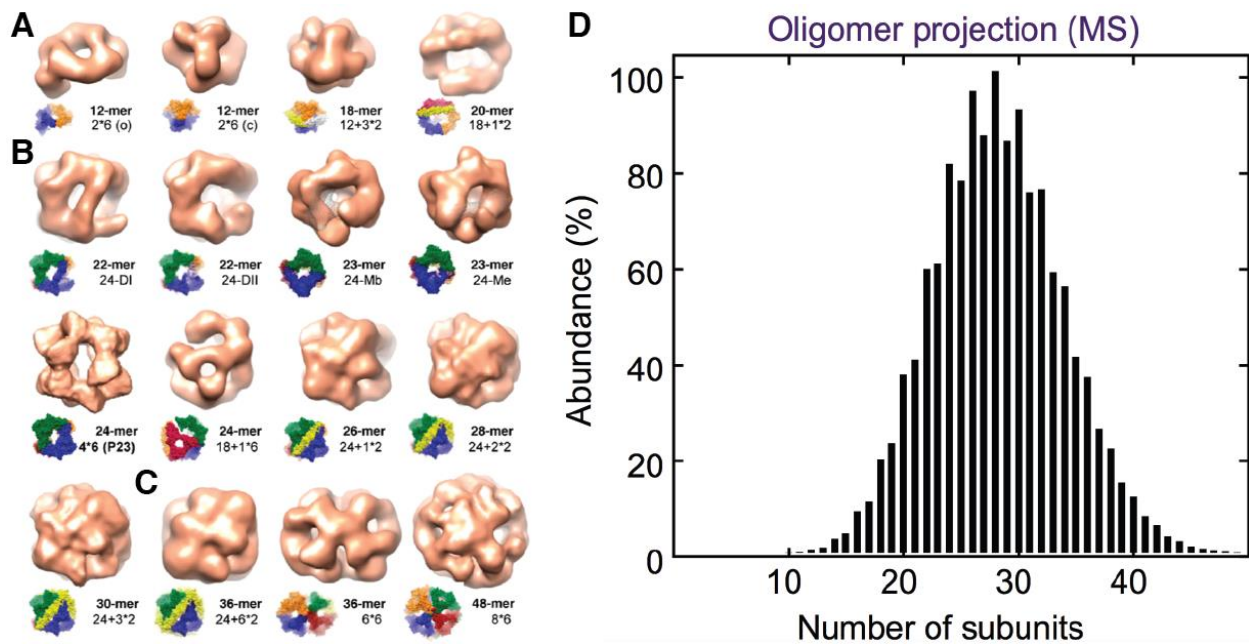


Fig. 1.11. (A) Three-dimensional reconstructions of α B-crystallin oligomers and their distribution using EM and IM-MS. Oligomers were found in a “small” (A), in a “24-mer” (B) and in a “large” (C) dataset. The insets show different oligomer models. Copyright from the National Academy of Sciences (Braun et al. 2011). (D) Full oligomeric distribution using MS experiments shows that the protein exists as a range of oligomeric forms containing between approximately 10 and 40 subunits. The heterogeneity in size observed by IM is independently confirmed by the diversity in the sizes of particles observed by EM. Reproduced with permission from Elsevier (Baldwin et al. 2011a).

Oligomers of α B well-studied by single particle analysis of EM data have revealed the envelope of a 24-mer with tetrahedral symmetry (**Fig. 1.12C**) (Peschek *et al.* 2013; Braun *et al.* 2011; Peschek *et al.* 2009; Haley *et al.* 1998) and according to the reconstructed α B 24-mers, α B is a hollow, spherical complex of approximately 13.5 nm diameter (**Fig. 1.10**) (Braun *et al.* 2011). The combination of solid-state NMR (Jehle *et al.* 2011), EM and cross-linking MS (Braun *et al.* 2011), led to the generation of a model based on hexameric sub-complexes (Braun *et al.* 2011; Jehle *et al.* 2011). Moreover, the analysis revealed a broad range of oligomeric sizes and masses with variable symmetries (Haley *et al.* 1998). However, IM-MS and cross validation with EM data, revealed a broad distribution of stoichiometries centered around 28 subunits and alternative structures for this proteins system (**Fig. 1.11**) (Baldwin *et al.* 2011b; Aquilina *et al.* 2003).

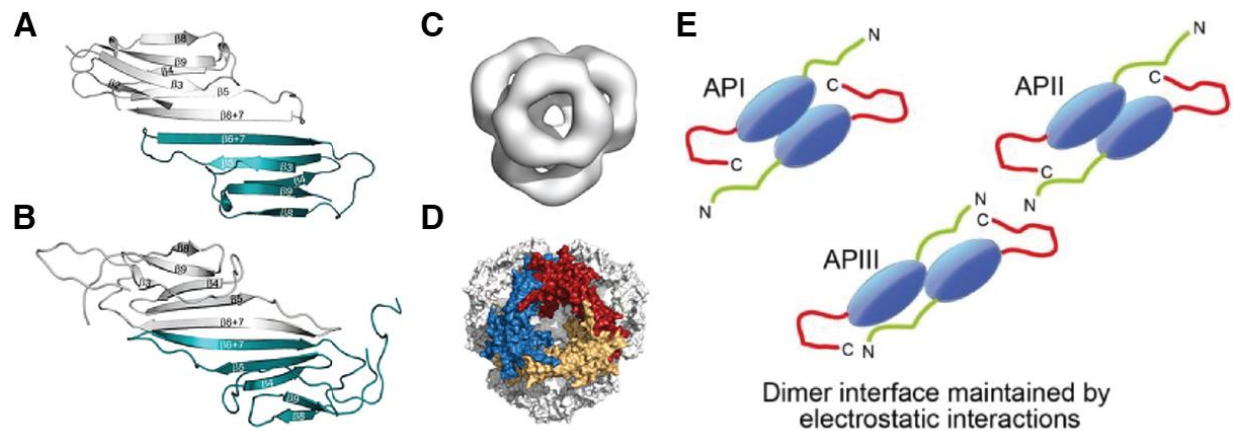


Fig. 1.12. Structural information of the α B assembly. (A) Crystal structure of the isolated α B ACD dimer (residues 67–157). Adapted from Bagn ris *et al.* 2009. (B) Solid-state NMR structure of the ACD dimer as present in full-length α B multimers (residues 64–152 are shown). Adapted from Jehle *et al.* 2010. In both A and B the two monomers are colored cyan and gray, respectively, while β -strands are also labeled. In comparison to the isolated ACD, the shared groove becomes more accessible as the dimer is much more curved in the context of α B multimers. (C) EM density map of the α B 24-mer showing the tetrahedral arrangement of four hexameric rings, each formed by three dimeric building blocks. Adapted from Peschek *et al.* 2009. (D) Structural model of the 24-mer of α B as obtained by combined data from solid-state NMR, EM and SAXS. Adapted from Jehle *et al.* 2011. Three dimeric building blocks are highlighted in red, blue and yellow, respectively. The flexible C-terminal extensions are excluded for clarity. (E) After synthesis and folding, α B monomers associate to form dimers, which are stabilised by electrostatic interactions and disulphide bonds. Dimers of α B can adopt a range of elongated antiparallel interaction (AP) registries (termed API, APII, APIII) along the dimer interface. Figure designed based on Hochberg *et al.* 2014 and Bagn ris *et al.* 2009.

The defining element and most highly conserved region of a sHsp sequence is the ACD. The ACD is flanked in α B by a variable \sim 60 residues NTD and a 25 residues CTD that accomplish the multimeric assembly. Structures for dimers of the core domain exist from either X-ray crystallography (truncated constructs without NTD or CTD) (pdb ID: 3L1G, pdb ID: 2WJ7) (**Fig. 1.12A**) (Laganowsky *et al.* 2010; Jehle *et al.* 2010; Bagn ris *et al.* 2009) or from solid-state magic-angle spinning (MAS) NMR (in the context of full-length oligomers, pdb ID: 2KLR) (**Fig. 1.12B**) (Jehle *et al.* 2010). Jehle *et al.* (2010) showed, using a combination of solid state-NMR, EM and SAXS (**Fig. 1.12D**) (Jehle *et al.* 2011) that human α B is a curved dimer with a \sim 121 $^\circ$ angle between a series of β -sheets (β 4- β 5- β 6+7) present in the ACD (Jehle *et al.* 2010). In all atomic-level structures the ACD of α B forms an immunoglobulin-like β -sheet sandwich of two layers with three antiparallel β -strands each (**Fig. 1.12A,B**) (Mainz *et al.* 2012; Jehle *et al.* 2009). The dimer interface is formed by an antiparallel (AP) (Laganowsky *et al.* 2010) β -sheet of strands β 6+7, which forms hydrogen bonds to strand β 6+7 of another core domain, hence called α B dimer. The separated β 6 and β 7 strands, as observed for HSP16.5 and HSP16.9, have merged into one strand β 6+7 in α B. The two top sheets (β 2- β 3- β 9- β 8) form a shared groove above the AP interface. The variable β 2 strand was refined only for two

of five molecules in the asymmetric unit (Bagneris *et al.* 2009). This point-symmetric, dimeric building block shows in the solid-state NMR structure a characteristic bent that is absent in the X-ray diffraction structures and therefore, might be of functional importance (Jehle *et al.* 2010). In both sides of the dimer there are regions of ionic interactions, leading to the hypothesis that specific residue pairs (e.g. G99-H119 and G117-H101) form pH-dependent electrostatic interactions on both sides of the dimer, resulting in its curvature and increased stability (Jehle *et al.* 2010). Later structures of the ACD confirmed that the dimer is curved and indicated that the dimer interface can adopt three different elongated AP registries (termed API, APII, APIII) (Fig. 1.12E), which result in a shift of two residues in the $\beta 6+7$ sheet (Hochberg *et al.* 2014; Laganowsky *et al.* 2010; Bagneris *et al.* 2009). All these structural variations may play a role in determining the chaperone efficacy.

The 'hybrid' approaches except for helping to address the structural heterogeneity of αB , highlighted also that the NTD (residues 54-70) of one αB dimer appears to interact with a neighbouring αB dimer through a yet to be determined process (Jehle *et al.* 2011). Additionally, the NTD is thought to play a key role in binding to partially folded clients, as determined by limited proteolysis-MS (Aquilina and Watt 2007; Sreelakshmi and Sharma 2005) and solid-state NMR (Mainz *et al.* 2015).

1.6.1. The Role of Post-Translational Modifications on αB -crystallin

sHsps undergo extensive post-translational modifications (PTMs) and as they do not possess ATPase activity their chaperone function is regulated from early on the organism's lifespan by PTMs (Ito *et al.* 1999). The modifications include phosphorylation, truncation (especially within the unstructured CTD), deamidation and glycation (Trewick *et al.* 2015). The mechanisms and functional roles of the alterations mentioned remain still unclear.

1.6.1.1. Phosphorylation of αB

Most common modification, occurring both intra- and extra-lenticularly in response to various kinds of stresses, e.g. temperature or pH (Kato *et al.* 1998; Ito *et al.* 1997), ischemia (Golenhofen *et al.* 1998), and hypoxia (Kase *et al.* 2010), is phosphorylation (Kampinga and Garrico 2012). The levels of phosphorylation increase with age and stress conditions (van den Ijssel *et al.* 1998; Ito *et al.* 1997; Kato *et al.* 1994; Landry *et al.* 1991). αB undergoes phosphorylation at three key serine residues (Ser19, Ser45 and Ser59) (Fig. 1.13) (Kato *et al.* 2001; Ito *et al.* 1997; Smith *et al.* 1992; Voorter *et al.* 1989). The majority of these post-translational changes are performed by mitogen activated protein kinase activated protein (MAPKAP) kinases (Landry *et al.* 1992a). In particular, phosphorylation at Ser45 is mediated by p44/p42 MAP kinase (ERK) and at Ser59 by MAPKAP kinase-2 (p38) (Kato *et al.* 1998; Ito *et al.* 1997), while the signalling pathway responsible for the phosphorylation of Ser19 is presently not known. Upstream of p38, RhoK, PKC and PKA are selectively involved in the activation of p38 and phosphorylation of αB at Ser59 (Launay *et al.* 2006). Phosphorylation is also common to other sHsps such as HSPB4 (Ser122) (Takemoto 1996), HSP27 (Ser15, Ser78 and Ser82) (Landry *et al.* 1992) or HSP20 (Ser16, mediated by cyclic nucleotide-dependent protein kinases) (Edwards *et al.* 2012; Beall *et al.* 1999).

Serine phosphorylation of αB primarily occurs within the NTD (Kato *et al.* 1998; Ito *et al.* 1997). The introduction of a strong negative charge at serine residues alters the oligomerization state of αB . Numerous structural and functional studies investigated the effect of phosphorylation on the chaperone

activity, polydispersity and oligomeric state of α B (Ecroyd *et al.* 2007; Aquilina *et al.* 2004). Phosphorylation mimics of α B (S19D/E, S19/45D/E and S19/45/59D/E) have been shown to either increase or decrease its chaperone activity compared to the wild-type protein (Peschek *et al.* 2013; Ahmad *et al.* 2008; Ecroyd *et al.* 2007; Aquilina *et al.* 2004). The overall effect of phosphorylation remains in general controversial, as some of the existing studies have reported conflicting data. For example, Peschek *et al.* (2013), Ahmad *et al.* (2008) and Ecroyd *et al.* (2007) have demonstrated that phosphorylation enhances chaperone activity, while others that it reduces it (Aquilina *et al.* 2004; Ito *et al.* 1997). In particular, phosphorylation of α B at the three serine residues (α B-3E mutant) does not result in the complete dissociation of oligomers, nor reduce its polydispersity (Peschek *et al.* 2013; Peschek *et al.* 2009; Ecroyd *et al.* 2007), but in an increase in the rate of subunit-exchange that leads to an increase in the abundance of the dissociated species (mainly 12-mers) (Fig. 1.14), enhancing its interaction with destabilised substrate proteins (Peschek *et al.* 2013; Ecroyd *et al.* 2007).

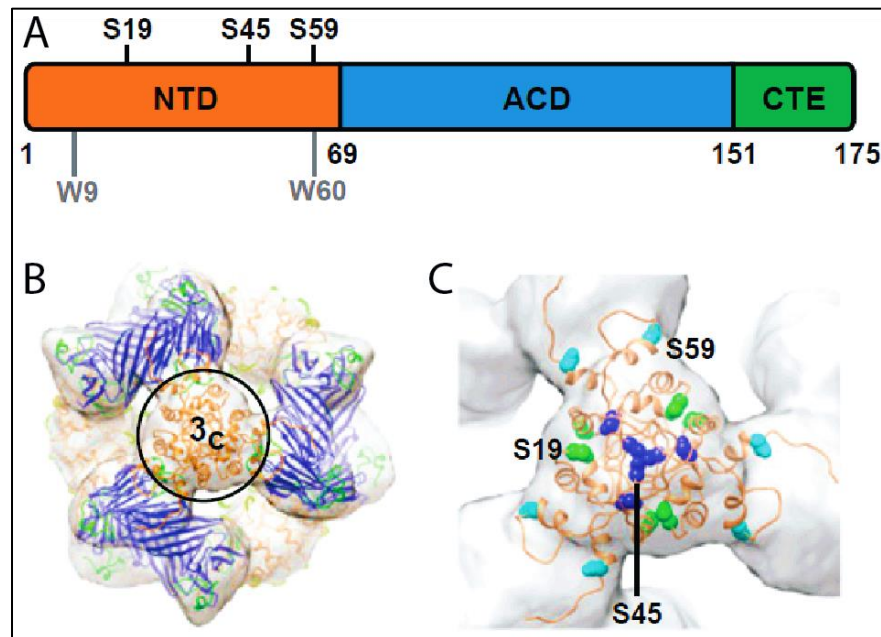


Fig. 1.13. Domain organization of human α B. (A) NTD (orange) with the three major phosphorylation sites (S19, S45 and S59), ACD (blue) and CTD (green) are shown. (B) The cryo-EM density map of the α B 24-mer with the docked pseudoatomic model according to Braun *et al.* (2011). (C) Zoom into the 3c area of the pseudoatomic model. The colored spheres depict residues S19 (green), S45 (blue) and S59 (cyan). Modified from Peschek *et al.* 2013.

This variation in the results, however, could be explained by the fact that the effect of phosphorylation on the chaperone activity of α B is specific to the client protein being used and depends on the number of sites of phosphorylation (Ecroyd *et al.* 2007), as client proteins possess different tertiary and quaternary structures and it is thought that the binding affinity of α B for client proteins is higher for clients, which are more destabilised, resulting in increased chaperone activity (Ecroyd *et al.* 2007; Koteiche and McHaourab 2003). In addition, phosphorylation affects the cellular distribution of some sHsps, like for α B and Hsp27, where phosphorylation causes them to be translocated into the nucleus (Bryantsev *et al.* 2007; den Engelsman *et al.* 2005; Adhikari *et al.* 2004; van den Ijssel *et al.* 2003; Voorter *et al.* 1992), in order to protect nuclear proteins from the stress conditions. Therefore, phosphorylation has been characterized as a 'molecular switch' that activates oligomeric dissociation and/or enhances subunit-exchange (by destabilisation of inter-dimer contacts), and thus, regulating the structure and also the cellular localization of the sHsps during stress periods.

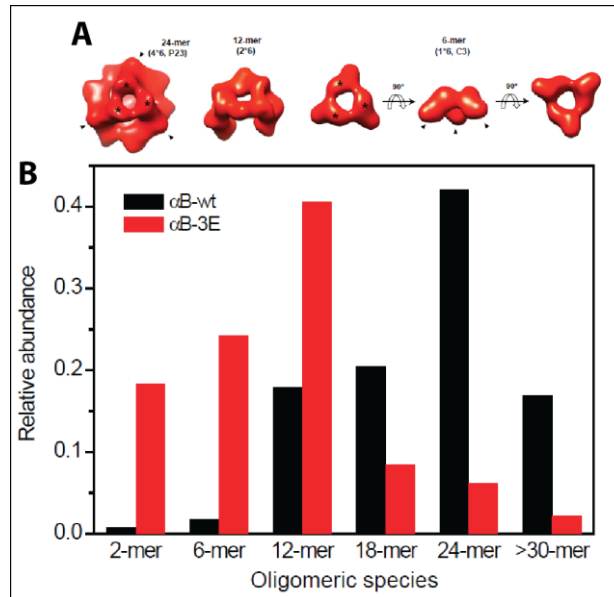


Fig. 1.14. Phosphomimicking mutants of α B. (A) 3D reconstructions of α B-3E oligomers observed in cryo-EM. The isosurface threshold was set to enclose a molecular mass of 485 kDa for the 24-mer, 242 kDa for the 12-mer, and 121 kDa for the 6-mer. (B) Distribution of the main oligomer populations in α B-WT (black) and α B-3E (i.e. S19E, S45E and S59E) (red) showing that the most abundant population for the wild-type protein is the 24-mer, while for the α B-3E mutant the 12-mer. Adapted from Peschek *et al.* 2013.

1.6.1.2. Other Post-Translational Modifications

There are additional PTMs, except for phosphorylation, like truncation, deamidation and glycation that influence the lens. They usually occur with age and are mostly associated with aggregation of the crystallin proteins, thus cataract formation. For example, four residues of the CTD of α B undergo truncation *in vitro*, when the C-terminal extension is exposed and this decreases the solubility of both α A and α B, reduces their protective ability and increases cataract formation (Tweek *et al.* 2007; Kamei *et al.* 2000). Further studies have shown by enzymatic truncation of the CTD *in vitro* with calpain II or trypsin (Takemoto *et al.* 1993; Kelley *et al.* 1993) or immobilization of the flexibility of the CTD by mutagenesis (Smulders *et al.* 1996) that there is a reduction in its chaperone ability against amorphously aggregating client proteins. Altogether, however, suggest that the C-terminal extension plays an important role in the chaperone function. Deamidation is another common PTM that occurs extensively to α A and α B and may be a key factor in the age-related denaturation of such lifelong proteins (Hains and Truscott 2010). During deamidation an additional negative charge from aspartic or glutamic acid is introduced to the protein and this leads to potential destabilising structural changes (Wilmarth *et al.* 2006). Moreover, during glycation, which is associated with diabetes, where the blood glucose is increased (Blakytyn *et al.* 1997; Stevens *et al.* 1978), occurs formation of covalent cross-links, aggregation and compromised chaperone activity of α -crystallins that can lead to diabetic cataract (Kumar *et al.* 2007).

1.6.2. Disease-related Mutations in the α B-Crystallin Sequence

In order to understand the role of α B in various diseases many studies tried to identify mutations directly associated with specific pathologies as seen in Table 1.2. R120G is a natural missense mutation occurring in the conserved ACD, in the α B dimer interface and it is identified as being responsible for a form of

desmin-related myopathy (DRM) and for cataract (Vicart *et al.* 1998). α B-R120G is associated with aggregation of the chaperone with the intermediate filament protein, desmin, in the cytoplasm of myofibrils (Xiao *et al.* 1999). Desmin is essential for tensile strength in myofibrils of muscles and this results to progressive muscle weakness. This mutation causes an increase of the oligomeric size and a decrease in the *in vitro* chaperone efficiency (Bova *et al.* 1999). Co-precipitates of desmin and α B-R120G are found in cardiac muscle tissue of patients suffering from desmin-related cardiomyopathy (Vicart *et al.* 1998). Similarly, α B-D140N mutation exhibits abnormal oligomerization and impaired chaperone activity, causing cataract (Liu *et al.* 2006; Berry *et al.* 2001). Mutations in the ACD of α B interfere with important interactions between subunits and they have a great impact on the association and dissociation properties of the oligomeric form (Hilton *et al.* 2013b). The locations of natural occurring disease-related mutations are presented in the α B model in Fig. 1.15.

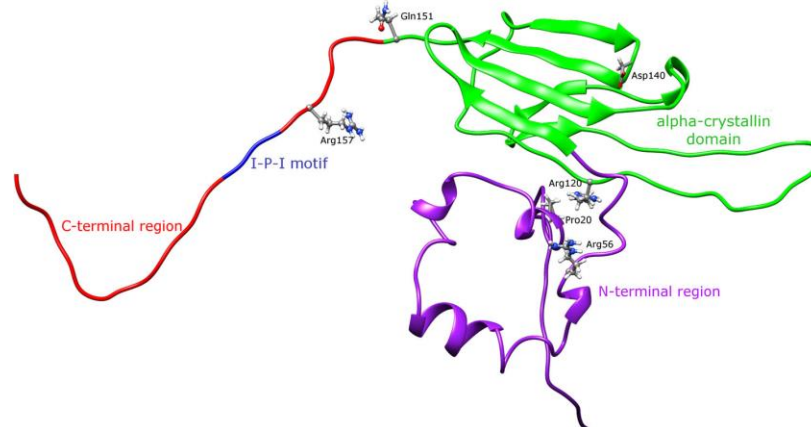


Fig. 1.15. Homology model of human α B monomer. The model shows approximate locations of naturally-occurring disease-causing mutations. Reproduced with permission from Clearance Center's RightsLink® service (Treweek *et al.* 2015).

Table 1.2 | Known disease-related mutations of α A- and α B-crystallin in humans. Numerous point mutations as well as deletions and truncations, have been associated with congenital diseases. These mutations alter the chaperone function and provide a link between the molecular chaperone action and disease manifestation.

α -crystallin	Mutant	Disease	References
αA (HspB4)	W9X, R12C, R12W, R21L, R49C, R45H, G98R, R116C, R116H	Cataract	Litt <i>et al.</i> 1998; Devi <i>et al.</i> 2008; Gu <i>et al.</i> 2008; Richter <i>et al.</i> 2008; Hansen <i>et al.</i> 2007; Graw <i>et al.</i> 2006; Sanithiya <i>et al.</i> 2006; Xia <i>et al.</i> 2006; Mackay <i>et al.</i> 2003
αB (HspB5)	R120G	Desmin-related myopathy, cataract	Vicart <i>et al.</i> 1998
	P20S, R56W, D140N, 450delA	Cataract	Safieh <i>et al.</i> 2009; Li <i>et al.</i> 2008; Liu <i>et al.</i> 2006; Berry <i>et al.</i> 2001
	R157H, G154S	Dilated cardiomyopathy	Inagaki <i>et al.</i> 2006; Pilotto <i>et al.</i> 2006
	Q151X (STOP)	Desmin-related myopathy	Selcen <i>et al.</i> 2003
	454delCT CRYAB gene	Desmin-related myopathy	Selcen <i>et al.</i> 2003
	450delA CRYAB gene	Cataract	Berry <i>et al.</i> 2001

Additional mutations associated with diseases are also presented in the NTD and the CTD regions (Fig. 15). The only cataract-causing mutation in the NTD of α B occurs in residue 20, where Pro is mutated to Ser. This mutation impairs also the chaperone function of α A (Li *et al.* 2008). Furthermore, in the C-terminal region mutations α B-R157H and α B-G154S lead to dilated cardiomyopathy (Selcen *et al.* 2003). In addition, another form of DRM arises from a deletion mutation (Q151X) and several other naturally-

occurring mutations/deletions have been identified to cause distributions in various tissues as shown in [Table 1.2](#).

1.7. Structure and Function of α A – crystallin

As opposed to human α B, human α A-crystallin (also termed as HSPB4) is a not well-studied protein and not much is known regarding its structure or mechanism of action. The α A gene is found on chromosome 21 (Ngo *et al.* 1989; Quax-Jeuken *et al.* 1985), encodes a 173 amino acid residue protein and possesses a monomer mass of 19.9 kDa (Haslbeck *et al.* 2016; Groenen *et al.* 1994). In addition, α A has two cysteines at positions C131 and C142, which can form disulphide bonds. α A performs its function in the eyes in a hetero-oligomeric complex with α B (800 kDa) ([Fig. 1.16](#)) (Horwitz *et al.* 1999) and for this interaction it was suggested earlier that residues 42-57 and 60-71 are involved for the oligomer formation (Sreelakshmi *et al.* 2004). The α A/ α B ratio in the α -crystallin complex may differ for different organisms (Ghahghaei *et al.* 2009; Posner *et al.* 2008). Furthermore, a recent study has shown that α A has many interaction partners. The use of microchips revealed 127 target proteins associated with phosphorylation, alternative splicing, acetylation, binding to DNA and RNP, cell cycle, membrane transport, transcription, GTP-binding, and cell response to unfavorable conditions of the surrounding (Fan *et al.* 2014).

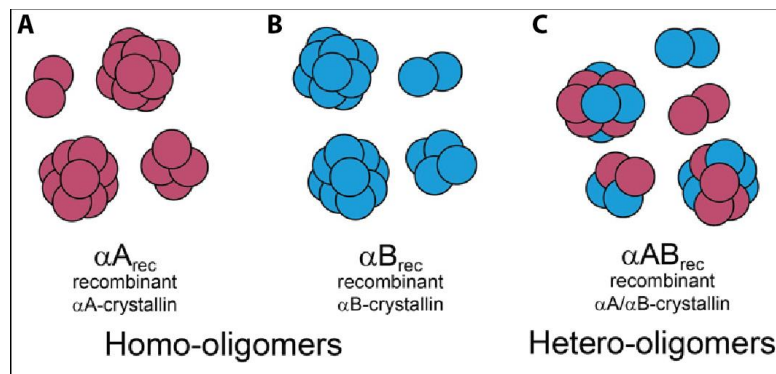


Fig. 1.16. α A and α B oligomers. α A and α B form dynamic homo- (A) α A (purple) and (B) α B (blue) and hetero-oligomers (C) of varying stoichiometries. Adapted from Haslbeck *et al.* 2016.

α A and α B have also a differential tissue distribution. α A was initially thought to be lens specific, but its non-lenticular expression was also described as it is expressed additionally in the spleen, thymus, brain and retina (Horwitz *et al.* 1992; Srinivasan *et al.* 1992; Kato *et al.* 1991) in concentrations no less than 40% of all proteins (Bloemental *et al.* 2004). In the eye lens, increased concentrations of α A provides its transparency (Delaye and Tardieu 1983) and protects epithelial cells of the lens from adverse effects of the surrounding by preventing aggregation of damaged eye lens proteins (Horwitz *et al.* 1992). Defects in the α A gene are associated with lens turbidity thus, early cataract formation (Wei *et al.* 2016; Sun and MacRae 2005; Brady *et al.* 1997). The role of α A is easily demonstrated in gene knockout studies published by Brady *et al.* (1997), where α A knock out mice resulted in cataract development starting in the nuclear area with progression involving the entire lens. In addition to cataract formation, dense inclusion bodies were also discovered, consisting of α B (Brady *et al.* 1997). This study concluded that the expression of α A is necessary not only for the maintenance of lens transparency, but also for controlling the solubility of other crystallins in the lens (Xi *et al.* 2003; Brady *et al.* 1997).

Table 1.3 | Sequential homology of α A- and α B-crystallin for different representatives of Chordata. The pair alignment and calculations of the identity of amino acid sequences were made using the Jalview v.2.9.0b2 program.

Organism	<i>Sus scrofa</i>	<i>Squalus acanthias</i>	<i>Rattus norvegicus</i>	<i>Ovis aries</i>	<i>Oryctolagus cuniculus</i>	<i>Mus musculus</i>	<i>Mesocricetus auratus</i>	<i>Lithobates catesbeiana</i>	<i>Homo sapiens</i>	<i>Gallus gallus</i>	<i>Bos taurus</i>
Degree of Homology (%)	55	47	47	56	54	46	48	53	58	55	56

In general, the molecular mechanism of the chaperone-like properties of α A is to be clarified, as the three-dimensional structure of full-length human α A is not yet determined. Until now, due to the heterogeneity and the difficulty in purifying and crystallizing α A homo-oligomers, two crystal structures have been solved. The one of the truncated bovine α A, i.e. residues 59-163 (Laganowsky *et al.* 2010a) and the one of the truncated zebrafish α A, i.e. residues 60-166 (Laganowsky *et al.* 2010b). Both constructs are lacking the NTD, but they contain part of the C-terminal extension. Electron microscopy of negatively stained human recombinant α A suggests that α A appears as almost globular assemblies with size heterogeneity and with a small fraction of elongated particles, which are almost absent in α B (Peschek *et al.* 2009).

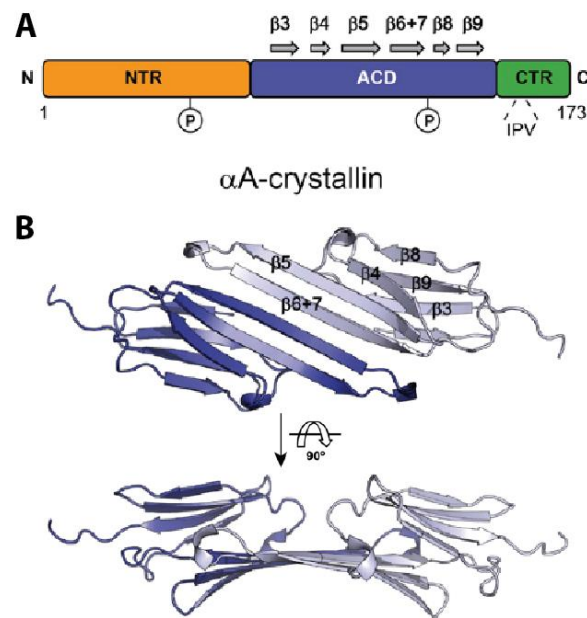


Fig. 1.17. (A) Domain organization of α A-crystallin. N-terminal region (NTR) (orange), α -crystallin domain (ACD) (blue), C-terminal region (CTR) (green). The conserved IPV motif and the major phosphorylation sites (Ser45 and S122) are indicated. **(B)** Structure of the respective ACD-dimer (X-ray, pdb ID: 3L1F). Modified from Haslbeck *et al.* 2016.

The three-dimensional structure of the α A monomer is similar to the α B monomer as their homology is high (Table 1.3). α A is organized into three regions like all sHsps: the central α -crystallin domain (ACD), and the flanking N-terminal and C-terminal regions (NTR and CTR, respectively) (Fig. 1.17A) (Haslbeck *et al.* 2016). The ACD of α A looks also like a β -sandwich of seven β -strands stabilized by hydrogen bonds and hydrophobic interactions of amino acid residues (Fig. 1.17B), where dimers are formed by bonds between β 6+7 strands. The bovine C-terminal region contains an IPV motif and a pseudopalindromic sequence

ERAIPVSRE, which indicates that the interaction between αA monomers can proceed in two directions (Fig. 1.18A,B) (Laganowsky et al. 2010a). In contrast, in the αB structure the same region is a true palindrome. In the crystal structure of the truncated zebrafish αA , which is dimeric in solution, two molecules dimerize via their $\beta 6+7$ strands and two such dimers form a tetramer by approaching of the $\beta 2$ -strands of the ACD, as Ser67 in $\beta 2$ -strands form hydrogen bonds with histidine and lysine residues in unstructured regions between $\beta 6+7$ and $\beta 5$ strands of neighbouring monomers (Fig. 1.18C,D). The IPV motif is not involved in intermolecular interactions within the tetramer in zebrafish αA , but it binds into the $\beta 4/\beta 8$ pocket formed by the same chain. Therefore, truncated zebrafish αA represents so far the only non-domain swapped configuration among the α -crystallins of known structure (Haslbeck et al. 2016; Laganowsky et al. 2010b). Taken together, the oligomer formation and structure of αA seems similar to the modular architecture of αB .

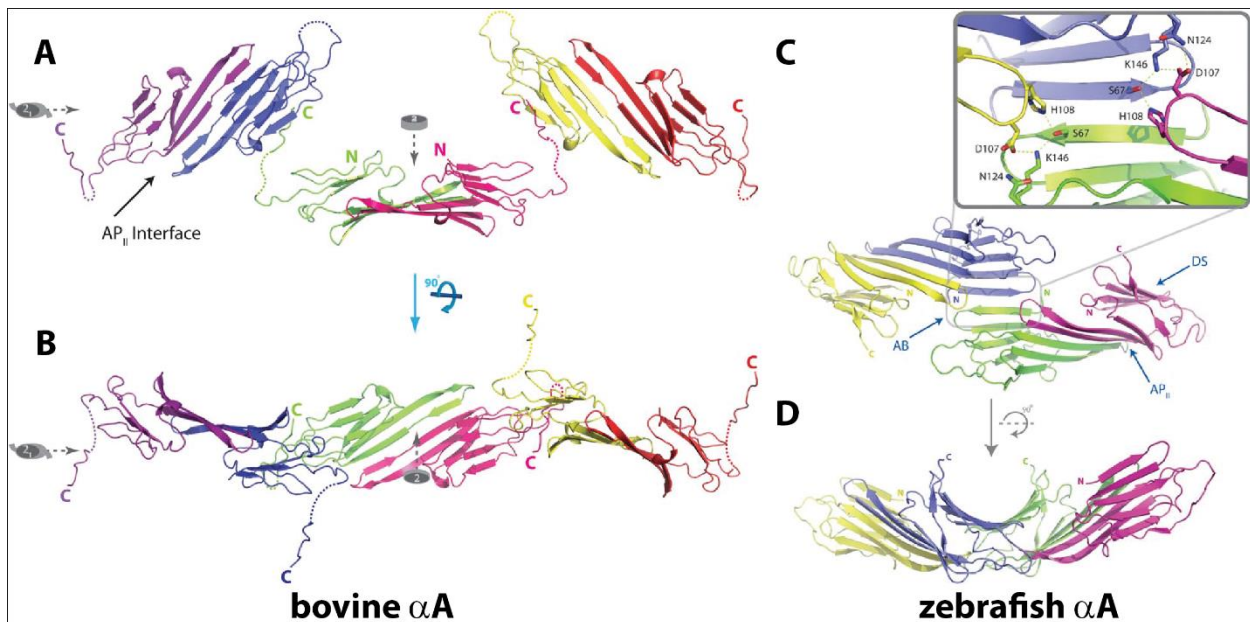


Fig. 1.18. Crystal structures of truncated αA -crystallin. (A) The bovine αA (residues 59-163) reveals C-terminal tail binding to adjacent chains and protrude from each end of the central dimer. The extended C-terminal extensions bind to adjacent dimers. (B) The C-terminal extensions of the bound adjacent chains (colored blue and yellow) can interact with differing adjacent dimers (Laganowsky et al. 2010a). (C) In the zebrafish αA (residues 60-166) four chains form a closed tetramer mediated through a previously unobserved dimeric interface (AB), where each C-terminal extension binds to its own domain (DS). The inset is an enlarged view of the dimeric interface, AB, created by $\beta 2$ -strand and the loop, located in between strands $\beta 5$ and $\beta 6$. Hydrogen bonds are shown by dashed yellow lines. (D) A 90° rotation of the closed tetramer about a horizontal axis. Adapted from Laganowsky et al. 2010b.

1.7.1. The Role of Post-Translational Modifications on αA -Crystallin

The reason for the loss of the functional activity of αA can be different mutations and post-translational modifications. This may result in its aggregation, lens turbidity, and cataract development.

1.7.1.1. Phosphorylation of αA

Unlike αB -crystallin, detailed studies for αA phosphorylation are rare. Earlier *in vivo* studies showed that the phosphorylation sites of αA in the lens are at Ser122 and Ser148 (Chiesa et al. 1987; Voorter et al.

1986) and the major phosphorylation site (Ser122) is age regulated (Takemoto 1996). Regarding the phosphorylation sites of α A there are different studies. Schaefer *et al.* (2006) identified eight different phosphorylation sites (Thr4, Ser20, Ser45, Ser59, Ser148, Ser155 and Ser172 or 173) in mouse lenticular samples *in vivo*, while Chiou *et al.* (2010) identified *in vivo* from porcine nine (Ser20, Ser59, Ser62, Ser66, Ser81, Ser86, Ser148, Ser155 and Ser173) sites. Further, very little is known about the function of the phosphorylation sites and of the mechanism of phosphorylation, however, it is believed that serine-specific phosphorylation is occurring via cAMP-dependent protein kinase pathways (Spector *et al.* 1985).

1.7.1.2. Other Post-translational Modifications

Acetylation of Lys70, Lys99 and Lys166 in α A sequence leads to a change in the surface charge and affects the conformation and functional activity of α A (Nagaraj *et al.* 2012; Lin *et al.* 1998). Another type of modification is isomerization of aspartic acid, where due to conformational transitions in the secondary structure of the chaperone, there is partial loss of its functional activity (Fujii *et al.* 2003). α A undergoes also spontaneous deamidation of asparagine and glutamine residues. Asn101 in human α A undergoes deamidation during the initial 30 years (Takemoto 1998). Deamidation has no real effect on the chaperone like activity, but there is a decrease in the activity upon isomeric transition of Asn123 (Chaves *et al.* 2008). The amino acid sequence of α A includes Cys131 and Cys142, but no S–S bond is formed in the native water-soluble form of the protein. Upon deamidation however, conformational changes draw together the cysteine residues resulting in the formation of a disulfide bond, which transfers α A to a water-insoluble state (Lund *et al.* 1996).

1.7.2. Disease-related Mutations in the α A-crystallin Sequence

The mutation α A-R116C in the ACD results in hereditary cataract (Litt *et al.* 1998) and can also lead to a reduction in its protective ability against epithelial cell apoptosis in the lens (Andley *et al.* 2002). Specifically, the substitution of an arginine for a cysteine at position 116 exposes a previously buried residue that seems to disrupt salt bridges and potentially leads to the formation of non-native, intersubunit disulphide bonds. Therefore, this perturbation causes a decrease in chaperone activity and subsequent aggregation of the natural target proteins of α A in the lens (Clark *et al.* 2000) and is the reason for the abnormal oligomeric assembly (Berengian *et al.* 1997). The same residue is affected in the α A-R116H mutant, which also causes cataract (Gu *et al.* 2008). A number of other site-specific mutations within the ACD have been shown to be responsible for the development of either whole (lenticular) or nuclear cataract in humans (α A-R49C and α A-G98R) (Sanithiya *et al.* 2006). Other disease-related mutations of α A occurring also in the NTD (i.e. α A-W9X, R12C, R12W, R45H and R21L) are presented in [Table 1.2](#).

1.8. Alzheimer's Disease

Alzheimer's disease (AD) is named after Dr. Alois Alzheimer, who in 1906 noticed changes in the brain tissue of a woman that had died of an unusual mental illness. AD is the most common form of dementia resulting in the loss of memory and intellectual abilities. It is an irreversible, progressive neurodegenerative disease affecting millions of people worldwide. The greatest risk factor for this neurodegenerative disorder is age (Mao and Reddy 2011). Therefore, the number of AD patients the last

century has increased dramatically, due to the extended life span in modern countries. The pathology of AD is characterized by extracellular accumulation of amyloid plaques and intracellular neurofibrillary tangles (Selkoe 1994a), which are referred to as senile plaques and neurofibrillary tangles, respectively (Findeis 2007). Amyloid plaques are composed primarily of amyloid fibrils of self-assembled A β -peptides (Glennner and Wong 1984). In **Fig. 1.19A** a healthy and a diseased AD brain is shown.

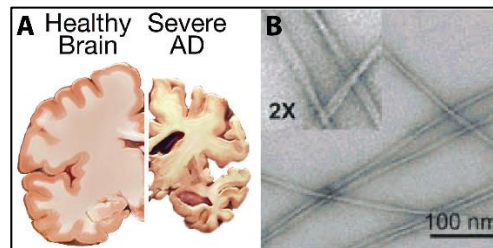


Fig. 1.19. Alzheimer's Disease. (A) The left side shows a healthy and the right side a diseased with Alzheimer brain (<https://www.nia.nih.gov/alzheimers/scientific-images>). (B) Transmission Electron Microscopy (TEM) image of amyloid fibrils formed by the human A β_{40} peptide, negatively stained with uranyl acetate. The image was modified from Petkova *et al.* 2005.

1.8.1. The A β Amyloid Peptide

The two major forms of A β in human brain are peptides A β_{40} and A β_{42} , differing from each other only by two amino acids. The A β_{42} fragment is the dominant A β species in the amyloid plaques of AD patients (Gravina *et al.* 1995; Iwastubo *et al.* 1994; Selkoe 1994b; Roher *et al.* 1993) and typically displays a higher propensity to form amyloid fibrils *in vitro* (El-Agnaf *et al.* 2000; Jarrett *et al.* 1993a; Jarret *et al.* 1993b), while it appears to be a more toxic species than A β_{40} . However, most high-resolution structural studies have been performed on A β_{40} amyloid fibrils (Schutz *et al.* 2015; Bertini *et al.* 2011; Petkova *et al.* 2006; Petkova *et al.* 2002). The A β protein is a 4 kDa proteolytic cleavage product (Glennner *et al.* 1984) of the transmembrane β -amyloid precursor protein (APP), which is a ubiquitously expressed, 110-130 kDa receptor-like protein (Haass and Selkoe 2007; Selkoe 2001). The cleavage of APP is primarily mediated by β - and γ -secretase, which generate the two major cleavage products A β_{40} and A β_{42} (**Fig. 1.20**) (Lichtenthaler *et al.* 2011). The different fragments possess different self-aggregating potentials, but only A β_{42} shows a strong oligomerization propensity *in vivo*. In a healthy individual, the shorter fragment A β_{40} is the most abundant species (> 85%) (Younkin 1998), whereas the production of the elongated peptide A β_{42} increases by a factor of 1.5-1.9 in patients with familial forms of AD (Suzuki *et al.* 1994). The early-onset familial AD can be ascribed to mutations in the genes for APP (chromosome 21), presenilin-1 (chromosome 14) and presenilin-2 (chromosome 1) (Tilley *et al.* 1998; Hardy *et al.* 1997). Those mutations result either in elevated levels of total A β peptides or an increase of A β_{42} only (Jankowsky *et al.* 2004; Tomita *et al.* 1994).

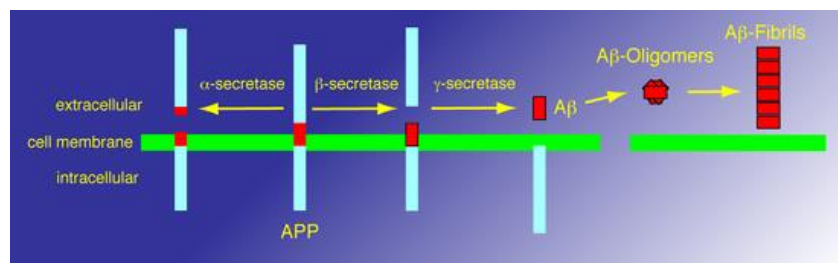


Fig. 1.20. Metabolic processing of the transmembrane protein APP by the endoproteases α -, β - and γ -secretase. Processing by the β - and γ -secretases yields the fragment A β (red), which is a 39-42 residue peptide. The figure was designed using Adobe Illustrator CS6.

1.8.2. The Structure of A β Amyloid Fibrils

The amyloid fibrils of A β are a pathological hallmark of AD disease and may play a central role in cell-to-cell transmissibility (Costanzo *et al.* 2013). Although their precise role in toxicity is unclear, the oligomeric entity of A β is known to be most neurotoxic (Selkoe *et al.* 2016). The structure of A β fibrils is therefore important for a detailed understanding of the aggregation process and a molecular understanding of the progression of the disease, as well as for the development of therapeutic and diagnostic approaches. A β belongs to the class of intrinsically disordered proteins (IDPs), meaning that these polypeptides are inherently devoid of any structural order in solution (Babu *et al.* 2011). AD is thus, referred to as a misfolding or conformational disease (Uversky 2009).

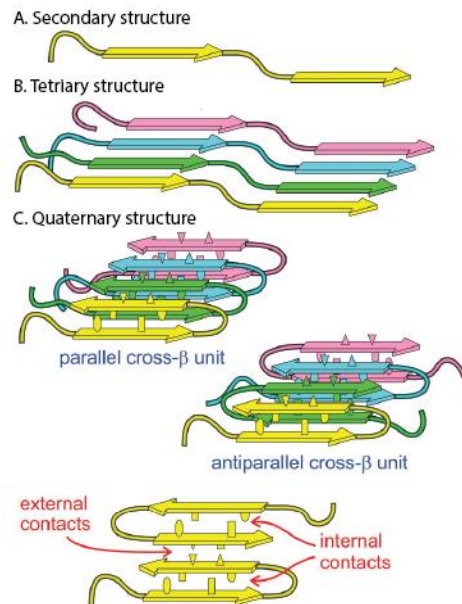


Fig. 1.21. Levels of molecular structure within an amyloid fibril. (A) Secondary structure refers to the identities of β -strand and non- β -strand segments (arrows and tubes). Non- β -strand segments can be either ordered or disordered. (B) Tertiary structure refers to the organization of β -strand segments into parallel or antiparallel β -sheets. (C) Quaternary structure refers to the stacking or interactions among β -sheets, mediated by amino acid side chains. Adapted from Tycko 2016.

The hydrophobic nature of the A β peptide causes the self-association into soluble oligomers, protofibrils, and finally mature filaments of 10-20 nm diameter (Sachse *et al.* 2008). Fibril formation is controlled by two kinetic parameters: the nucleation rate and the elongation rate (Wu and Shea 2011; Lomakin *et al.* 1997) and the fibrils are typically straight, filamentous aggregates with lengths of 100 nm to several μ m (Tycko 2006; Sipe 1992). They can be visualized by Transmission Electron Microscopy (TEM) with negative staining, as shown in Fig. 1.19B and they are associated with several diseases, except for AD, such as type 2 diabetes and Parkinson's disease (Sacchettini and Kelly 2002). In addition, A β has been identified as a metalloprotein binding specifically Cu(II) in the N-terminal region (Atwood *et al.* 2000) and the Cu(II)-A β complex has been shown to generate ROS *in vitro* (Tabner *et al.* 2002; Huang *et al.* 1999). Increased levels of lipid peroxidation, as well as DNA and protein oxidation products in AD brains, point towards a significant role of oxidative stress in AD pathology. Furthermore, the production of free radicals most likely provokes oxidation of A β residues M35 and Y10 (Jomova *et al.* 2010; Smith *et al.* 2007).

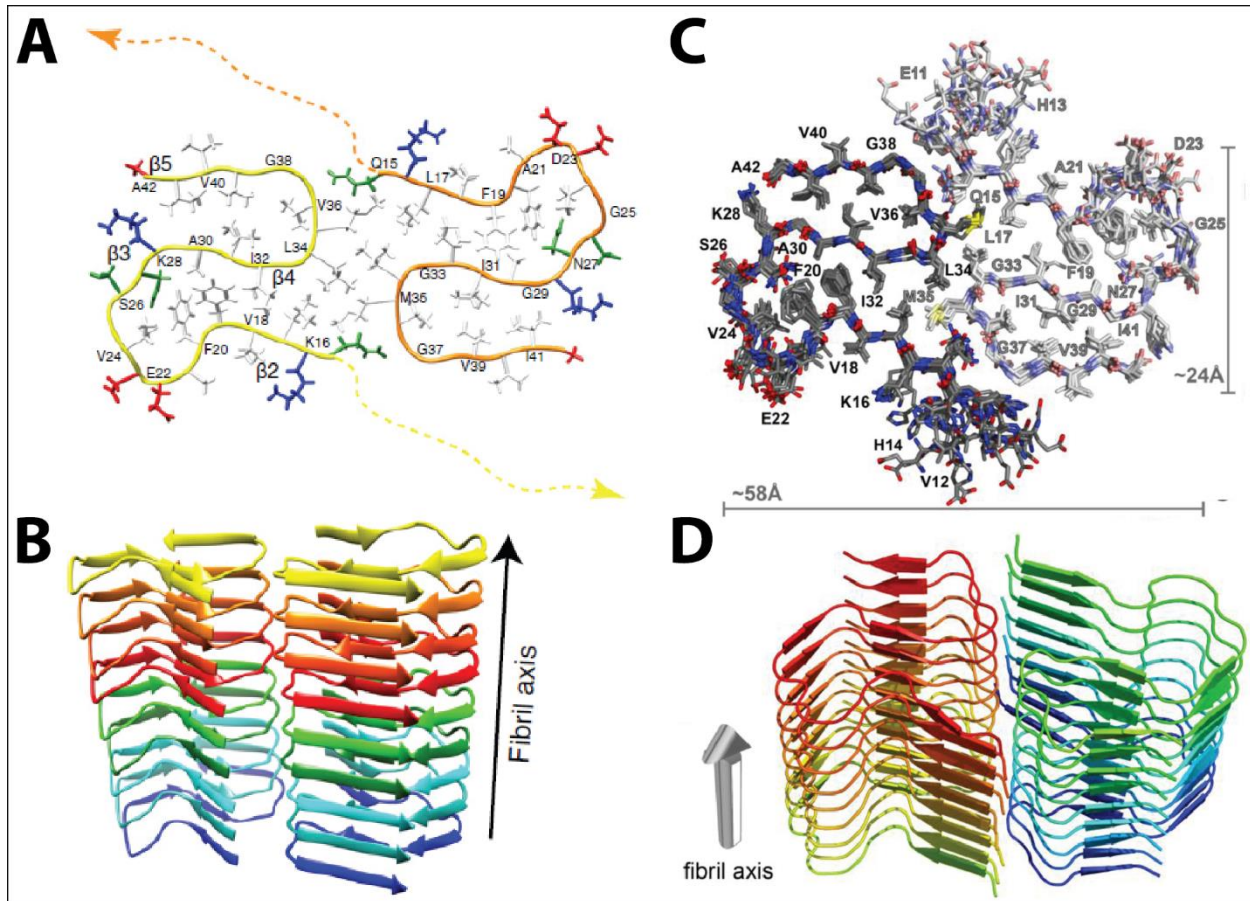


Fig. 1.22. The 3D structure of Aβ₍₁₋₄₂₎ solved by solid-state NMR. (A) The structure of Aβ₍₁₋₄₂₎ fibrils represented with the conformer showing the smallest CYANA target function. The backbone of the two symmetric molecules is shown as yellow and orange. The N-terminal region is indicated by dashed lines, while the side chains of the positively charged residues are shown in red, the negatively charged in blue, the hydrophobic residues in white, and polar residues in green. (B) A ribbon-based cartoon of the Aβ₍₁₋₄₂₎ fibrils showing nine molecules of Aβ₍₁₋₄₂₎ along the fibril axis. Adapted from Wälti *et al.* 2016. (C) Stick model representation of the 10 lowest energy structures (one monomer is in bright and one in pale colors). (D) Ribbon representation of the lowest energy structure showing the alignment of the dimers along the fibril axis. Modified from Colvin *et al.* 2016.

Aβ fibrils are visible in electron microscope images, but it is very difficult to go to an atomic level of detail. The standard high-resolution methods used in structural biology to achieve this, such as X-ray crystallography and solution-state NMR spectroscopy, assume that the macromolecule is present as a single crystal or in the form of individual molecules that are dissolved in water. However, fibrils are elongated structures that adhere to each other and neither form crystals, nor can be dissolved in water. Due to the insolubility of the fibrils, solid-state NMR spectroscopy became an invaluable tool for structural investigations, capable of offering a view of the fibrils at atomic level. New developments in methods in solid-state NMR made it possible to measure a network of distances between the atoms in the protein molecules that make up a fibril. The levels of molecular structure within an amyloid fibril are summarized in Fig. 1.21. Extensive calculations enabled the atomic structure of the fibril to be reconstructed from these measurements (Tycko 2016). For Aβ fibrils, complete structural models that are based primarily on solid-state NMR data now exist (Wälti *et al.* 2016; Colvin *et al.* 2016; Xiao *et al.* 2015; Sgourakis *et al.* 2015; Schutz *et al.* 2014; Bertini *et al.* 2011; Paravastu *et al.* 2008; Petkova *et al.* 2006) and an additional complete model for Aβ₄₀ fibrils is derived from human brain tissue (Lu *et al.* 2013). The two most recent models, however, arise from Griffin's (Colvin *et al.* 2016) and Riek's (Wälti *et al.* 2016) groups. The two

teams in these studies confirm each other, and have caused excitement in expert circles, as they enable a targeted, structure-based search for medicine that could attack the β -amyloid fibrils. In the 3D structure the $A\beta_{42}$ peptide is composed of two molecules per fibrillar layer, forming a double-horseshoe-like β -sheet entity with maximally buried hydrophobic side chains, while pairs of identical molecules form layers, which are stacked onto each other to form a long fibril and numerous hydrogen bonds parallel to the long axis lend the fibrils their high stability (Fig. 1.22) (Colvin *et al.* 2016; Wälti *et al.* 2016). Solid state NMR data show that amyloid fibrils are frequently polymorphic, with structural variations that can include variations in symmetry and in the nature of β -sheet structures (Tycko 2011).

1.8.3. The Role of α B-Crystallin in Alzheimer's Disease

Several members of the sHsp family have been attributed a protective role in the development of neurodegenerative diseases. α B is expressed at high levels in the neurons and glial cells of patients with neurodegenerative diseases such as Alzheimer's, Parkinson's, Huntington's, Creutzfeldt-Jacob and amyotrophic sclerosis (Carra *et al.* 2013). Interestingly, the expression of α B has been shown to be up-regulated in brains of patients suffering from AD compared to that in the normal human brain (Renkawek *et al.* 1994; Iwaki *et al.* 1992), presumably because of the cellular stress caused by the disease. Despite its protective role as a member of the protein quality control machinery, α B has been found to be colocalized with $A\beta$ peptides in AD's amyloid plaques (Wilhelmus *et al.* 2006; Muchowski and Wacker 2005; Liang 2000; Stege *et al.* 1999). Interestingly, α B is associated with $A\beta$ deposition in supranuclear cataracts in lenses from patients with AD (Goldstein *et al.* 2003).

The observation that $A\beta$ and α B are colocalized *in vivo* (Liang 2000; Stege *et al.* 1999) has led to several independent investigations to study the effect of α B on $A\beta$ aggregation under *in vitro* experimental conditions (Shammas *et al.* 2011; Wilhelmus *et al.* 2006; Raman *et al.* 2005; Santhoshkumar and Sharma 2004; Liang 2000; Stege *et al.* 1999). Some of these studies showed that upon interaction, α B enhanced β -sheet structure in $A\beta$ (Liang 2000; Stege *et al.* 1999) and stabilized $A\beta$ into toxic β -sheet rich oligomers as evidenced by increased toxicity in cultured rat neuronal cells (Stege *et al.* 1999). In addition, Narayanan *et al.* (2006) found that instead of preventing the cell from toxicity of $A\beta$, α B induced an increased toxicity, which could arise from the oxidation of the side chain of the Met35 in $A\beta$ by α B. Moreover, it has been reported that α B inhibited fibril formation (Shammas *et al.* 2011; Dehle *et al.* 2010; Wilhelmus *et al.* 2006; Raman *et al.* 2005) and presented evidence for a protective effect of α B in $A\beta$ -induced cytotoxicity (Dehle *et al.* 2010; Wilhelmus *et al.* 2006). All in all, there is controversy regarding the ability of α B to inhibit the toxicity associated with $A\beta$ fibril formation (Ecroyd and Carver 2009) and the existing data depend on how experiments were performed, including the method of preparation, purification and handling of the $A\beta$ peptide, the incubation conditions and in particular whether $A\beta$ and α B were pre-incubated.

1.9. Nuclear Magnetic Resonance Spectroscopy in Structural Biology

Structural biology aims at determining the structures of macromolecules, such as proteins and nucleic acids, and their complexes in order to provide a mechanistic understanding of biological systems. The knowledge of high resolution structural studies of biomolecules is very important in understanding the functional dynamics of different protein systems. In recent years, Nuclear Magnetic Resonance (NMR) spectroscopy and X-ray crystallography are well-established techniques for obtaining atomic-resolution

structures. Each of these methods has its own strengths and limitations. However, they both yield highly similar structures (Wagner *et al.* 1992). Within the domain of eukaryotes, up to now, 81% and 13% of the structures were solved by X-ray diffraction (resolution ≤ 3 Å) and solution-state NMR spectroscopy, respectively, according to the RCSB Protein Data Bank. The first X-ray structures were determined in the late 1950s (Blake *et al.* 1965; Muirhead and Perutz 1963; Kendrew *et al.* 1958), whereas first NMR structures were reported in the early 1980s (Wagner *et al.* 1987; Clore *et al.* 1985; Kaptein *et al.* 1985; Williamson *et al.* 1985; Braun *et al.* 1983). Therefore, however X-ray has in principle a time lead over NMR spectroscopy of about 20 years, nowadays thousands of structures have been solved by X-ray and NMR, hinting a faster access to three-dimensional structures of biomolecules.

As opposed to X-ray, where obtaining diffraction-quality crystals can be challenging or in many cases impossible, or where the structures can be influenced by crystallization conditions and crystal-packing forces (Chayen and Saridakis 2008; Durbin and Feher 1996), in solution-state NMR this step is avoided, as it requires only sample solubility at sufficient concentrations for data collection. NMR spectroscopy is a unique method that allows characterization of the structure and their complexes at atomic- and residue-resolution, either in a soluble or aggregated state. In addition, yielding information on kinetics and dynamics can be used to identify specific interactions. However, solution-state NMR studies are limited by the size of the molecule. Therefore, for the validation of structures it is necessary to combine different structural biology methods (such as X-ray, solution- and solid-state NMR, cryo-EM, SAXS or SANS) in an integrated structural biology approach complemented with functional data in order to provide a more precise understanding of biological systems.

NMR spectroscopy has evolved to a highly sophisticated method and many research groups are continuously improving the theories behind NMR. This chapter introduces the basics of nuclear magnetic resonance (NMR) spectroscopy with respect to relaxation properties and the investigation of large biomolecules. For a comprehensive understanding of the physical principles of NMR, the reader is referred to the literature (Levit 2013; Keeler 2011; Cavanagh *et al.* 2010; Claridge 2009; Ernst *et al.* 1999).

1.9.1. The Basic Principles of NMR

The nucleus consists of neutrons and protons, which contain an intrinsic property called *spin*. Nuclei of all atoms may be characterized by a nuclear spin angular momentum quantum number, I , which may have values greater (i.e. ^2H) than or equal to zero (i.e. ^{12}C , ^{16}O) and that are multiple of $\frac{1}{2}$ (i.e. ^{13}C , ^{15}N). Atomic nuclei with even mass numbers of protons and neutrons have zero spin and all the other atoms with odd mass numbers have a non-zero spin. Furthermore, all molecules with a non-zero spin have a magnetic moment, μ , related to the angular momentum by

$$\mu = \gamma I \quad (\text{Eq. 1.9.1})$$

where γ is the gyromagnetic ratio, a characteristic constant between the magnetic dipole moment and the angular momentum, specific to each nucleus (Table 1.4) (Cavanagh *et al.* 2010).

Table 1.4 | Properties of selected common nuclei (Cavanagh et al. 2010).

Nucleus	I	μ	Natural abundance (%)
^1H	$\frac{1}{2}$	2.6752×10^8	99.99
^2H	1	4.107×10^7	0.012
^{13}C	$\frac{1}{2}$	6.728×10^7	1.07
^{14}N	1	1.934×10^7	99.63
^{15}N	$\frac{1}{2}$	-2.713×10^7	0.37
^{17}O	$5/2$	-3.628×10^7	0.038
^{19}F	$\frac{1}{2}$	2.518×10^8	100.00
^{31}P	$\frac{1}{2}$	1.0839×10^8	100.00

The magnetic moment of the nucleus forces the nucleus to behave as a tiny bar magnet. In the absence of an external magnetic field, each magnet is randomly oriented. During the NMR experiment the sample is placed in an external magnetic field, B_0 , which forces the bar magnets to align with (low energy) or against (high energy) the B_0 (Fig. 1.23A). During the NMR experiment, a spin flip of the magnets occurs, requiring an exact quanta of energy. To understand this rather abstract concept it is useful to consider the NMR experiment using the nuclear energy levels (Cavanagh et al. 2010). In the presence of an external magnetic field, the spin states of the nucleus have energies given by

$$E = -\mu\mathbf{B} \quad (\text{Eq. 1.9.2})$$

in which \mathbf{B} is the magnetic field vector. At equilibrium, the different energy states are unequally populated because lower energy orientations of the magnetic dipole vector are more probable. The relative population of a state is given by the *Boltzmann* distribution:

$$\frac{N_\alpha}{N_\beta} \approx 1 - \frac{\gamma\hbar B_0}{kT} \quad (\text{Eq. 1.9.3})$$

with N_α and N_β number of spins in α - or β -state, k = Boltzmann constant, T = temperature. An exact quanta of energy must be used to induce the spin flip or transition. For any m , there are $2m+1$ energy levels. In particular, in the presence of an external magnetic field (B_0) for a spin $1/2$ nucleus two spin states exist. The $m = +1/2$, which is referred to as the lower energy or α -state that is parallel to B_0 , and the state with $m = -1/2$, referred to as the higher energy or β -state (antiparallel to the magnetic field). Each energy level is given by

$$E = -m\hbar\gamma\mathbf{B}_0 \quad (\text{Eq. 1.9.4})$$

where m is the magnetic quantum number, in this case $\pm 1/2$ and \hbar is the Planck's constant. The energy difference between the two states depends on the strength of the external magnetic field and it is given by

$$\Delta E = -\hbar\gamma\mathbf{B}_0 \quad (\text{Eq. 1.9.5})$$

A schematic showing how the energy levels are arranged for a spin $\pm 1/2$ nucleus is shown in Fig. 1.23B. In the absence of an applied field the nuclear energy levels are degenerate. The splitting of the degenerate energy level due to the presence of a magnetic field is known as *Zeeman* splitting (Cavanagh et al. 2010).

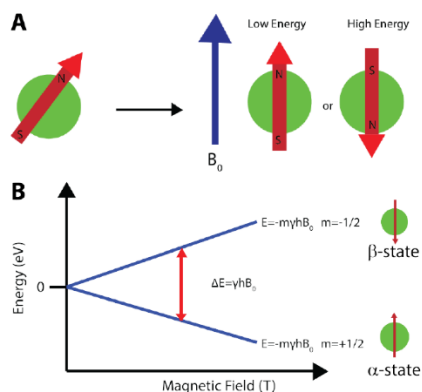


Fig. 1.23. (A) Application of a magnetic field to a randomly oriented bar magnet. The red arrow denotes magnetic moment of the nucleus. The application of the external magnetic field aligns the nuclear magnetic moments with or against the field. (B) The splitting of the degenerate nuclear energy levels under an applied magnetic field. The green spheres represent atomic nuclei, which are either aligned with (low energy) or against (high energy) the magnetic field. The figure was designed using Adobe Illustrator CS6.

As shown in **Fig. 1.24**, in equilibrium the difference between spins aligned to the external field and opposed to, create a net magnetization that is aligned to the external magnetic field (z-axis). Upon application of radio frequency (rf) pulses, the net magnetization vector tilts away from the z-axis. A static magnetic field applied to the nucleus causes it to precess at a rate dependent on the field strength and on the gyromagnetic ratio of the spin. A spinning particle precesses about the external field with an angular frequency known as the *Larmor frequency* (with $\omega_L = \gamma B_0$ Eq. 1.9.6) of a nucleus. Larmor frequency is measured in Hertz.

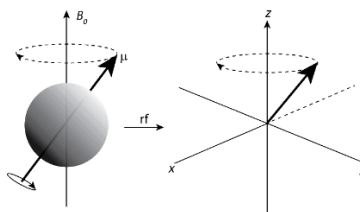


Fig. 1.24. A nucleus of spin 1/2 in a magnetic field B_0 is represented. This nucleus is in the lower energy level (i.e. its magnetic moment does not oppose the applied field). The nucleus is spinning on its axis. In the presence of a magnetic field, this axis of rotation will precess around the magnetic field. The frequency of precession is termed the Larmor frequency. The figure is adapted from Claridge (2009).

In the NMR spectrometer the bulk magnetization is manipulated with an electromagnetic field in the transverse plane, x-y. The spectrometer consists of large superconductive magnet, not applicable to alternate so drastically the field. Therefore, an additional B_1 field perpendicular to B_0 is applied to create frequency pulses at near-Larmor frequency. This B_1 field generates radio frequency in form of a rf pulse. As long as this pulse is applied, the vector deviates accordingly, but as soon as this external influence is stopped, the vector will return to the z-axis, at equilibrium state. This decay from the equilibrium to the rotating state gives rise to free induction decay (FID), which is recorded. At the end, this time-domain signal is converted to frequency-domain by Fourier Transformation (FT).

1.9.2. Chemical Shift

The NMR spectra should appear identical for each nucleus type. However, this is not the case since every nucleus experiences a slightly different chemical environment. The observed resonance frequencies then

differ slightly from the frequencies predicted by Eq. 1.9.6. These differences in resonance frequencies are referred to as *chemical shifts* and offer the possibility of distinguishing between otherwise identical nuclei in different chemical environments. The chemical shift is measured in parts per million (ppm). NMR resonance frequency is directly related to the energy gap between the ground state and the excited state of the respective nuclear spin by

$$\nu = \frac{\Delta E}{\hbar} \quad (\text{Eq. 1.9.7})$$

with ν being the NMR resonance frequency and ΔE the difference between energy levels (Keeler 2011). In order to be able to compare chemical shift values from different instruments, the reference molecule 4,4-dimethyl-4-silapentane-1-sulfonic acid (DSS) is used to calibrate the chemical shifts for ^1H and ^{13}C atoms (Eq. 1.9.8).

$$\delta_{ppm} = 10^6 \times \frac{\nu - \nu_{DSS}}{\nu_{DSS}} \quad (\text{Eq. 1.9.8})$$

with δ_{ppm} being the chemical shift in parts per million (Keeler 2011). The ppm value is calculated as the ratio of the detected frequency from the sample and the absolute resonance frequency of a standard reference compound (Fig. 1.25) (Levit 2013; Keeler 2011; Cavanagh et al. 2010). The phenomenon of chemical shift arises because of motions of electrons, induced by the external magnetic field, generate secondary magnetic fields. The net magnetic field for a specific nucleus depends on the static magnetic field and the local secondary fields. This effect is called ‘nuclear shielding’ and can increase or diminish the effect of the main field (Cavanagh et al. 2010). In proteins, the ^1H chemical shift typically results from a combination of electric fields due to charges, aromatic ring currents and magnetic anisotropy around bonds (Williamson 2013).

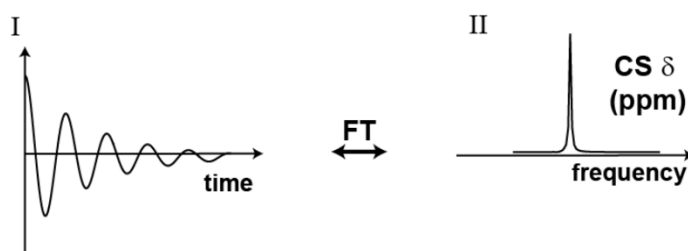


Fig. 1.25. NMR signal. The free induction decay (FID) (I) is Fourier transformed to yield a signal in the frequency domain. The resonance frequency is given in ppm with respect to a reference. The figure was designed using Adobe Illustrator CS6.

In general, the electronic charge distribution in a molecule is anisotropic. For this reason, the chemical shift is also anisotropic and changes the orientation of a molecule with respect to the magnetic field changes. In solution NMR, this anisotropy is averaged out by fast molecular tumbling and only a single isotropic chemical shift value is observed. This, however, does not apply to rigid solids, in which molecular reorientation is absent (see Chapter 1.9.6.). Chemical Shift Anisotropy (CSA) is defined as the chemical shift difference between the isotropic and anisotropic states. Thus, chemical shifts can provide useful structural information due to their anisotropy.

The observed chemical shifts in a protein are divided into the sum of two components: the so-called random coil chemical shifts, δ_{rc} , and the conformation-dependent secondary chemical shifts, $\Delta\delta$. The random coil chemical shift is the chemical shift, which is observed in a conformationally disordered peptide, while the secondary chemical shift contains the contributions from secondary and tertiary structures. All in all, secondary chemical shifts display characteristic patterns for structural elements that

provide structural information for the system studied (Cavanagh *et al.* 2010) and chemical shifts can be used to predict backbone torsion angles, e.g. with TALOS+ (Shen *et al.* 2009) and protein structures, e.g. with CS-ROSETTA (Shen *et al.* 2008).

The precise chemical shift of a resonance is not always easy to determine as often there is spectral overlap that blocks the determination of the chemical shift and in order to resolve this problem, scientists exploit multidimensional experiments, use higher magnetic fields or design experiments that improve spectral resolution.

1.9.3. Protein Dynamics in NMR Spectroscopy

Dynamics is one of the major interests of modern NMR spectroscopy. In biomolecules, dynamics involve conformational changes, which can be traced by NMR. Motions in globular proteins that are typically tightly packed, have a time scale ranging from pico- to milliseconds. Often this motion is linked to function (Markwick *et al.* 2008; Henzler-Wildman *et al.* 2007; Henzler-Wildman and Kern 2007; Karplus and Petsko 1990; Levy *et al.* 1981a). On the NMR timescale protein motions can be divided into a fast (ps-ns) and slow motional (ms-ks) regime, respectively as presented in Fig. 1.26. Methyl rotations occur next to molecular tumbling on a fast time scale, while folding and loop or domain motions on slower. Further, X-ray diffraction samples have a larger range of motions compared to NMR, reaching a time scale of femtoseconds (Kleckner and Foster 2011; Henzler-Wildman and Kern 2007).

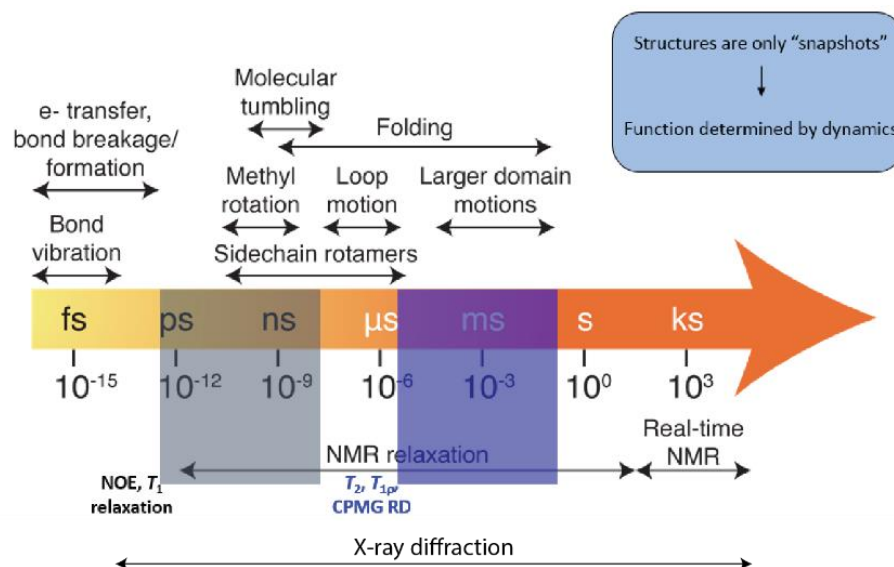


Fig. 1.26. Functional Relevant Time Scales of Protein Dynamics. The different processes (top) and biophysical methods (bottom) are related to a time scale of femto- to kiloseconds. The figure was modified from Kleckner and Foster 2011 and Henzler-Wildman and Kern 2007.

1.9.3.1. Paramagnetic Relaxation Enhancement (PRE)

Paramagnetic NMR has emerged as an alternative and powerful tool to investigate various dynamic processes involving macromolecules. In particular, the PRE phenomenon arises from magnetic dipolar interactions between a nucleus and the unpaired electrons of the paramagnetic center that result in an increase in nuclear relaxation rates. PRE can provide structural information depending on the distance of

the paramagnetic center and the nucleus of interest. In contrast to NOE for example, where the effects are small and limited to short-range (6 Å) interactions between protons, the PRE effect is very large, permitting distances up to 35 Å (depending on the paramagnetic group) to be detected (Clore and Iwahara 2009). PRE can be used as a way to investigate lowly populated states of intermediates in macromolecular binding events and the observed PRE rates in the fast exchange regime are population weighted averages of the PREs for the major and minor species (Iwahara and Clore 2006). Therefore, PRE provides structural information on the minor species to be extracted that cannot be obtained by any other biophysical technique (Xu *et al.* 2008; Suh *et al.* 2007; Iwahara and Clore 2006; Tang *et al.* 2006; Volkov *et al.* 2006).

The use of PRE is dependent on the introduction of an extrinsic paramagnetic tag via conjugation to a specific, solvent exposed site (Kosen 1989). Chemical probes used for paramagnetic NMR can be divided into two classes: (i) nitroxide stable radicals and (ii) metal chelators (such as EDTA, DTPA, and metal binding peptides) that bind paramagnetic metal ions with very high affinity. These two classes of paramagnetic probes can be covalently attached to both, proteins and nucleic acids, and used for the observation of intramolecular or intermolecular PREs (Fig. 1.27A,B). Free probes, in the form of paramagnetic cosolute molecules, are also useful to identify solvent accessible regions of the molecular surface of a macromolecule (Fig. 1.27C) (Clore and Iwahara 2009).

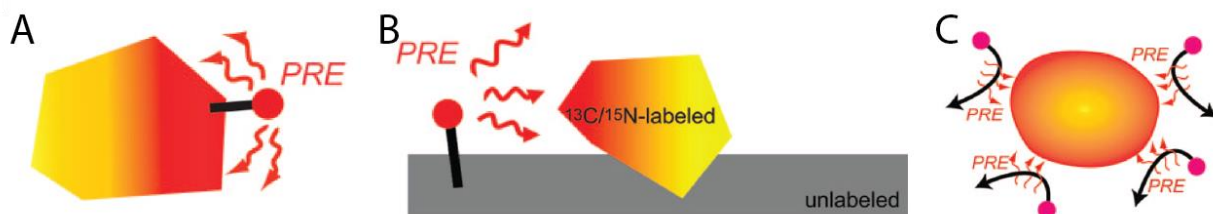


Fig. 1.27. Three types of PRE. (A) Intramolecular PREs arising from the paramagnetic group within the same molecule. (B) Intermolecular PREs arising from the paramagnetic group located on the interaction partner. (C) Solvent PREs arising from random collisions between a macromolecule and paramagnetic cosolute molecules. Modified from Clore and Iwahara 2009.

1.9.3.2. Relaxation

Any excited by radiofrequency pulses magnetic moment relaxes back to equilibrium on the z-axis. This recovery of a spin into its lower energy state is called *relaxation*. Relaxation needs four principle mechanisms that will induce the spin transitions, as it is not a spontaneous process. These mechanisms include dipole-dipole interaction, CSA, spin rotation (SR) and quadrupolar mechanisms. Magnetic dipole-dipole interaction occurs between the magnetic moment of a nucleus and the magnetic moment of another nucleus or other entity (electron, atom, ion, and molecule). This interaction depends on the distance between the pair of dipoles (spins), but also on their orientation relative to the external magnetic field. The CSA relaxation mechanism arises when the electronic environment around the nucleus is non spherical. The magnitude of the electronic shielding of the nucleus then will be dependent on the molecular orientation relative to the external magnetic field. CSA has greater significance at higher B_0 . The SR relaxation mechanism arises from an interaction between the nuclear spin and a coupling to the overall molecular rotational angular momentum. Small, symmetric molecules or freely rotating methyl groups in a protein tumble faster and this increases the SR relaxation. SR relaxation is thus, dependent on the temperature of the sample. Nuclei with spin $I \geq \frac{1}{2}$ will not only have a nuclear dipole but a quadrupole. The nuclear quadrupole is influenced by electric field gradients and depends on the interaction with the electric and not the magnetic field (Cavanagh *et al.* 2010; Claridge 2009).

There are two types of relaxation: spin-lattice and spin-spin. The *longitudinal (or spin-lattice) relaxation time* T_1 describes the return to equilibrium in the z-direction (**Fig. 1.28A**) and it is also responsible for the loss of signal intensity. Alternatively, T_1 can be measured by the decay of a signal under spin-lock conditions that generate a rotating magnetic field near the resonant frequency perpendicular to the static magnetic field (conventionally the x-y plane, **Fig. 1.28A**). In this case the T_1 is termed as $T_{1\rho}$ or *spin-lattice relaxation in the rotating frame*. The *transverse (or spin-spin) relaxation time* T_2 describes the decay of the excited magnetization perpendicular to the applied magnetic field, B_0 (**Fig. 1.28A**) (in the x-y plane). The line width of an NMR signal is determined by T_2 (short T_2 means broader lines in the NMR spectra), while the maximum repetition rate during acquisition of an NMR signal is governed by T_1 (short T_1 means signal can be acquired faster). Both T_1 and T_2 depend on the rate of molecular motions. T_2 is less than or equal to T_1 (T_2 relaxation is the same as or faster than T_1 relaxation, $R = \text{relaxation rate}$, $R_2 = 1/T_2$, $R_2 \geq R_1$), since return of magnetization to the z-direction causes loss of magnetization in the x-y plane (**Fig. 1.28B**). Moreover, for T_1 relaxation to occur there must be magnetic field fluctuations in the x-y direction. Such fluctuations are most effective when they occur at the Larmor precession frequency (ν_0). T_1 relaxation is thus field dependent, since ν_0 varies with the field. T_2 relaxation is caused by fluctuations in any direction and T_2 values are unrelated to field strength (Levitt 2013; Keeler 2011; Cavanagh *et al.* 2010; Becker 1999).

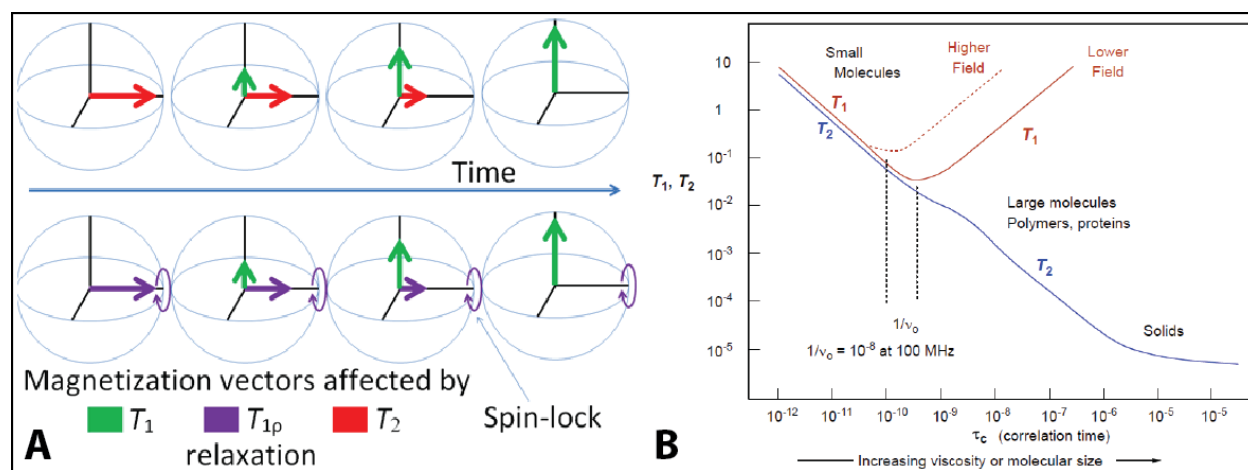


Fig. 1.28. (A) Relaxation of magnetization vectors after a 90° pulse. T_1 relaxation along the z-axis is shown in green, T_2 relaxation in the x-y plane in red and $T_{1\rho}$ with the spin-lock in the x-y plane in purple. **(B)** Schematic illustration of the dependence of T_1 and T_2 on the correlation time, τ_c , the magnetic field and the molecular weight of the system studied.

1.9.4. Diffusion-Ordered NMR Spectroscopy (DOSY)

The translational motion of molecules in solution is in contrast to rotational motion and is often called diffusion. The diffusion NMR technique is referred to as Diffusion-Ordered Spectroscopy (DOSY). This is achieved by combining radiofrequency pulses with magnetic field gradients. 2D DOSY depends on a lot of physical parameters like size and shape of the molecule, temperature and viscosity. By using a gradient molecules can be spatially labelled, i.e. marked depending on their position in the sample tube. While the molecules move during a diffusion time D that follow the pulse sequence, their new position can be decoded by a second gradient (**Fig. 1.29**). The measured signal is the integral over the whole sample volume and the NMR signal intensity is attenuated depending on the diffusion time Δ and the gradient parameters (g, δ). The intensity change is given by

$$I = I_0 \cdot e^{-D \cdot \gamma^2 \cdot g^2 \cdot \delta^2 \left(\Delta - \frac{\delta}{3}\right)} \quad (\text{Eq. 1.9.9})$$

where I is the observed intensity, I_0 the reference intensity, D the diffusion coefficient, g the gyromagnetic ratio of the observed nucleus, g the gradient strength, δ the length of the gradient and Δ the diffusion time.

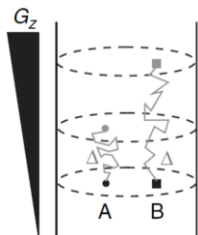


Fig. 1.29. Effect of a magnetic field gradient pulse. Modified from Claridge 2009.

1.9.5. Assignment Experiments in Solution-state NMR Spectroscopy

For assignment experiments chemical shifts need to be assigned to the respective atoms in a protein and until now 3D heteronuclear correlation experiments have been well-established. Assignment experiments in proteins are classified into two kinds of interactions that are characterized by the magnetization transfer between the nuclei: the through-bond and the through-space interaction. Both interactions correlate amide ^1H and amide ^{15}N with ^{13}C dimension, therefore, ^{15}N and ^{13}C labeled nuclei are required (Sattler *et al.* 1999). The ^1H dimension is used for detection due to high sensitivity. ^{15}N is used as additional dimension to increase dispersion and ^{13}C (^{13}C can be either $^{13}\text{C}\alpha$, $^{13}\text{C}\beta$ or ^{13}CO) dimensions are used to establish sequential contacts. The most standard experiments used for backbone assignment, based on through-bond interactions, are: 2D ^1H , ^{15}N HSQC (Kay *et al.* 1990) and standard triple resonance experiments like HNCA, HNCB (Kay *et al.* 1990), HNCACB (Wittekind *et al.* 1993), CBCA(CO)NH (Grzesiek *et al.* 1992) and HNCACO (Clubb *et al.* 1992). The through-space interactions can be probed employing the Nuclear Overhauser Effect (NOE) to yield distances between atoms (Fesik *et al.* 1988; Marion *et al.* 1989). Once backbone resonances are assigned, side chains assignment can be completed using 3D TOCSY-based experiments, which correlate amide ^1H and ^{15}N with all ^1H and ^{13}C side chain resonances, respectively (Ulrich *et al.* 2008). Combination of the mentioned types of assignment experiments and various isotope-labeling enhances the possibility to obtain information about biomolecules' structure, interaction and dynamics.

1.9.6. Investigation of Large Biomolecules by NMR Spectroscopy

The application of conventional NMR in solution is limited to smaller sizes of about 50 - 110 kDa. The larger the molecule in the sample the broader the spectra. The increased number of signals results in crowded spectra and the nuclei relax faster due to slow tumbling, so except for overlapping and broader lines, sensitivity and S/N ratio are also influenced. Therefore, new methods (e.g. Transverse Relaxation Optimized Spectroscopy [TROSY], methyl-TROSY), hardware (e.g. cryoprobes, higher magnetic field magnets) or labeling strategies (e.g. deuteration, selective isotope labeling) have been evolved in order to optimize to the relaxation properties of larger proteins.

Relaxation is affected by the dipole-dipole interaction and the CSA. By deuterating a protein, the protons of the studied protein are replaced by deuterium. There are two approaches for deuteration: perdeuteration and random fractional deuteration. Perdeuteration is the removal of all (95%) side chains protons. The deuteration level is as high as possible and everywhere in the protein there is an identical labeling pattern. In the second approach, random fractional deuteration, the side chains' protons are removed to a certain percentage, 0-80%, and this results to a mixture of different isotopomers (Gardner and Kay 1998; Sattler and Fesik 1996). Both approaches however, drastically weaken the dipolar interactions network, and thus, decrease the transverse relaxation of nearby nuclei resulting to increased spectral sensitivity (sharper lines) and resolution.

Another way to study even higher molecular weight proteins up to 120 kDa is to use the TROSY experiment (Pervushin *et al.* 1997). In general TROSY is more efficient in combination with deuteration and generates spectra with greater S/N and improved resolution (Ollershaw *et al.* 2003). TROSY uses a modified conventional HSQC pulse sequence with no decoupling and at least two different interfering relaxation mechanisms must contribute to relaxation (dipole-dipole/CSA) (Pervushin *et al.* 1997; Wider and Wuthrich 1997). If the interference is additive, the effective relaxation is reduced and this gives rise to narrower linewidths (Fernandez and Wider 2003). The development of TROSY-type techniques enabled the characterization of supramolecular protein assemblies like GroEL-GroES (Fiaux *et al.* 2002), p53/HSP90 (Tugarinov *et al.* 2003), ClpP (Sprangers *et al.* 2005; Tugarinov *et al.* 2003), L7/L12 of the ribosome (Christodoulou *et al.* 2004), the 13 MDa viral capsid protein (Szymczyna *et al.* 2007), and the 20S proteasome (Religa *et al.* 2010; Sprangers and Kay 2007).

Besides the above mentioned methods, there are additional approaches to study larger biomolecules. Methyls localized at the peripheries of the side chains tend to be dynamic, so they have slower relaxation rates compared to the backbone. Therefore, methyl-TROSY uses a HMQC instead of a HSQC pulse sequence and takes the advantage of a TROSY effect. The HMQC pulse sequence contains less pulses and thus, less magnetization is lost due to the homogeneity of the radiofrequency coil. Additionally, the line narrowing appears because two dipolar interactions interfere, but only in the carbon dimension. Furthermore, the methyl-TROSY is independent of the field, therefore the sensitivity is more increased in a HMQC than in a HSQC spectra (Tugarinov and Kay 2003).

Recent examples that illustrate nicely the utility of isotope labeling for detailed NMR structural studies of proteins between 40 and 50 kDa involves Stereo-Array Isotope Labeling (SAIL, addition of stereo-specific labels achieves stereospecific protonation/deuteration of protein side chains) (Kainosho *et al.* 2006), Label Express and Generate Oligomers (or LEGO NMR, applicable for eukaryotic cells, a sequential co-expression method for the preparation of large asymmetric complexes that combines the advantages of *in vivo* reconstitution and the benefits of partial NMR isotope labeling to reduce NMR spectral complexity) (Mund *et al.* 2013) and Sequence-Specific Assignment of Methyl (SeSAM, assignment of methyl groups by mutagenesis) (Crublet *et al.* 2014).

1.9.6.1. Solid-state NMR Spectroscopy

Methyl-based experiments, new labeling techniques or higher magnetic fields, however they low the molecular tumbling rates, they still limit the applicability of solution-state NMR in the investigation of large systems. In particular, backbone assignments become increasingly difficult for macromolecular complexes beyond 200 kDa. Therefore, solution-state NMR is still restricted in studying supramolecular

complexes due to its dependence on rotational diffusion rates, and a promising approach to overcome these size-limitations of large assemblies is the application of solid-state NMR. Additional solid-state NMR has become a popular tool for the investigation of heterogeneous or insoluble systems, like protein aggregates and amyloid fibrils that are difficult or impossible to be studied by other high-resolution techniques.

1.9.6.2. Magic-Angle-Spinning (MAS)

Solid-state samples do not undergo molecular reorientations, like in solution NMR, as molecular tumbling is absent in rigid solids (i.e. crystals, powder, precipitates). The molecules in solids will be normally oriented in all possible directions with respect to B_0 and superposition of all possible chemical shifts is observed for each nucleus. This gives rise to broad peaks with very characteristic shape. The averaging of these anisotropic interactions, in order to circumvent the problem, is achieved actively by Magic-Angle-Spinning (MAS) (Fig. 1.30) (Lowe 1959; Andrew *et al.* 1958). This method removes all contributions from anisotropic interactions and only the isotropic chemical shift is observed (Duer 2008). The CSA and the dipolar coupling Hamiltonian depend on the second Legendre polynomial $P_2(\cos\theta) = \frac{1}{2}(3\cos^2\theta - 1)$, where θ is the angle between the magnetic field B_0 and the z-axis in the principal axis frame of the shielding tensor (for CSA) or the internuclear dipole vector (for the dipolar coupling), respectively. Therefore, for averaging of anisotropic interactions, the sample is rotated at the magic angle $\theta_{MA} = (\arccos 1/\sqrt{3} = 54.7^\circ)$ at which $P_2(\cos\theta_{MA}) = 0$. The CSA Hamiltonian reduces to its isotropic part and the dipolar coupling to zero, as the dipolar coupling tensor is traceless (Duer 2008). The extent, to which the anisotropic interactions are averaged, depends on the frequency of the rotation ω_r (Herzfeld and Berger 1980). Nowadays, MAS probes are available, which enable spinning frequencies up to 60-70 kHz, which efficiently average dipole-dipole interactions, as well as CSA (Balduis 2006). However, higher rotation frequencies of up to 100-150 kHz are required to average the strong ^1H , ^1H dipolar coupling network, which predominantly limits the resolution in a solid-state spectrum (Marchetti *et al.* 2012; Samoson *et al.* 2001). Due to the high gyromagnetic ratio, ^1H spins are a source of strong dipolar couplings, which cannot be easily removed by MAS. Protein solid-state NMR thus, of uniformly protonated samples is essentially based on ^{13}C - and ^{15}N -detection, respectively, since heteronuclear dipolar couplings are sufficiently averaged at currently available rotation frequencies.

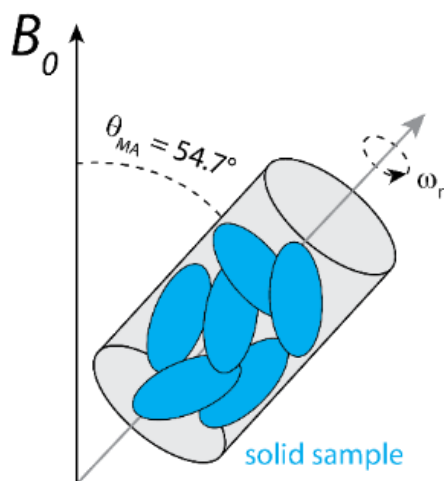


Fig. 1.30. Representation of the principle of MAS in solid-state NMR. The sample rotates in the magnetic field (B_0) under an angle of 54.7° and ϑ is the angle between the static magnetic field (B_0) and the axis of rotation. The figure was designed using Adobe Illustrator CS6.

1.9.6.3. Proton-Driven Spin Diffusion (PDSD) Experiments

PDSD stands for Proton-Driven Spin Diffusion (Manolikas *et al.* 2008; Szeverenyi *et al.* 1982). In this experiment magnetization is transferred from the hydrogen to ^{13}C nuclei, and from there it is transferred to other ^{13}C nuclei, which are close in space. PDSD is the most standard experiment in solid-state NMR and can be considered as the equivalent of the HSQC in solution NMR. Basically, all ^{13}C atoms within a certain distance of one another are correlated to cross-peaks in the solid spectrum. In such a spectrum short mixing times show all carbons within a spin-system (residue) which are coupled to one another, while longer mixing times give also rise to correlations between residues (Bloembergen 1949).

2. Aim of the Study

The sHsps play a very important role in the cellular proteostasis network. Therefore, it is critical that their structure and molecular mechanisms by which they act as molecular chaperones is better understood. The overall aims of this work were to use a combination of different approaches, like solution- and solid-state NMR Spectroscopy, Electron Microscopy and other biophysical techniques in order to interrogate the structure and function of these dynamic and polydisperse proteins. In order to investigate the structure, function and interactions of the human α B- and α A-crystallin, this work had the following aims:

α B – crystallin:

- To focus in particular on the substrate binding of α B with different client proteins (Alzheimer's disease A β peptide, lysozyme).
- Interactions of the A β ₍₁₋₄₀₎ amyloid peptide in complex with α B and Cu²⁺ using titration experiments.
- To probe the role of a post-translational modification (i.e. phosphorylation) on the structure and chaperone function of α B. Phosphorylation-mimicking mutants (S19E, S21E, S43E, S45E, S53E, S59E) of α B were shown to have enhanced chaperone activity and result in a protein complex of an average molecular weight of ca. 120 kDa, paving the way for a solution-state NMR analysis of α B-6E and α B-6D mutants.
- EM analysis of α B-WT and α B-6E with respect to fibrillar substrate.
- PEGylation of α B, in order for the oligomer to get a higher molecular weight and give well-resolved spectra in solid-state NMR.

α A – crystallin:

- Sequential assignment in solution – NMR of the wild – type α A-crystallin.
- Study the flexible C-terminal region of the α A, either in its reduced or oxidized state, using Paramagnetic Relaxation Enhancement and ¹⁵N relaxation experiments in solution and comparison with α B.
- Proline cis-/trans isomerization in the C-terminal regions of α A reduced and oxidized.
- Preliminary biochemical assays and NMR studies on the truncated reduced and oxidized α A-crystallin construct (containing residues 62-166).

3. Materials and Methods

3.1. Materials

3.1.1. Chemicals

If not indicated otherwise, chemicals and supplementary materials were supplied by Sigma-Aldrich Chemie (Taufkirchen, Germany), Merck KGaA (Darmstadt, Germany), VWR international (Ismaning, Germany), SERVA Electrophoresis GmbH (Heidelberg, Germany), Roche Diagnostics (Unterhaching, Germany) and Carl Roth (Karlsruhe, Germany), unless otherwise stated. PEGs were purchased from JenKem Technology (Texas, USA). Isotopically labeled chemicals and D₂O were supplied by Cambridge Isotope Laboratories (Massachusetts, USA) and Sigma-Aldrich Chemie (Taufkirchen, Germany), respectively.

3.1.2. Equipment and Software

NMR spectrometers and associated equipment were manufactured by Bruker BioSpin GmbH (Rheinstetten, Germany). The rotor filling tool for the ultracentrifuge was provided by Giotto Biotech (Florence, Italy) (Bertini *et al.* 2012). Äkta Purifier systems (organic, H₂O) for liquid chromatography, as well as the UNICPRN 3.51 software were purchased from GE Healthcare GmbH (Munich, Germany). The used columns comprise analytical Superose6 10/300 GL (24 ml), HiLoad Superose6 (500 ml), Superdex200 prep grade (320 ml) all produced by GE Healthcare and Q Sepharose FF (200 ml) and Source30 RPC (65 ml), which were self-packed. Thermomixer Comfort and PCR Mastercycler Pro were provided by Eppendorf (Hamburg, Germany). SDS-PAGE from Bio-Rad Laboratories GmbH (München, Germany), NanoDrop 2000/2000c Spectrophotometer and benchtop centrifuges both from Thermofisher Scientific (Darmstadt Germany), and Ultracentrifuge from Beckmann Coulter (Indianapolis, USA).

The NMR data were acquired and processed using TopSpin 2.1 or 3.2 (Bruker BioSpin, Rheinstetten, Germany). Spectra analysis, peak picking and assignment was performed with CcpNMR Analysis 2.4.1 software (University of Cambridge, United Kingdom) (Vranken *et al.* 2005). PDB structures were analysed using Pymol (Delano *et al.* 2002). Protein sequence alignments were calculated using Clustal W (Larkin *et al.* 2007). NMR analysed data were fitted with in-house scripts. Data were plotted with GraphPad Prism (GraphPad Prism version 5.0b for Mac OS, GraphPas Software, San Diego California USA, www.graphpad.com) and figures were created with Adobe Illustrator CS5 (Adobe Systems Inc., San Jose, USA).

3.1.3. Bacterial Strains, Plasmids and Primers

In all experiments the expressing strain *Escherichia coli* (*E. coli*) BL21 (DE3) or Rosetta 2 (DE3), both containing as antibiotic resistance marker, kanamycin, was supplied by Novagen (Merck Millipore, Darmstadt, Germany). The cloning *E. coli* XL1-Blue cells were purchased from Stratagene (Agilent Technologies Deutschland GmbH, Waldbronn, Germany).

The wild-type human α A-crystallin (CRYAA, UniProtKB - P02489) plasmid and the α A-ACD-CTE mutant, both cloned into a pET28b+ vector (Novagen-Merck, Darmstadt, Germany), were kindly provided by Dr. Christoph Kaiser (TU München, Germany). The wild-type human α B-crystallin (CRYAB, UniProtKB - P02511) plasmid and its variants, were cloned into a pET30 EK/LIC vector (Novagen-Merck, Darmstadt, Germany), and kindly provided by Dr. Andi Mainz (TU Berlin, Germany). All the vector maps and sequences of the proteins can be found in Appendix, **Supp. Table S1**. The α B- δ NTD, α B- δ CTE, α B-6E and α B-6D mutants were PCR amplified using the primers listed in Appendix, **Supp. Table S2**. The primers were used in a concentration of 10 pmol/ μ l for PCR reactions. For sequencing the concentration of the primers was 2 pmol/ μ l. A β ₍₁₋₄₀₎ was cloned into a pET28a(+) vector with a kanamycin resistance gene (the vector was kindly provided by Dr. Muralidhar Dasari). The construct was preceded by an N-terminal methionine, which does not alter the biochemical properties of the peptide (Walsh *et al.* 2009).

3.1.4. Cell Growth Media

Luria Bertani (LB) medium, which was autoclaved prior to use, was used for expression of unlabeled proteins, minipreps, precultures or test expressions. M9 medium for labeled proteins was supplemented with ¹⁵NH₄Cl (0.5 gr/L) as a nitrogen source and with uniformly-labeled-¹³C D-glucose (2 gr/L) as carbon source, respectively. Otherwise, unlabeled NH₄Cl and unlabeled D-glucose were added to the media. In case of ILV labeling, in the M9 medium Isoleucine (0.05 gr/L) and Valine/Leucine (0.1 gr/L) precursors were added around an hour before cells induction with IPTG. When deuterated protein was prepared then all M9 components were dissolved instead of ddH₂O, in deuterium oxide (D₂O) and ¹³C D-glucose was substituted by ²H, ¹³C-glucose at the same concentrations. Isotopes, biotin and thiamin-HCl were prepared freshly and sterile filtered. All other M9 components were autoclaved prior to use. **Table 3.1** summarized the media components.

Table 3.1 | Recipes for bacterial growth media and their composition.

Media	Components (per Liter (L))
LB medium (pH 7.5)	10 gr Peptone 5 gr Yeast Extract 10 gr NaCl ad 1L ddH ₂ O
10x M9 Medium (pH 7.0)	60 gr Na ₂ HPO ₄ 30 gr KH ₂ PO ₄ 5 gr NaCl ad 1L ddH ₂ O
100x Trace Elements	5 g EDTA pH 7.5 0.83 gr FeCl ₃ .6H ₂ O 84 mgr ZnCl ₂ 13 mgr CuCl ₂ .2H ₂ O 10 mgr CoCl ₂ .6H ₂ O 10 mgr H ₃ BO ₃ 1.6 mgr MnCl ₂ .6H ₂ O ad 1L ddH ₂ O
1x M9 Medium	100 ml 10x M9 salts 10 ml 100x trace elements 1 ml 1M MgSO ₄ (A) 0.3 ml 1M CaCl ₂ (A) 1 ml Thiamin-HCl (1 mgr/ml) (SF) 10 ml Biotin (0.1 mgr/ml) (SF) 5 ml NH ₄ Cl (10% w/v) (SF) 10 ml Glucose (20% w/v) (SF) ad 1L ddH ₂ O
A = autoclaved, SF = sterile filter	

3.1.5. Buffer Solutions

All buffers used for the protein purifications on the Äkta purifier were filtered and degassed prior to use.

Table 3.2 | Buffer solutions used in this work and their respective composition are listed below.

Buffer	Application	Buffer Composition
Resuspension	Cell Resuspension	20 mM Tris-HCl, pH8.5; 2 mM MgCl ₂
Purification buffers for αB-crystallin WT (αB-WT) and αB-crystallin 6D (αB-6D)		
Lysis Buffer	Cell lysis	20 mM Tris-HCl, pH8.0; 2 mM MgCl ₂ ; 1x Complete Protease Inhibitor; 1mgr/mL DNase
AEC Buffer A	AEC	20 mM Tris-HCl, pH8.5; 1 mM EDTA
AEC Buffer B	AEC	20 mM Tris-HCl, pH8.5; 1 mM EDTA; 1 M NaCl
SEC Buffer	Gel filtration	20 mM Tris-HCl, pH8.5; 1 mM EDTA; 50 mM NaCl
Buffer B-6D	HIC	20 mM Tris-HCl, pH8.5; 1 mM EDTA; 1 M (NH ₄) ₂ SO ₄
Purification buffers for αB-crystallin 6E (αB-6E)		
Lysis Buffer	Cell lysis	50 mM Tris-HCl, pH8.0; 2 mM MgCl ₂ ; 2x Complete Protease Inhibitor; 1mgr/mL DNase
AEC 1 Buffer A	AEC	50 mM Tris-HCl, pH8.5; 2 mM EDTA
AEC 1 Buffer B	AEC	50 mM Tris-HCl, pH8.5; 2 mM EDTA; 1 M NaCl
SEC Buffer	Gel filtration	50 mM Tris-HCl, pH8.5; 2 mM EDTA; 400 mM NaCl
uAEC Buffer A	Urea AEC	20 mM Tris-HCl, pH8.5; 2 mM EDTA; 5 M Urea
uAEC Buffer B	Urea AEC	20 mM Tris-HCl, pH8.5; 1 mM EDTA; 1 M NaCl; 5 M Urea
Buffer R	Protein refolding	250 mM Tris-HCl, pH 8.5; 10 mM EDTA; 100 mM L-Arginine
Lysis Buffer his-tag	Cell lysis	50 mM Tris-HCl, pH8.0; 100 mM NaCl; 20 mM Imidazole; 2x Complete Protease Inhibitor
Wash buffer	Ni-purification	50 mM Tris-HCl, pH8.0; 100 mM NaCl; 20 mM Imidazole
Elution Buffer	Ni-purification	50 mM Tris-HCl, pH8.0; 100 mM NaCl; 250 mM Imidazole
Purification buffers for Aβ₍₁₋₄₀₎ amyloid peptide		
Lysis Buffer	Cell Lysis	20 mM Tris-HCl, pH8.0; 1x Complete Protease Inhibitor; 1mgr/mL DNase
Tris/Triton	Wash of Inclusion Bodies	20 mM Tris-HCl, pH8.5; 0.4 % Triton-X (v/v)
Buffer A	Reverse – phase HPLC	10 mM NH ₄ OH
Buffer B	Reverse – phase HPLC	80 % Acetonitrile; 0.3 % TFA
GdHCl	Reverse – phase HPLC	20 mM Tris-HCl, pH8.5; 8 M Guanidine hydrochloride
Other buffers		
TAE	Agarose gel electrophoresis	40 mM Tris-acetate, pH 8.0; 0.1 mM Na ₂ EDTA
Buffer CC 1	Competent cells preparation	39 mM NaAc, pH 5.5; 100 mM CaCl ₂ ; 70 mM MnCl ₂
Buffer CC 2	Competent cells preparation	82.5 % Buffer CC 1; 17.25 % Glycerin (87 %)
PBS	Sample buffer for NMR	50 mM Na ₂ HPO ₄ / NaH ₂ PO ₄ ; 50 mM NaCl, pH 7.4
HEPES	Sample buffer for NMR	10 mM HEPES/KOH pH 7.4; 1 mM EDTA; 2 mM DTT
TBS	Sample buffer for EM	50 mM Tris-HCl, pH 7.5, 50 mM NaCl
10x Running Buffer	SDS-PAGE Electrophoresis	0.25 M Tris; 2 M Glycerin; 1% (w/v) SDS
4x Loader Buffer	SDS-PAGE Electrophoresis	0.25 M Tris-HCl, pH 6.8; 8% SDS; 40% Glycerol; 5% β -mercaptoethanol; 0.04% Bromoph. blue
Fixing Buffer	SDS-PAGE Electrophoresis	50% Methanol; 10% Acetic acid
Staining Buffer	SDS-PAGE Electrophoresis	0.1% Coomassie; 40% Methanol; 10% Acetic acid
Destaining Buffer	SDS-PAGE Electrophoresis	10% Methanol; 7% Acetic acid
Gel Buffer	Tricine-SDS-PAGE Electrophoresis	3 M Tris; 1 M HCl, 0.3% SDS
4x Loader Buffer	Tricine-SDS-PAGE Electrophoresis	200 mM Tris-HCl, pH 6.8; 400 mM DTT; 8% SDS; 40% Glycerol; 0.4% Bromoph. blue
Fixing Buffer	Tricine-SDS-PAGE Electrophoresis	50% Ethanol; 20% Acetic acid
Staining Buffer	Tricine-SDS-PAGE Electrophoresis	0.025% Coomassie blue; 10% Acetic acid
Destaining Buffer	Tricine-SDS-PAGE Electrophoresis	10% Acetic acid
10x Anode Buffer	Tricine-SDS-PAGE Electrophoresis	1 M Tris; 0.225 M HCl, pH 8.9
10x Cathode Buffer	Tricine-SDS-PAGE Electrophoresis	1 M Tris; 1 M Tricine; 1% SDS, pH 8.25

3.2. Methods

3.2.1. Molecular Biology and Microbiological Methods

3.2.1.1. Plasmid Purification

The plasmid DNA was purified from the *E. coli* LB overnight (O/N) cultures using the the Wizard® Plus SV Miniprep kit (Promega, Mannheim, Germany). The isolation was done according to the manual of the kit. The procedure consists of three basic steps: (i) preparation and clearing of a bacterial lysate, (ii) binding of DNA into the spin column membrane, and (iii) washing and elution of plasmid DNA. The DNA was always eluted in 50 µl mQ H₂O. The DNA was sequenced by GATC Biotech AG (Konstanz, Germany) and stored at -20° C. Pure plasmid concentration was determined by measuring the UV absorbance at 260 nm. The sequences were analyzed by using the Clone Manager Suite software (version 1.3.0.0.).

3.2.1.2. Preparation of Competent Cells

In order to chemically prepare competent *E. coli* cells for the DNA-transformation, a small amount of bacteria of a frozen culture were streaked out on a LB plate containing kanamycin and they were incubated at 37 °C O/N. The next day a few colonies were picked, given in 5 mL falcon LB culture with kanamycin and incubated again at 37 °C O/N. When OD₆₀₀ of this O/N culture reached 0.4 – 0.6, then it was diluted in 500 mL LB with 1 mL kanamycin, and the cells were grown at 37 °C until OD₆₀₀ reached 0.4 – 0.7. Afterwards 10 mL sterile and filtered 1 M MgCl₂ was added and it was again incubated, firstly 10 min at 37 °C and then 60 min on ice. The culture was split in 50 mL falcons and spun down (Sorvall GSA rotor) at 6000 rpm for 10 min at 4 °C. The supernatant was discarded and the pellet of each falcon was gently resuspended in 10 mL of buffer CC 1. The falcons were cooled on ice for 60 min, again spun down at the same conditions and the supernatant was discarded. Each pellet was afterwards resuspended in 1 mL ice-cold buffer CC 2. Distribute the cell suspension in 100-200 µl aliquots in 0.5 or 1.5-ml microfuge tubes. Flash freeze the cell suspension in liquid nitrogen and store the tubes at -80°C.

3.2.1.3. Polymerase Chain Reaction and Site – directed Mutagenesis

The polymerase chain reaction (PCR; Erlich 1989) is a technique that amplifies specific DNA fragments, even when that source DNA is of relatively poor quality. PCR was performed as shown in **Table 3.3**, with 200 ng template DNA, 1x Pfu buffer, 0.25 µM dNTPs, 2-5 µM of each primer and 1 µl Pfu Ultra Polymerase (New England Biolabs) in a total volume of 50 µl. The cycler was run with an initial step of 5 min at 94 °C, followed by 25 cycles with 1 min 94 °C, 1 min 56 °C and 2 min/kb at 68 °C. Final extension for 10 min at 68 °C followed and then the PCR products were cooled down to 4°C. Samples containing 500 ng DNA and the T7 forward primer were sent to GATC to perform sequencing. After PCR, the templates were digested by adding 1 µl Dpn I and incubating for 2 hrs at 37° C. 5 µl of the each product were used for transformations.

Mutagenesis primers for point mutations or deletions of single amino acids or whole protein regions were designed by adjusting the DNA sequence to the aimed mutation and considering codon bias (Maloy 2002).

Upstream and downstream of the mutation site, 20 nucleotides from each side were added to complete the primer designing. The mutagenesis protocol was adapted from the QuikChange site-directed mutagenesis kit from Stratagene (Santa Clara, USA). The mutagenesis for the α B-6D mutant was performed in two steps. In the first PCR the mutations E19D, E21D, E43D, E45D and E53D were introduced, and in the second PCR the last mutation, E59D, was also inserted.

Table 3.3 | The PCR reactions were prepared in the following scheme in a total volume of 50 μ l. The cycling steps are highlighted in light grey.

PCR Reaction Mixture	(μ L)	Temperature	Time
dd H ₂ O	fill up to a $V_{final} = 50 \mu$ l	94 °C	5 min (initial denaturation)
1x Pfu Ultra Buffer	5.0	94 °C	1 min
Template	x μ l (200 ng)	56 °C	1 min
2-5 μ M forward primer	1.0	68 °C	2 min/kbp of template plasmid
2-5 μ M reversed primer	1.0		x 25
0.25 μ M dNTPs	0.4	68 °C	10 min (final elongation)
Pfu Ultra DNA polymerase	1.0	4 °C	∞

3.2.1.4. Transformation of *E. coli* Cells

For transformation 200 ng plasmid DNA were added to one 50-100 μ l frozen aliquot of competent cells. For plasmid amplification the plasmid was transformed to competent XL1blue cells, for protein expression the plasmid was transformed to competent BL21 (DE3) cells. Incubation on ice for 30 min to allow plasmid adhesion on cell surface was followed by heat shock at 42 °C was performed for 45 s. Then the cells were incubated 10 min on ice and 750 μ l LB medium was added. Cells were incubated for 1 hr at 37 °C under shaking (650 rpm) to allow expression of antibiotic resistance. The cells were centrifuged for 1 min at 4000 xg. Cells were pelleted, supernatant was discarded and cell pellet was resuspended in 100 μ l LB. Cells were plated in LB agar petri plates containing 50 mg/l kanamycin incubated O/N at 37° C.

3.2.1.5. Glycerol Stocks

750 μ l of an O/N LB culture of BL21 (DE3) cells were mixed with 250 μ l of sterile 80% glycerol (Roth). The mixture was gently vortexed, immediately flash frozen in liquid nitrogen and stored at -80 °C.

3.2.1.6. Agarose Gels Electrophoresis

Depending on the size of the PCR bands produced and the discrimination needed, band visualization was accomplished by 1.2% agarose gel electrophoresis and analyzed under UV light. The separation here occurs because smaller molecules pass through the pores of the gel easier than larger ones, i.e. the gel is sensitive to the physical size of the molecule. DNA samples were analysed by 1.2% agarose gel electrophoresis. Samples were mixed with SYBRsafe for DNA and 6x loading buffer. For separation 1.2% agarose in 1x TAE buffer was used. The gel was run at 120 V/200 mA for 30 min.

3.2.1.7. Determination of DNA Concentration

DNA concentration was assessed by measuring the absorption at a wavelength of 260 nm (A_{260} nm). Drops of 1-2 μ l were measured in triplicate using the NanoDrop.

3.2.1.8. Recombinant Protein Expression

The *E. coli* strain BL21 (DE3) was used as the expression host for recombinant production of α B-WT, α B-6E and its variants, α B-6D, α B- δ NTD, α B- δ CTE, α A-WT, α A-ACD-CTE and $A\beta_{40}$. Protein expression always started with freshly transformed cells. A well-separated single colony was picked from LB agar plates and used for inoculation of 5 mL pre-cultures in LB-Kan medium. These were grown aerobically at 37 °C for approximately 3 h and their growth was monitored by measuring the cell density ($OD_{600} \sim 0.6$). LB-Kan medium of 50 mL was then inoculated with the pre-culture. Protein expression was induced by the addition of isopropyl-b-D-thiogalactopyranoside (IPTG, SERVA) to a final concentration of 1 mM. After induction, α B and its variants were shaken O/N at 150 rpm at 22 °C, α A and its variants were shaken O/N at 150 rpm at 20 °C, and $A\beta_{40}$ cells were shaken for another 4–6 hrs at 150 rpm at 37 °C in order to achieve maximal protein yields. In the following, the expression protocols for unlabeled, ^{13}C , ^{15}N - and ^2H , ^{13}C , ^{15}N -enriched proteins are separately described.

3.2.1.8.1. Unlabeled Protein

Expression was performed in LB-medium with 50 mg/ml kanamycin. Cultures were inoculated from a fresh overnight culture to an OD_{600} of 0.1 and grown in 2 L baffled shake flasks with constant shaking (150 rpm) at 37 °C to an OD_{600} of 0.6–0.8. After induction with 1 mM IPTG, cells were shaken O/N at 150 rpm at the desired temperature, and subsequently harvested by centrifugation at 6000 xg for 20 min at 4 °C. The pellet was resuspended in resuspension buffer and centrifuged at 4000 xg for 20 min. Pellets were frozen in liquid nitrogen and stored at -80 °C.

3.2.1.8.2. ^{15}N or ^{13}C , ^{15}N Enrichment in Proteins

For the expression of ^{15}N - or ^{13}C , ^{15}N -labeled proteins, 25 mL of the LB-Kan O/N culture was gently centrifuged for 10 min at 4000 xg and 10 °C. The cell pellet was carefully resuspended in unlabeled 1x M9 minimal medium. The cells were grown O/N and the fresh cell pellet was used afterwards for inoculation of the main labeled 1L 1x M9 culture (starting OD_{600} of 0.15). The 2 L baffled shake flasks used contained 500 mL of the labeled 1x M9 culture and they were incubated at 37 °C with constant shaking at 150 rpm for aerobic cell growth. When cell density reached an OD_{600} of 0.6–0.8, IPTG was added to a final concentration of 1 mM. Protein expression was performed according to the protocol for each protein sample, mentioned in chapter 3.2.1.7.1. For full-length α B and α A, the expression period was on the order of 18 hrs, whereas for their mutants the expression was aborted earlier, after 14 hrs, in order to prevent proteolytic degradation.

3.2.1.8.3. ^2H , ^{13}C , ^{15}N and ILV – Labeling

Perdeuteration of αB demanded careful adaptation of the expression host cells to the cell-toxic D_2O . Therefore, freshly transformed cells were used to inoculate a 10 ml LB-Kan pre-culture, which was transferred to 100 ml LB-Kan and further incubated O/N at 37 °C until OD_{600} reached 0.8. After 10 min centrifugation at 4000 xg, the cell pellet was gently resuspended in another 100 ml freshly made LB-Kan culture, containing 50% D_2O and was grown O/N at 37 °C at 160 rpm. The next day the cells were again spun down for 10 min at 400 xg, and the pellet was resuspended in 100 ml D_2O -based 1x M9 minimal medium containing, glucose and NH_4Cl with natural abundance of isotopes. The cells were grown O/N at 37 °C shaking at 160 rpm and the main 1 L culture, containing 100% D_2O 1x M9, ^{15}N -labeled NH_4Cl and ^2H , ^{13}C -labeled glucose, was finally inoculated from the previous culture till OD_{600} reached 0.2–0.3. Cells were grown all day till OD_{600} was around 0.6 – 0.8 and induced with 1mM IPTG. Protein expression was performed according to the protocol for αB , shown in chapter 3.2.1.7.1. Overnight expression gave rise to a final OD_{600} of approximately 1.2 – 1.9. For the ILV-labeled αB -WT and αB -6E samples, 100% D_2O 1x M9 medium was used and the precursors were added before the IPTG induction. It should be noted that all employed solutions and additives were D_2O -based and that contamination by H_2O was rigorously avoided. The ILV precursors used are listed in **Appendix 7.5** and also their structure is shown.

3.2.1.9. Cell Harvest and Storage

Following protein expression, cells were transferred in 500 ml buckets (Nalgene) and harvested by centrifugation at 6000 xg for 30 min and at a temperature of 4 °C. The supernatant was discarded and since all α -crystallin constructs were purified via anion exchange chromatography as the initial purification step, the pellet was resuspended in resuspension buffer on ice and centrifuged further in 50 mL falcon tubes for 20 min at 4000 xg and 4 °C. Pellets were weighted, frozen in liquid nitrogen and stored at -80 °C.

3.2.2. Biochemical Methods and Sample Preparation

Protein sequences and parameters are summarized in the Appendix in **Supp. Table S3 and S4**, respectively. αA -WT and αA -ACD-CTE were expressed in our group and purified by Christoph Kaiser (TU München, Germany).

3.2.2.1. Cell Lysis

Cell lysis for all different protein samples was accomplished with a sonicator SonoPlus (Bendelin) keeping the cells on ice. Frozen cell pellets were thawed, subsequently resuspended in approximately 35 ml cell lysis buffer and stirred for 30 min on ice. α -crystallin cells were disrupted by applying 40% amplitude (Amp) for 30 min with pulse on 1 s to pulse off 15 s. The lysate was then diluted to 80 ml, centrifuged for 30 min at 24000 xg and the supernatant was filtered over a 0.22 μm filter (Pall Corporation) and kept on ice for subsequent protein purification. A continuous work flow was especially important for the degradation-prone αB variants.

Following the expression protocol described before, the major fraction of $A\beta_{40}$ was expressed into inclusion bodies (Dasari *et al.* 2011). In this case the previously frozen $A\beta_{40}$ cell pellet was thawed at +4 °C and after cell pellet resuspension in the lysis buffer, the inclusion bodies had to be washed out. Therefore, after incubating the cells for 1 h at 4°C, the suspension was sonicated (30% Amp; pulse on 1s; pulse off 1s; total sonication time 3-5 mins) on ice and afterwards centrifuged for 1 h at 24000 xg and 4 °C. The pellet was resuspended in about 40 mL Tris/Triton buffer. The inclusion bodies were subsequently dissolved by sonication on ice (30% Amp; pulse on 1s; pulse off 1s; total sonication time 3-5 mins) and again centrifuged for 30 min at 24000 xg and 4 °C. The new pellet was dissolved in 40 ml ice cold 20 mM Tris-HCl, pH 8.5 buffer to remove the Triton-X, sonicated and centrifuged as before. This step was repeated 3-4 more times in order to remove all Triton-X remaining. After the last washing step, the final pellet was resuspended in freshly prepared GdHCl buffer, centrifuged for 20 min at 24000 xg and 4 °C and the supernatant was collected for purification by reverse-phase HPLC chromatography (Dasari 2011).

3.2.2.2. Purification of α -crystallins

3.2.2.2.1. Anion-Exchange Chromatography (AEC)

Anion-exchange chromatography was the initial purification step after lysis for full-length α B-WT and its mutants. In AEC negatively charged patches of the protein interact with the positively charged bead matrix in the column. The theoretical isoelectric points (pI) are 6.8 for α B-WT, 6.5 for α B- δ NTD, and 5.7 for α B-6E and α B-6D, as obtained from the ExPASy ProtParam tool (Gasteiger *et al.* 2003). All proteins are thus negatively charged at the provided pH of 8.5. Whilst α B-6D was first subjected to weak and subsequently to strong AEC, full-length α B was directly applied to strong AEC, since its large *M_w* ensured efficient separation during the final size-exclusion chromatography (SEC). All buffers contained 1 mM EDTA in order to chelate divalent metal ions.

3.2.2.2.1.1. Weak Anion-Exchange Chromatography

The weak anion-exchanger HiPrep 16/10 DEAE-(diethylaminoethyl)-Sepharose column (90 μ m particle size, GE Healthcare) was employed as a first attempt to purify the α B-6D mutant. The column was equilibrated in buffer A, and then 10 ml of 2.3 mg/ml sample were loaded onto the column using a 17 ml superloop. The column was washed with buffer A until the A_{280} signal reached a baseline. Then the gradient was applied as follows: 0-60 % buffer B in 20 CV at a flow rate of 4 ml/min followed by a second gradient 60-100 % buffer B in 10 CV. Eluted protein was collected in 6 mL fractions, which were analyzed by SDS-PAGE. Respective fractions containing α B-6D were pooled and diluted threefold in buffer A for subsequent application to strong AEC.

3.2.2.2.1.2. Strong Anion-Exchange Chromatography

A preparative 200 ml Q Sepharose FF column at 4 °C on an Äkta purifier system was used for strong AEC. The column was washed with 3 CV buffer B and equilibrated with 3 CV buffer A. The program for α B-WT and α B- δ NTD elution was as follows: wash with buffer A (12 CV), gradient of buffer B from 0% to 18% (8.5

CV) and a final wash with 100% buffer B (2 CV). The program for α B-6E and α B-6D elution was as follows: wash with buffer A (6 CV), gradient of buffer B from 0% to 60% (8.5 CV), gradient of buffer B from 60% to 100% (2 CV) and a final wash with buffer B (1 CV). By linearly increasing the NaCl concentration on the column, the Cl⁻ ions displace the proteins that are bound to the column. The stronger the proteins interact with the column (depending on the surface exposed negative charges), the higher NaCl concentrations are necessary for displacing the protein from the column. The flow rate was 3 - 4 ml/min, the fraction size was 15 ml, and maximum pressure was 0.5 MPa. Eluted protein was collected in 6-8 mL fractions and analyzed by SDS-PAGE. Fractions containing the target protein with reasonable purity were pooled and concentrated for subsequent SEC.

3.2.2.2.2. Size Exclusion Chromatography (SEC)

In the final purification step, SEC separated the proteins with respect to their molecular size. SEC was performed using either a 500 ml Superose 6 column for α B-WT and α B- δ NTD, or a 300 ml Superdex200 prep grade α B-6E and α B-6D on an Äkta purifier system at 4 °C. Each column was equilibrated with SEC buffer. The fractions derived from the AEC were pooled and concentrated with a 400 ml stirred cell concentrator (Fisher Scientific) up to a total volume of 10 ml. The sample was loaded into a 17 ml superloop and injected on the SEC column. The columns were equilibrated with 2 CV of SEC buffer and the elution volume was 1.5 CV. The flow rate was 1 ml/min with a maximum pressure of 0.5 MPa. The eluted volume was collected in 7 ml fractions, which were analyzed by SDS-PAGE. Pure fractions containing the target protein with low protein background were pooled and concentrated to a final concentration of approximate 20 mg/ml. After the size exclusion chromatography further purification was necessary for α B-6D to exclude residual impurities, while for α B-WT and α B- δ NTD an additional analytical SEC was performed in order to finalize the sample purity and to buffer exchange it to the NMR buffer.

3.2.2.2.3. Strong Anion-Exchange Chromatography II

Another attempt to further purify the α B-6D mutant was by using a 6 ml ResourceQ column (GE Healthcare). The column contains strong anion exchange material with average particle size of 15 μ m and quaternary ammonium as ligand. The column was equilibrated on buffer A, 10 ml of 2.3 mg/ml sample were loaded onto the column and washed with buffer A until a baseline was reached. Afterwards a gradient was set as described above (chapter 3.2.2.2.1).

3.2.2.2.4. Strong Anion-Exchange Chromatography with Urea (uAEC)

In order to find the right purification protocol for α B-6E mutant after AEC and SEC runs, an additional AEC with Urea step was added. In this case the sample was diluted in 8 M Urea in order to reach 5 M Urea in the final uAEC buffers A and B. The same gradient described in chapter 3.2.2.2.1.2. was used and the eluted fractions were collected and analysed further with SDS-PAGE. The sample was refolded in buffer R, concentrated again till 10 ml and injected into the 500 ml SEC column. The desired 7 ml eluted fractions were run on an SDS gel and the final sample was run on the analytical SEC for buffer exchange.

3.2.2.2.5. Hydrophobic Interaction Chromatography (HIC)

Furthermore, hydrophobic interaction chromatography (HIC) was performed using a 5 ml Phenyl column (GE Healthcare) at 4 °C to further purify α B-6D. The protein was precipitated slowly adding ammonium sulfate until reaching 25% of saturation at 4 °C (0.139 g/ml) and incubated overnight. The protein solution was filtered with a 0.22 μ m filter and loaded to an appropriate loop and injected on a Phenyl column with 0.5 ml/min, which was pre-equilibrated first with buffer A, and subsequently with buffer B(AS) with a flow rate of 1 ml/min. A gradient was run from 100 to 20 % B(AS) in 2 CV, and then from 20 to 0 % B(AS) in 16 CV. Fraction size was 2 ml and flow rate was 1 ml/min. The fractions containing the protein were analyzed with SDS-PAGE, and pure fractions were pooled and concentrated with an Amicon 30K concentrator (Merck Millipore).

3.2.2.2.6. Analytical Size Exclusion Chromatography (aSEC)

A 24 ml analytical Superose 6 Increase 10/300 GL column was employed in order to assess the molecular weight of all protein samples and do buffer exchange. The column was pre-equilibrated with 2 CV of PBS buffer. After filtration (0.2 μ m), samples of 500 μ l were injected and eluted at a flow rate of 0.5 mL/min. The fraction size was 0.5 ml. Fractions containing protein were analyzed by SDS-PAGE, and pure fractions were pooled and concentrated with an Amicon 30K concentrator. Standard proteins (GE Healthcare) and mixtures of those were applied to the columns for calibration. The observed retention volumes were correlated with the known molecular weights of standard proteins (bovine Thyroglobulin 669 kDa, horse Ferritin 440 kDa, rabbit Aldolase 158 kDa, hen Ovalbumin 43 kDa, bovine Chymotrypsinogen 25 kDa, bovine Ribonuclease-A 13.7 kDa).

3.2.2.2.7. Ni – NTA Purification of α B-6E

In order to find the best purification protocol α B-6E was also mutated by adding a his-tag in the C-terminal region of the protein by PCR and purified by Ni – NTA column. Cells were lysed in 40 ml lysis buffer (50mM Tris-HCl pH 8.0; 100mM NaCl; 20mM Imidazole; 2 tablets EDTA Protease Inhibitor). 1 mg/ml DNaseI was added to the suspension and then cells were incubated for 30 min at 4°C while rotating. After cell disruption with the sonicator (40% Amp; 30 min; pulse on 1 s – pulse off 15 s), the cells were centrifuged at 24000 xg for 1 h at 4 °C. The beads were equilibrated in 25 ml H₂O 4x and then washed 3x with the lysis buffer before applying the supernatant. Flow-through was collected in falcons. After the lysate was added slowly to the beads, the beads were washed with the wash buffer 5x. The wash followed addition of 10 ml elution buffer. The mixture was let for 10 min to incubate and then the protein was collected. The procedure was repeated 2x and the whole purification took place at 4 °C. Protein purity was analysed by SDS-PAGE and by mixing in 2-4 μ l of eluted sample, 20 μ l of 4x loader. In the next step using a desalting column the imidazole was removed and a gel filtration equilibrated in PBS, using a Superose 6 column, followed to reach maximum purity of the sample. Fractions of 1.5 ml volume were collected and loaded in SDS-gel for analysis.

3.2.2.3. Dialysis

For buffer exchange, except for aSEC, also dialysis was performed. Protein solutions were usually dialyzed against 5 L of the desired buffer. Typical sample volumes was around 30-80 ml. The regenerated cellulose membranes were chosen according to the desired molecular weight cut-off (MWCO) and incubated in deionized water for 30 min before use. Dialysis was performed over night at 4 °C under constant stirring.

3.2.2.4. SDS-PAGE Electrophoresis

Polyacrylamide gel-electrophoresis (PAGE) was performed under denaturing conditions employing sodium dodecyl sulfate (SDS). The proteins were separated according to their sizes by SDS-page (Laemmli 1970). Polyacrylamide percentage of 15% was used for analysis of the samples. The composition of the gels is given in **Table 3.4**. Samples were mixed with 4x loader and following incubation at 95 °C for 5 min, they were chilled at room temperature, and 12 µl from each sample was loaded onto the stacking-gel. Electrophoretic separation of proteins was accomplished in an electrophoresis chamber (BioRad) and by applying a voltage of 230 V and 20 W per gel until the sample reached the end of the separating gel (at least 45 min) and subsequently fixed for 20 min and stained by Coomassie Blue staining solution for at least 30 min (Merril 1990). After destaining the gels were analyzed.

Table 3.4 | Composition of SDS gels. The volumes are given for 11 gels.

Components	Seperating gel 15%	Stacking gel 4%
H2O	34 mL	37.8 mL
40% Bisacrylamide	36 mL	6 mL
1.5M Tris (pH 8.8)	24 mL	15 mL
10% SDS	960 µl	600 µl
10% APS	960 µl	600 µl
TEMED	96 µl	60 µl

3.2.2.5. Determination of Protein Concentration

The concentration of protein solutions was assessed by measuring the absorption of aromatic residues at a wavelength of 280 nm (A_{280} nm). Drops of 2 µl were measured in triplicate using the NanoDrop spectrophotometer. Sample purity was judged from the ratio A_{280} nm / A_{260} nm (protein contamination) being optimal in the range of 0.5-0.7. In case of very high A_{280} nm values, e.g. for FROSTY sample preparation, protein solutions were diluted before the measurement. Relevant parameters, were obtained from the ExPASy ProtParam tool (Gasteiger *et al.* 2003) and used to calculate the concentration of the respective protein, are summarized in Appendix in **Supp. Table S4**.

3.2.2.6. Concentration of Protein Samples by Ultrafiltration

Protein samples were concentrated by ultrafiltration. Large volumes (> 20 mL), e.g. during protein purification, were concentrated in 400 ml stirred concentrator cell (Millipore, Amicon Model 8400) with ultrafiltration-membranes (Millipore). During application of 2-3 bar pressure, the solution was gently stirred at 4 °C. Small sample volumes were concentrated in centrifugal filter units (Millipore, Amicon Ultra-

0.5/4/15) according to the manufacturer's instructions. The MWCO was selected depending on the size of the target protein ($MWCO < Mw/2$).

3.2.2.7. Storage of Protein Samples

Aliquots of 300 - 500 μ L of each protein sample in PBS were flash-frozen in liquid nitrogen and directly stored at -80 °C. For $A\beta_{40}$, the flashfrozen samples were subsequently sealed with meshed caps and subjected to lyophilisation. Lyophilization was performed at approximately -80 °C and 0.014 mbar for 3 days. The dry protein powder was then tightly sealed and stored at -80 °C.

3.2.2.8. Mass Spectroscopy

The integrity of the final protein sample was confirmed by MALDI-TOF. Acquisition of MALDI data was kindly performed by Martin Haslbeck (TU Munich, Germany).

3.2.2.9. Monitoring Degradation

Degradation of α B-6D was monitored to obtain its stability at room temperature. Therefore a batch of protein after SEC was incubated at room temperature and samples were taken every 24 h and analyzed by SDS-PAGE.

3.2.2.10. Limited Proteolysis

Limited proteolysis was performed using the protease α -chymotrypsin (Sigma-Aldrich, Taufkirchen, Germany) to compare the proteolytic stability of α B-6D to the stability of α B-WT. α -Chymotrypsin is a protease that cleaves proteins selectively after the aromatic amino acids Trp, Tyr, Phe and also after the big hydrophobic amino acids Met and Leu. Limited proteolysis uses small amounts of protease to have a slow digestion and potentially allowing identification of stabilized fragments. Proteins with destabilized sequences are more prone to degradation by proteases at these regions.

The assay was performed similar to Kumar *et al.* (2004). The total sample volume was 200 μ L containing 50 μ M α B and 1 mM $CaCl_2$ in PBS buffer. α -chymotrypsin was dissolved to 1 mg/ml in 1 mM HCl. The reaction was started by adding 2 μ L of protease to a final concentration of 0.4 μ M α -chymotrypsin (molecular weight 25 kDa). Samples were taken and immediately boiled in Laemmli buffer at the following times: 0 (before addition of α -chymotrypsin) and 1, 5, 30 and 60 minutes after addition of the protease. Results were monitored by SDS-PAGE.

3.2.2.11. Analytical ultracentrifugation (AUC)

For sedimentation velocity experiments all proteins were buffer exchanged to phosphate buffer. The concentration of the proteins was 1 mg/ml (α B-WT and α B-6D) and 0.4 mg/ml (α B-6E). 450 μ L of each

sample was filled in a standard double-sector Epon charcoal-filled centerpiece sample cell with quartz windows. The AUC experiments were carried out using a Beckman XL-I with a rotor speed of 34 000 rpm at 20 °C measuring absorbance at 280 nm and they were measured by Philipp Schmid (TU München, Germany).

3.2.2.12. PEGylation Reaction of the Full-length α B-Crystallin

A linear 10 kDa methoxy PEG Succinimidyl Carboxymethyl Ester (M-SCM-10K, JenKem, USA) is a highly quality amine PEG product with a strong non-degradable linker between the PEG polymeric chain and the NHS ester. M-SCM-10K reacts with the amine group of lysines increasing the size of the protein. Before using the PEG, the bottle containing the reagent was allowed to warm at room temperature slowly. A stock solution of PEGylation reagent M-SCM-10K was prepared, dissolving 15 mg of reagent in 100 μ l of DMSO. The PEG was then added into the protein sample in a 10x fold excess with respect to the α B, which was dissolved in PBS buffer pH 7.4. The mixture was left stirring for 1 h at room temperature under slow shaking. The reaction followed a purification with PD10 column in order to remove the non-reacted and the hydrolyzed PEGylation reagent. Products and yield of the reaction were evaluated by SDS-PAGE and mass spectrometry. The final sample was purified by analytical SEC and the result was evaluated again with SDS-PAGE.

3.2.2.13. Purification of Recombinant $A\beta_{40}$ Amyloid Peptide

The inclusion bodies were purified using an Äkta purifier system. The extract was loaded in a 40 ml superloop and injected into a reverse-phase (RP) HPLC column (material: source 30RPC). Initially, the column was equilibrated with 20% B for 5 CV. The sample was loaded in 0.6 CV, and the column was washed for 4 CV, both at 20% B. This was followed by a gradient from 20% B to 60% B over 15 CV, in which $A\beta_{40}$ usually elutes at around 42% B. Fractions of 11 ml were collected throughout the gradient. The concentration of B was increased to 100% in 1.5 CV and remained at 100% B for 1.5 CV until the completion of the run. A constant flow of 4 ml/min was used for the entire HPLC run. Protein elution was monitored by UV at 280 nm. The protein content of the fractions was analyzed by Tricine-SDS-PAGE. Fractions containing $A\beta_{40}$ were gathered in glass tubes, flash frozen in liquid nitrogen, lyophilized and stored at -80 °C until further use.

3.2.2.14. Tricine-SDS-PAGE Electrophoresis

Tricine-Sodium Dodecyl Sulfate-Polyacrylamide Gel Electrophoresis (SDS-PAGE) was carried out in order to analyse protein content of $A\beta_{(1-40)}$ samples based on Schägger (2006) (Table 3.5). This method is optimized for the separation of small (<30 kDa) and hydrophobic proteins. 30 μ l of the fractions collected from the RP-HPLC run, were mixed with 10 μ l of sample loading buffer (4x). The samples were incubated at 95 °C for 15 min with 800 rpm. Around 5 μ l of samples from bacterial cell pellet samples and 10 μ l of samples from RP-HPLC fractions were loaded onto the gels. The Ultra-low Range Molecular Weight Marker (Sigma-Aldrich) was loaded onto the gels as a reference for molecular weight. Gels were run with a constant voltage of 100 V. After the run was completed, gels were incubated in fixing solution for 30 min, transferred to staining solution for at least 1 h and incubated in destaining solution.

Table 3.5 | Composition of Tricine-SDS gels. The volumes are given for 10 gels.

For 10 gels	Seperating gel 16%	Stacking gel 4%
H2O	16.6 mL	52 mL
ProtoGel (40%)	40 mL	8 mL
Gel Buffer (3x)	33.4 mL	20 mL
Glycerol	10 ml	---
10% APS	40 μ l	80 μ l
TEMED	1 ml	800 μ l

3.2.2.15. Transmission Electron Microscopy (TEM)

3.2.2.15.1. Preparation of A β ₄₀ Fibrils

Lyophilized A β ₄₀ was initially solubilized in 10 mM NaOH and sonicated for 15 min. Subsequently, an equivalent volume of TBS was added to ensure a physiological pH of 7.4. After final sonication for 15 min, the solution was filtered (0.2 μ m) and its concentration determined. The preparation was done on ice with pre-cooled solutions. The procedure assured that the peptide and possible aggregates were completely dissolved. After preparation of monomeric A β ₄₀, the peptides were incubated for 4 days at 37 °C under slow agitation in order to provoke fibril formation. The concentration of A β ₄₀ amounted to 150 μ M in TBS to a final volume of 100 μ l. Co-incubation with α B was performed at different chaperone concentrations (150 μ M, 30 μ M, 10 μ M, 5 μ M, 2.5 μ M) and the structural changes of the A β ₄₀ fibrils were observed. Amyloid samples had to be sonicated for 2 min in order to disrupt clusters of fibrils. The preparation of grids was similar for all samples.

3.2.2.15.2. Negative Staining

Protein samples were prepared for TEM visualization by negative staining on a formvar coated grid stabilized with carbon film. The hydrophilization of the grids was enhanced by glow discharging in argon atmosphere for 30 s and 2 mA (the grids should be used within 30 min after the glow-discharging), to increase sample adsorption on the grids. Sample volumes of 3.5 μ l were placed on the grid and incubated for 60 s to achieve particle adsorption to the surface. For negative staining, the excess solution was blotted off from the grids carefully using filter paper. The sample was stained with 3.5 μ l 2% (w/v) uranylacetate for 30 s. Finally, the extra uranylacetate was again removed using a filter paper. The data were acquired by Andre Heuer (Gene Center, LMU, Munich) on an AN 100 KV transmission electron microscope (Zeiss) and the samples were viewed under different magnifications and images were captured on a side-mounted SIS Megaview 1K CCD camera.

3.2.2.15.3. Immunoelectron Microscopy

The fibril-chaperone complex for immuno-EM was obtained by the addition of α B to A β fibrils in buffer A, with final concentrations of 30 μ M and 150 μ M, respectively. The mixture was incubated for as described (in 3.2.2.14.1.) and then spun at 16000 \times g for 30 min. The supernatant was carefully aspirated to remove free α B and the pellet was resuspended in one volume of PBS buffer, prior to dilution for immunogold

labelling as required. The grids were prepared by the addition of 4 μl of a 100-fold dilution of the fibril-chaperone complex in PBS. Samples were deposited onto grids immediately following dilution. Grids were washed 3x with 10 μl H_2O , blocked with 15 μl 0.1% (w/v) bovine serum albumin-BSA in 10 mM PBS/100 mM NaCl (BSA/PBS buffer) buffer pH 7.4 for 15 min, then incubated for 30 min with the αB monoclonal primary 2 antibody (100 $\mu\text{g}/\text{ml}$, Assay Designs, Michigan, USA) diluted 250-fold in 0.1% BSA/PBS buffer. The grids were blotted with filter paper between each washing step. Next, the grids were 3x washed with 50 μl 0.1% BSA/PBS buffer, for 4 min each time, before a 30 min incubation at room temperature with goat anti-mouse 10 nm immunogold conjugate (GMHL10, BBI International, Cardiff, UK), diluted 150-fold into 0.1% BSA/PBS buffer. The grids were then 3x washed with 50 μl 0.1% BSA/PBS buffer, again for 4 min each time, then 3x with 50 μl H_2O and negatively stained with 20 μl of 2% uranyl acetate.

3.2.3. NMR Spectroscopy

NMR experiments were carried out employing Bruker Avance spectrometers operating at a ^1H Larmor frequency of 950 (22.3 T), 900 (21.1 T), 750 (17.6 T), 600 (14.1 T) or 500 (11.7 T) MHz that were all (except for the 750 MHz) equipped with CPTI triple-resonance ($^1\text{H}/^{13}\text{C}/^{15}\text{N}$) cryoprobes.

3.2.4. Solution – state NMR Spectroscopy

All 1D ^1H spectra contained a watrgate pulse sequence for solvent suppression (Liu *et al.* 1998). 2D ^1H , ^{15}N correlations were recorded as SOFAST heteronuclear multiple quantum coherence (HMQC) (Schanda and Brutscher 2005) or as heteronuclear single quantum coherence (HSQC) (Kay *et al.* 1990) experiments. 2D ^1H , ^{13}C correlations were recorded as HSQC experiments.

3.2.4.1. Sample Preparation

Most of the NMR experiments were performed using a shigemi tube (Shigemi, Tokyo, Japan), where the sample volume was 280–300 μl . In all samples the buffer for αB , its variants and $\text{A}\beta$ contained PBS pH 7.4, while for αA the NMR buffer contained HEPES/KOH pH 7.4, but both in 95% H_2O and 5% D_2O (unless stated otherwise). Buffer composition is shown in Table 3.2. Samples concentration in all case were varying from 500 μl – 3 mM. For titrations, the molecules of interest were added directly to standard NMR tubes (Norell, Landisville, USA) filled with ca. 500 μl of sample, mixed gently and measured immediately. For filling 3 mm or shigemi tubes an electrical syringe eVol XR (SGE Analytical Science) was used.

3.2.4.2. Peak Integration and Chemical Shift Perturbation (CSP)

Unless otherwise stated 2D spectra were integrated using CcpNmr. Protein amide signals were integrated in the region between 6.0 ppm to 10.0 ppm in 1D ^1H spectra.

Chemical shift perturbations obtained from ^1H , ^{15}N HSQC spectra were calculated using the following formula:

$$\Delta\delta^{NH} = \sqrt{\frac{1}{2} \left[\delta_{1H}^2 + \frac{1}{25} \delta_{15N}^2 \right]} \quad (\text{Eq. 3.2.3.1.})$$

with $\Delta\delta$ = difference of chemical shift in different spectra.

3.2.4.3. DOSY Experiments

The samples used for DOSY were all in the same conditions (buffer, T, concentration) and the experiments were recorded with unlabeled proteins using the following parameters: gradient strength g of 2 - 98 %, Δ = 300 ms, δ = 3 ms. DOSY experiments were recorded at 950 MHz and 300 K.

3.2.4.4. Resonance Assignment Experiments

For the backbone resonance assignment of the CTR of α A, a ^{13}C , ^{15}N -labeled sample with 3 mM concentration was added in a shigemi tube in a final volume of 300 μl 10 mM HEPES/KOH pH 7.4. Standard triple resonance experiments were recorded: HNCA, HNCO (Kay *et al.* 1990), HNCACB (Wittekind *et al.* 1993), CBCA(CO)NH (Grzesiek *et al.* 1992), HNCACO (Clubb *et al.* 1992) and ^{15}N -edited ^1H , ^1H NOESY (τ_{mix} = 120 ms) (Fesik *et al.* 1988; Marion *et al.* 1989). Assignment of aliphatic side-chain resonances was accomplished using 2D ^1H , ^{13}C HSQC, 3D (H)CCCONH and 3D H(C)CCONH experiments (Montelione *et al.* 1992; Grzesiek *et al.* 1993; Lyons *et al.* 1993; Logan *et al.* 1993). DSS was used as direct ^1H chemical shifts reference and indirect reference for ^{15}N and ^{13}C chemical shifts (Wishart *et al.* 1995). The assignment experiments were recorded at 27 °C, 950 MHz and in 5% D_2O . **Table 3.6** summarizes the NMR experiments and relevant acquisition parameters.

Table 3.6 | NMR experiments performed for α A-WT assignment. Spectral widths and carrier frequencies are given for the indirect dimensions, whereas that of the direct ^1H dimension was set to 10 ppm and 4.7 ppm, respectively, in all cases. Complex data points are given in the order of acquisition times t_3 , t_2 , t_1 . The recycle delay was set to 1.2 s.

Experiment	Data points	Number of Scans	Spectral Widths	Carrier Frequencies
^1H , ^{15}N HSQC	4096 x 1024	8	18 ppm (^{15}N)	119 ppm (^{15}N)
^1H , ^{13}C HSQC	2048 x 512	4	80 ppm (^{13}C)	36 ppm (^{13}C)
HNCA	2048 x 76 x 170	4	18 ppm (^{15}N) 30 ppm (^{13}C)	119 ppm (^{15}N) 54 ppm (^{13}C)
HNCO	2048 x 76 x 128	4	18 ppm (^{15}N) 22 ppm (^{13}C)	119 ppm (^{15}N) 176 ppm (^{13}C)
HNCACB	2048 x 80 x 150	16	18 ppm (^{15}N) 75 ppm (^{13}C)	119 ppm (^{15}N) 40 ppm (^{13}C)
CBCA(CO)NH	2048 x 80 x 150	8	18 ppm (^{15}N) 75 ppm (^{13}C)	119 ppm (^{15}N) 40 ppm (^{13}C)
HNCACO	2048 x 76 x 128	4	18 ppm (^{15}N) 22 ppm (^{13}C)	119 ppm (^{15}N) 176 ppm (^{13}C)
^{15}N -edited ^1H , ^1H NOESY	2048 x 128 x 150	8	18 ppm (^{15}N) 13 ppm (^1H)	119 ppm (^{15}N) 4.7 ppm (^1H)
(H)CCCONH	2048 x 84 x 128	4	18 ppm (^{15}N) 11.5 ppm (^1H)	119 ppm (^{15}N) 4.7 ppm (^1H)
H(C)CCONH	2048 x 84 x 128	4	18 ppm (^{15}N) 75 ppm (^{13}C)	119 ppm (^{15}N) 39 ppm (^{13}C)

The data were usually processed with a square sine-bell apodization in direct and indirect dimensions with SSB (shift of the sine-bell) values of 2.0-3.0, depending on spectral resolution and sensitivity. Zero filling

was applied to yield data matrices of 2048x512x512. Linear forward prediction was applied to improve the spectral quality, when required.

3.2.4.5. Secondary Structure Prediction

The secondary structure of the C-terminal domain of α A was predicted from the difference between the chemical shift values of $^{13}\text{C}\alpha$, $^{13}\text{C}\beta$ atoms (Spera and Bax 1991), the corresponding chemical shift index (CSI 3.0; Hafsa et al. 2015) calculated using the following equation

$$CSI = (\delta_{observed}^{C\alpha} - \delta_{random\ coil}^{C\alpha}) - (\delta_{observed}^{C\beta} - \delta_{random\ coil}^{C\beta}) \quad (Eq. 3.2.3.2.)$$

and the random coil index (RCI) (Berjanskii and Wishart 2005; Shen et al. 2009; Shen and Bax 2012), against the residue number. Negative values for $\Delta\delta\text{C}\alpha$ (ppm) and $\Delta\delta\text{C}\alpha - \Delta\delta\text{C}\beta$ (ppm) indicate β -strand, positive values indicate α -helical structural elements, while values around 0 indicate random coil. At least 4 consecutive positive values are required to define a helix and at least 3 consecutive negative values are required to define a β -strand.

3.2.4.6. Titration Experiments

NMR titrations were carried out using uniformly ^{15}N -labeled samples in PBS buffer and pH 7.3. For all $\text{A}\beta$ titration experiments either with copper, $\alpha\text{B-WT}$ or $\alpha\text{B-6E}$, the concentration of $\text{A}\beta$ was 50 μM and in a step-wise manner the titrated protein was added in different molar ratios. ^1H , ^{15}N HSQC spectra were recorded after each addition.

3.2.4.7. NMR Relaxation Analysis

NMR ^{15}N transverse relaxation experiments (T_1 , $T_1\rho$ and heteronuclear NOE) were recorded on two different fields, 950 and 500 MHz at 300 K. The ^1H , ^{15}N heteronuclear NOE values were determined as the ratio of peak intensities in two experiments, with and without proton saturation. ^{15}N T_1 and $T_1\rho$ relaxation times were determined from pseudo-3D HSQC-based experiments recorded in an interleaved fashion with different relaxation delays (varying from 2 – 350 ms). For relaxation data peaks were integrated and fit with in house python scripts. Peaks with severe overlap were omitted from further analysis. Error estimation was calculated based on the signal to noise ratio. R_1 and $R_1\rho$ rates were calculated by dividing $1/T_1$ and $1/T_1\rho$.

3.2.4.8. Paramagnetic Relaxation Enhancement

In spin labeling experiments 3-(2-iodoacetamido)-proxyl (IPSL) (Sigma – Aldrich, Germany, 50 mM stock dissolved in DMSO) was used for the spin-label reaction. Before titration of a 5-fold molar excess of IPSL, 500 μM of the protein solution was completely reduced by adding 2 mM dithiothreitol (DTT). The buffer was exchanged afterwards to 1 M Tris-HCl (pH 8.0), 200 mM NaCl using a protein desalting spin column (Thermo Fisher Scientific Inc., USA). Following an overnight reaction in the dark at 4°C, the IPSL – tagged protein was passed two times through a desalting spin column to remove all unreacted spin label and

change the buffer to 10 mM HEPES/KOH (pH 7.4) and 1 mM EDTA. Two different samples were employed, which are referred to as ^{15}N $\alpha\text{A-IPSL}$ and ^{15}N $\alpha\text{A-}^{14}\text{N}$ $\alpha\text{A-IPSL}$. To prepare the mixed sample, ^{15}N - αA was added in the reaction mixture to ^{14}N - $\alpha\text{A-IPSL}$, in a 1:1 ratio, yielding a final concentration of 300 μM for each protein component. The mixed sample was subsequently incubated for 4 hrs at 37 °C. In both samples reduction of the protein-bound IPSL was achieved with a 10 molar excess of freshly prepared ascorbic acid in HEPES/KOH buffer to yield the diamagnetic species.

PREs arising from the spin label were determined using the ratio of peak intensities of the ^1H , ^{15}N -HSQC spectra obtained for the paramagnetic (oxidized) and the diamagnetic (reduced) state (I_{para}/I_{dia}), in the absence and presence of 10 molar equivalents of ascorbic acid. Peak volumes were extracted by box integration, using in-house Python scripts.

3.2.4.9. $^1\text{H}^{\text{N}}$ R_1 Relaxation Rates

$^1\text{H}^{\text{N}}$ R_1 relaxation rates were determined using a modified ^1H , ^{15}N HSQC pulse sequence with a saturation recovery element prior to the first INEPT step with the following relaxation delays: 0.05, 0.11, 0.26, 0.46, 0.73, 1.10, 1.59, 2.25, 3.15, 4.36 and 6.00 s. PREs were calculated as the difference of the R_1 rates ($\text{PRE} = R_{1(\text{para})} - R_{1(\text{dia})}$). Peak volumes were extracted by box integration, using in-house Python scripts. The experimental error was set to two times the standard deviation of the noise and the uncertainty of the T_1 values was estimated by 1000 Monte Carlo runs. R_1 rates were determined by fitting decay curves by an exponential function.

3.2.4.10. Methyl – TROSY Experiments

^{13}C methyl-TROSY NMR spectroscopy has emerged as a powerful method for studying the dynamics of large systems such as macromolecular assemblies and membrane proteins. Well-resolved multi-dimensional NMR spectra are essential for obtaining structural and dynamic information on backbone and sidechain within proteins. However, such spectra of large macromolecules have poor peak dispersion and line broadening due to rapid transverse relaxation of nuclear magnetization and spectral crowding. To overcome this problem we perform methyl NMR, which utilizes the advantageous spectroscopic properties of CH_3 -groups (Kay and Gardner 1997) that arise from their three-fold symmetry and fast rotation around the connecting C–C bond. This results in highly favorable relaxation properties that are exploited in methyl TROSY HMQC experiments (Amero *et al.* 2009; Ollershaw *et al.* 2003; Tugarinov *et al.* 2003) that yield well-resolved and sensitive NMR spectra even for high-molecular weight systems. Introduction of NMR-active methyl groups can be achieved with metabolic precursors to label the Ile- $\delta 1$ or Leu- δ and Val- γ positions in proteins expressed in *Escherichia coli* (Goto *et al.* 1999; Gardner and Kay 1997). However, labeled methyl groups can also be introduced in Thr (Velyvis *et al.* 2012; Sinha *et al.* 2011), Ile- $\gamma 2$ (Ayala *et al.* 2012; Ruschak *et al.* 2010), Ala (Ayala *et al.* 2009; Isaacson *et al.* 2007) and Met residues (Zheng *et al.* 2009; Jones *et al.* 2007; Fischer *et al.* 2007; DellaVecchia *et al.* 2007; Beatty *et al.* 1996), and in Leu and Val in a residue-specific and stereospecific manner (Miyanoiri *et al.* 2013; Mass *et al.* 2013; Lichtenecker *et al.* 2013; Gans *et al.* 2010). When paired with selective protonation in an otherwise deuterated background (Rosen *et al.* 1996), this approach takes advantage of the favorable relaxation properties of ^{13}C -methyl groups with the application of Transverse Relaxation Optimized Spectroscopy (TROSY) (Ollershaw 2003; Pervushin 1997).

3.2.4.11. ^{13}C , ^{13}C NOESY-type Experiments in Solution – state NMR

The advantage of using ^{13}C - ^{13}C NOESY experiments for systems of higher molecular weight was proposed some years ago and illustrated by the comparison of the spectra for monomeric (16 kDa) and dimeric (32 kDa) forms of the protein superoxide dismutase (SOD) (Bertini *et al.* 2004b; Bertini *et al.* 2004c). ^{13}C - ^{13}C NOESY is an alternative approach to ^1H -detected NMR by using ^{13}C -direct detection experiments (Bermel *et al.* 2006b; Bermel *et al.* 2006a; Bermel *et al.* 2005; Bertini *et al.* 2004a; Bertini *et al.* 2004b; Bertini *et al.* 2004c; Bermel *et al.* 2003). In these case the smaller magnetic moment of ^{13}C with respect to ^1H reflects in a reduction of signal linewidth. ^{13}C - ^{13}C NOESY-type experiments (Bertini *et al.* 2004b; Bertini *et al.* 2004c) can be used to study large molecular systems in solution-state NMR, therefore, we decided to test the use of ^{13}C - ^{13}C NOESY for the detection of one and two-bond carbon correlations in αA - and αB -crystallins (about 500 kDa). The purified protein was 95% deuterated for αB and not deuterated for αA , but for both samples 50 mM PBS pH 7.4 dissolved in 100% D_2O was used. The ^{13}C - ^{13}C NOESY experiments were carried out on a 21.1 T Bruker AVANCE 900 MHz spectrometer equipped with a triple-resonance cryo-probe optimised for ^{13}C -direct detection experiments, at 300 K on a sample that was around 1.3 mM in monomer concentration. Composite pulse decoupling on ^1H and ^2H was applied during the whole duration of the experiments (Bertini *et al.* 2004b). ^{13}C - ^{13}C NOESY maps were recorded at different mixing times (50 ms, 100 ms, 200 ms, 300 ms, 400 ms) on the full spectral width and on the aliphatic region. The best compromise between signal to noise and number of cross-peaks was found at a mixing time of 200 ms. Experiments on a sample, 1.3 mM in monomer, lasted about 40 hrs each to achieve good signal-to-noise ratios.

3.2.5. Magic-Angle Spinning in Solid – state NMR Spectroscopy

3.2.5.1. Sample Preparation – Packing of Rotors

Approximately 2-5 mg of αA and 6-10 mg of αB was used in all solid-state NMR studies. Samples were packed into a 3.2 mm thin wall ZrO_2 rotor with vespel caps without spacers, using a filling tool (Bruker BioSpin, Fig. 3.1), an OptimaL-100 XP Ultracentrifuge and a SW 32 Ti swinging rotor (Beckman Coulter GmbH, Krefeld, Germany). The proteins (αB or αA) were sedimented into the NMR rotor (Bertini *et al.* 2012) for 4 days at 4 °C at a rotation frequency of the centrifuge set to 28000 rpm. The supernatant was carefully removed afterwards. Samples packed into rotors were stored at 4 °C.

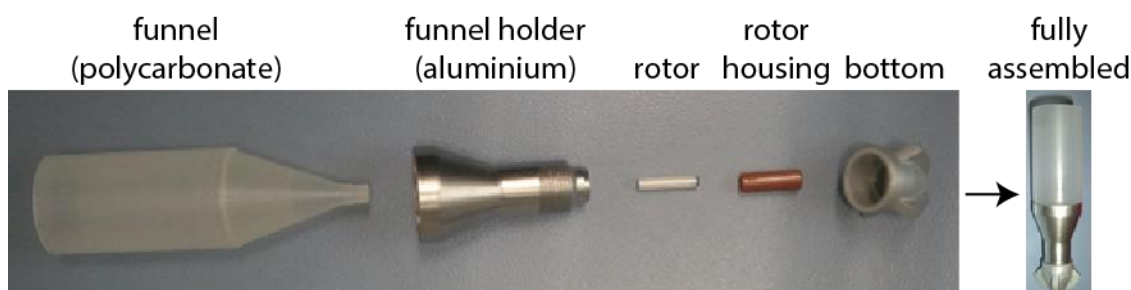


Fig. 3.1. MAS rotor filling tool for ultracentrifuges. Tools were kindly provided by David Osen (Bruker BioSpin).

All experiments were conducted at a nominal temperature of about 0 °C (MAS then increases temperature slightly above freezing temperature).

3.2.5.2. ^{13}C , ^{13}C -Correlation PDSD Experiments

^{13}C , ^{13}C -Correlations were acquired as proton driven spin diffusion (PDSD) (Grommek *et al.* 2006). The PDSD mixing time were set to 50 ms for intraresidue correlations. A recycle delay of 3 s was used for both αB and αA , while set temperature was 275 K. The acquisition times were 8 ms and 15.6 ms for the indirect and the direct ^{13}C dimensions for αB , and 10.3 ms and 15.6 ms for αA , respectively. MAS frequency was set to 12 kHz. This frequency was adjusted to avoid rotational side bands in the signal region.

4. Results

4.1. Growth Curves of $A\beta_{40}$, αB -WT, αB -6E and αA -WT in Different Media

In order to compare and analyze the growth behavior of the four strains ($A\beta_{40}$, αB -WT, αB -6E and αA -WT) in different growth media: LB, unlabeled M9, ^{13}C , ^{15}N -labeled M9 and in unlabeled M9 medium with 100% D_2O (Fig. 4.2), we recorded the growth curves of each protein. In comparison to the measured growth curves an ideal curve of bacterial growth is additionally shown in Fig. 4.1, where the four phases that take place during growth of cells are presented: lag phase, log phase, stationary phase and death.

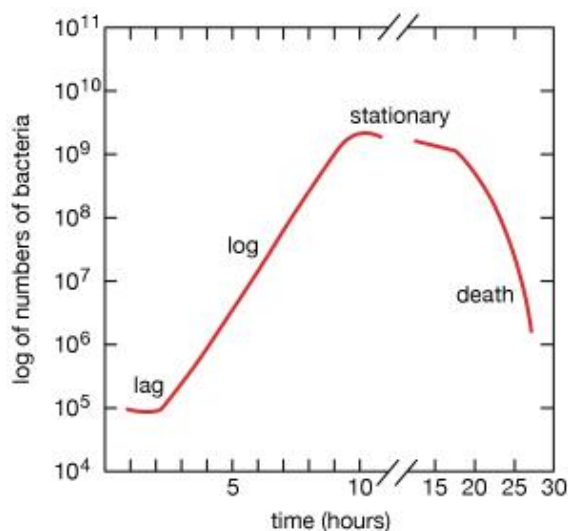


Fig. 4.1. Generalized bacterial growth curve showing the phases in the growth of bacterial cultures. In the lag phase no growth occurs. In the log phase there is an exponential growth, where the culture theoretically doubles every 20 minutes. When the stationary phase is reached, the bacterial disrupts until it comes to cell death. Adapted from Encyclopedia Britannica, Inc..

The starting OD_{600nm} for each kind of cells was similar (about $OD_{600nm} = 0.15 - 0.17$) and the measurements were used as a rough estimation of the cells' growth useful for protein expression later on. The curves were recorded over a time period of 10 h till they reach close to stationary phase. The general growth behaviour was better in every medium for αB -WT and poorer for the αB -6E mutant. The double-labeled cells in M9 medium grew slower than in unlabeled M9. Cells in LB grew for all proteins rapidly, compared for example to deuterated M9 medium where the cells were grown in a much slower rate. This indicates that for larger scale cultures the starting OD_{600nm} for deuterated proteins should be higher (about $OD_{600nm} = 0.2 - 0.3$).

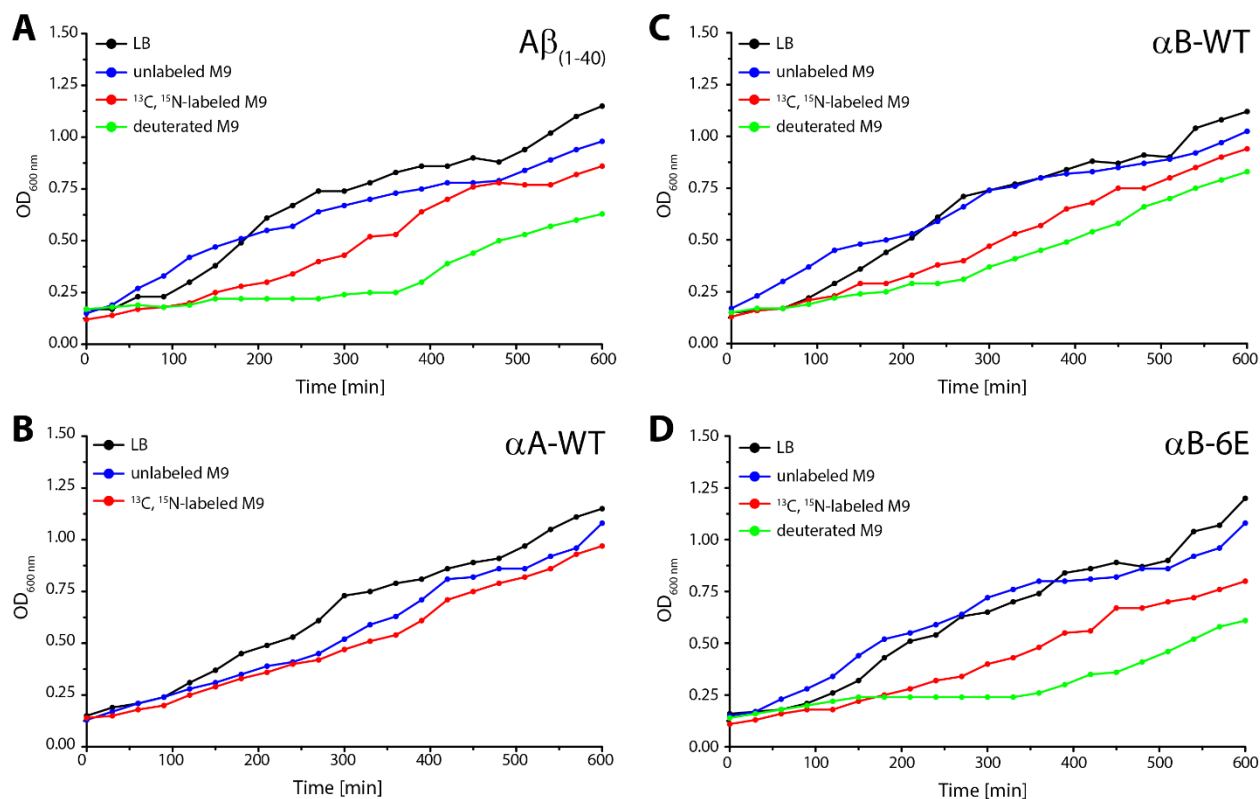


Fig. 4.2. Growth curves for (A) $A\beta_{40}$, (B) αA -WT, (C) αB -WT and (D) αB -6E in LB (black), unlabeled M9 (blue), ^{13}C , ^{15}N -labeled M9 (red) and in unlabeled M9 with 100% D_2O (green) media.

4.2. Expression and Purification of $A\beta_{40}$

The $A\beta_{40}$ peptide was recombinantly expressed and purified via RP-HPLC (Fig. 4.3B). The purification protocol produced a yield of around 5 - 7 mg per 1 L of ^{13}C , ^{15}N -labeled culture. The expression and purity of the recombinantly produced peptide was controlled by tricine SDS-PAGE (Fig. 4.3A). Elution fractions (F1 – F8), which showed high purity on the tricine SDS-PAGE gels (Fig. 4.3C), were pooled, lyophilized and analyzed by mass spectrometry. A single peak was obtained in the mass spectrometric analysis at a peptide mass of 4709.1 Da for uniformly ^{13}C , ^{15}N -labeled $A\beta_{40}$ (theoretical mass = 4714.0 Da).

The monomeric entity of $A\beta_{40}$ gives rise to well defined solution-state NMR spectra as shown in the 1H , ^{15}N HMQC (Fig. 4.4). Backbone and side chain resonances of the peptide were assigned, although no backbone assignments were found for D01, H06 and H14, and some of the assignments in the side chains are ambiguous. Assigned $A\beta_{40}$ resonances were published by Mainz *et al.* (2015). It is well known that the monomeric $A\beta_{40}$ peptide adopts a random coil conformation in solution (Riek *et al.* 2001), which is conformed also by the lack of dispersion in the 1H dimension of the 1H , ^{15}N HMQC that demonstrates this unstructured character of $A\beta_{40}$. Additionally, several residues (Q15-F19) show a tendency to the formation of β -strands based on the secondary chemical shifts of $\Delta\delta C\alpha$ (ppm) and $\Delta\delta C\alpha - \Delta\delta C\beta$ (ppm) of $A\beta_{40}$, indicating the presence of transient intermediates, as these residues are part of the hydrophobic core (Zhang *et al.* 2000).

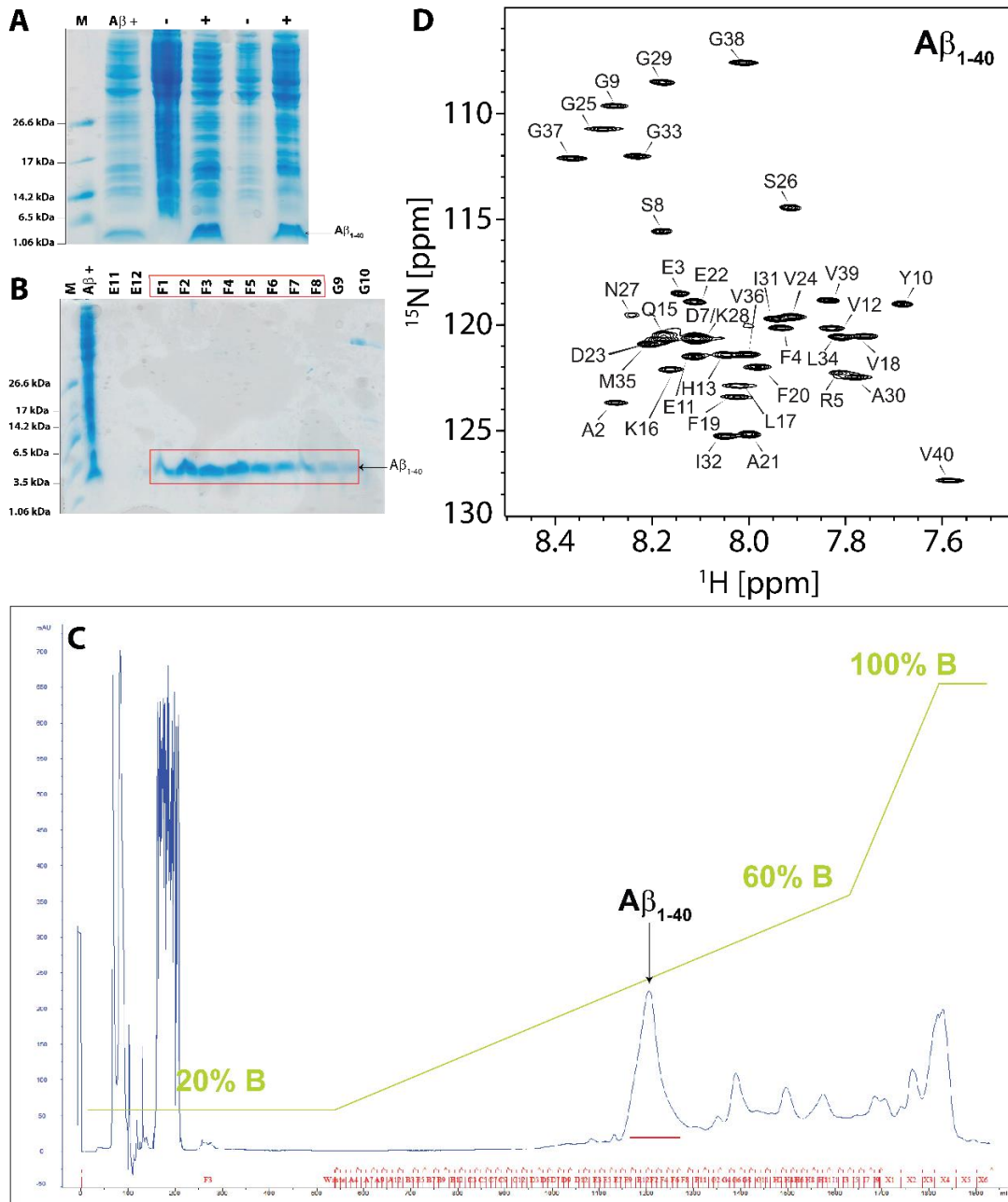


Fig. 4.3. Expression and purification of A β ₄₀. (A, B) Representative gels of A β ₄₀ expression and the fractions collected from the RP-HPLC run. (C) Typical RP-HPLC run for the purification of ¹³C, ¹⁵N-labeled A β ₄₀. The chromatogram at UV 280 nm is shown in blue and the gradient of % B is shown in green. (D) Solution - state NMR ¹H, ¹⁵N HSQC spectra and backbone assignment of A β ₄₀. At a concentration of 50 μ M, recorded at 277 K and 500 MHz.

4.3. Expression and Purification of α B-WT and α B- Δ NTD

Overexpression of full-length α B (Fig. 4.4A) and α B- Δ NTD (Fig. 4.5A) revealed to be highly efficient, presumably due to their pronounced solubility. Ion-exchange chromatography employing a 200 ml strong anion exchange Q-Sepharose yielded a well-separated, though broad α B fraction (Fig. 4.4B,C; 4.5B,C). Negative charges of proteins bind to the bead material and are displaced by Cl⁻ ions with increasing NaCl

concentration in the buffer. **Fig. 4.4B,C** and **4.5B,C** showed that both proteins elute at similar NaCl concentrations (about 5-8% buffer B). The SDS-PAGE gels showed that there is a large amount of protein purified in both cases. The theoretical isoelectric point (pI) of the proteins was calculated using ExPasy ProtParam software (Gasteiger *et al.* 2003). The pI values for α B-WT and α B- Δ NTD are 6.7 and 6.5, respectively, indicating that they should elute at around the same NaCl concentration as shown here.

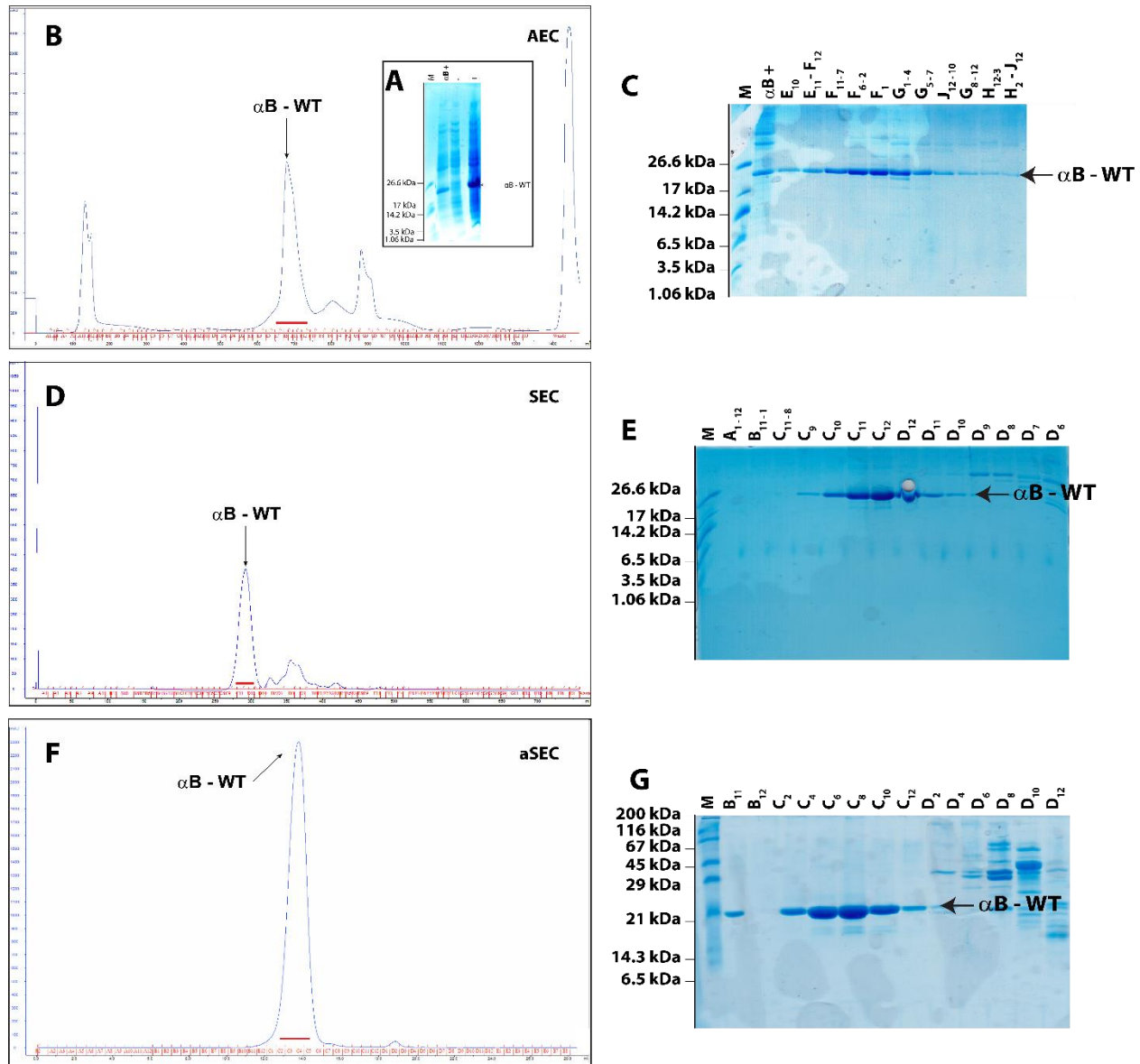


Fig. 4.4. Representative protein purification of human α B-WT. (A) Representative gels of α B-WT expression. Lanes are labeled as marker (M), α B positive control (α B+), before induction (-) and after induction (+). (B) AEC (Q-Sepharose) of cell-lysate eluted with a gradient till 1 M NaCl in 20 mM Tris-HCl pH 8.5 (buffer B). The absorbance at 280 nm (A280nm) is shown in blue. The flow-through (FT) contained only small amounts of α B. Fractions in the elution profile refer to lanes in (C). (C) SDS-PAGE of the elution profile shown in (B). α B eluted in a fairly broad peak (lanes E-H). There were negligible amounts of α B in fractions of high-salt washing steps. The molecular weight marker (M) is labeled and bands of α B are indicated with a black arrow. (D) SEC (Superose 6) of the AEC pool. The elution profile shows a major peak at approx. 250 ml corresponding to full-length α B. (E) SDS-PAGE of purified α B after anion-exchange and size-exclusion chromatography. Lanes A to D were loaded to evaluate sample purity. The molecular weight marker (M) is labeled and bands of α B are indicated with a black arrow. (F) Analytical SEC (Superose 6) of the AEC pool. The elution profile shows a major peak at approx. 13 ml corresponding to full-length α B. (G) SDS-PAGE of purified α B after AEC and SEC. Lanes B to D were loaded to evaluate sample purity. The molecular weight marker (M) is labeled and bands of α B are indicated with a black arrow.

Subsequent size-exclusion chromatography (superose6, 500 ml for α B-WT and Superdex200 pg, 320 ml for α B- Δ NTD) of the eluted fractions ensured a high purity grade for both samples (Fig. 4.4D,E; 4.5D,E). In this step proteins are separated according to their hydrodynamic radius. Several peaks were eluted for both proteins after gel filtration, however, in the SDS-PAGE gels it was easy to discriminate between the desired proteins and impurities. The pooled pure fractions were loaded to an analytical SEC column of 24 ml with a separation range from 5 kDa to 5000 kDa, where no impurities could be seen and the samples were further used in NMR spectroscopy. Based on the column calibration α B-WT elutes where a 24-mer should be in terms of molecular weight and the same applies to the α B- δ NTD mutant. Protein yields of unlabeled α B-WT were on the order of 40-50 mg α B/L cell culture. For ^{13}C , ^{15}N - α B and ^2H , ^{13}C , ^{15}N - α B, protein yields decreased to approximately 10-20 mg α B/L cell culture for the protonated and about 10 mg α B/L for the deuterated protein. Protein yields of unlabeled α B- Δ NTD were on the order of 10-20 mg α B/L cell culture. For ^{13}C , ^{15}N - α B- Δ NTD protein yields decreased to approximately 5-10 mg α B/L cell culture.

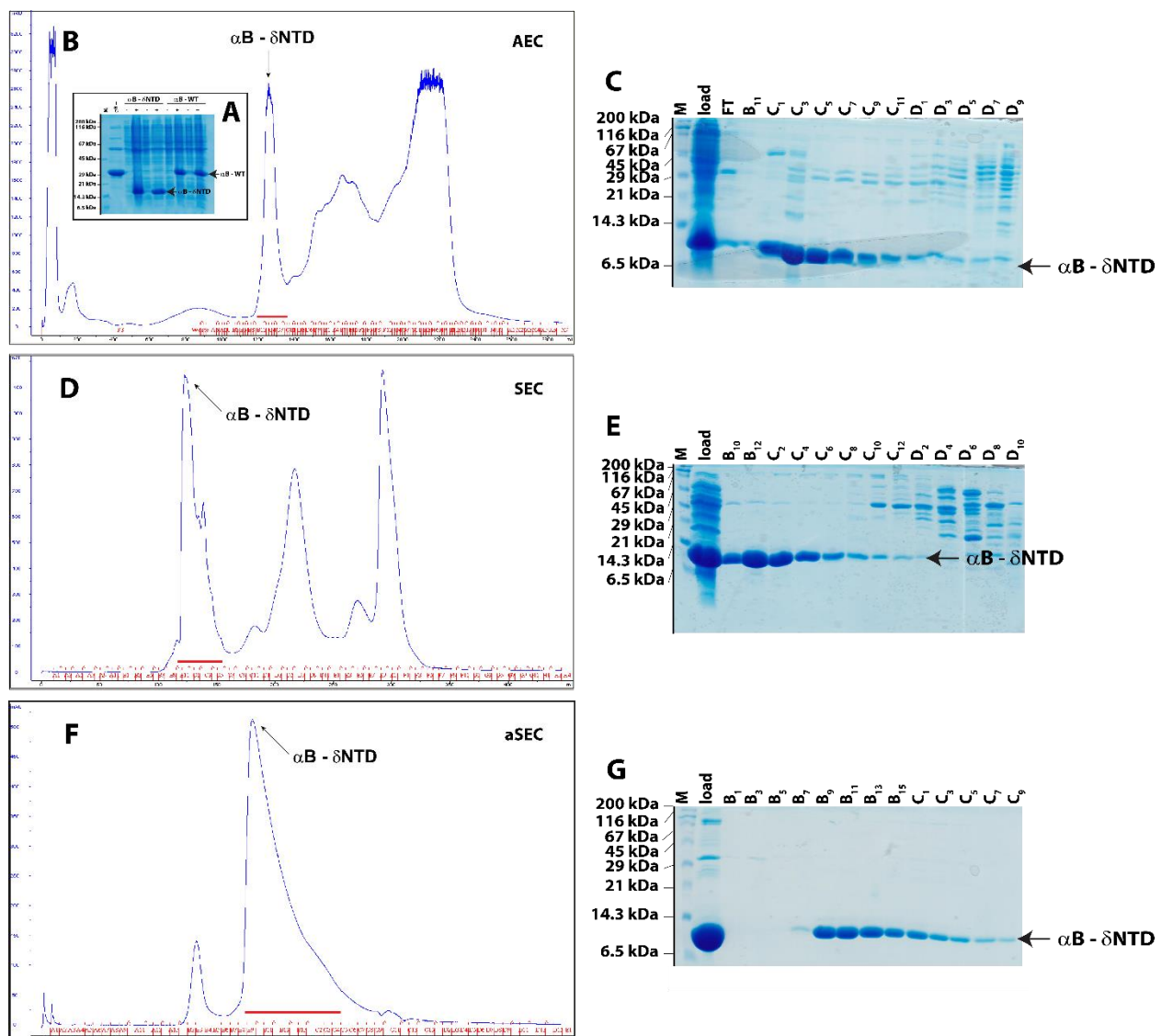


Fig. 4.5. Representative protein purification of the α B- Δ NTD mutant. (A) Representative gel of α B- Δ NTD expression. α B-WT was used as a reference additionally to show the difference in the molecular weight. (B) Anion-exchange chromatogram (Q-Sepharose) of cell-lysate was eluted

with a gradient till 1 M NaCl in 20 mM Tris-HCl pH 8.5 (buffer B). The absorption at 280 nm (A280nm) is shown in blue. The flow-through (FT) contained only small amounts of α B. Fractions in the elution profile refer to lanes in (C). (C) SDS-PAGE of the elution profile shown in (B). α B- δ NTD eluted in a fairly broad peak (lanes C-D). There were negligible amounts of α B in fractions of high-salt washing steps. The molecular weight marker (M) is labeled and bands of α B are indicated with a black arrow. (D) Size-exclusion chromatogram (Superdex200 pg, 320 ml volume) of the AEC pool. The elution profile shows a major peak at approx. 125 ml. (E) SDS-PAGE of purified α B after AEC and SEC. Lanes B to D were loaded to evaluate sample purity. The molecular weight marker (M) is labeled and bands of α B are indicated with a black arrow. (F) Analytical size-exclusion chromatogram (Superose 6) of the SEC pool. The elution profile shows a major peak at approx. 13 ml corresponding to full-length α B. (G) SDS-PAGE of purified α B after a ion-exchange and size-exclusion chromatography. Lanes B to C were loaded to evaluate sample purity. The molecular weight marker (M) is labeled and bands of α B are indicated with a black arrow.

^1H , ^{15}N HSQC solution-state NMR spectra of temperature screening of the deletion mutant of α B was measured at 280, 290, 300 and 310 K at 600 MHz (Fig. 4.6). The Δ NTD mutant consists of 117 residues, containing the W60 as the second residue in the mutant's sequence after the methionine (Met) in the beginning. Based on the recorded spectra however, the mutant seems to be similar in size with the full-length protein (Fig. 4.7) supporting that the absence of the NTD does not affect the structural rearrangement of the protein after the deletion. Furthermore, in higher temperature the spectral resolution improves and also the W02 is seen (Fig. 4.6C,D).

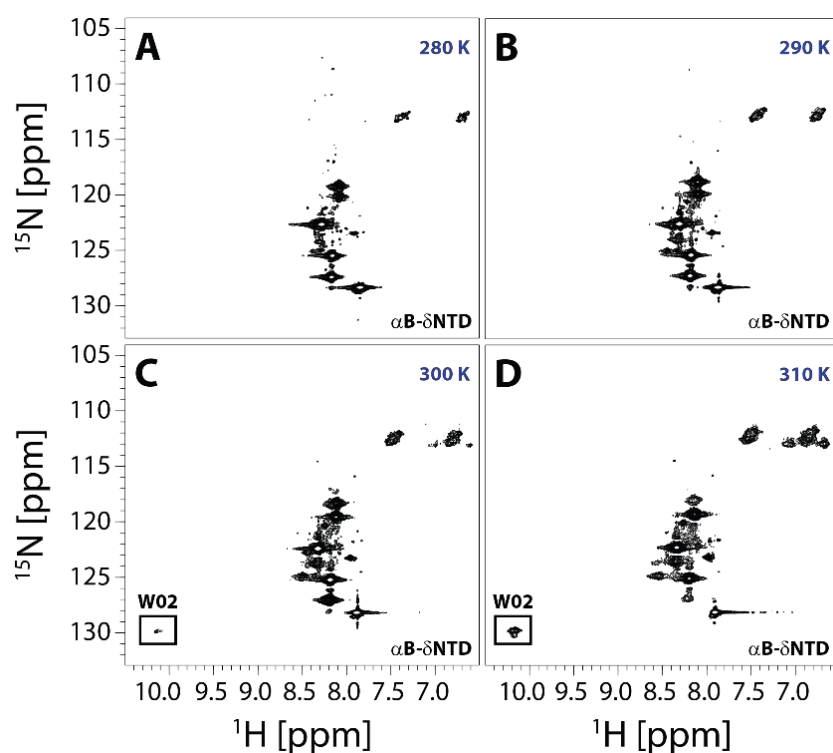


Fig. 4.6. ^1H , ^{15}N HSQC spectra of the Δ NTD mutant. A temperature screening of the mutant at (A) 280 K, (B) 290 K, (C) 300 K and (D) 310 K, recorded at 600 MHz.

In a typical α B-WT ^1H , ^{15}N HSQC spectra (Fig. 4.7A, shown in black) only residues arising from the C-terminal region are observed (residues: G154-K175). In the case of α B- Δ NTD overlapped with the α B-WT spectra (Fig. 4.7A) some additional with lower intensity peaks are appearing except the W02 at around 10.00 ppm, but most of the part of the mutant is overlapping with the CTD of the full-length protein in the ^1H , ^{15}N HSQC spectra. Moreover, in the ^1H , ^{13}C HSQC spectra peaks that do not overlap with the wild-type protein (around 25, 35, and 50-60 ppm) should arise from the N-terminal region that is not present

in the mutant (Fig. 4.7B). A zoom into the methyl region of the same spectra, but in very low contour levels is shown also in Fig. 4.7C.

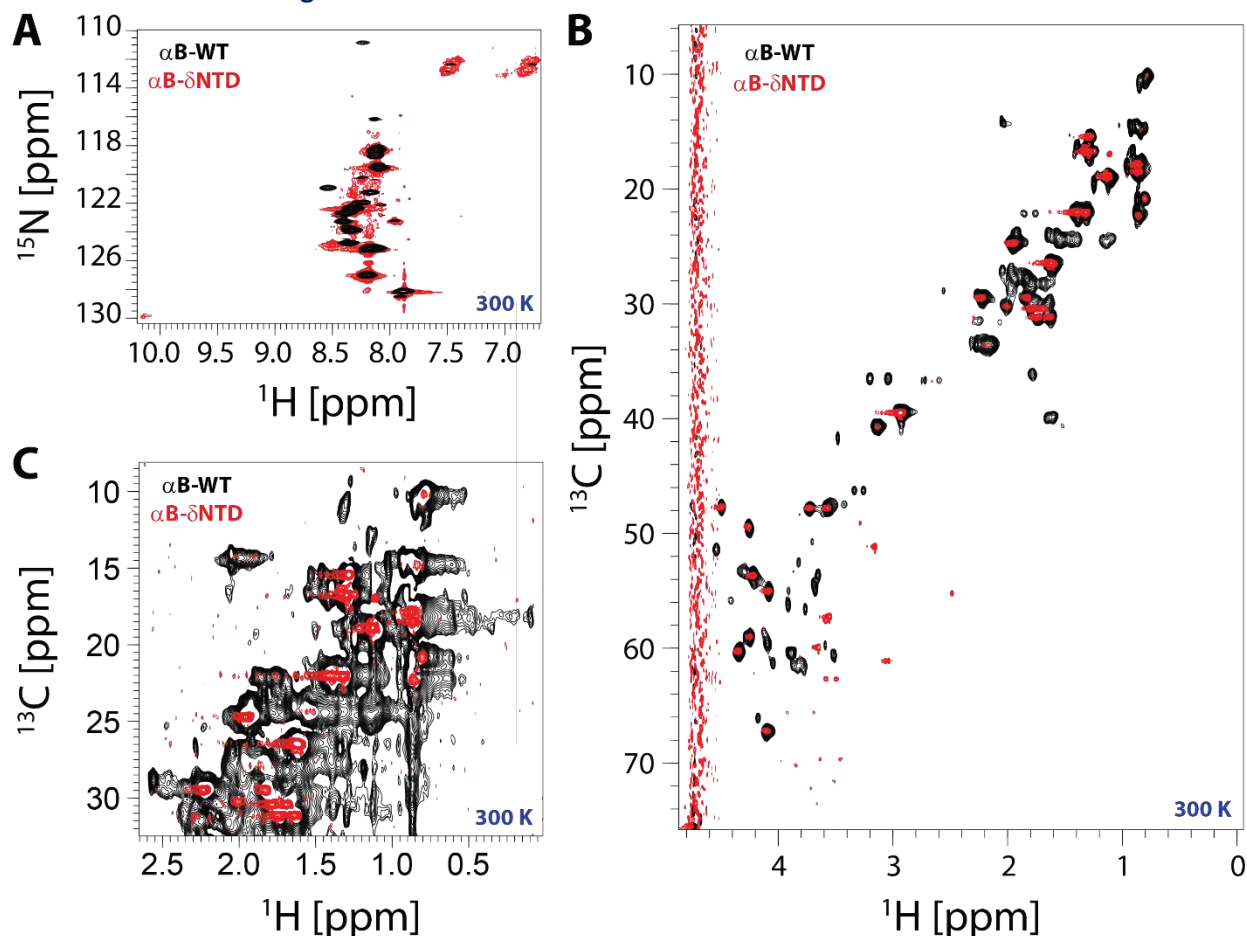


Fig. 4.7. Solution -state NMR spectra recorded at 300 K and 500 MHz. **(A)** ^1H , ^{15}N HSQC of $\alpha\text{B-WT}$, **(B)** ^1H , ^{13}C HSQC $\alpha\text{B-}\Delta\text{NTD}$, and **(C)** zoom into the methyl region of the ^1H , ^{13}C HSQC spectra. The concentration of each protein was 500 μM .

4.4. Expression and Purification of $\alpha\text{B-6E}$ with and without Urea

The $\alpha\text{B-6E}$ plasmid, where 6 serines are replaced by glutamate (S19, S21, S43, S45, S53 and S59), was kindly provided by Prof. Buchner (TU München) and was firstly introduced by *Peschek et al.* (2013) where it was presented as a phosphomimicking mutant of the full-length αB appearing to form lower oligomeric states compared to the wild-type protein. Here, we try to find the best expression and purification protocol in order to use the sample later on for NMR studies. **Fig. 4.8** shows a test expression of $\alpha\text{B-6E}$ in LB and M9 minimal media and using a variety of competent cells: BL21, BL21 (DE3), BL21 (DE3) pLys and Rosetta 2 (DE3). In addition, an overnight or 4 h incubation after 1mM IPTG induction was tested in order to find the best yields for the protein. Finally, Rosetta 2 (DE3) cells and overnight incubation appeared to give a better yield, therefore, in the next studies the $\alpha\text{B-6E}$ sample is expressed into Rosetta 2 (DE3) competent cells.

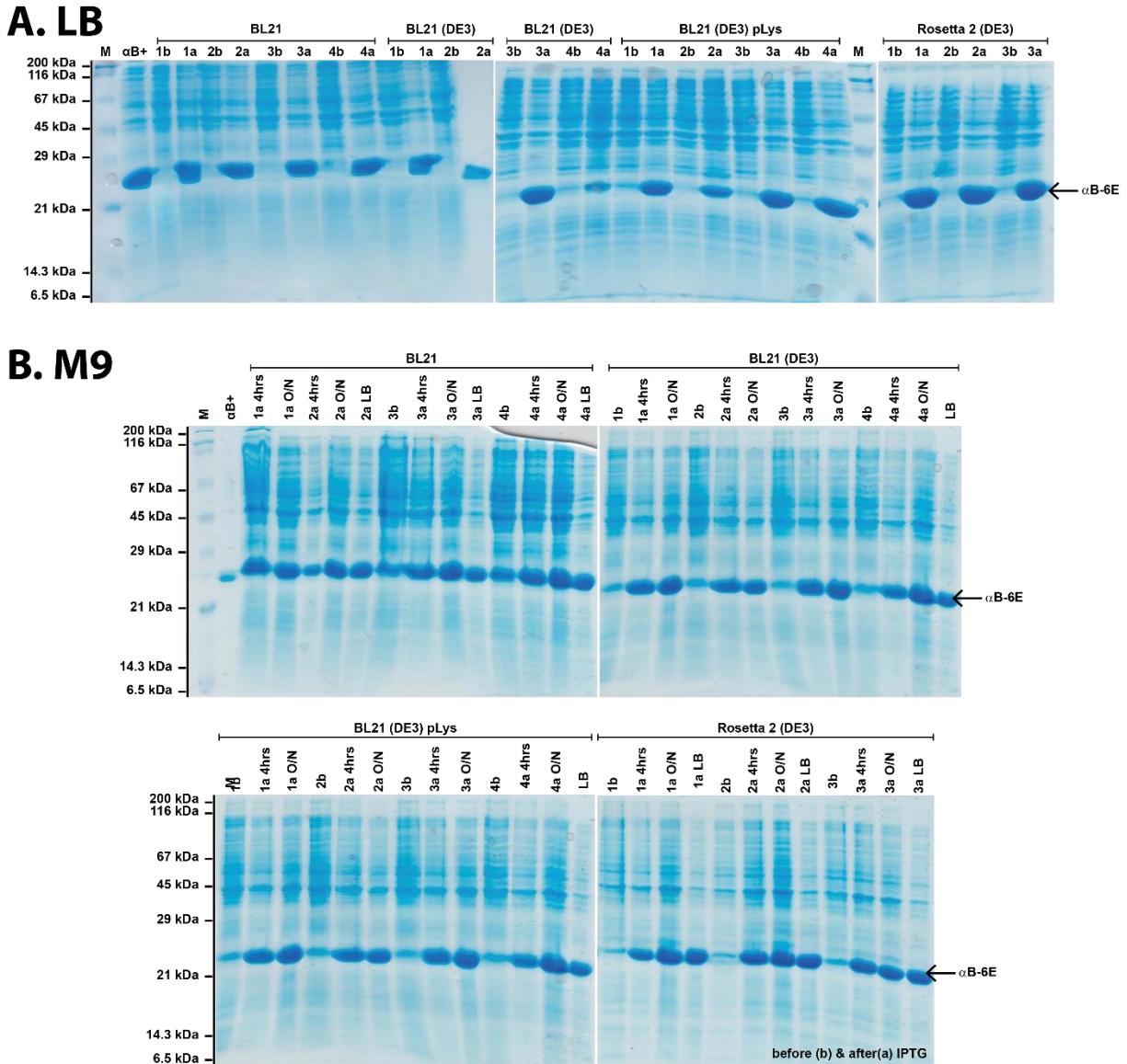


Fig. 4.8. Test Expression of the α B-6E mutant. The expression was done using different competent cells (BL21, BL21 (DE3), BL21 (DE3) pLys and Rosetta 2 (DE3)) and the cells were incubated either for 4 h after induction with IPTG or overnight. Small -b in the figures indicates before induction and -a after states, while the protein band is indicated by a black arrow.

In order to find the best purification protocol for the α B-6E mutant different approaches were tested. With the basic purification protocol of α B-WT (see chapter 4.3.), α B-6E is not pure enough (**Fig. 4.9A-D**), as in all fractions there is a significant degradation band (proved with mass-spectrometry) at about 15 kDa, and an additional purification step was added after the first AEC and SEC columns. The pI point of α B-6E is 5.7 and that's why the protein is eluted at higher NaCl concentrations compared to α B-WT (at about 35-45% buffer B). The additional negative charges in the N-terminus of α B-6E support the fact that the protein is forming stronger interactions with the bead material of the column.

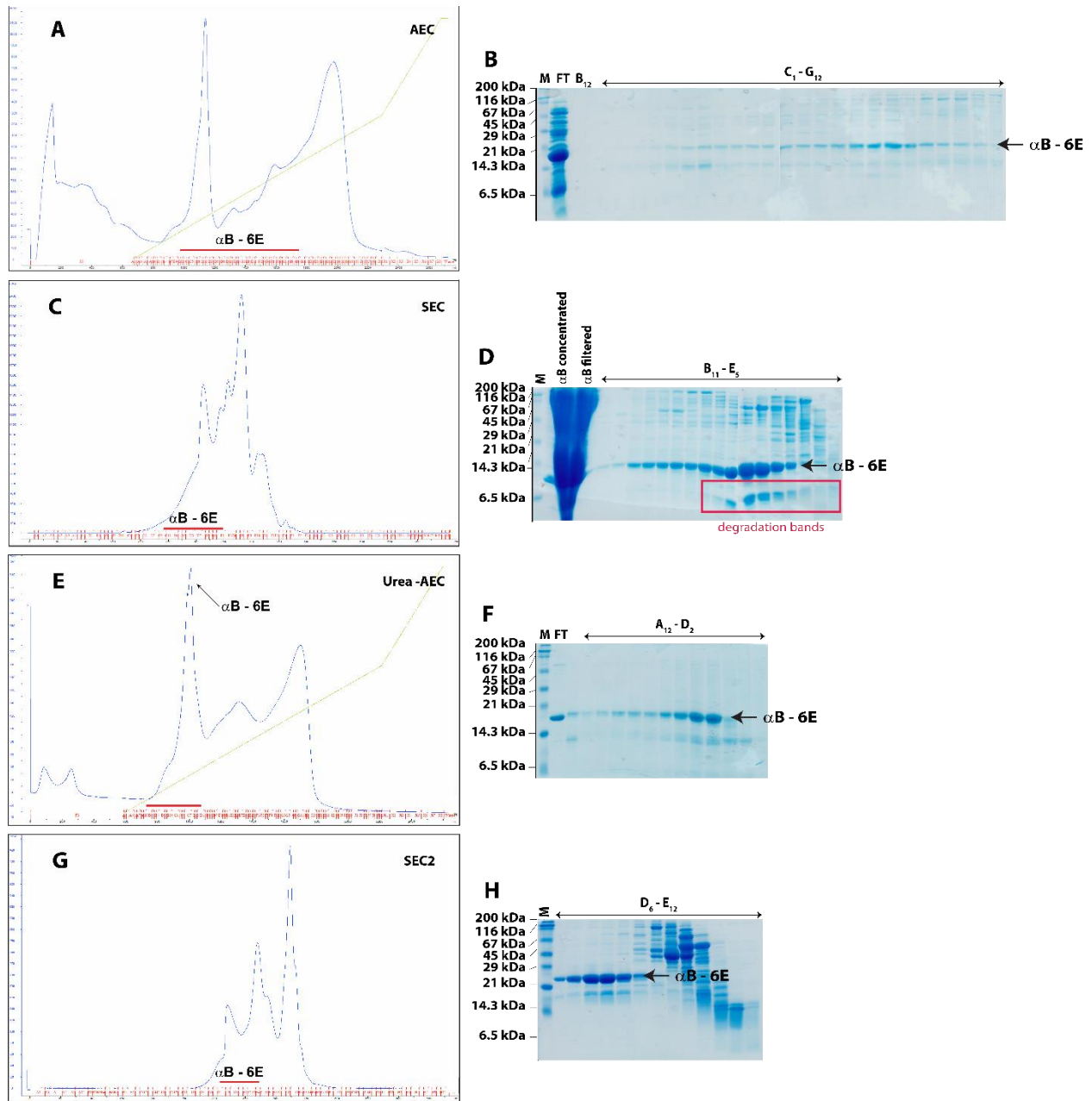


Fig. 4.9. Representative protein purification of the $\alpha\text{B} - 6\text{E}$ mutant. (A) AEC (Q-Sepharose) of cell-lysate eluted with a linear gradient of 1 M NaCl in 50 mM Tris-HCl pH 8.5. αB eluted in a very broad peak at around 42% buffer B (lanes C-G). The absorption at 280 nm (A_{280nm}) and the fraction of buffer B during elution (%B) are shown in blue and green, respectively. (B) SDS-PAGE of the elution profile shown in (A). (C) SEC (Superose 6) of the AEC pool. The elution profile shows a major peak at approx. 350 ml. The degradation bands are labeled with a red box. (D) SDS-PAGE of purified $\alpha\text{B} - 6\text{E}$ after size-exclusion chromatography. Lanes B to E were loaded to evaluate sample purity. (E) Urea-anion-exchange chromatogram (Q-Sepharose) of the eluted protein after SEC with a stepwise gradient of 1 M NaCl in 5M Urea and 50 mM Tris-HCl pH 8.5. αB eluted in a very broad peak at around 18% buffer B (lanes A-D). The absorption at 280 nm (A_{280nm}) and the fraction of buffer B during elution (%B) are shown in blue and green, respectively. (F) SDS-PAGE of the elution profile shown in (E). (G) SEC (Superose 6) of the Urea-AEC pool. The elution profile shows a major peak at approx. 350 ml. (H) SDS-PAGE of purified $\alpha\text{B} - 6\text{E}$ after the second anion-exchange and size-exclusion chromatography. Lanes D to E were loaded to evaluate sample purity. In all the gels the molecular weight marker (M) is labeled and the bands of $\alpha\text{B} - 6\text{E}$ are indicated with a black arrow.

In the subsequent gel filtration run α B-6E was eluted later than the full-length protein as expected, at about 350 ml. Based on the SEC chromatogram presented on **Fig. 4.9C**, the mutant seems to be more heterogeneous than α B-WT and the degradation band is still present. Therefore, as a next purification step 5 M Urea in 50 mM Tris-HCl pH 8.5 (for both buffer A and B) were used to unfold the protein and an Urea-AEC run was performed after the protein was diluted in Urea-TE buffer, followed by protein refolding and by a second SEC and a final analytical SEC, all presented in **Fig. 4.9E-H**. In this case a big amount of protein is lost, due to the sequential purification steps, unfolding and refolding, but also at the end, the SDS gels show that the sample is still not pure enough for NMR (**Fig. 4.9D,F,H**). However, as indicated in **Fig. 4.10A** there is a clear shift of the molecular weight from the full-length protein to the mutant, suggesting smaller oligomer sizes. Calibration of the analytical column suggests that α B-WT is a 24-mer and α B-6E appears to be a hexamer, eluting at around 19 ml of the column. In addition, based on the chromatogram, α B-6E seemed again to be more heterogeneous (many peaks were additionally eluted after the desired protein). α B-6E in this figure looks quite pure. However, this is a low concentrated sample and when the sample was highly concentrated for NMR experiments the protein was fast degraded. The lower oligomeric state of α B-6E was further supported by the 2D MAS PDS ^{13}C - ^{13}C correlation spectra presented in **Fig. 4.10B** as we observe very few cross-peaks in the rigid region of the mutant, indicating that the molecule is smaller than the wild-type protein.

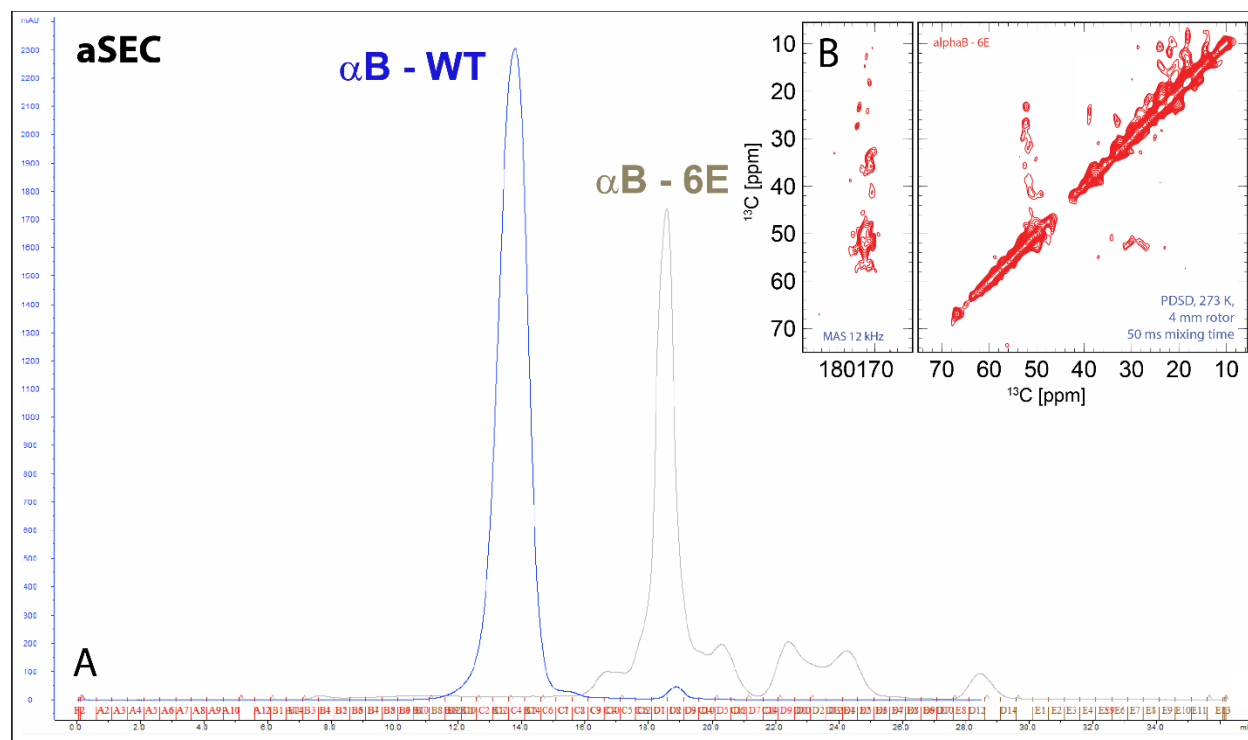


Fig. 4.10. (A) Comparison of the analytical SEC run of α B-WT and α B-6E. The α B-6E mutant elutes later than α B-WT at around 19 ml, while α B-WT elutes at 13 ml indicating a smaller oligomer molecular size. (B) 2D MAS PDS ^{13}C - ^{13}C correlation spectra of α B-6E FROSTY sample. The experiments were measured at 273 K and 750 MHz in a 4 mm rotor and 50 ms mixing time.

4.5. Expression and Purification of the C-terminal His-tagged α B-6E

The previously described purification protocol did not give rise to a highly pure α B-6E sample for NMR analysis. Therefore, and in order to improve the purification, a his-tag sequence was added by side-

directed mutagenesis at the C-terminal part of the protein and α B-6E was expressed in BL21 (DE3) cells and purified using a Ni-NTA column followed by SEC and analytical SEC (Fig. 4.11A-F). The flow-through, the wash and the elution profile of the Ni-NTA column are shown in the SDS gel in Fig. 4.11A. A big amount of protein was lost in the flow-through, however, in wash there were only small concentrations of α B-6E. The final α B-6E sample was used for subsequent size exclusion chromatography, as it was not pure enough in this first purification step. Before the SEC column, the sample was loaded to a HiPrep 26/10 desalting column (53 ml) in order to remove the remaining imidazole from the buffer (Fig. 4.11B). For the SEC a 320 ml Superdex200 pg column was used and the protein was eluted at around 170 ml, while during the analytical size exclusion α B-6E was eluted at 15 ml, indicating a high molecular weight oligomer like the wild-type protein.

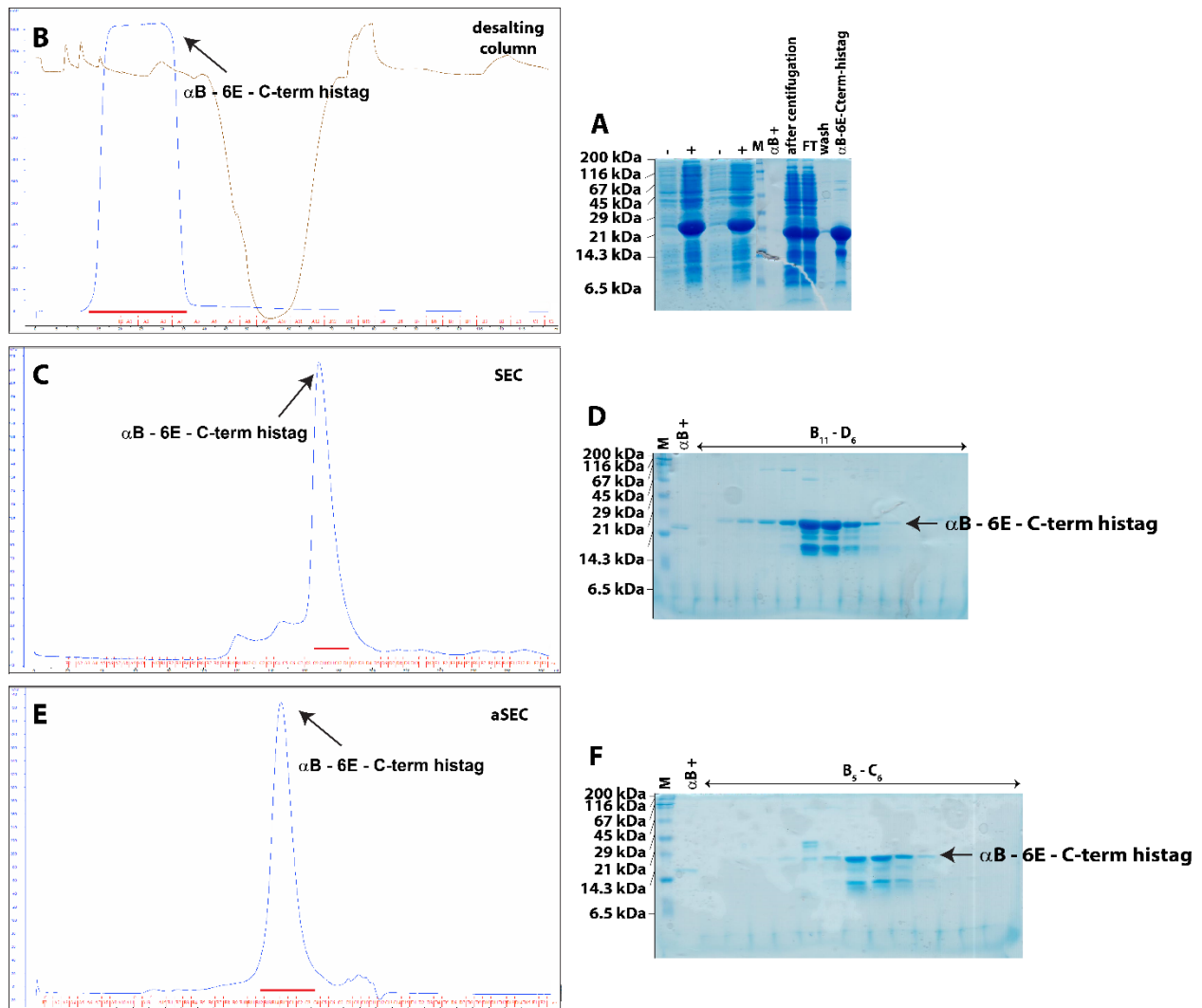


Fig. 4.11. Representative expression and protein purification of the α B-6E-C-term-histag mutant. (A) Representative gels of α B-6E-C-term-histag expression (-: -IPTG, +: +IPTG) (left) and the purification steps after the Ni-NTA column on the right side of the gel showing the flow-through (FT), the wash and the eluted protein. The FT contained huge amounts of α B and negligible amounts of α B in wash. α B-WT was used as a reference additionally to show the difference in the molecular weight. (B) A HiPrep 26/10 desalting column was used in order to remove the imidazole left from the previous step. The column was run in SEC buffer and the absorption at 280 nm (A280nm) if the protein is shown in blue, while the conductivity is shown in brown. (C) SEC (Superdex200 pg) of the Ni-NTA pool. The elution profile shows a major peak at approx. 170 ml. (D) SDS-PAGE of the purified protein after SEC. Lanes B to D were loaded to evaluate sample purity. (E) Analytical SEC (Superose 6) of the SEC pool. The elution profile shows a major peak at approx. 15 ml corresponding to α B-6E-C-term-histag. (F) SDS-PAGE of purified α B-6E-C-term-histag after

analytical SEC. Lanes B to C were loaded to evaluate sample purity. In all the gels the molecular weight marker (M) is labeled and the bands of α B-6E-C-term-histag are indicated with a black arrow.

Although on the SDS gels of the final samples for α B-6E (Fig. 4.9H) and α B-6E-C-term-histag (Fig. 4.11F) shown here were not 100% pure, this was a random phenomenon, and there were samples that were pure enough in order to record a first ^1H , ^{15}N SOFAST-HMQC spectra of the different samples in solution and test whether there are changes between the two purifications and which gives the best resolution. The spectra are presented in Fig. 4.12, where the numerous dispersed cross peaks in each spectrum indicate a lower oligomeric state for every kind of purification as compared to the wild-type protein. In Fig. 4.12A, the sample was purified using the wild-type protocol and the spectrum shows a well-dispersed protein indicating that it is folded. When purified with the urea step (Fig. 4.12B) or with a Ni-NTA column (Fig. 4.12C), α B-6E appeared to have a higher molecular weight as in the solution spectra less peaks are observed due to the slower molecular tumbling of the protein. Moreover, the proteins seem to be partially unfolded compared to Fig. 4.12A, as there is a clustering of residues in the centre of the spectra indicating unstructured regions. However, the his-tagged sample gives a more reasonable result of how the mutant is expected to look like in solution, as based on analytical SEC or AUC experiments (see chapter 4.5.3) α B-6E mutant is around 120 kDa (6-mer).

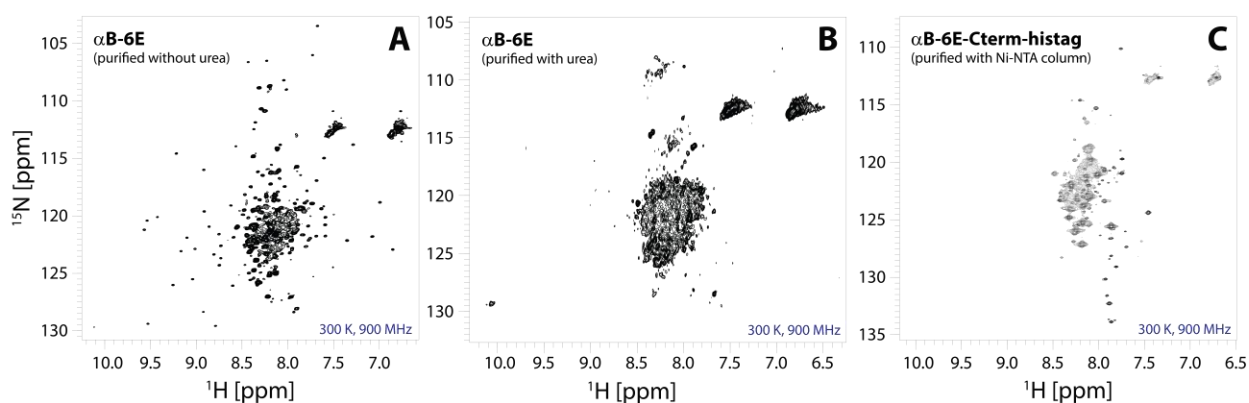


Fig. 4.12. Solution - state NMR ^1H , ^{15}N SOFAST-HMQC spectra recorded at 300 K and 900 MHz. (A) α B-6E purified with AEC and SEC only, (B) α B-6E purified with urea and (C) α B-6E-C-term-histag purified with Ni-NTA column and SEC. The samples were measured at a concentration of 1.2 mM for (A) and (B) and 600 μM for (C).

In the ^1H , ^{15}N SOFAST-HMQC spectra, due to the degradation band that exists in the SDS gel from the final purification step, part of these peaks that do not overlap with α B-WT (Fig. 4.13A) or the truncated α B construct (Fig. 4.13B), might come from the degraded part of α B-6E or could also be a substrate tightly bound to the protein that couldn't be removed during AEC or SEC, as it could have similar pI or it can be eluted at the same position with α B-6E in gel filtration. Another option would be that after mutagenesis the protein is folded in a different conformation that allows residues to be more flexible, and thus visible in a ^1H , ^{15}N HSQC spectrum. Additionally, assignment experiments that were performed for this sample were not useful as the sample seemed to be really heterogeneous making it impossible to assign. Only residues arising from the C-terminal region and the two tryptophans of the N-terminal region (W9 and W60), which usually appear around 9-10 ppm were able to be assigned and are given here by superimposing the α B-6E spectrum with the wild-type protein (Fig. 4.13A). Fig. 4.13B shows an overlay of the truncated α B-10m mutant (containing only the ACD residues: 64-152) (Mainz *et al.* 2012) and the α B-6E sample. Residues that could overlap in both spectra are labeled with grey boxes suggesting a few

tentative assignments for these amino acids, however, in total there are not many similarities between the two samples. Differences also in peak position are attributed to slight temperature differences and shifts at the oligomeric interface. Plotting the ^1H , ^{13}C HSQC methyl spectra of $\alpha\text{B-10m}$ grown in H_2O -based medium and ILV-labeled $\alpha\text{B-6E}$ grown in D_2O -based medium (Fig. 4.13C), enables the transfer of a few tentative assignments (shown in figure in green) and the identification of resonances belonging to the ACD in the $\alpha\text{B-6E}$.

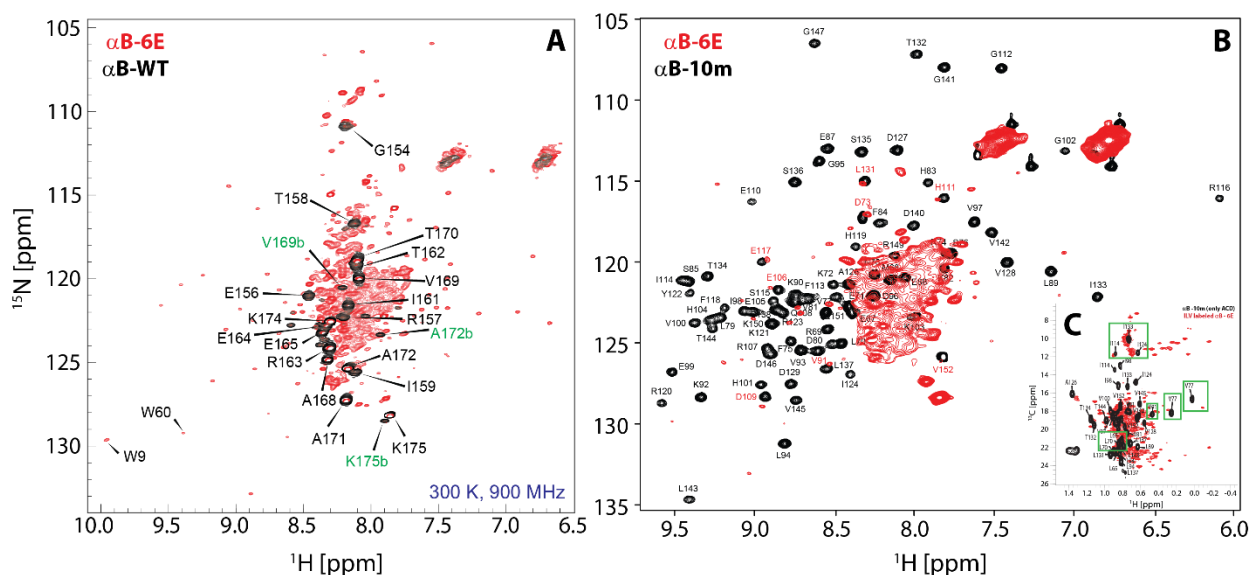


Fig. 4.13. Overlay comparison of $\alpha\text{B-6E}$, $\alpha\text{B-WT}$ and $\alpha\text{B-10m}$. (A) Overlay of ^1H , ^{15}N SOFAST HMQC spectra of $\alpha\text{B-6E}$ (purified with AEC and SEC only, shown in red) and $\alpha\text{B-WT}$ (black). The samples were measured at a concentration of 1 mM at 300 K and 900 MHz. (B) Overlay of ^1H , ^{15}N SOFAST HMQC spectra of $\alpha\text{B-6E}$ (red) and $\alpha\text{B-10m}$ (black). Grey boxes are indicating residues that could overlap with the truncated αB mutant. The samples were measured at a concentration of 600 μM at 300 K and 600 MHz. Assignments and spectra of $\alpha\text{B-10m}$ were kindly provided by Dr. Andi Mainz (TU, Berlin). (C) Overlay of the ^1H , ^{13}C methyl spectra of ILV-labeled $\alpha\text{B-6E}$ (red) and $\alpha\text{B-10m}$ (black) grown in D_2O -based medium with ^2H , ^{13}C -glucose as carbon source and in H_2O -based medium with ^1H , ^{13}C -glucose, respectively. Residues that could overlap between the two spectra are shown in green boxes. The spectra were recorded at 300 K and 600 MHz.

Transmission electron microscopy (TEM) images of the $\alpha\text{B-6E}$ mutant in high (25 μM) and low (2.5 μM) concentration and different magnifications are presented in Fig. 4.14A,C, showing that the mutant appears more heterogeneous compared to the full-length protein (Fig. 4.14B). Additionally, the oligomer size distribution of the mutant seems to be concentration dependent as at higher concentration large aggregates of the protein are formed in comparison to the lower concentrated sample, which is not the case for $\alpha\text{B-WT}$ that can be concentrated for example up to 10 mM for a solid-state NMR measurement.

Additional SAXS and CD data were recorded in order to compare the full-length with the mutant protein, presented in Fig. 4.15. The CD spectra showed that the two proteins have a high similarity, as the β -sheet structure is predominant in $\alpha\text{B-6E}$ like in $\alpha\text{B-WT}$. Furthermore, looking at the SAXS data (Fig. 4.15A,C), recorded for both samples at the same conditions and concentration (about 1 mg/ml), $\alpha\text{B-WT}$ appears as globular, folded protein, while $\alpha\text{B-6E}$ due to the ‘tail’ it has in the graph (region between 150–300 r(\AA)), seems to be partially folded. So it either has unstructured regions or that it is more heterogeneous (multidomain) than the wild-type.

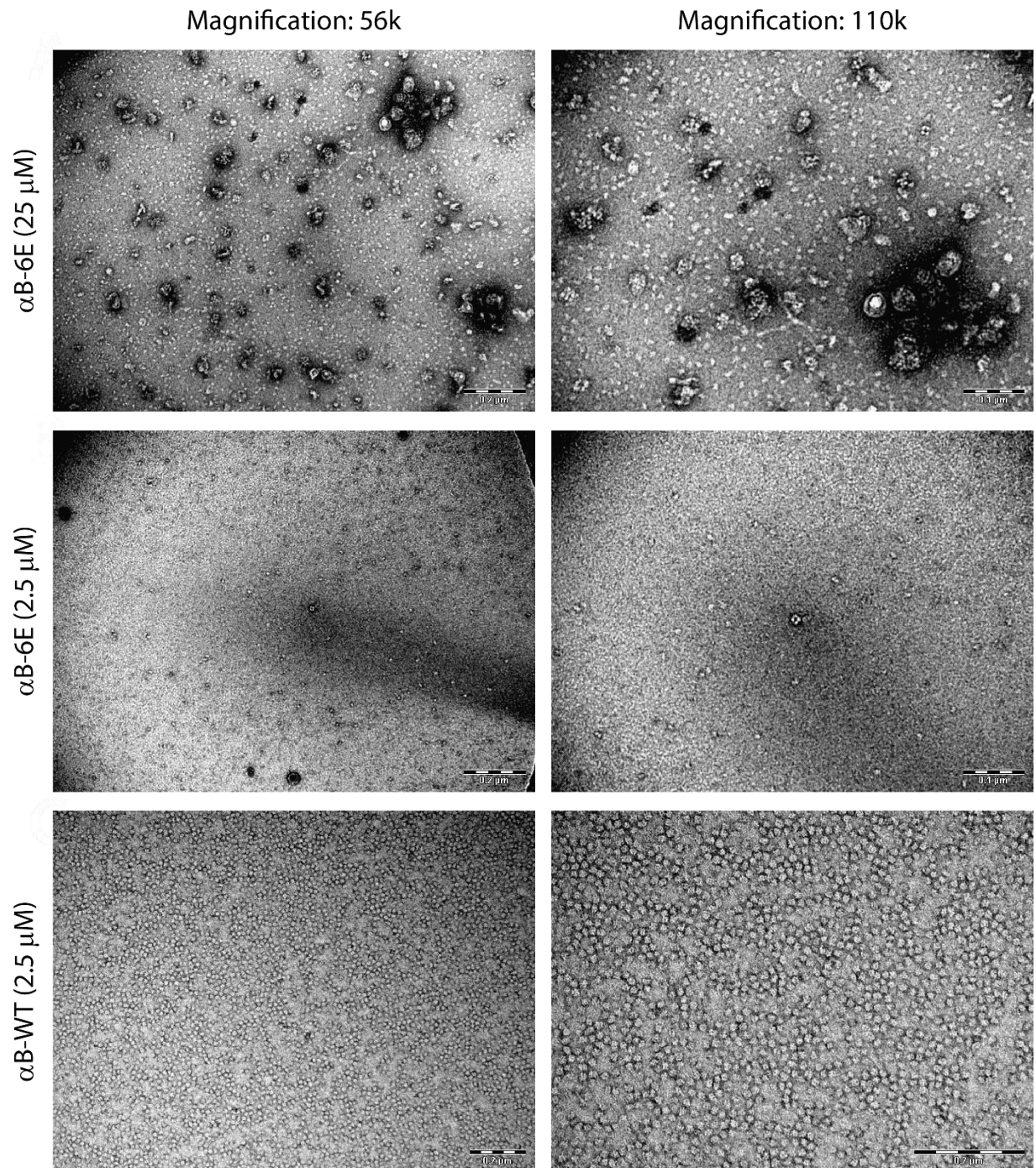


Fig. 4.14. Transmission electron micrographs of the α B-6E and α B-WT. (A) 25 μ M α B-6E at two different magnifications (56 and 110 k). (B) 2.5 μ M α B-6E at the two different magnifications (56 and 110 k). (C) 2.5 μ M α B-WT at two different magnifications (56 and 110 k). Scale bars for α B-6E are at 0.2 μ m and 0.1 μ m for 56 and 110 k, respectively, while for α B-WT are at 0.2 μ m.

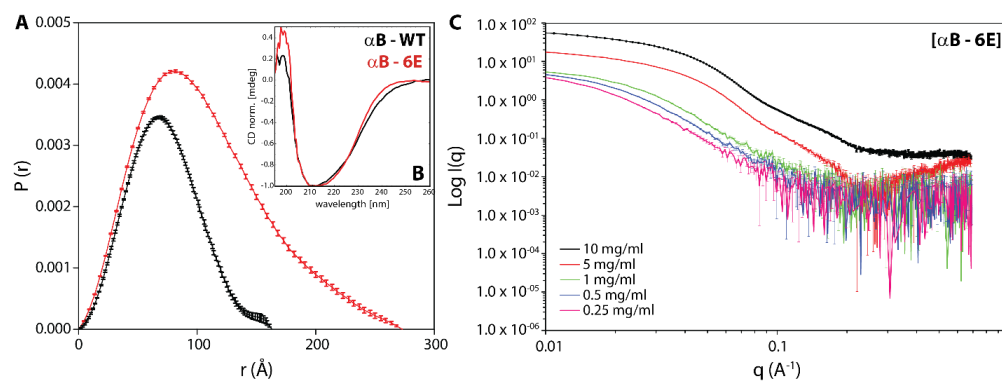


Fig. 4.15. SAXS and CD data of α B-6E. (A) Kratky plot of scattering data, illustrating changes in the behaviour of the curve for the folded (or spherical) α B-WT (black) and for the partially folded (sphere-random coil) α B-6E (red). (B) High similarity was observed also by CD spectroscopy, showing the predominant presence of β -sheet structures in α B-6E. (C) Experimental SAXS merged intensity distribution curves, collected for 5 different α B-6E concentrations (0.25, 0.5, 1, 5 and 10 mg/ml).

4.6. Expression and Purification of α B-6D

Peschel et al. (2013) showed that the α B-6D mutant forms smaller oligomers like the α B-6E mutant than the wild-type protein. Therefore, in order to be able to study the phosphomimicking mutants of α B with NMR, we tried to purify the α B-6D mutant, as it might be more stable than the α B-6E. For this reason, site-directed mutagenesis was used and the 6 mutations (serines were mutated to aspartic acid: S19, S21, S43, S45, S53, S59) were introduced in the wild-type protein. As a starting point the protocol and conditions shown in chapter 4.3. for purification were applied (Fig. 4.17). To estimate whether the desired protein was well-expressed, SDS-PAGE was performed for unlabelled and 15 N-labeled α B-6D using cells lysed in Lämmli buffer as shown in Fig. 4.16.

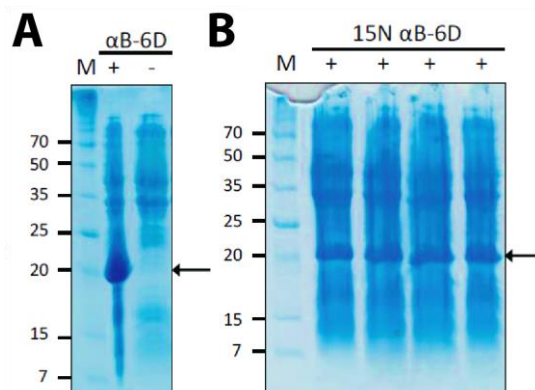


Fig. 4.16. Representative expression SDS-PAGE gels. (A) unlabeled α B-6D and (B) 15 N-labeled α B-6D. the wild-type protein is not loaded on the gel. Arrows indicate the overexpressed protein bands, M the marker and + or – symbols denote the induced and uninduced cells.

The theoretical pI of α B-6D mutant is 5.7 and the protein in the AEC was eluted at similar NaCl concentration to α B-6E. However, in the SEC the protein was eluted similar to the wild-type, but with much more impurities shown in the SDS gel (Fig. 4.17B-D,F). For NMR experiments only fractions D1-D4 from the SEC were used and in order to find out additional purification steps that will increase the purity of the sample fractions D5-D11 were pooled. In contrast to the α B-6E mutant, α B-6D showed a drastically

decreased degradation band at around 15 kDa that suggests that aspartate as a phosphomimetic mutation results in a more stable protein in terms of degradation. Furthermore, α B-6D in analytical gel filtration using again either PBS or HEPES buffer (Fig. 4.18), shows a marked difference in the elution profile. The α B-6D mutant in PBS elutes at 14.5 ml in PBS and at 12 ml in HEPES. Of great interest is that the protein seems larger under no salt conditions, as generally under low salt interaction with the column, matrix is stronger and proteins appear smaller. However, either α B-6D interacts less strongly with the column when salt is absent, or it becomes indeed larger, which is counterintuitive when salt to shield charges is absent.

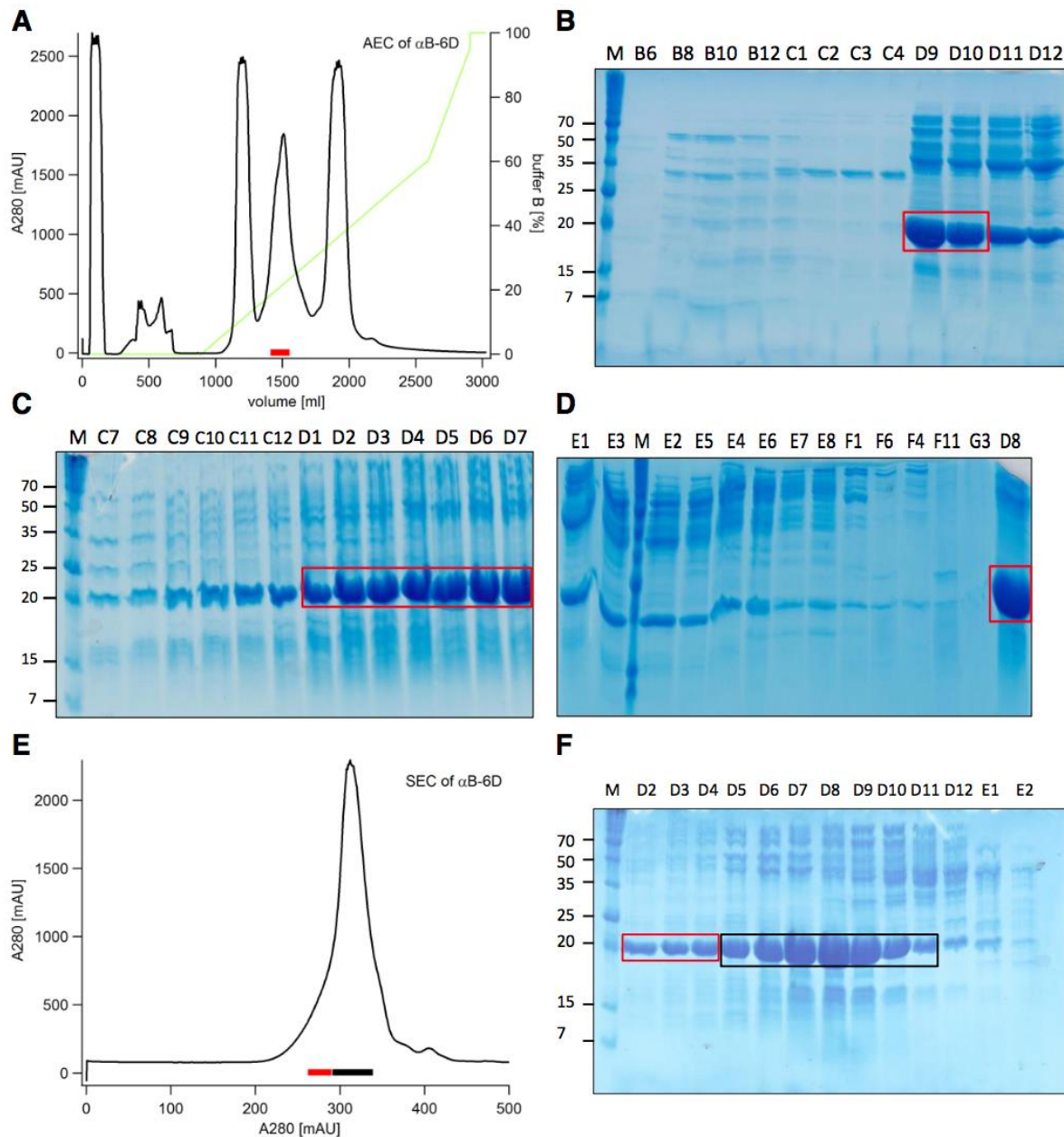


Fig. 4.17. Purification of unlabeled α B-6D. (A) Chromatogram of the AEC of α B-6D. Black, absorbance at 280 nm; green, percentage of buffer B-6D (contains 1M NaCl); red bar, pooled volume for SEC. (B, C, D) Corresponding SDS-Gels from AEC. The red boxes mark the pooled fractions. (E) Chromatogram of the SEC of α B-6D. Black, absorbance at 280 nm; red bar, pooled volume for NMR; black bar, pooled for further purification attempts. (F) SDS-Gel corresponding to the SEC run. The red box marks the pooled fractions; the black box marks a second pool for further purifications experiments.

As it is complicated to separate the protein from the impurities two additional strategies were tried. First by using an additional AEC column either (i) a DEAE column or (ii) a ResourceQ column, and the other by using hydrophobic interaction chromatography (HIC). The DEAE column is a weak anion exchange column. The ligand has hydrophobic ethyl-sidechains resulting in sterical hindrance for the interaction of protein and column material. The ResourceQ column is another strong anion exchange column with a significant decreased particle size (15 μm instead of 90 μm in diameter). A smaller particle size in the bead material of AEC columns results in improved peak separation.

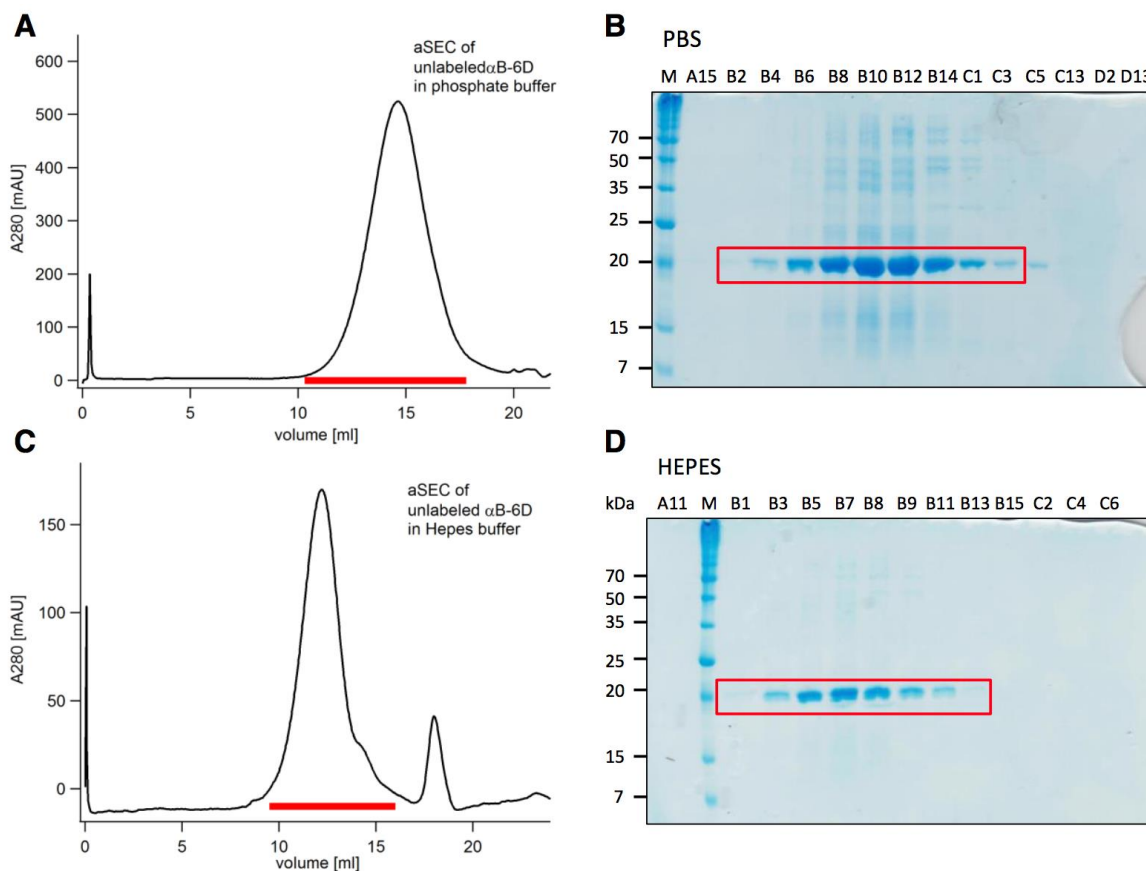


Fig. 4.18. Analytical size exclusion chromatography of unlabeled $\alpha\text{B-6D}$ (pool from Figure 9F, SEC fractions D1-D4, red box). (A) Chromatogram of the aSEC run with phosphate buffer. Black, absorbance at 280 nm; red bar, pooled volume. (B) Corresponding SDS Gel of the aSEC run with phosphate buffer. The red box marks the pooled fractions. (C) Chromatogram of the aSEC run with HEPES buffer. Black curve, absorbance at 280 nm; red bar, pooled volume. (D) Corresponding SDS-Gel from the aSEC run with HEPES buffer. The red box marks the pooled fractions.

Fig. 4.19 shows that none of the AEC columns resulted in satisfying purity increase. Both columns separated the protein from the smaller 15 kDa degradation band in the end of the descending branch (fractions 25-28 in **Fig. 4.19B** and fractions 20-22 in **Fig. 4.19D**) with intermediate success. Bigger impurities were not separated. The weak anion exchange column did not distinguish between the protein and the impurities. The ResourceQ column resulted in several peaks over the gradient of buffer B (**Fig. 4.19C**) as it was expected. Unfortunately, $\alpha\text{B-6D}$, its degradation product and other impurities were found in all fractions (**Fig. 4.19D**), which means that not even the very fine 15 μm bead material of the ResourceQ column was able to separate protein and impurities. This might be due to very similar ionic properties of all present proteins. Therefore, another strategy was chosen, the hydrophobic interaction chromatography (HIC).

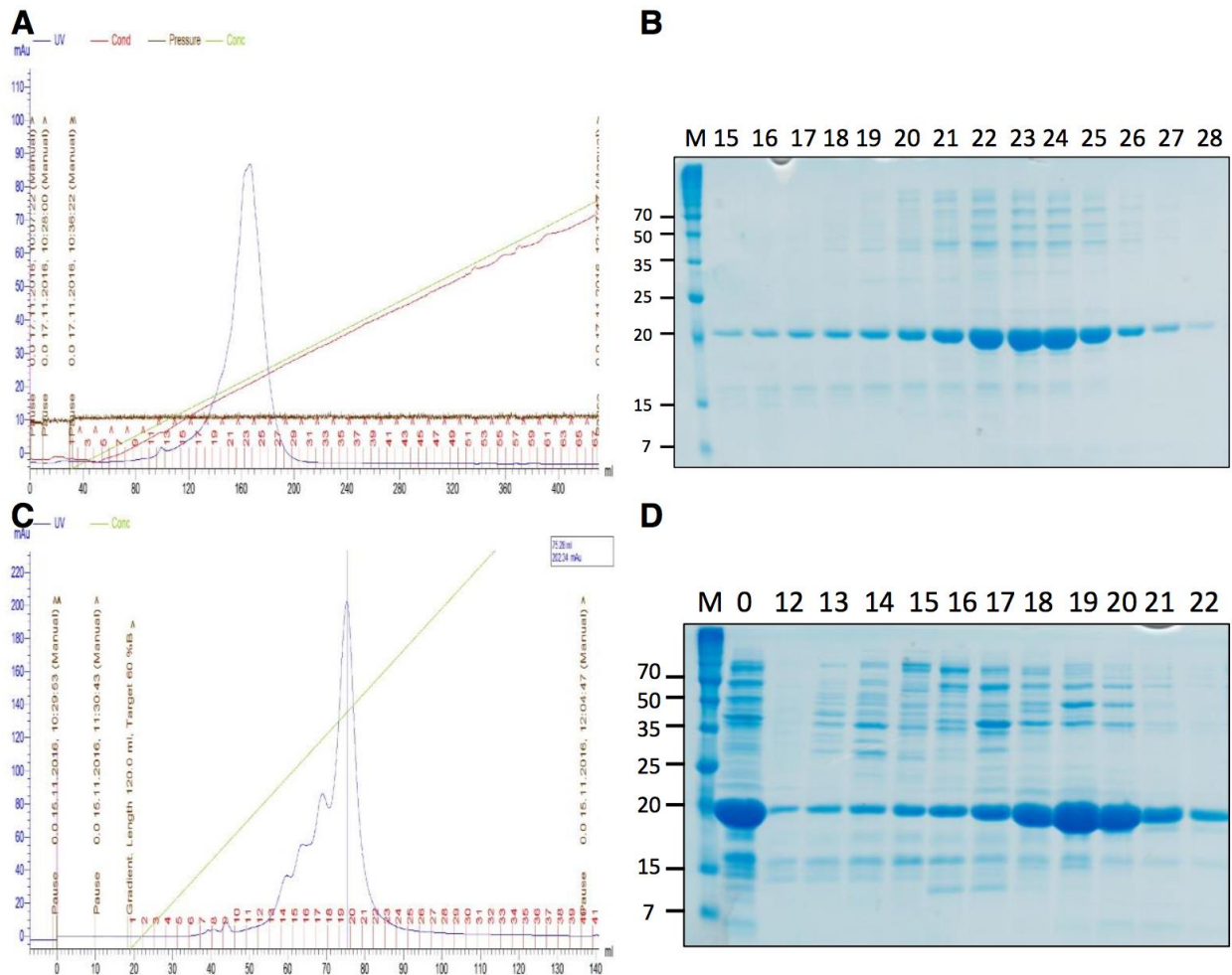


Fig. 4.19. Purification approaches with different AEC columns. (A) Chromatogram of weak AEC DEAE column. **(B)** Corresponding SDS Gel from DEAE column. **(C)** Chromatogram of ResourceQ column with particle size of 15 μm . **(D)** Corresponding SDS Gel from Resource Q column.

Due to the fact that αB -crystallin assembles into oligomers, it is possible that it has hydrophobic surface patches that can interact with the hydrophobic bead material of a phenyl column. This column has a hydrophobic phenyl ligand and is the least hydrophobic column from GE Healthcare. Before loading αB -6D onto the column it was incubated over night in buffer B, containing either 1 M NaCl or 1 M $(\text{NH}_4)_2\text{SO}_4$. $(\text{NH}_4)_2\text{SO}_4$ is more kosmotropic (stronger 'salting out' effect) than NaCl, and should, compared to NaCl, lead to a stronger hydrophobic interaction between the column material and the protein. From **Fig. 4.20A and B** it is evident that the NaCl gradient is not appropriate for further purification of αB -6D. The chromatogram shows that most of the protein elutes at 0 % buffer B. On the SDS gel one can see αB -6D eluting with most of the impurities and together with its degradation band.

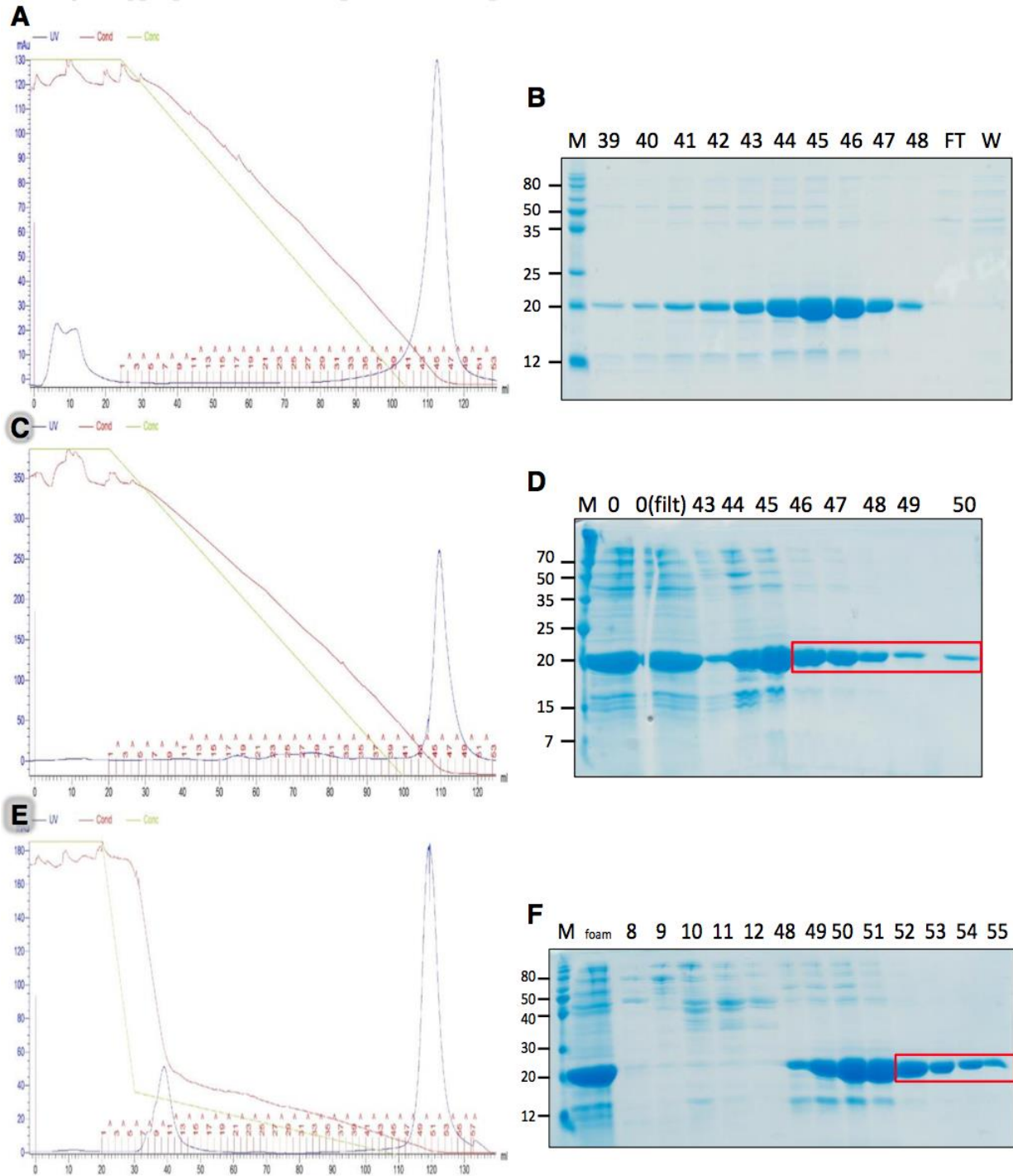


Fig. 4.20. Precipitation of α B-6D and subsequent phenyl column approaches. (A) Chromatogram of α B-6D. NaCl was potentially added to 1 M and the solution applied to the column, which was equilibrated with buffer B-6D (at pH 8.8). A gradient from 100-0% buffer B-6D in 16 CV was run. (B) Corresponding SDS gel from the phenyl column with NaCl gradient. (C) Chromatogram of α B-6D precipitated with 25% $(\text{NH}_4)_2\text{SO}_4$ saturation and buffer B(AS) gradient 100-0% in 16 CV. (D) Corresponding SDS gel from the phenyl column with $(\text{NH}_4)_2\text{SO}_4$ gradient. (E) Chromatogram of α B-6D prepared as in C but two gradients: 100-20% B(AS) in 2 CV, then 20-0% in 16 CV. (F) Corresponding SDS gel from the phenyl column run with two $(\text{NH}_4)_2\text{SO}_4$ gradients. Red boxes indicate pooled fractions.

Using strong salting out salt ammonium sulfate resulted in better separation of α B-6D and its 15 kDa degradation band, as shown in Fig. 4.20D. The degradation band significantly disappears at fraction 46. To further increase the separation between α B-6D and its degradation band the gradient was divided in a fast gradient 100 – 20 % B(AS) in 2 CV, and a really slow gradient 20 – 0 % B in 16 CV. Fig. 4.20E shows that increasing the gradient slope results in a first A_{280} peak in the chromatogram. The main peak elutes again at 5 – 0 % buffer B. The corresponding SDS gel (Fig. 4.20F) showed that the first peak has high kDa impurities, whereas the main peak coming later contained α B-6D protein and the degradation band. Fraction 51 contains much α B-6D, but negligible amounts of both, degradation product and high kDa impurities. This shows that a 2-gradient-strategy using a phenyl column is the most promising approach to increase the purification result of the phospho-mimetic mutant α B-6D.

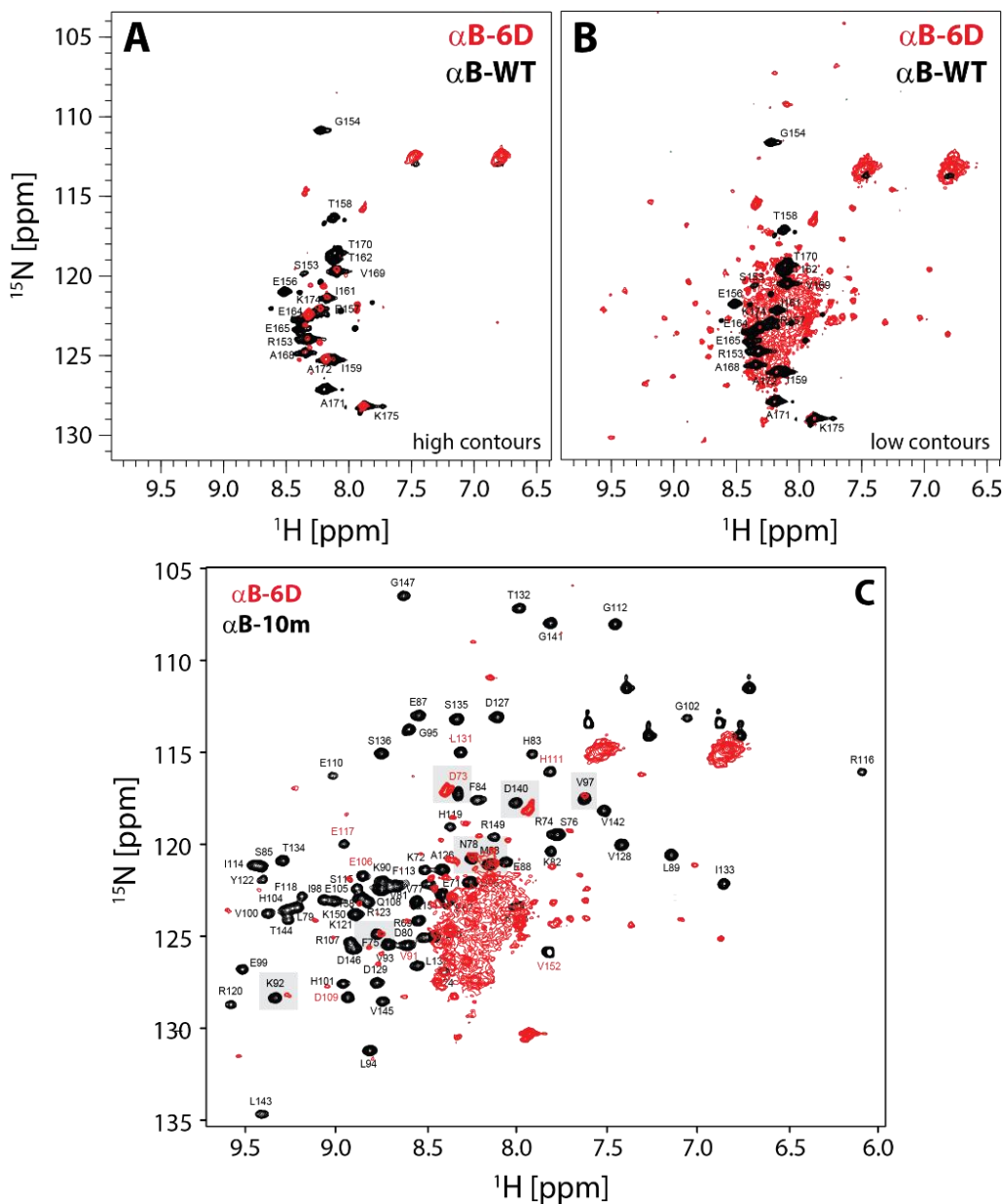


Fig. 4.21. Overlay of ^1H , ^{15}N HSQC spectra of α B-6D and α B-WT in phosphate buffer. (A) ^{15}N -labeled α B-6D (red) and α B-WT (black) in high and (B) in low contours. Assignments corresponding to the C-terminal region of the full-length protein are shown in black in both spectra. (C) Overlay of ^1H , ^{15}N HSQC spectra in phosphate buffer of α B-6D (red) and α B-6E (blue). The spectra were recorded at 300 K and 600 MHz.

The final sample purified with the HIC column was concentrated and used to record an HSQC spectrum of the α B-6D phosphomimicking mutant. In **Fig. 4.21A-B** ^{15}N -labeled α B-6D mutant is superimposed to the assigned ^{15}N -labeled α B-WT in high and low contours, respectively. The well-dispersed peaks in the spectra indicate a folded protein, however in the region between 7.8 – 8.5 ppm, in the middle of the spectrum in **Fig. 4.21B** the severely overlapped peaks that include also the C-terminal region, suggest unstructured parts in the protein. Furthermore, there are more resonances coming up in the spectrum of the α B-6D mutant and some residues that are assigned for the wild-type and no longer visible or maybe shifted for α B-6D, as for example residues E156, T170, A171. This indicates that phospho-mimicking mutagenesis changes the oligomer's behavior and has also an impact on the chemical environment and structure around the C-terminal region.

4.6.1. Monitoring Degradation of α B-6D at Room Temperature

When studying a new protein sample it is important to know if the protein can be handled at room temperature or needs to be placed on ice continuously, while working with it. Therefore, the stability of the α B-6D mutant was tested by monitoring degradation upon long-term incubation at room temperature. Samples were taken every 24 hours, mixed with Lämmli buffer and placed in the freezer for SDS-PAGE.

Fig. 4.22 shows the SDS gel of the degradation assay at room temperature. At the beginning of the experiment (day 0), already some degradation to the first degradation product (1) was visible. This degradation product ran at about 19 kDa, 1 kDa less than our target protein. The fraction of full length α B-6D decreased over time and at the end the ratio between full length protein and the degradation product (1) was approximately 1 to 1. Additionally, α B-6D was further degraded to degradation product (2), which ran at around 15 kDa. This is in a similar range as the degradation product seen in all purification steps (including α B-6E mutant), emphasizing that the smaller band is a degradation product of α B-6D. The gel shows many impurities of the sample and it is not excluded that one of these impurity-bands could contain any *E. coli* protease capable of degrading α B-6D. This assay demonstrates that it is necessary to store α B-6D continuously on ice in order to avoid degradation of the protein as far as possible.

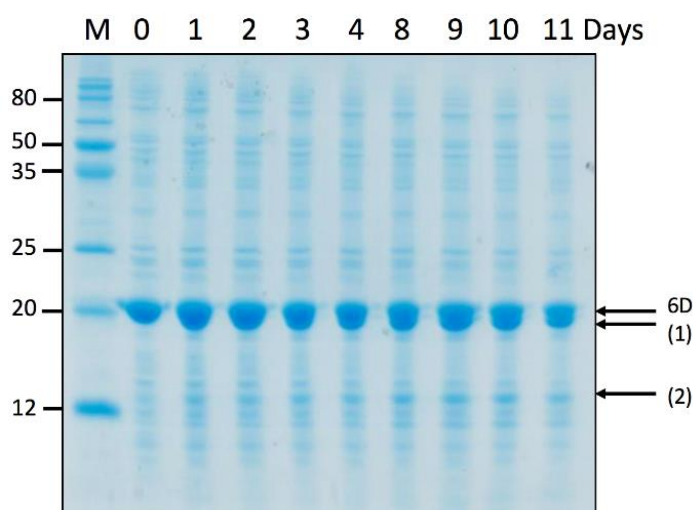


Fig. 4.22. SDS gel of the degradation of unlabeled α B-6D at room temperature. Arrows indicate the full length protein (6D), the first degradation band at 19 kDa (1) and a second degradation band at 14 kDa (2).

4.6.2. Limited Proteolysis of α B-6D with α -chymotrypsin

4.6.2.1. Comparing the Stability of α B-6D and α B-WT

For investigations on the conformational features of α B-6D, limited proteolysis was used. In this assay the stability of α B-WT and α B-6D against the protease α -chymotrypsin was compared. In general, disordered or flexible regions of proteins are more susceptible for proteolytic degradation compared to folded regions of the protein. The decline of α B during time was monitored by SDS-PAGE.

The SDS gel shows that both proteins were completely degraded after 30 minutes (**Fig. 4.23**). For α B-6D this process is even faster than for the wild-type protein. Both proteins had a concentration of 20 μ M in the beginning and the bands decreased according to their degradation. After 1 min the 20 kDa and 19 kDa bands of α B-6D were paler than the bands of α B-WT. After 5 minutes the wild-type had stronger bands than α B-6D. Furthermore, the second degradation fragment (2) was more stable for α B-WT, as indicated by the darker band after 5 min.

To identify where the protein was cleaved, N-terminal sequencing and/or MS approaches would be a good idea to get the amino acid sequence of peptides. This assay was done in a similar way by Pescheck *et al.* before with α B-WT and α B-3E mutant (Pescheck *et al.* 2013). Their result was comparable to this, having a 1 kDa less degradation band and another degradation band around 14 kDa. They performed LC-MS to identify the peptide and showed that degradation fragment (1) corresponds to amino acids 10-175 and the smaller fragment (2) corresponds to amino acids 48-175. This means that degradation of α B happens specifically from the N-terminus and furthermore, the phospho-mimetic mutants are more susceptible for degradation by α -chymotrypsin. The decreased stability of the 14 kDa fragment (2) indicates that the N-terminus in the α B-6D mutant gains flexibility around the residue F47, and thereby, becomes more prone for degradation, as described for the α B-3E mutant (Pescheck *et al.* 2013).

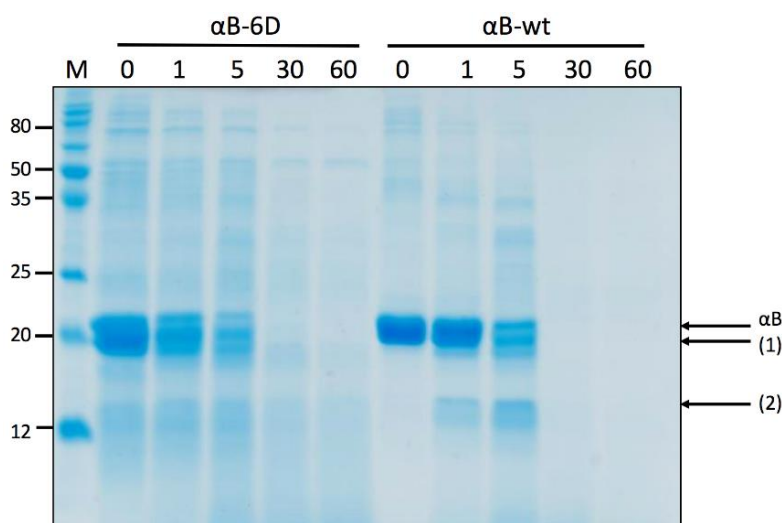


Fig. 4.23. SDS gel of α B-6D and α B-WT after limited proteolysis with α -chymotrypsin. Arrows indicate the full length protein (α B), a degradation fragment of 19 kDa (1) and a degradation fragment of about 14 kDa (2).

4.6.2.2. Influence of Lysozyme on Proteolytic Digestion of α B-6D

In the work published by Aquilina and Watt (2007) it was stated, that binding of a substrate would stabilize the N-terminus of α B crystallin. To investigate the influence of the phospho-mimetic mutants on this, interaction proteolysis was repeated adding lysozyme as substrate to α B and destabilizing it with DTT. The results were monitored with SDS-PAGE. The used α B concentration was 20 μ M and lysozyme was 40 μ M (stoichiometry 1:2).

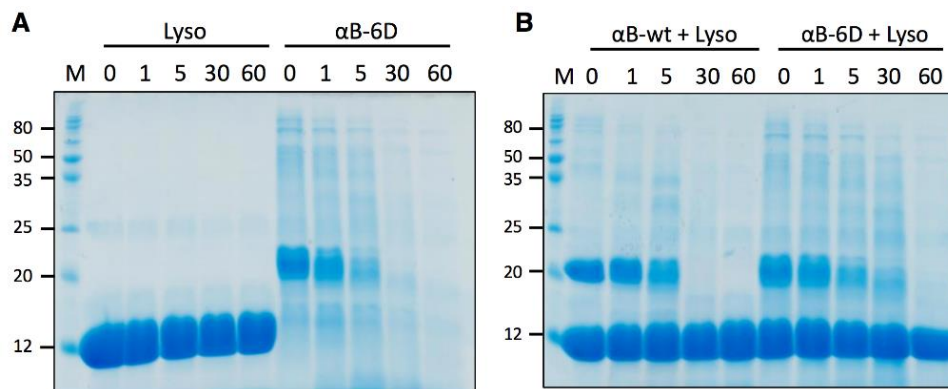


Fig. 4.24. SDS gels of lysozyme (Lyso), α B-6D, as well as α B-wt and α B-6D with lysozyme after proteolytic degradation with α -chymotrypsin. (A) Lysozyme and α B-6D pre-incubated 1 min with additional 1 mM DTT. (B) α B-WT + lysozyme and α B-6D + lysozyme pre-incubated 1 min with additional 1 mM DTT.

Lysozyme itself proves to be a stable protein against α -chymotrypsin even after incubation with the reducing agent DTT (Fig. 24A). This indicates that Lysozyme was either not denatured by DTT or assembled itself in stable aggregates with hydrophobic residues (targets of α -chymotrypsin) oriented away from the surface of the aggregates. The A_{340} of the degraded lysozyme sample had increased signal, indicating aggregates. The α B-6D mutant without lysozyme, but pre-incubated with DTT showed the same degradation pattern as described above (see Fig. 23): strong degradation after 5 min, fully degraded after 30 min. So DTT had no influence on the stability of α B-6D. The wild-type protein was as well degraded as described above (see chapter 4.5.2.1) suggesting that α B-WT was not stabilized by lysozyme against degradation by α -chymotrypsin. It was expected to be stabilized as described by Aquilina and Watt (2007), because lysozyme is a substrate that is known to bind the N-terminal region of α B and α B is N-terminally degraded. The binding of lysozyme should shield degradation prone regions of α B-WT from the attack by α -chymotrypsin. This indicates that lysozyme was (i) either not bound to α B-WT, or (ii) only bound to regions that are too far away from the cleavage sites, or (iii) only transiently bound, so that the protease was still able to gain access to the cleavage sites.

Comparing the degradation pattern of α B-6D without lysozyme and the degradation pattern of α B-6D with lysozyme, the major difference was that α B-6D was not fully degraded after 30 min in presence of lysozyme. The degradation fragment (1) was still there after 30 min. Also after 5 min of incubation the ensemble of bands at 20 kDa and 19 kDa of α B-6D was stronger visible in presence of lysozyme. This suggests that α B-6D was able to form stable complexes with degrading lysozyme and this protected the mutant protein from proteolytic degradation by α -chymotrypsin. Nevertheless, these results are not too convincing, as the differences between the bands were not too strong. These experiments should be repeated with an additional sample taken after 15 min and it could be considered to perform this assay at 25 $^{\circ}$ C and slightly increased pH (e.g. pH 7.8) as described by Peschek et al. (2013).

4.6.3. Analytical Ultracentrifugation (AUC) of the Phospho-mimicking Mutants

Analytical ultracentrifugation experiments (AUC) were used for investigations of the quaternary structures of the full-length and mutant proteins. The sedimentation coefficients, determined by AUC, correlate with the molecular mass and the diffusion coefficient of the oligomers.

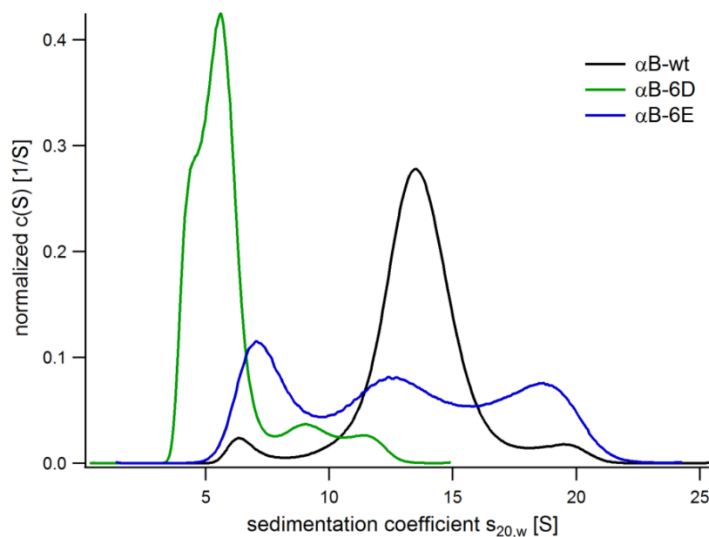


Fig. 4.25. Sedimentation velocity AUC analysis of α B-wt, α B-6E and α B-6D. The S-value distributions were obtained by $c(s)$ analysis.

Sedimentation velocity AUC experiments (Fig. 4.25) revealed a shift of the weight average sedimentation coefficient from 14 S (Svedberg) for α B-WT (24-mer) towards smaller values for the mutants. The α B-6D mutant has a sedimentation coefficient of 5 S, corresponding to a 6-mer or a 4-mer, and the α B-6E mutant has a maximum in the distribution of its sedimentation coefficient at 7.5 S, corresponding to a 12-mer. Additionally, it is observed that the phosphomimicking mutants are more heterogeneous than the wild-type protein, as the samples displayed an asymmetric distribution indicating the presence of at least three populations of different oligomeric species.

4.6.4. ^1H DOSY Experiments of the Phospho-mimicking Mutants

To further validate the aUC results, ^1H DOSY experiments were performed for α B-WT and the phospho-mimicking mutants, α B-6D and α B-6E (Fig. 4.26) in order to monitor the diffusion behaviour of each protein in solution using a pulse gradient field. This method gives information about the oligomeric state of each sample. To be comparable all samples were measured at the same conditions (concentration: 200 μM , temperature: 300 K, field: 900 MHz, 50 mM PBS buffer, little δ : 3 ms, big δ : 300 ms). The DOSY experiments show, that α B-6D consists of a smaller number of oligomers as compared to wild-type and the α B-6E mutant, and based on the simulated curves shown in the figure, it is suggested to be a tetramer (4mer) as it diffuses between the hexameric and the dimer simulated curves. This indicates that the overall size of the protein is significantly decreased (corresponding to a molecular weight of 80 kDa). However, due to the calculated error bars α B-6D could also be a 6mer. In addition, α B-6E mutant diffuses in a manner corresponding to a hexameric oligomer (i.e. 120 kDa) or a 12mer (i.e. 340 kDa), while α B-WT to a 12mer, 24mer (i.e. 480 kDa) or even higher ordered oligomer.

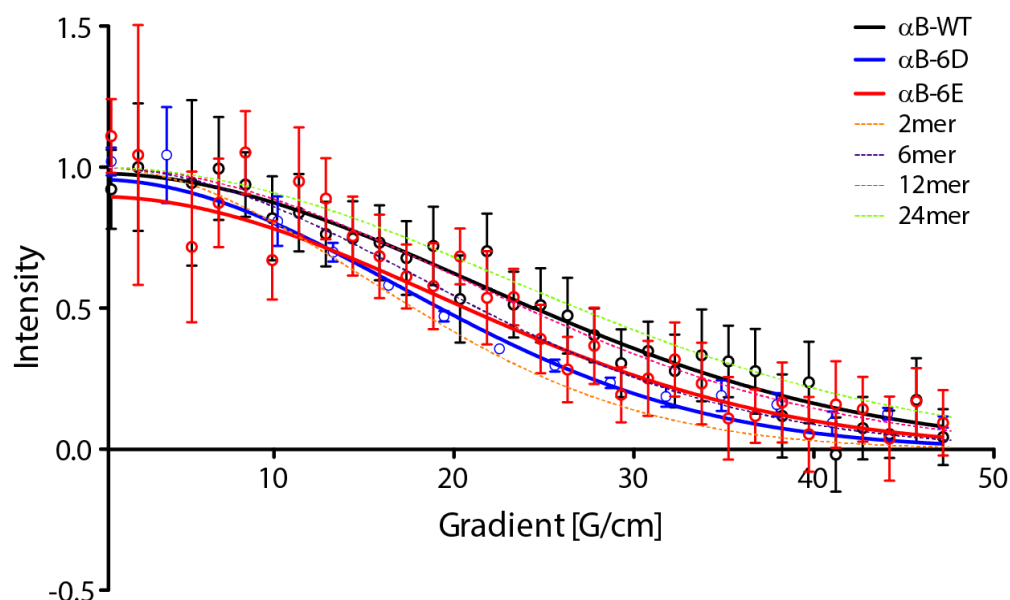


Fig. 4.26. DOSY correlation curves of ^{15}N -labeled αB -WT (black), αB -6D (blue) and αB -6E (blue) in phosphate buffer. Simulation of attenuation profiles (dashed lines) for various αB n-mers as indicated in the legend: 2mer (orange), 6mer (dark blue), 12mer (magenta) and 24mer (light green). Samples were concentrated to 200 μM in a shigemi tube, and recorded at 300 K and 900 MHz.

4.7. Interaction Studies in Solution-state NMR

4.7.1. Binding Interactions of $\text{A}\beta_{40}$ with αB -WT

The concomitant exposure of hydrophobic residues in proteins causes non-native interactions that finally result in protein aggregation. As a general protective mechanism, the cell enhances the expression of small heat-shock proteins (sHsps) (Haslbeck *et al.* 2015; Horwich 1997). These ATP-independent molecular chaperones, can form soluble complexes with partially-unfolded client proteins and thereby rescue them from irreversible aggregation.

The major constituents of the extracellular plaques in Alzheimer's disease are amyloid- β_{40} ($\text{A}\beta_{40}$) peptides (Danielsson *et al.* 2007). Other proteins, including sHsps, like αB -crystallin (αB), are also found colocalized with $\text{A}\beta_{40}$ peptides in extracellular plaques, functioning as molecular chaperones (Mainz *et al.* 2012). Therefore, with the following combination of experiments (solution-state NMR and transmission electron microscopy, TEM), we set out to characterize the interaction between αB and $\text{A}\beta_{40}$ peptide and obtain an understanding of the atomic mechanisms, which yield the disaggregation of Alzheimer's disease β -amyloid fibrils induced by the small heat shock protein. As presented in the TEM images of the negative-stained sample (Fig. 4.27), $\text{A}\beta_{40}$ fibrils were grown from monomeric $\text{A}\beta_{40}$ and upon incubation under agitation for 4 days in the row at 37 $^{\circ}\text{C}$, in absence and presence of αB , TEM images were obtained at 2 different magnifications, 28 and 110 k. In absence of the chaperone mature fibrillar structures are formed. However, in presence of αB , and despite the 30-molar excess of $\text{A}\beta_{40}$ to the sHsp, αB binds to $\text{A}\beta_{40}$ and efficiently inhibits the fibril elongation *in vitro*, revealing formation of large aggregates (Fig. 4.27B) instead of mature fibrils, which are considered to be causative for AD pathogenesis. Because the most effective means of extending the lag phase for amyloid fibril growth is to reduce the elongation (or fragmentation)

rate (Knowles *et al.* 2009), this is likely to represent a highly successful chaperone mechanism for suppressing fibril proliferation. Additionally, in **Fig. 4.27B**, there are much less αB oligomers on the surface than it would be expected from the concentration (5 μM) and as compared to **Fig. 4.27C** (2.5 μM). This could be explained by the fact that αB is mostly bound to the fibrils and this overlapping does not allow us to observe the 5 μM concentration.

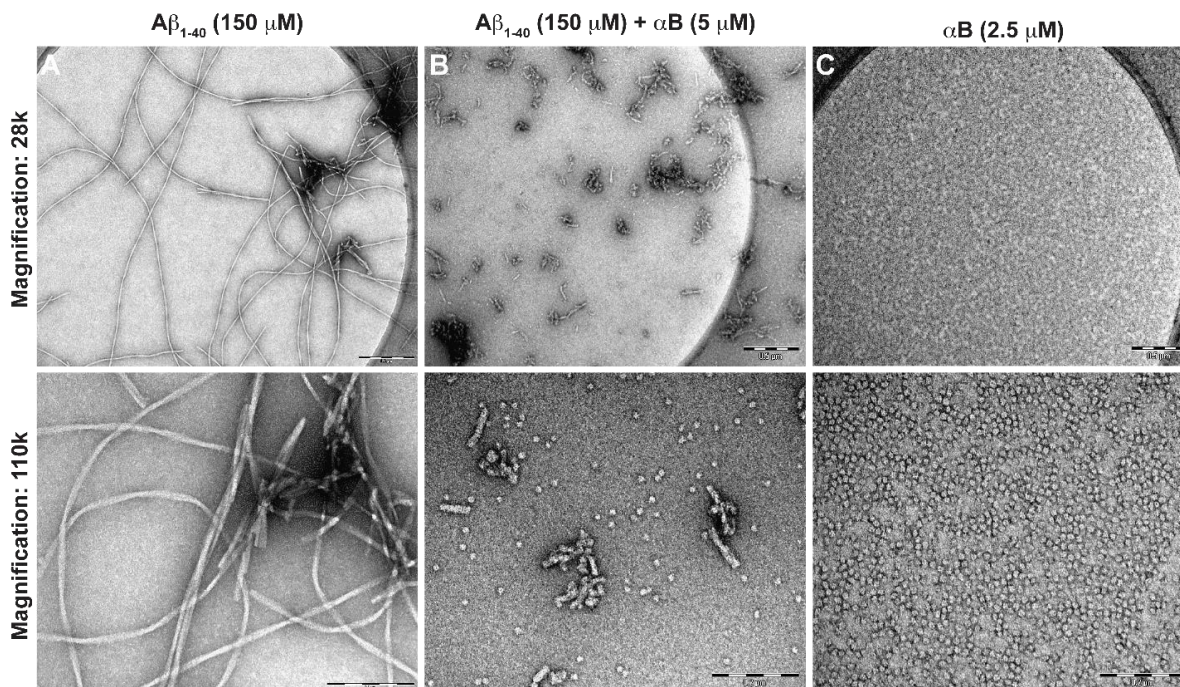


Fig. 4.27. αB -Mediated inhibition of $A\beta_{40}$ fibril formation *in vitro*. (A, B) Negative-stained Transmission Electron Microscopy (TEM) images of $A\beta_{40}$ samples incubated for 4 days under agitation, at 37 °C in the absence (A) and presence of αB (B), in two different magnifications: 28k (left) and 110k (right). The following concentrations were employed: 150 μM solubilized $A\beta_{40}$ and 5 μM αB . Incubation of $A\beta_{40}$ only, as shown in (A), usually results in mature fibrillar structures. Despite a 30-molar excess of the client $A\beta_{40}$, the chaperone αB efficiently inhibits the fibril formation, revealing formation of large aggregates instead of mature fibrils (as shown in B). (C) TEM images of negatively-stained αB , as a reference, were incubated for 4 days under agitation, at 37 °C, in a concentration of 2.5 μM . Two different magnifications were obtained: 28k (left) and 110k (right). All samples were prepared in TBS buffer (50 mM Tris, 50 mM NaCl, pH 7.5). Scale bars of 500 nm (for 28k) and 200 nm (for 110k) are shown at the bottom.

To look at the interaction at atomic resolution we employed also solution-state NMR spectroscopy to a ^{15}N -labeled $A\beta_{40}$ sample. Therefore, we recorded 1H , ^{15}N SOFAST HSQC spectra (**Fig. 4.28**), where for every residue we expect to see one peak for the backbone. $A\beta_{40}$ is a 4 kDa protein consisting of 40 amino acids and its assignment is already known (Mainz *et al.* 2015). Solution-state NMR spectra of ^{15}N -labeled $A\beta_{40}$ and unlabeled αB in a molar ratio of 1:7.5, revealed a N-terminal binding site from Phe4 till Ser8 and from His13 till Leu17 (regions labeled with grey boxes in **Fig. 4.28A**). Additionally, looking at the intensities versus residues graph (**Fig. 4.28E**), we observe a drop of peak intensities, upon addition of αB . The fact that we see signal/intensity drop, means that $A\beta_{40}$ binds the oligomer, and this induces chemical shifts in the spectrum. The pronounced chemical shifts obtained in this specific region, indicate firstly, that there is interaction between the two proteins and also that the binding of $A\beta_{40}$ with αB , despite the excess of the chaperone, is in a low oligomeric state, as binding to the fully assembled oligomer would induce severe line broadening. Based on Williamson (2013), we calculated the chemical shift perturbation (CSP) of $A\beta_{40}$ upon αB binding (**Fig. 4.28C**) and the CSPs as a function of residues were plotted. Clearly a clustering of perturbations at the N-terminus is observed, indicating further a binding interface between $A\beta_{40}$ and αB .

Fitting the concentration dependent chemical shift changes, yields the dissociation constant, which is on the order of 100-400 μM for the $\text{A}\beta_{40}/\alpha\text{B}$ complex.

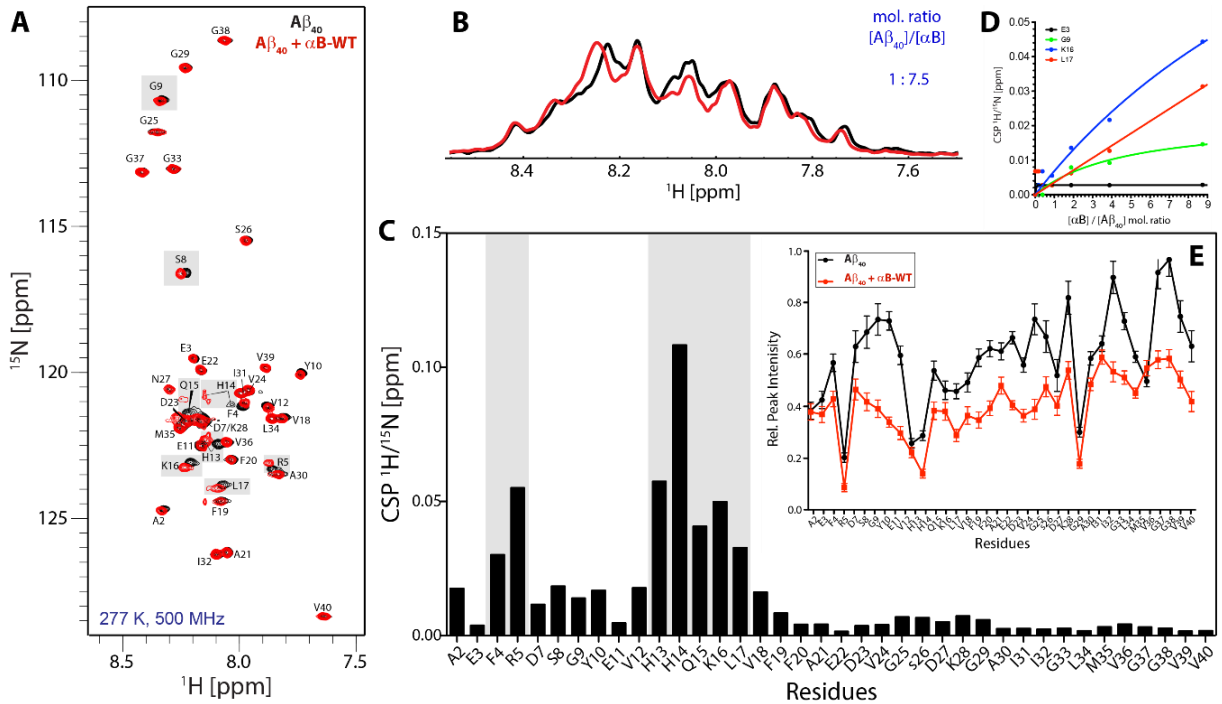


Fig. 4.28. ^1H , ^{15}N chemical shift perturbations (CSPs) of $\text{A}\beta_{40}$ upon αB -WT binding. **(A)** ^1H , ^{15}N SOFAST HMQC 2D spectra of solubilized $\text{A}\beta_{40}$ monomers in absence (black) and presence of αB (red). The first increments of both spectra are represented in **(B)**. The molar ratio of copper to Abeta is shown in blue. **(C)** The CSP at a molar ratio of 7.5 to 1 [$\alpha\text{B}/\text{A}\beta_{40}$] is plotted as a function of the primary sequence of $\text{A}\beta_{40}$. Clearly, a clustering of perturbations was observed at the N-terminus of $\text{A}\beta_{40}$, indicating the binding interface between $\text{A}\beta_{40}$ and αB , in a low oligomeric state. **(D)** The CSP of $\text{A}\beta_{40}$ was obtained as a function of the concentration of αB . The K_d (Williams on 2013) was determined to be in the range of 100-400 $\times 10^{-6}$ M. **(E)** Normalized intensities of the two samples showing also a dropping of signal in the N-terminus of $\text{A}\beta_{40}$. The samples were all prepared in a 100 mM PBS buffer, pH 7.3. The monomeric $\text{A}\beta_{40}$ concentration was 50 μM and is presented in all graphs in black, while the $\text{A}\beta_{40} + \alpha\text{B}$ sample in red. In **(A)** and **(C)** the interacting residues are labeled with grey boxes. All experiments were performed at a ^1H Larmor frequency of 500 MHz (11.7 T) and 277 K.

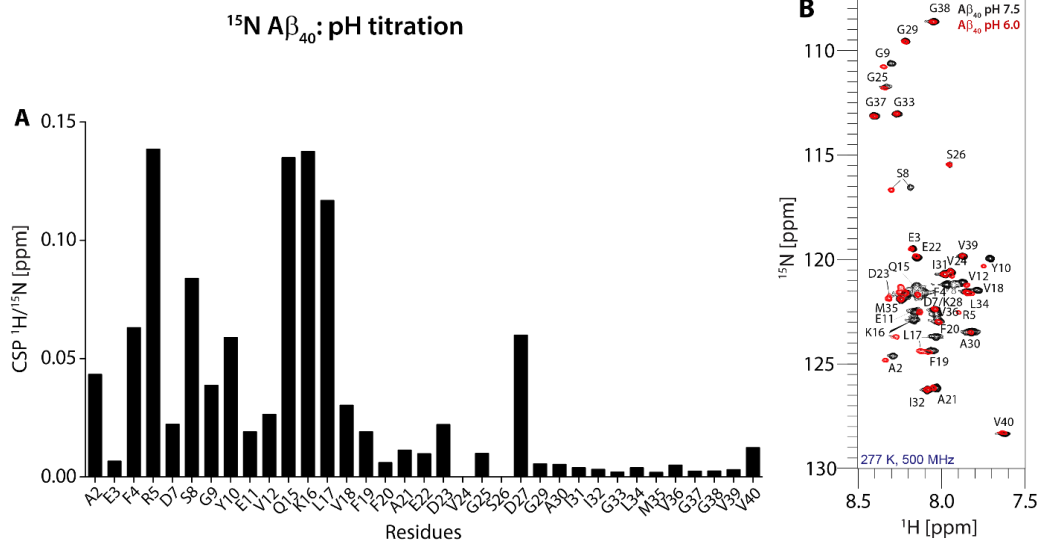


Fig. 4.29. ^1H , ^{15}N chemical shift perturbations (CSPs) of $\text{A}\beta_{40}$ upon pH titration. **(A)** The CSP plotted as a function of the primary sequence of $\text{A}\beta_{40}$. Clearly, a clustering of perturbations was observed at the N-terminus of $\text{A}\beta_{40}$. **(B)** ^1H , ^{15}N SOFAST HMQC 2D spectra of solubilized $\text{A}\beta_{40}$ monomers

in pH 7.5 (black) and pH 6.0 (red). The monomeric $A\beta_{40}$ concentration was 50 μ M. All experiments were performed at a ^1H Larmor frequency of 500 MHz (11.7 T) and 277 K.

In order to confirm that the chemical shifts in the NMR spectra are not arising from a pH effect upon addition of α B, we additionally performed a pH titration experiment where $A\beta_{40}$ was titrated with PBS buffer in order to end up from a pH of 7.5 to a 6.0. The CSP and HSQC from this experiment is presented in **Fig. 4.29**. The overall motif of the CSP plot versus the residues appears to be similar to the initial titration with α B, however, we observe that the chemical shifts in **Fig. 4.28**, are not arising from the pH change as in **Fig. 4.29** it is obvious that there is a high effect of pH in the primary sequence of $A\beta_{40}$ in almost all the residues of the N-terminus (i.e. resonances A2-F19), but also for residues of the C-terminus, like D23, D27 and V40.

4.7.2. Binding Interactions of $A\beta_{40}$ with α B-WT and Cu^{2+}

It was shown previously (Ahmad *et al.* 2008; Danielsson *et al.* 2007), that copper targets both $A\beta_{40}$ and α B. It is known that in AD, the ion homeostasis is damaged, and high concentrations of copper are present. $A\beta_{40}$ is a metalloprotein, which binds copper with an affinity of nanomolar at the N- and C-terminus. This binding induces the redox chemistry and neurotoxicity. Additionally, $A\beta_{40}$ produces ROS through the reduction of copper II to copper I (Hatcher *et al.* 2008; Danielsson *et al.* 2007). Moreover, copper can act as a modulator of the chaperone activity of α B, which has a picomolar affinity to copper. Copper affects the secondary structure and the oligomeric size of α B, which is also able to reduce copper-mediated formation of ROS, and that way to promote cytoprotection under conditions stressful for the cells (Mainz *et al.* 2012; Prabhu *et al.* 2011; Biswas and Ras 2008; Ahmad *et al.* 2008; Reif and Narayanan 2007; Ganadu *et al.* 2004). Therefore, titration studies of $A\beta_{40}$ with $\text{Cu}(\text{Gly})_2$ were carried out in the presence and the absence of α B in order to understand the mechanism of interaction between the three molecules.

As shown in the representative 1D and 2D spectra in **Fig. 4.30A-C**, increasing copper concentrations are bleaching the majority of the peaks, which could be explained by the solvent PRE phenomenon induced by copper. Solvent PREs arise from random collisions between a macromolecule and paramagnetic molecules, in this case, $\text{Cu}(\text{II})$. The enhanced relaxation in case of interaction, causes line broadening and peaks disappear or bleach. The 1D spectrum on top of each spectra shows directly that there is a signal drop in intensity in absence of α B, which however, remains less affected in presence of α B.

By observing the shift in the inflection point (presented as a dashed black line in **Fig. 4.30D,E**) resonances get bleached with higher molar ratios in the presence of α B. Employing only monomeric $A\beta$, we plotted the relative peak intensities as a function of copper to $A\beta$ molar ratio and a significant signal loss already at equimolar concentrations of the complex was observed (**Fig. 4.30F**). Further, looking at specific residues revealed that residues in the N-terminus are stronger affected by the copper interaction in the titration series. However, in the presence of 7.5 fold α B, signal attenuation was detected only at molar ratios beyond 1 to 4 ($A\beta:\text{Cu}(\text{Gly})_2$) (**Fig. 4.30G**). The drop of intensity in the presence of four fold $\text{Cu}(\text{Gly})_2$ is attributed to an altered equilibrium between the molecules and an interaction of soluble $A\beta$ with Cu^{2+} complexed to α B. $A\beta$ chemical shifts do not change in the presence of Cu^{2+} , indicating that Cu^{2+} might stabilize α B in its high-oligomeric state. In turn, $A\beta$ molecules associate to and dissociate from the α B/ Cu^{2+} complex, which induces a signal drop due to line broadening as a result of the slow tumbling regime.

Continuous addition of Cu^{2+} to the complex increases the the PRE phenomenon, which further attenuates $\text{A}\beta$ signal intensities.

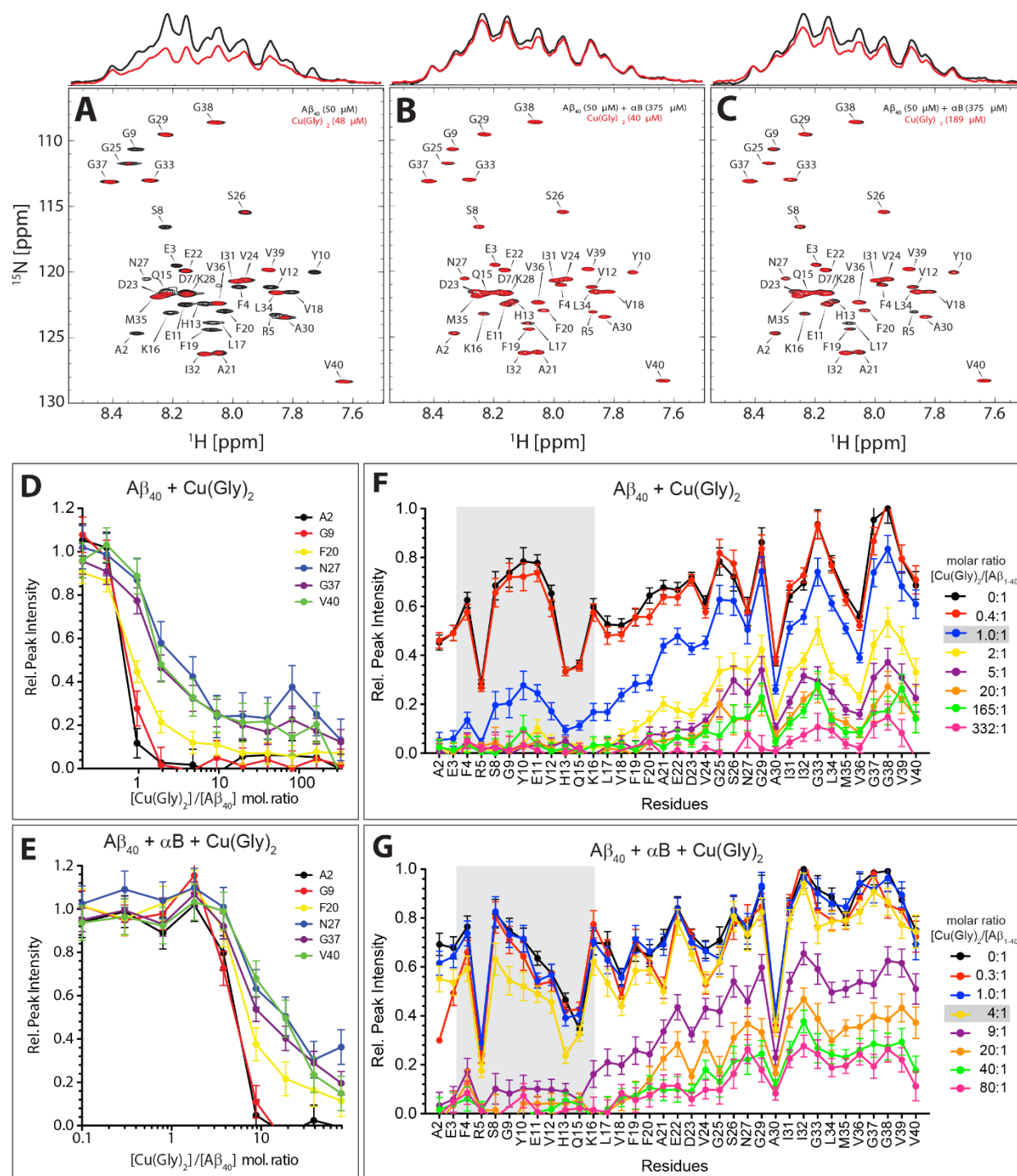


Fig. 4.30. Quantification of $\text{A}\beta_{40}$ titrations with $\text{Cu}(\text{Gly})_2$. (A) ^1H , ^{15}N SOFAST HMQC overlay of the 1D and 2D titration spectra of $\text{A}\beta_{40}$ reference spectrum (50 μM , black) with $\text{Cu}(\text{Gly})_2$ (48 μM), (B) $\text{Cu}(\text{Gly})_2$ (40 μM) and αB (375 μM), and (C) $\text{Cu}(\text{Gly})_2$ (189 μM) and αB (375 μM). On the top of the figures, the first increments of the respective 2D spectra are plotted. In (B) 375 μM of αB was added to a monomeric $\text{A}\beta_{40}$ sample. Addition of $\text{Cu}(\text{Gly})_2$ in a ~ 1 to 1 molar ratio displayed no significant spectral changes, as opposed to (A). Bleaching of resonances were observed at molar ratios beyond ~ 1 to 4 ($\text{A}\beta_{40}:\text{Cu}(\text{Gly})_2$), as shown in (C). In (D) and (E) the relative peak intensities for several residues are plotted as a function of the $\text{Cu}(\text{Gly})_2$ concentration for two $\text{A}\beta_{40}$ samples (50 μM), in the absence and presence of αB (375 μM), respectively. As apparent from the shift

of the inflection point and from curve fitting, the dissociation constant, K_d , was determined to be about 20×10^{-6} M in (D, $A\beta_{40}$ only) [5] and 200×10^{-6} M in (E, $A\beta_{40}/\alpha B$). In (F) and (G) the relative peak intensities are plotted as a function of the primary sequence of $A\beta_{40}$, using either the $A\beta_{40}$ or the $A\beta_{40}/\alpha B$ sample, respectively. Evidently, the drop of signal intensities occurs already at a $\sim 1:1$ molar ratio ($A\beta_{40}:\text{Cu}(\text{Gly})_2$), employing the $A\beta_{40}$ sample, whereas signals disappear in the $A\beta_{40}/\alpha B$ sample at a molar ratio larger than 1:4. Furthermore, both reference curves in (F) and (G) show intensity differences in absence of $\text{Cu}(\text{Gly})_2$. However, the most severe signal attenuations occur for N-terminal residues, in both samples. All intensities were extracted from 2D spectra. The error bars were set to two times the standard deviation of the spectral noise. The experiments were performed at a ^1H Larmor frequency of 500 MHz (11.7 T) and 277 K, and the samples were prepared in a 100 mM PBS buffer.

4.7.3. Binding Interactions of $A\beta_{40}$ with $\alpha B-6E$

Because $A\beta$ binds to αB -WT, we would like to investigate whether the amyloid peptide binds also the $\alpha B-6E$ mutant. Therefore, a titration of $\alpha B-6E$ to $A\beta$ was also performed in solution-state NMR using different ratios (8x, 4x, 2x, 1x and 0.5x $\alpha B-6E$ to $A\beta$) between the two proteins, starting with 50 μM for the amyloid peptide in 100 mM PBS buffer. In this case ^1H , ^{15}N SOFAST HSQC spectra were recorded and presented here in an 8 to 1 molar ratio of $\alpha B-6E$ to $A\beta$ (Fig. 4.31A) showing that there are chemical shifts for residues A2, D7, S8, Q15, H14, K16 and L17 and that the peaks for residues R5, S26 and N27 disappeared upon addition of the mutant. The intensity ratios and the relative intensities of the two proteins are also plotted (Fig. 4.31B,C) and suggest that there is a signal loss of about 50% from the reference data indicating a binding which is further supported by calculating the CSP as a function of residues (Fig. 4.31D) especially in the N-terminus in the region V12 – L17.

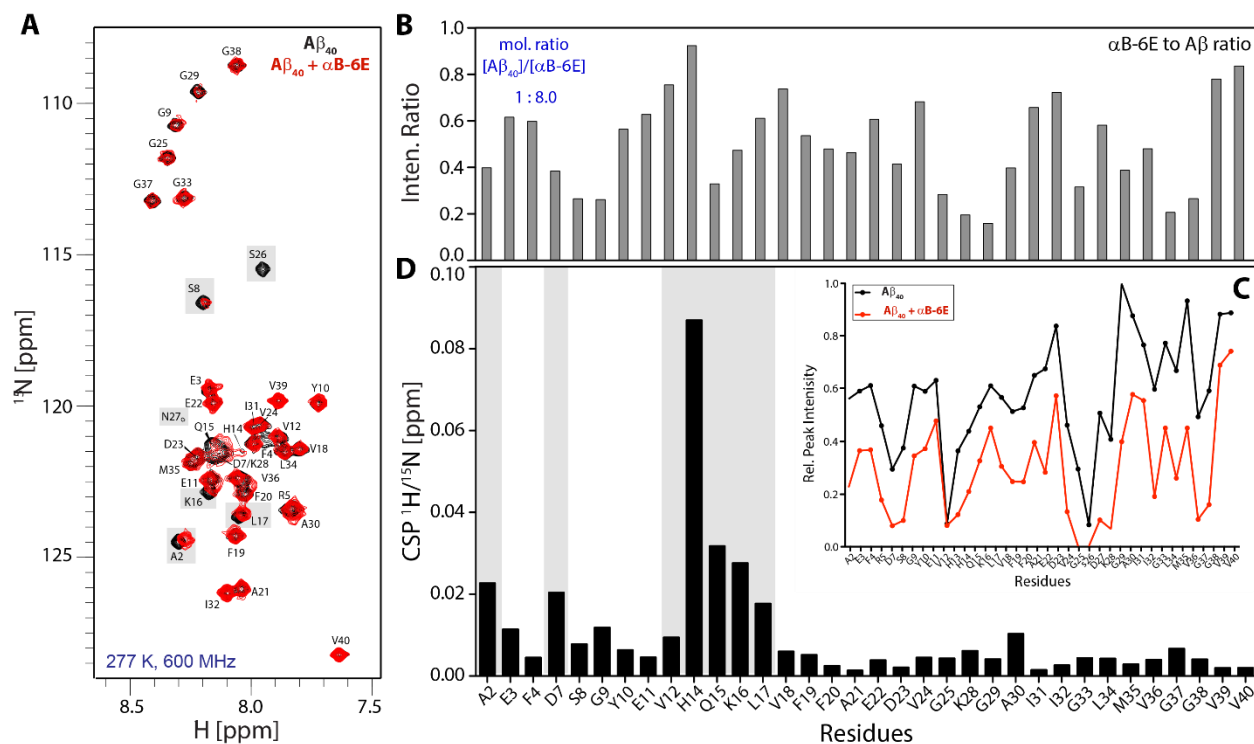


Fig. 4.31. ^1H , ^{15}N chemical shift perturbations (CSPs) of $A\beta_{40}$ upon $\alpha B-6E$ binding. (A) ^1H , ^{15}N SOFAST HSQC 2D spectra of solubilized $A\beta_{40}$ monomers in absence (black) and presence of $\alpha B-6E$ (red). The molar ratio of $\alpha B-6E$ to $A\beta_{40}$ is presented here as a function of residues. (B) Relative peak intensities versus the residue number of the two samples show also a about 50% dropping of signal of $A\beta_{40} + \alpha B-6E$ sample. (C) Relative peak intensities versus the residue number of the two samples show also a about 50% dropping of signal of $A\beta_{40} + \alpha B-6E$ sample. (D) The CSP at a molar ratio of 8 to 1 [$\alpha B-6E/A\beta_{40}$] is plotted as a function of the primary sequence of $A\beta_{40}$. Clearly, a clustering of perturbations was observed at the N-terminus of $A\beta_{40}$, indicating the binding interface between $A\beta_{40}$ and $\alpha B-6E$, in a low oligomeric state. Residues involved in the binding interaction are labeled with grey boxes. The monomeric $A\beta_{40}$ concentration was 50, while the $A\beta_{40} + \alpha B$ sample had an eight times fold higher concentration. The samples were all prepared in a 100 mM PBS buffer, pH 7.3. All experiments were performed at 600 MHz and 277 K.

4.8. α B uses Different Interfaces to Capture an Amorphous and an Amyloid Client

Due to the large molecular weight and the heterogeneity of α B, solution-state NMR and crystallographic approaches are not, however, suited to address questions regarding the protein's binding sites with substrates. On the other hand, solid-state NMR requires a co-precipitate to obtain a suitable sample. As the interaction between a misfolding peptide or protein and a chaperone is rather weak, co-precipitation works only in case an excess of the amyloidogenic protein is employed. It was established therefore an approach, termed FROSTY (Freezing Rotational diffusion Of protein Solutions at low Temperature and high viscosity), which allows us to investigate soluble protein complexes in solution employing magic-angle spinning (Mainz *et al.* 2009).

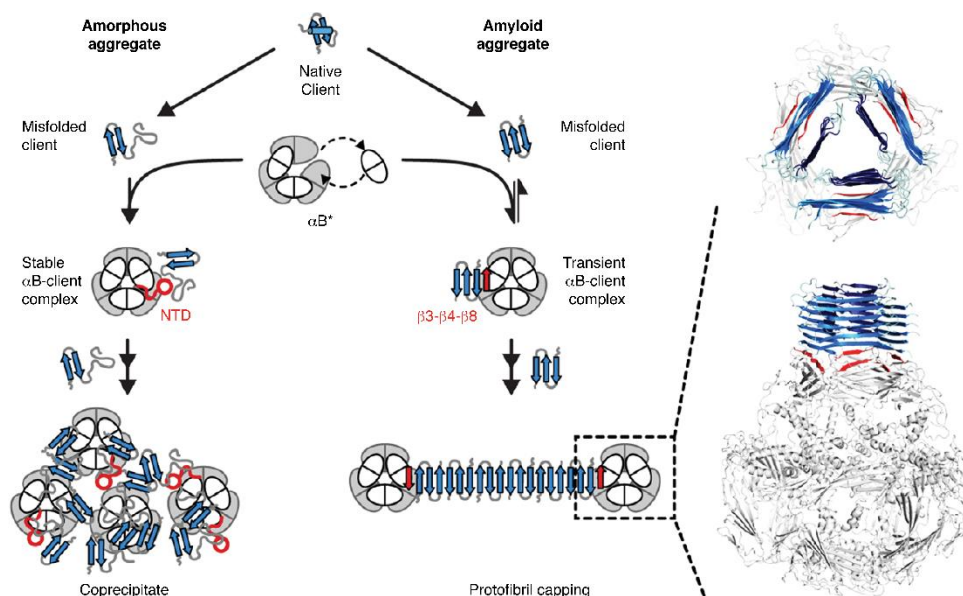


Fig. 4.32. Model of α B-mediated inhibition of amorphous and amyloid aggregation. Destabilized proteins may self-associate due to the exposure of hydrophobic segments. The asterisk denotes that α B potentially undergoes subunit exchange (monomers/dimers), which has been reported to be an important property for chaperone function. The structural plasticity of α B, in particular that of its partially disordered NTD, facilitates binding of structurally undefined clients in a stable and soluble α B-client complex, and thereby suppresses a morphous aggregation. Saturation of the holdase causes larger α B-client clusters that may finally co-precipitate. Amyloidogenic clients have pronounced β -strand propensity. α B targets the hydrophobic β -strand core of amyloid species by interacting transiently with protomers as well as with pre-fibrillar assemblies thereby impeding fibril nucleation and fibril elongation, respectively. The β -sandwich core of α B (in particular the edge strands β 3, β 4 and β 8) can be viewed as a structurally related unit that mimics the cross- β structure of amyloid systems and that is well suited to adhere, e.g. to the ends of protofibrils as illustrated in the showcase docking model (top and side view). The three-fold symmetric $A\beta_{40}$ fibril adopts β -strand conformation for residues 11–22 (light blue), including the hydrophobic core $L^{17}VFFA^{21}$, and residues 30–37 (dark blue). For simplicity, α B is shown in grey and the β 4– β 8 strands of the extended conformers of one hexamer are highlighted in red. Reproduced with permission from the Nature Publishing Group (Mainz *et al.* 2015).

Previous studies have shown that α B interacts with a wide range of client proteins that either form amorphous (disordered) or amyloid (ordered) aggregates (Treweek *et al.* 2015; Shammas *et al.* 2011; Houck *et al.* 2011; Regini *et al.* 2010; Waudby *et al.* 2010; Ghosh *et al.* 2007; Rekas *et al.* 2004). It has been suggested that the chaperone mechanism is distinct for amorphous and amyloid aggregation pathways (Treweek *et al.* 2015; Kulig *et al.* 2012; Raman *et al.* 2005). Several regions of α B have been identified to be involved in client binding, e.g. residues W9–P20 and S43–P58 of the NTD, as well as residues D73–K92 (β 3– β 4) and L131–V142 (β 8) of the ACD (Ghosh *et al.* 2006; Bhattacharyya *et al.* 2006; Ghosh *et al.* 2005).

Those results have been obtained either by site-directed mutagenesis or by studying the chaperone capabilities of isolated peptides. The large molecular weight and conformational diversity, however, have hampered further structural insights into α B–client complexes.

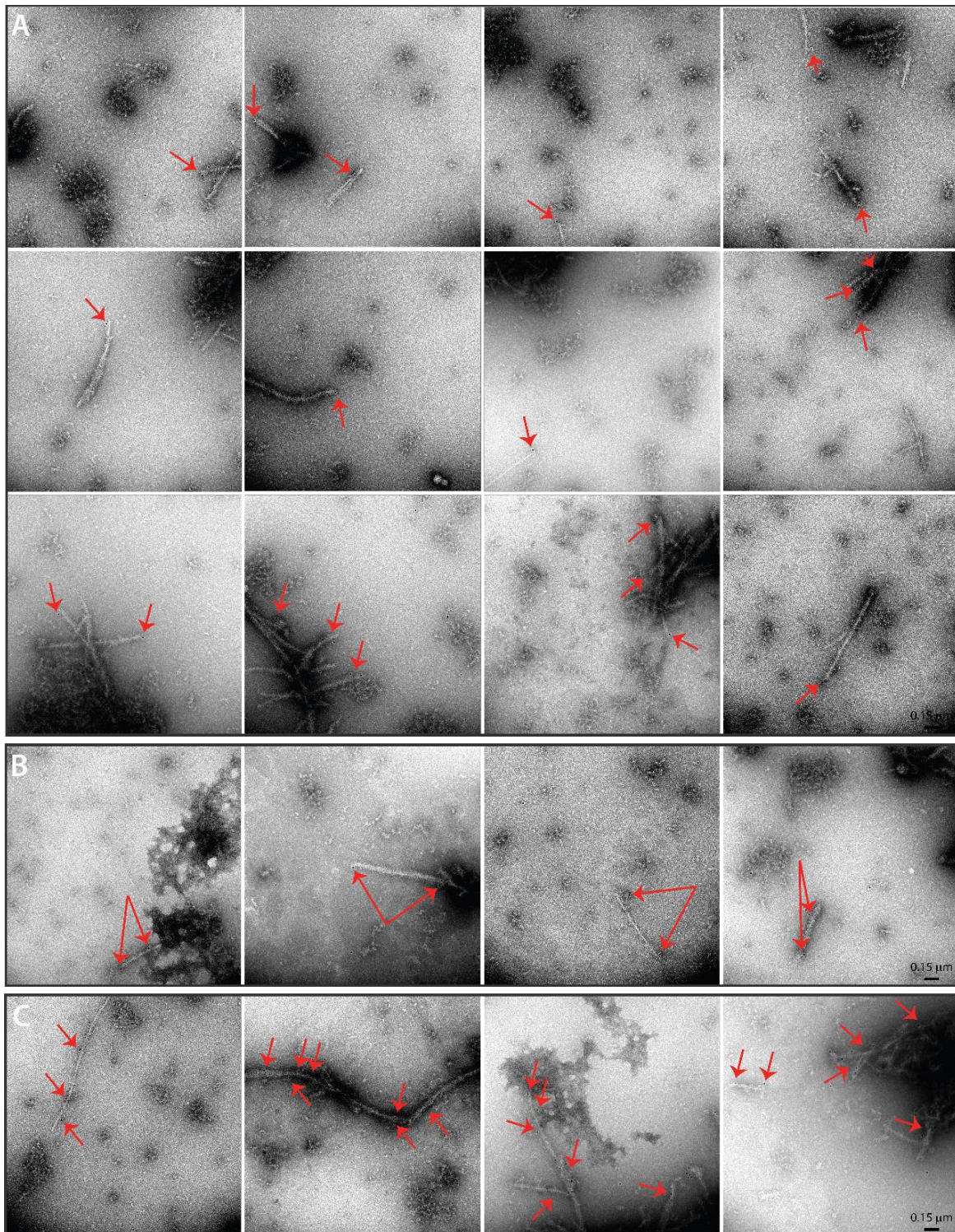


Fig. 4.33. Representative immunoelectron microscopy images of $A\beta_{40}$ fibrils in the presence of α B. In the figure α B is bound (A) to the one end and to (B) both ends of the fibrils, while in (C), α B binds along the entire $A\beta_{40}$ fibrils. 150 μ M of $A\beta_{40}$ fibrils were prepared and incubated in

presence of 15 molar excess of A β ₄₀ to α B. The mixtures were centrifuged at 16.000 xg for 30 min, and the pellets were resuspended and treated as described in Materials and Methods section. Red arrows indicate the presence of α B as a small black dot. All scale bars represent 0.15 μ m and the magnification was set at 71 k for all images.

We found that proton detected ¹H, ¹⁵N correlation spectra yield two sets of resonances, which reflect the heterogeneous architecture of α B and the possible role of asymmetry in its dimeric building block. Heteronuclear correlation spectra yielded only degenerate chemical shifts. CSP and PRE interaction studies showed that the fibril-forming Alzheimer's disease A β ₄₀ peptide preferentially binds to a hydrophobic edge of the central β -sandwich of α B. By contrast, the amorphously aggregating client lysozyme is captured by the partially-disordered N-terminal domain of α B (Fig. 4.32). We suggest that α B utilizes its inherent structural plasticity to expose distinct binding interfaces to interact with a wide range of structurally variable clients (Mainz et al. 2015).

Based on this study we decided to investigate further the interaction of these species, and whether fibril binding serves as a generic chaperone mechanism. So, we tried to prove *in vitro*, if α B actually binds the A β ₄₀ amyloid protofibrils by capping them at the end of each fibril as suggested in Mainz et al. (2015). Therefore, starting with monomeric and not seeded A β ₄₀ (as shown by Shamma et al. 2010), fibrils were grown at 37 °C under agitation for 4 days in presence (various ratios were used) and absence of the chaperone. The samples were negatively stained with uranyl acetate and observed under TEM. The fibrils showed a morphology similar to that typically observed for A β fibrils (Fändrich et al. 2009) (Fig. 4.27A). By contrast, the α B oligomer was less readily resolved, due to its smaller relative size, and the fact that many α B molecules were overlapped with the fibrils. Therefore, the samples were immunolabeled with an antibody directed against α B, which was then stained with a secondary antibody conjugated to 10 nm gold nanoparticles (see also Chapter 3.2.2.15.3). Representative immunoelectron micrographs of A β ₄₀ fibrils incubated with α B (Fig. 4.33) show α B to be associated with the fibrils, with gold nanoparticles (labeled as a black dot in the images) restricted mostly at the one end of the fibrils (Fig. 4.33A), with apparent periodicity, while there is also occasional binding along the entire length (Fig. 4.33C), or capping to both ends of the fibrils (Fig. 4.33B), observed.

4.9. PEGylation of wild-type α B-Crystallin

During the process of PEGylation, the covalent conjugation of a PEG derivative onto molecules, improves the water solubility and biocompatibility of those molecules, which can be a beneficial feature for protein drug development (Hutanu et al. 2014). There are currently about one dozen of PEGylated pharmaceuticals on the market with FDA approval. These products include PEGylated enzymes, monoclonal antibodies, glycoproteins, cytokines, human growth hormones, aptamers, synthetic peptides, and liposomes.

Here, a 10 kDa linear methoxy PEG Succinimidyl Carboxymethyl Ester that enables simple and efficient modification of proteins and other biological agents that contain lysines, was dissolved in DMSO and attached to the amines of the lysines of α B-crystallin. Full-length α B has in total 10 lysines. Upon addition of the PEG, the exact amount of lysines that will bind to the PEG are now known, however, it is expected that the size of the molecule should increase and solid-state NMR could be applied in order to test the sample.

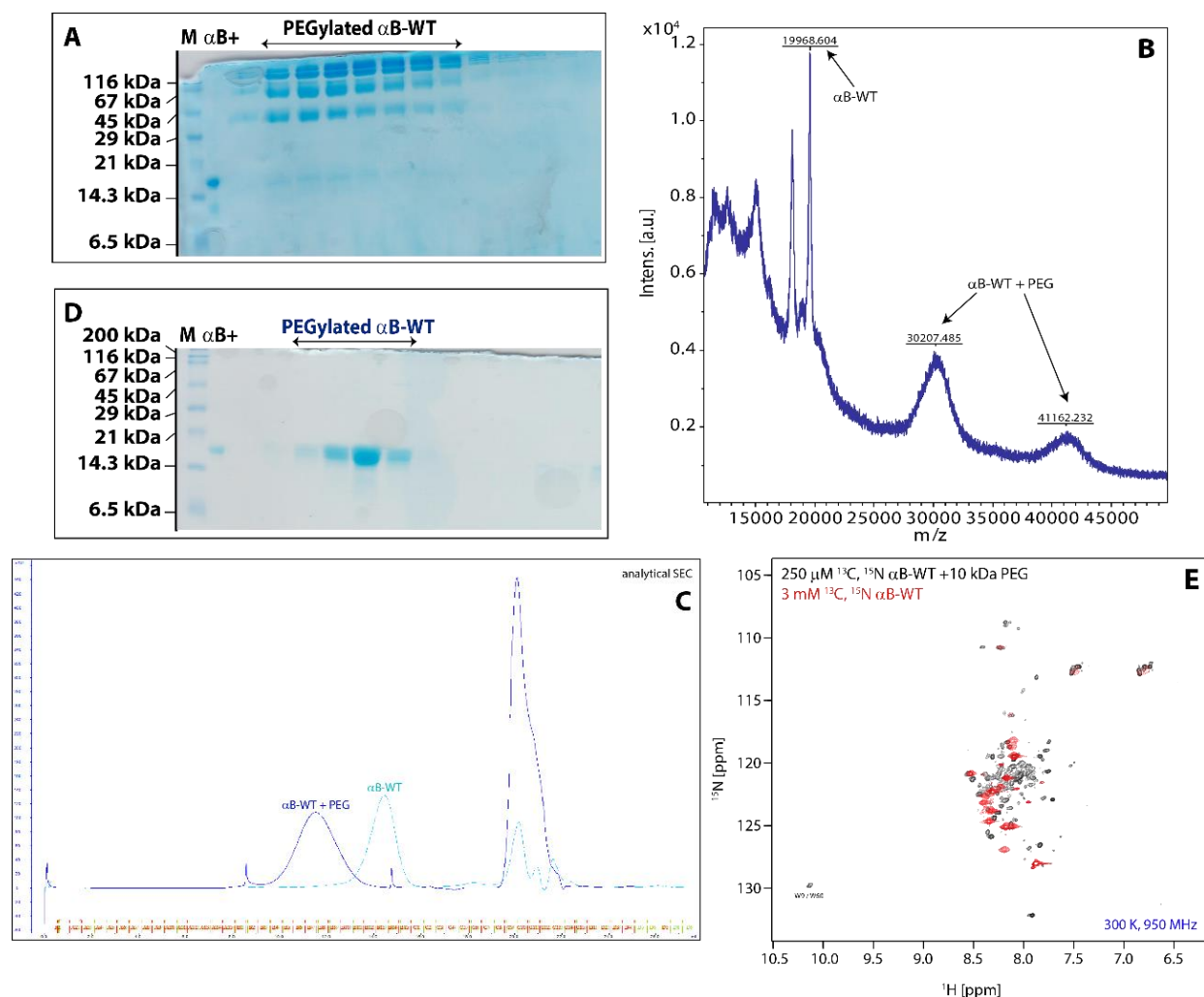


Fig. 4.34. PEGylation of α B-crystallin. **(A)** SDS-PAGE gel for the reaction mixture of α B and the PEG. **(B)** Mass spectrometry shows that the reaction was successful. **(C, D)** Analytical SEC and SDS-PAGE gel of the PEGylated α B. **(E)** ^1H , ^{15}N HSQC overlay of the wild-type and the PEGylated α B. Spectra were recorded at 300 K and 950 MHz

In this case the reaction of the PEG with α B was performed for 1 hr at room temperature as described in chapter 3.2.2.12. The reaction mixture was run on a SDS gel (**Fig. 4.34A**) that showed that three additional bands higher than the wild-type protein (20 kDa) appear at about 45, 60 and 120 kDa each. In addition, mass spectrometry suggested that the reaction was carried out successfully (**Fig. 4.34B**). The sample was further purified by analytical size exclusion (**Fig. 4.34C,D**), which also showed that compared to the wild-type protein there is a shift in the elution of the PEGylated- α B. PEGylated- α B elutes at about 10 ml, whereas the non-PEGylated protein at 14 ml, indicating again that the molecular size of the protein increased. Therefore, a FROSTY sample of the PEGylated- α B was prepared in a 3.2 mm rotor and measured at 750 MHz, however, the spectra showed that the sample could not sediment and the ^{13}C - ^{13}C PSDS there were no cross-peaks at all (data not shown). The same sample was reused afterwards in solution-state NMR. An overlay of the PEGylated- α B and the α B-WT is presented in **Fig. 4.34E** and shows that the PEGylated- α B appears smaller in size than the full-length protein and this could be an explanation why in the solid-state spectra we do not observe any cross-peaks. If the protein is too small then the molecular tumbling is faster and it cannot sediment into the rotor, while it is being ultra-centrifuged. In

the wild-type spectra we observe always only the C-terminal domain that is unstructured in α B. However, here, while the PEG binds the lysines' amines, it seems that it is unfolding the protein in the N-terminus as we can observe in the HSQC spectra at about 10 ppm the two tryptophans (W9 or W60) that the whole α B-WT contains. N-terminus is then exposed, becomes more flexible and therefore, we detect additional peaks in the spectrum.

4.10. α A-crystallin: NMR Study of the Dynamic Part of a Redox-sensitive sHsp

The study of human α A-crystallin was carried out in collaboration with Prof. Weinkauf's group (TU, Munich). Labeled samples used in this work, were grown and expressed in our group, while the purification of the wild-type or truncated α A was performed by Dr. Christoph Kaiser (TU Munich). The data presented here are to be published.

4.10.1. Biochemical Studies on the Reduced and Oxidized state of α A

Cryo-TEM micrograph of the human α A recorded on a FEI Titan TEM with Gatan K2 GIF suggested that the protein is polydisperse and displayed mostly elongated, as well as round classes compared to α B-crystallin. After reconstruction of D3-, D4- and D5-symmetric barrel-shaped oligomer states, assuming a rod-like basic architecture, it was concluded that the α A oligomer is a barrel-shaped assembly of tetrameric building blocks, where each tetramer consists of two N-terminally linked dimers and at the equator, the tetramers are linked by C-terminal interactions, whose abundance depends on the oligomer size (Kaiser et al. in preparation).

Oxidation is considered to be a major physiological challenge to lens proteins. The lens appears to be subjected to increasing oxidative stress with aging because of the progressively weakening antioxidant system. α A-crystallin, as mentioned previously, contains only two cysteine residues susceptible to oxidation, at positions 131 and 142, in a distance of about 8.78 Å from each other (Fig. 4.35A). These Cys are oxidized in advanced cataracts and studying the role of oxidation in lens aging is possible by oxidation of SH- groups in α A *in vitro*, where an intramolecular disulfide bond is formed at a sufficiently high redox potential. In this case, the oxidation reaction is very slow, however, the chaperone is more active and intramolecular disulfide-bonded α A is differentially active towards the model substrates malate dehydrogenase (MDH), citrate synthase (CS) or the p53 DNA-binding domain. Moreover, it has a different tertiary and quaternary structure and is larger and more dynamic than the reduced form of α A (Kaiser et al. in preparation).

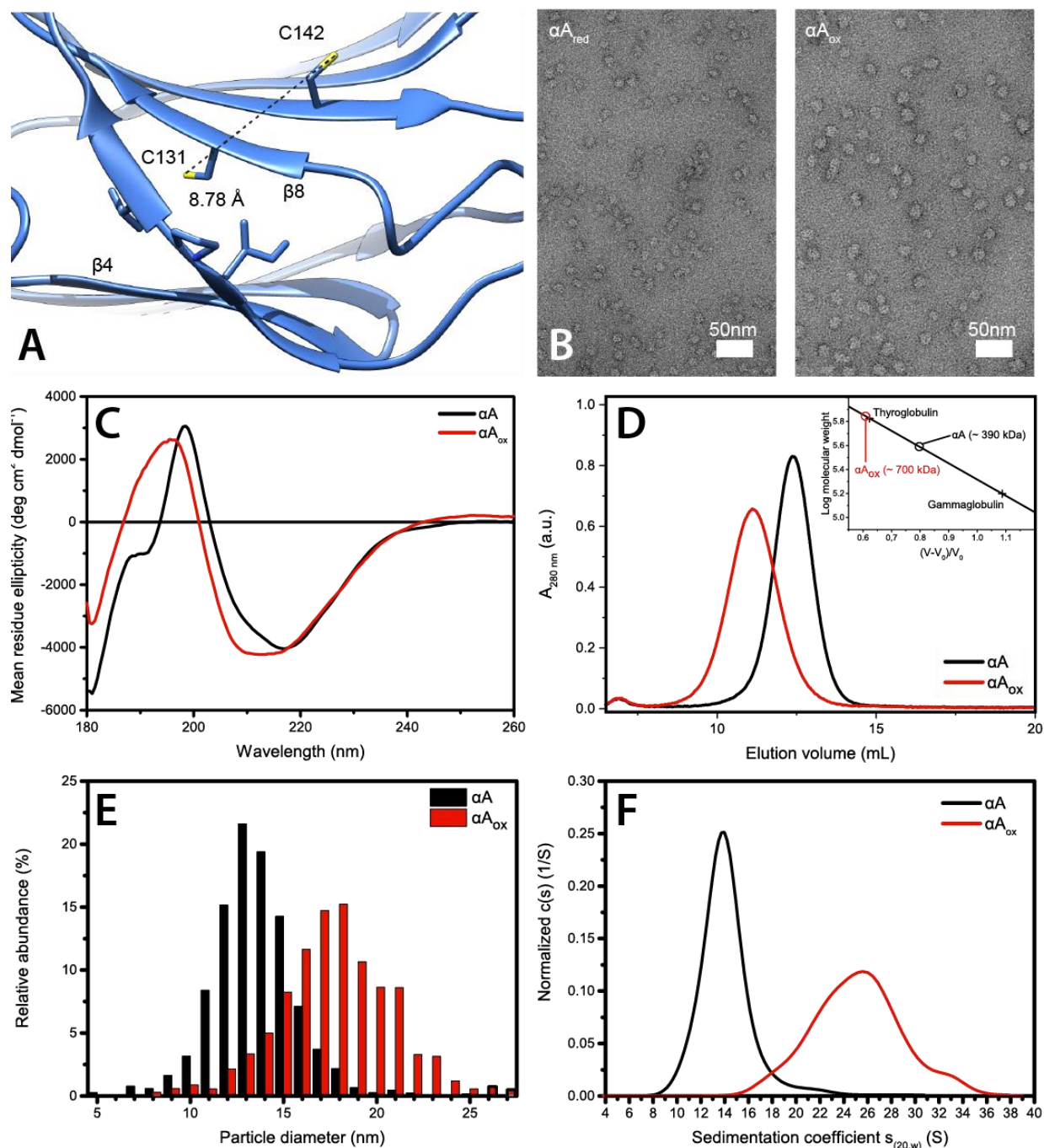


Fig. 4.35. Biochemical experiments comparing reduced and oxidized αA . (A) The two cysteines (131 and 142) are located at a distance of 8.78 Å. (B) EM images of the reduced (left) and the oxidized (right) state of αA . (C) CD spectra shows that the overall secondary structure of αA_{ox} is preserved. (D) Elution profile of the analytical SEC of the reduced and oxidized αA shows that αA_{ox} elutes earlier than its reduced form. (E, F) Disulfide formation affects the oligomer state. The oligomer diameter increases by 30 %, correlating well to a doubling in apparent molecular weight and an increase from 13S to 25S in SV-AUC experiments is observed. In all figures the reduced and oxidized forms are presented in black and red, respectively. The data were kindly provided by Dr. C. Kaiser (TU München).

CD spectra suggest that both states of αA are folded and its overall secondary structure is preserved (Fig. 4.35C), while in negative stained electron microscopy images of the reduced (αA_{red}) and the oxidized (αA_{ox})

form of αA at the same scaling (50 nm), the oxidized state appears to have a higher molecular weight than the reduced (Fig. 4.35B). These data are further supported by analytical SEC (Fig. 4.35D), where the oxidized form is eluting earlier at about 10.5 ml than the reduced form that elutes at around 13 ml, and by sedimentation velocity (SV) – AUC experiments (Fig. 4.35F), where the sedimentation coefficient of αA_{ox} is shifted to 25S, while the αA_{red} is shifted to 13S. Additionally, the disulphide bond affects the oligomer state as the oligomer diameter is increased by 30 %, correlating well to a doubling in apparent molecular weight and the increase from 13S to 25S in SV-AUC experiments (Fig. 4.35E) (Kaiser *et al.* in preparation).

4.10.2. Backbone and Side-chain Assignments of the wild-type αA

Recently, two crystal structures of truncated bovine (Laganowsky *et al.* 2010a) and zebrafish αA -crystallin (Laganowsky *et al.* 2010b), lacking the NTD, but containing part of the C-terminal extension, have been solved. However, human αA is a not well-studied protein and not much is known regarding its structure or mechanism of action.

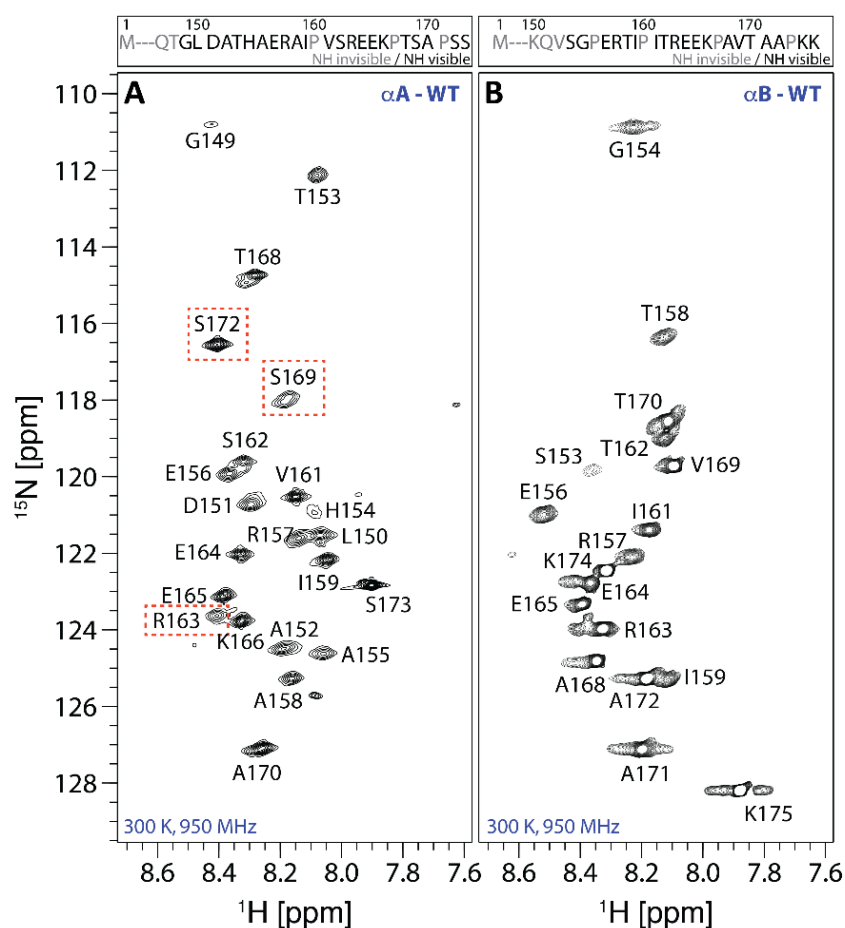


Fig. 4.36. Assignment of the backbone resonances of the human wild-type αA - and αB -crystallin in solution. ^1H - ^{15}N HSQC spectra of (A) αA -crystallin and (B) αB -crystallin (assignment for αB is taken from Mainz *et al.* (2015) showing the assignment of the flexible part of the C-terminal domain of each chaperone. The assignments are labeled by the one-letter code of amino acids accompanied by a sequence number. The assigned resonances (G149-S173 and S153-K175 for αA and αB , respectively) are drawn in black, while non-visible residues are in grey (inset, top). Residues S162, R163 and S169 that were assigned differently by Carver and coworkers are highlighted by red dashed boxes. All measurements were recorded at 950 MHz and 300 K.

Since α -crystallins exist in very large molecular weight oligomeric complexes, conventional solution-state NMR is not appropriate to yield high-resolution structural information to understand the structure/function aspects of these chaperones. However, as the CTD of α -crystallins is highly flexible, unpolar, unstructured and solvent accessible, CTDs give rise to well-resolved solution-state NMR spectra and have been the focus of various studies (Carver 1999; Carver and Lindner 1998; Carver *et al.* 1994, 1992). The CTDs are critical for chaperone activity (Morris *et al.* 2008; Treweek *et al.* 2007; Fernando and Heikkila 2000; Kamei *et al.* 2000; Lindner *et al.* 1998) and for oligomer formation assembly (Treweek *et al.* 2007; White *et al.* 2006; van Montfort *et al.* 2001a).

As a first step towards the structural characterization of the CTR of the human α A and in order to examine the backbone dynamics of α A in solution, we recombinantly expressed and purified human α A uniformly labeled ([U-]) with ^{13}C and ^{15}N . We next interrogated the conformations and dynamics of the CTR using NMR spectroscopy. Using [U- ^{13}C , ^{15}N]- α A, we recorded a two-dimensional (2D) ^1H , ^{15}N heteronuclear single quantum coherence (HSQC) spectrum at pH 7.4, which correlates the chemical shifts of ^1H nuclei that are covalently attached to ^{15}N nuclei (e.g., amide and amine bonds) (Fig. 36A). The protein sample in this study consists of 173 native residues and contains no additional affinity tags or extra residues. The buffer chosen for the assignment experiments was 10 mM HEPES/KOH pH 7.4, 1 mM EDTA and 2 mM DTT.

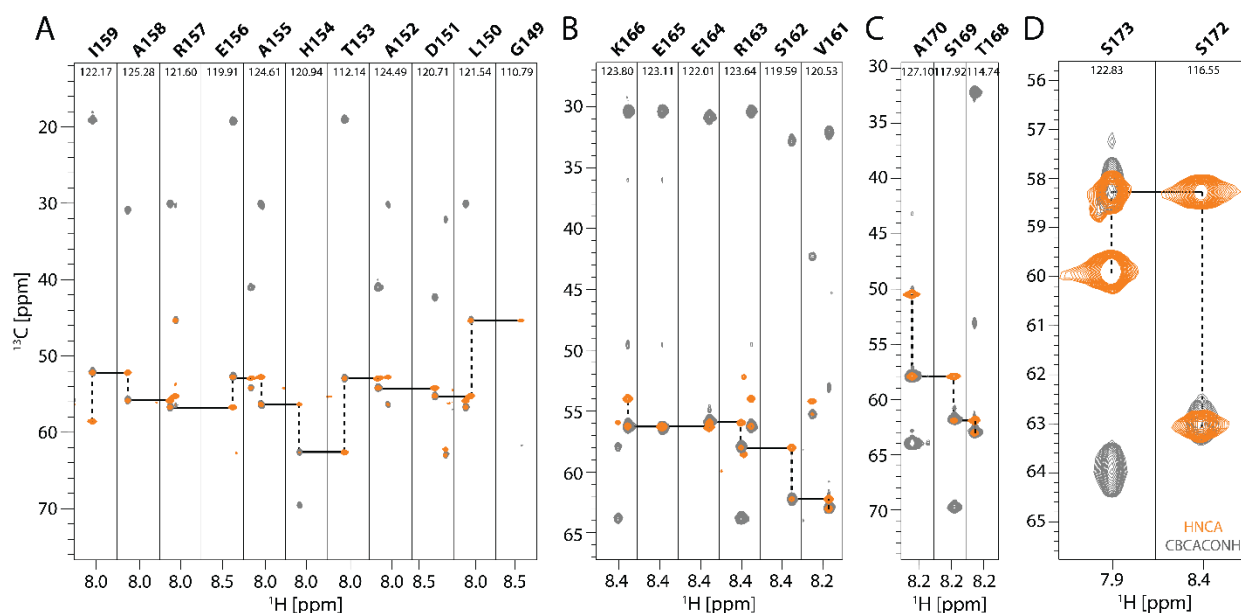


Fig. 4.37. HNCA (orange) and CBCA(CO)NH (grey) strip plots. Residues G149 - I159 (A), V161-K166 (B), T168-A170 (C) and S172-S173 (D) constituting the beginning of the CTD are shown. The ^{15}N chemical shift of residue i is shown on the top of each plot. The sequential walk along the protein backbone is illustrated by black solid lines representing the inter-residual connectivities to $\text{C}\alpha_{i-1}$ of the preceding residue. Dashed lines complete the trace by connecting the two HNCA correlations for the $\text{C}\alpha_i$ and the $\text{C}\alpha_{i-1}$ atoms. All measurements were recorded at 950 MHz and 300 K.

We observed sharp resonances with limited dispersion in the ^1H dimension, indicating that these resonances arise from dynamically disordered residues lacking a fixed tertiary structure. In order to assign the observed resonances to specific α A residues, we recorded three-dimensional (3D) NMR spectra from [U- ^{13}C , ^{15}N]-labeled α A that correlate ^{13}C , ^{15}N , and ^1HN chemical shifts of neighboring amino acids, whose

nuclei are linked through a network of covalent bonds (Sattler *et al.* 1999). This allowed us to unambiguously assign the observed resonances to residues G149–S173 (Fig. 36A), i.e. the complete CTD, and part of the ACD. Proline residues at positions 160, 167 and 171 could not be assigned due to the lack of an amide proton and the application of $^1\text{H}^{\text{N}}$ based assignment experiments. In contrast, in a previous study by Carver and co-workers (Treweek *et al.* 2010), only residues A158–S173 had been assigned using a ^{15}N -labeled sample and ^1H , ^1H TOCSY, ^1H , ^1H NOESY and ^1H , ^{15}N HSQC-TOCSY experiments (Sattler *et al.* 1999). The sequential assignment of the CTD of αA is presented in Fig. 4.37, showing representative HNCA/CBCACONH strips of the G149–I159. Fig. 4.37B–D show the sequential assignments for residues R163, S169 and S172 (highlighted in Fig. 4.36A in red dashed boxes), which were differently assigned by Carver and coworkers (Treweek *et al.* 2010). For a comparison between the two human sHsps, Fig. 4.36B represents additionally the 2D ^1H , ^{15}N HSQC spectrum of the human wild-type αB -crystallin at pH 7.4. Cross peaks are labeled with their respective backbone resonance assignments, which are obtained for the flexible C-terminal region that comprises the last 20–25 residues of each protein. NMR assignments for αB were provided from Mainz *et al.* (2015).

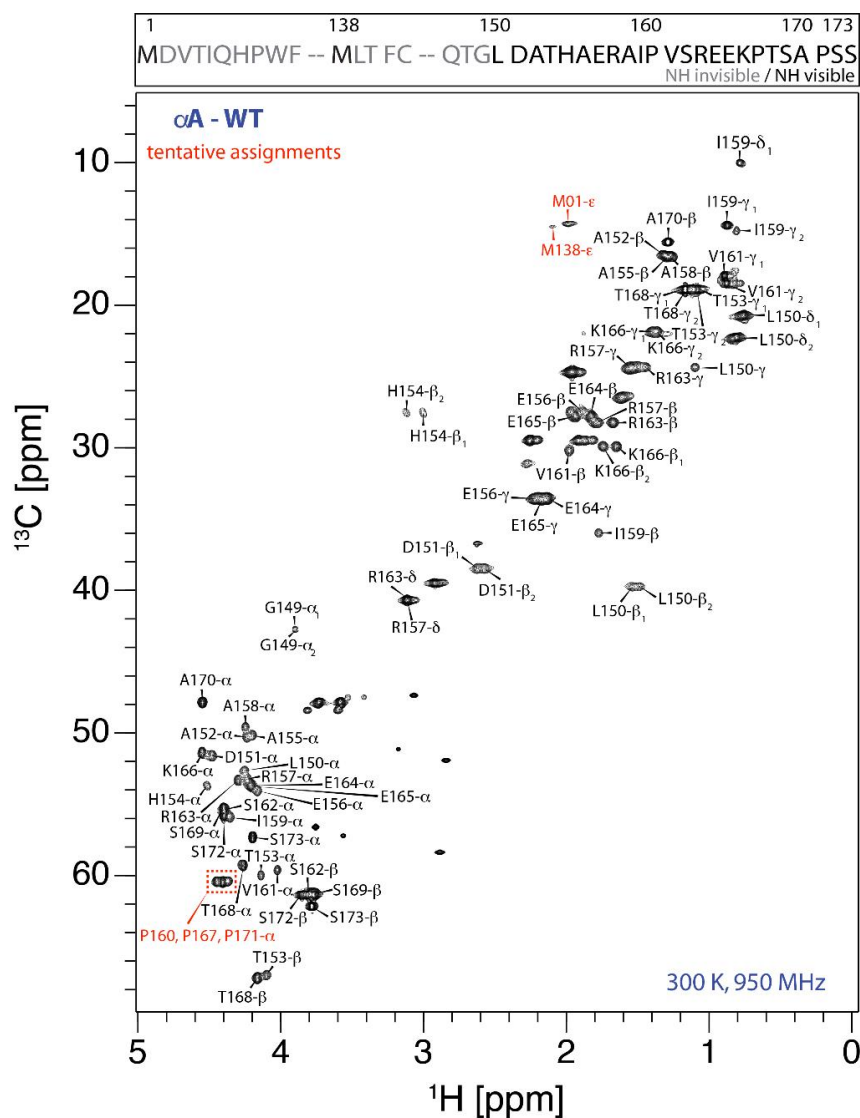


Fig. 4.38. Side chain assignments of the human wild-type αA -crystallin in solution. Assignments were obtained from H(C)CCONH and (H)CCONH experiments. Tentative assigned residues are represented in red. Assignments experiments were recorded at 950 MHz and 300 K.

In **Fig. 4.38**, we further present the side chain assignment of full-length α A involving the CTR that will be important for substrate binding experiments in the future. A table with the ^1H , ^{13}C and ^{15}N chemical shifts for H_N , N_H , H_α , C_α , C_β , C' is presented in the appendix in **Supp. Table S5**. The unassigned cross-peaks in both HSQC spectra (**Fig. 4.36, 4.38**) presumably arise from residues with enhanced flexibility within or outside of the CTD of α A. The amino acids G149-A158 are of particular importance as they are in direct proximity to the IPV motif, responsible for chaperone function. These data therefore reveal that the final 23 residues of α A, including the IPV motif, are predominantly disordered in solution.

The secondary structure of the CTD of α A was predicted from the difference between the chemical shift values of $^{13}\text{C}_\alpha$, $^{13}\text{C}_\beta$ atoms (**Fig. 4.39A**) (Spera and Bax 1991) and the corresponding chemical shift index (CSI 3.0; Hafsa *et al.* 2015) (**Fig. 4.39C**). **Fig. 4.39B** shows a plot of the predicted order parameters (S^2), on the basis of the random coil index (RCI) (Shen and Bax 2012; Shen *et al.* 2009; Berjanskii and Wishart 2005), against the residue number. Based on all three plots, the predictions strongly indicate that the CTD resonances exhibit stretches of unstructured and disordered elements, suggesting a random coil pattern (**Fig. 4.39B**, $S^2 > 0.8$ for almost all residues), as it is also known for α B-crystallin.

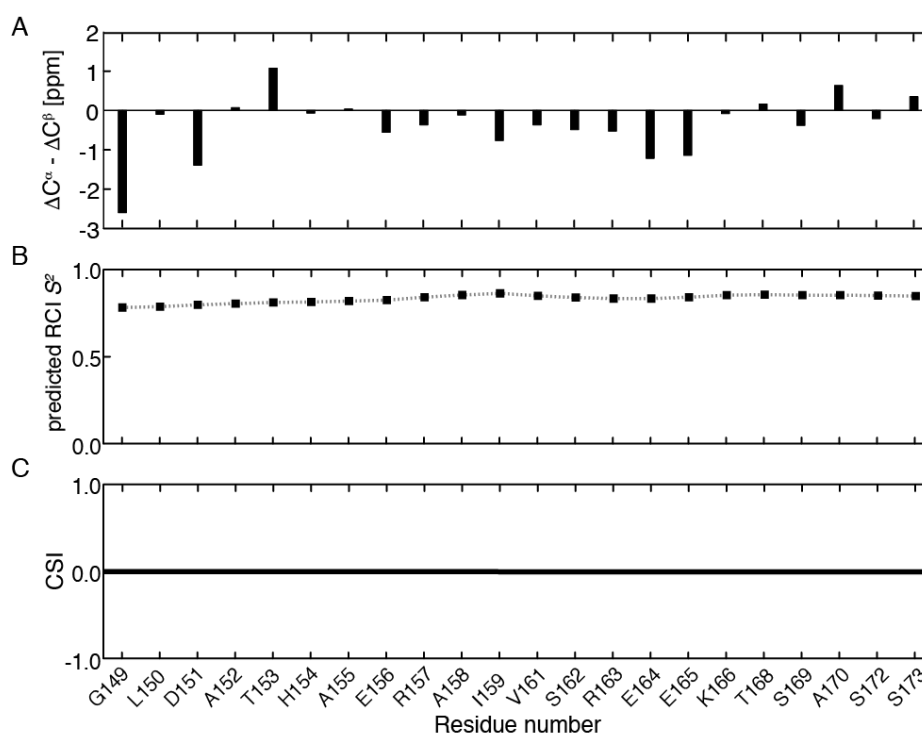


Fig. 4.39. Carbon chemical shifts and secondary structure prediction for the C-terminal domain of α A-crystallin plotted as a function of residue number. (A) Difference of C_α and C_β secondary chemical shifts ($\Delta^{13}\text{C}_\alpha - \Delta^{13}\text{C}_\beta$) for α A. A stretch, having negative values of $\Delta\text{C}_\alpha - \Delta\text{C}_\beta$, indicates β -strand sheet structure, whereas positive values indicate a regular β -helical region. (B) Random coil index (RCI) based order parameters (S^2) predicted by the RCI webserver based on Berjanskii and Wishart 2005. (C) Consensus chemical shift index (CSI) plot. Positive and negative CSI values indicate β -strand and α -helical segments, respectively, while values at 0 indicate random coil (Hafsa *et al.* 2015). The protein sequence is shown on the bottom for all plots.

4.10.3. Interactions of α A- with α B-crystallin in Solution-state NMR

α -Crystallins exhibit exceptional structural features and dynamics as they can assemble into large oligomers that exchange subunits and form polydisperse and dynamic ensembles. α A and α B are known

to form these kind of hetero-oligomeric species of a stoichiometry of 3 to 1 (αA to αB) in the eye lens. However, this ratio can differ as it is possible that different αA and αB splice variants can be incorporated.

The about 20 amino acids long C-terminal region (CTR) contains the highly conserved I-x-I/V motif (IXI), Ile159-Pro160-Val161 in αA and Ile159-Pro160-Ile161 in αB , that acts as an “anchor” in oligomer formation and contributes to the polydispersity of α -crystallins (Delbecq and Kleivit 2013). A common to many sHsps feature, are the flexible, polar and solvent accessible CTRs. This flexibility increases at the so-called C-terminal extension (CTE) of αA and αB , covering the residues downstream of the IXI-motif (E164-S173 in αA , E164-K175 in αB). 1H , ^{15}N NMR spectra of human αA and αB revealed sharp resonances from the last 9 amino acids in αA (E165-S173) and the last 11 amino acids in αB (E165-K175) consistent with their flexibility and solvent accessibility (Carver *et al.* 1998; Carver *et al.* 1992). NMR experiments monitoring backbone dynamics indicate a greater overall flexibility of the CTR of αA as compared to αB .

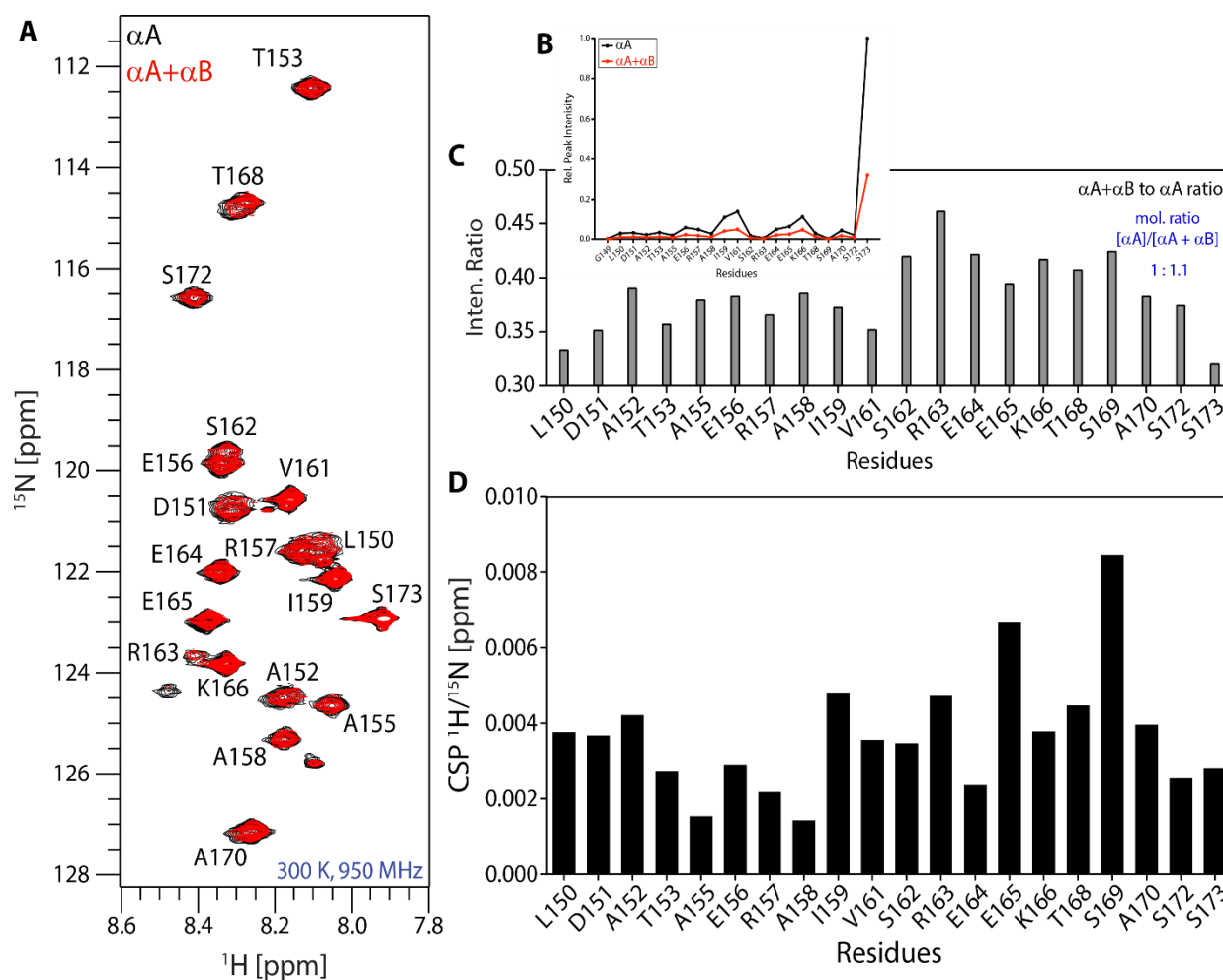


Fig. 4.40. Hetero-oligomers of labeled- αA and unlabeled- αB in solution-state NMR. (A) 1H , ^{15}N HSQC overlay of αA (black) and $\alpha A + \alpha B$ samples (red) recorded at 300 K and 950 MHz. **(B)** Relative peak intensities of αA (black) and $\alpha A + \alpha B$ samples (red) versus residues at a 1 to 1.1 molar ratio, showing a significant dropping of the signal. **(C)** Intensity ratio of αA and $\alpha A + \alpha B$ is shown in a bar plot versus the amino acids number. **(D)** Chemical shift perturbation (CSP) calculation of the two samples versus residue number. Analysed data suggest that the IXI-motif and part of the CTE are affected, indicating that the two molecules form hetero-oligomeric species.

In this study, in order to observe if there is any hetero-oligomer formed between the two proteins, we firstly, recorded a ^1H , ^{15}N HSQC spectra of ^{13}C , ^{15}N -labeled αA as a reference at an about $800\ \mu\text{M}$ concentration (presented in Fig. 4.40A in black), and titrated in the same sample in a 1 to 1.1 molar ratio unlabeled αB -crystallin. After incubating the mixed sample for a couple of hours at room temperature, we recorded a second HSQC at 300 K and 950 MHz. Based on the fact that the IXI-motif is responsible for the oligomerization of α -crystallins, and the CTR is giving rise to high resolution spectra in solution NMR, we expected to see important chemical shift changes in the spectra. However, in the overlay of the two samples not so many shifts were observed at least by eye. Though, looking at the intensities of each peak (Fig. 4.40B) and the intensity ratio of αA to the mixed sample versus the residues (Fig. 4.40C), someone can conclude that there is significant dropping of signal around the IXI-motif, and further around residues E165 – S169, which are part of the CTE. Additionally, in the chemical shift perturbation plot (Fig. 4.40D), although the chemical shifts are not so pronounced, the CSP supports further that the IXI-motif is affected together with part of the CTE of αA , indicating that the two proteins interact with each other forming the expected hetero-oligomer.

4.10.4. Paramagnetic Relaxation Enhancement Experiments of αA

The cryo – EM results suggested that the human αA -crystallin oligomer adopts a 16-mer (consisting of four tetramers) quaternary assembly. In addition, 3D classification analysis revealed minor structural heterogeneity in the equatorial N-terminal contact region, but clear structural variance in the equatorial C-terminal contact site. This indicates a C-terminal flexibility and supports CTR domain swapping of the human αA , which could further be confirmed by paramagnetic relaxation enhancement (PRE) experiments in solution-state NMR (Kaiser et al. in preparation).

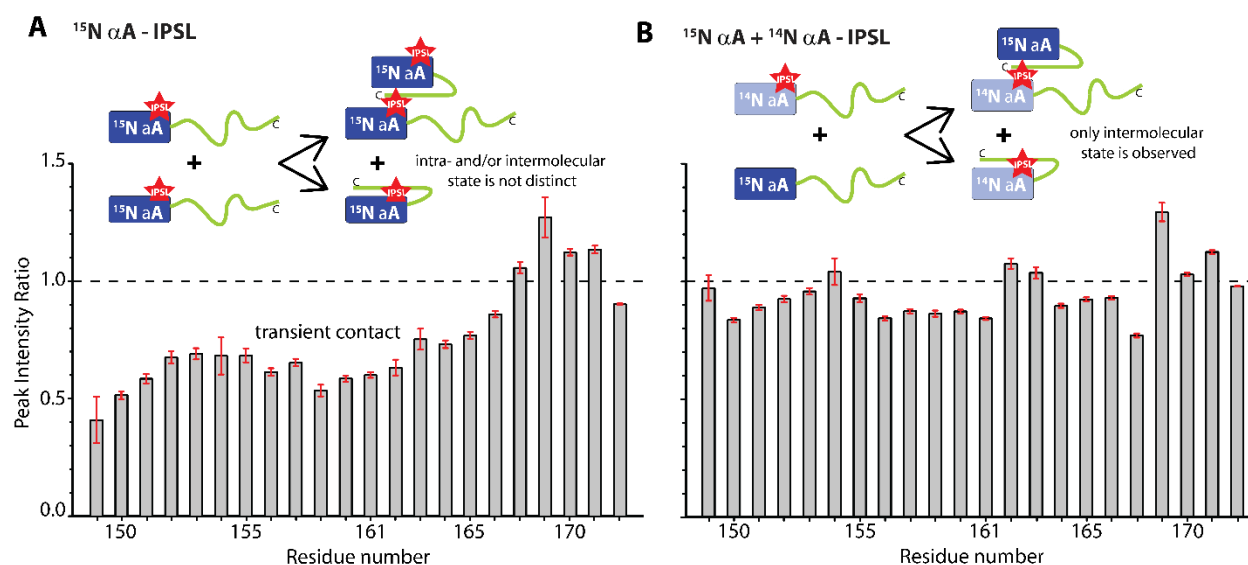


Fig. 4.41. Intramolecular versus intermolecular CTD-ACD interactions, using spin labeling and reduced αA . (A) ^1H , ^{15}N HSQC peak intensity ratio for oxidized (paramagnetic) versus reduced (diamagnetic) ^{15}N αA -IPSL (B) and ^{15}N αA - ^{14}N αA -IPSL (C) as a function of the residue number. (B, inset) Intra- and intermolecular PREs arising from the paramagnetic spin label are not distinguishable. (C, inset) Intermolecular PREs arising from the spin labeled ^{14}N αA -IPSL sample can be observed. All NMR experiments were recorded at 300 K and 950 MHz.

It has been shown recently that the C-terminus of α B-crystallin is in fast equilibrium between a major and minor populated state that is associated with the β 4/ β 8 strands of the crystallin domain (ACD) (Balwin *et al.* 2012). PREs can be observed in a system after introducing a suitable paramagnetic tag into the protein sequence by attaching it to cysteines. PRE spin labeling has been already used to identify intermolecular contacts in α B-crystallin (Balwin *et al.* 2011). There, the spin label was attached to residues S135C and N146C.

Here we carried out PRE measurements at 300 K and 950 MHz, to yield information about transient inter- and/or intra-protein interactions of the CTR of α A. α A-crystallin contains two naturally occurring cysteines, Cys-131 and Cys-142. The 3-(2-iodoacetamido)-proxyl (IPSL) spin label, used in this case, attaches to the sulfhydryl groups of cysteine residues (Gillespie and Shortle 1997). We titrated the IPSL to reduced α A to obtain information about potential involvement of the C-terminus of α A in domain swapping to concatenate oligomeric subunits. The paramagnetic spin label was either titrated to labeled ^{15}N α A (Fig. 4.41A) or to unlabeled ^{14}N α A that was subsequently mixed and incubated with ^{15}N α A (Fig. 4.41B). The paramagnetic tag yields an increase on the nuclear relaxation rates of residues within 20 Å from the unpaired electron (Iwahara and Clore 2006; Battiste and Wagner 2000). The sample in which the IPSL is directly connected to ^{15}N α A showed a significant decrease (of about 40 - 50 %) in peak intensity ratios in particular for residues located closer to the spin label, at the beginning of the CTR, such as residues G149, D151 or T153, as well as for the residues around the IPV-motif (A158, I159 and V161) (Fig. 4.41A). The drop of the intensity ratios indicates that the spin label transiently interacts with the crystallin domain. Furthermore, from this reaction we cannot discriminate between inter- or intra-molecular interactions, therefore, the dropping of the signal is an average of both reactions, as both binding oligomers are ^{15}N -labeled (Fig. 4.41A, inset).

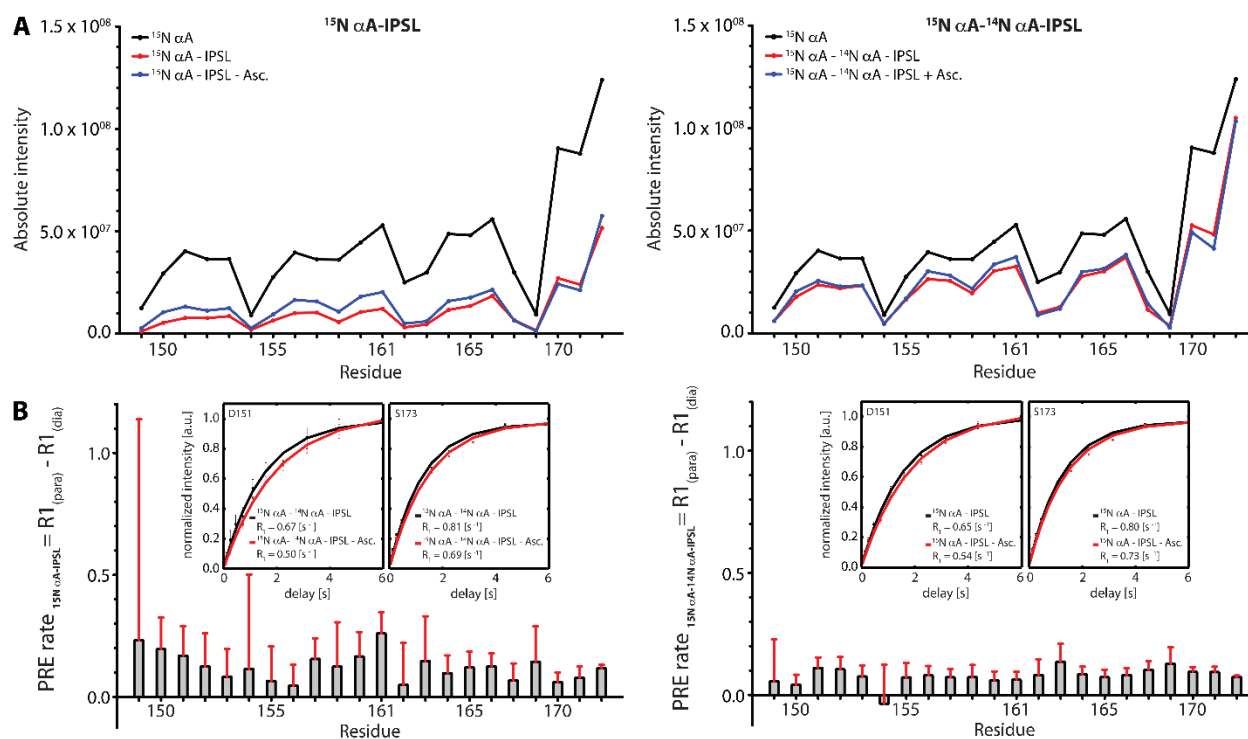


Fig. 4.42. Absolute intensities of the PRE samples. (A) Absolute intensities of the ^{15}N α A-IPSL (left) and ^{15}N α A- ^{14}N α A-IPSL (right) samples versus the residue number. For both samples the reference is shown in black, while addition of IPSL is shown in red and addition of ascorbic acid in blue. **(B)** ^1H R_1 rates were determined for the ^{15}N α A-IPSL (left) and ^{15}N α A- ^{14}N α A-IPSL (right). Representative decay curves are shown in the inset for

residues D151 and S173. The PRE rates were calculated as the difference of $R1_{(para)} - R1_{(dia)}$ and plotted as a function of the residue number. All NMR experiments were recorded at 300 K and 950 MHz.

To differentiate if the CTR interacts intramolecularly with its own crystallin domain, or with the crystallin domain of a neighboring crystallin oligomer, we performed also another experiment, in which the spin label was attached to ^{14}N αA (i.e. unlabeled αA). This sample was subsequently incubated at 37 °C for a few hours with ^{15}N αA . In this case, the dropping of signal intensity was less than before, however, only the signal arising from the ^{15}N αA is detected with NMR, indicating that the only interaction that we observe is intermolecular (Fig. 4.41B, inset). More specifically, we find that only a small amount of ca. 15-20 % of the CTR is involved in intermolecular contacts (Fig. 4.41B), which is in agreement with the cryo-EM data. The absolute intensities for both experiments are represented in Fig. 4.42A (left, right). Upon addition of ascorbic acid, the spin label gets reduced and the intensity of the signal should be recovered. We find, however, that the signal is not totally recovered in comparison to the reference spectra. This could be due to the fact that the spin labeled protein has a higher affinity to the CTR, which is then not detected by solution-state NMR.

The PRE effect was additionally probed directly through the measurement of ^1H R_1 relaxation rates (Simon *et al.* 2010) for all assigned residues (Fig. 4.42B). R_1 rates are less affected by sample concentration effects and pose a complementary probe for investigating the C-terminal tail dynamics in the presence of a paramagnetic tag. The contribution of the PRE to R_1 relaxation was quantified by taking the difference of R_1 rates before and after addition of ascorbic acid. Mainly the residues G149 – A152 and R157 – V161 show elevated R_1 rates, which is in accordance with the analysis of intensity ratios (Fig. 4.41A,B). The insets of Fig. 4.42B show the decay curves for two representative residues (D151, S173). The decay in both samples is faster in presence of IPSL in comparison to the curve obtained upon addition of ascorbic acid.

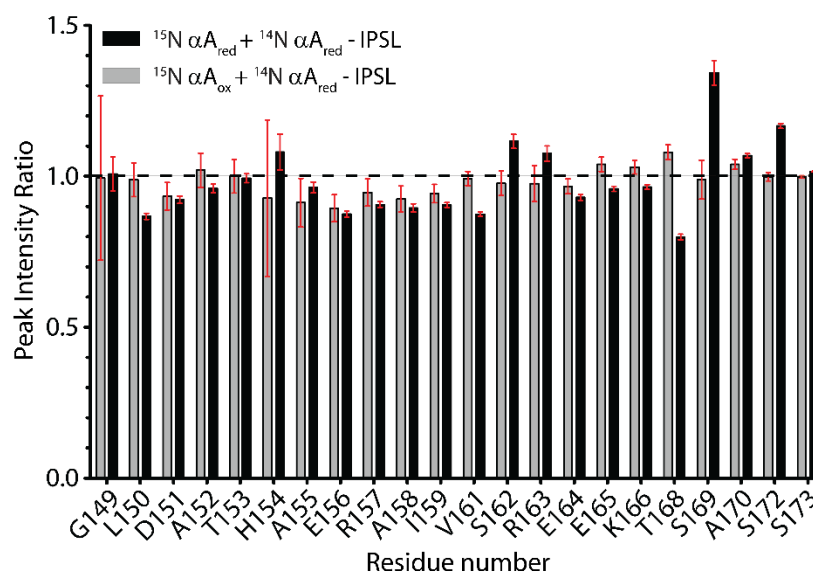


Fig. 4.43. Intramolecular versus intermolecular CTD-ACD interactions, using spin labeling and oxidized αA . Peak intensity ratio for $^{15}\text{N } \alpha\text{A}_{\text{ox}} + ^{14}\text{N } \alpha\text{A}_{\text{red}} - \text{IPSL}$ as a function of the residue number. The oxidized protein is shown with grey bars, while the reduced data from Fig. 4.40 are presented in black bars. Error bars are shown in red. All NMR experiments were recorded at 300 K and 950 MHz.

The same experiments were repeated using in the mixed sample ^{15}N -labeled $\alpha\text{A}_{\text{ox}}$ (oxidized) instead of reduced in order to compare the two states of the protein and investigate whether the oxidized form is

more flexible and/or is participating more in inter- than intra-molecular interactions than the reduced. The analysis of the peak intensity ratios for the two different experiments is plotted in **Fig. 4.43** (shown in grey-bars), while the experiments using the reduced protein (presented with black-bars) are added in the same plot in order to compare the results easier. Therefore, compared to **Fig. 4.41A**, the ^{15}N -labeled $\alpha\text{A}_{\text{ox}}$ upon addition of IPSL has a much lower peak intensity ratio than the reduced form, revealing that the CTRs of the protein are involved in inter- and intra-molecular interactions at a percentage of about 70 % and the binding sites are similar, but there is a significant drop of intensity around the IPV-motif. This suggests that the oxidized form is much more flexible than the reduced. In the case where ^{14}N $\alpha\text{A}_{\text{ox}}$ reacted with IPSL and subsequently mixed and incubated with ^{15}N -labeled αA , however, the oxidized form appeared to be also involved in inter-molecular interactions as there is a drop of intensity ratio of about 10-15% (**Fig. 4.43B**). This is slightly less than the reduced form. Though, the error bars for a few residues (like G149, H154 or A155) are relative big, so this is just a rough estimate and it is possible that the CTR of both the reduced and the oxidized form of αA participates in a similar way in domain swapping with neighboring oligomers.

4.10.5. Chemical Shift Perturbation Calculations for reduced and oxidized αA

In order to investigate whether oxidization affects oligomerization of αA to higher ordered oligomers (as shown in chapter 4.9.1.), we measured at 300 K and 950 MHz in the same conditions (buffer, pH, concentration etc), reduced and oxidized human ^{15}N -labeled αA and the chemical shift perturbation (CSP) for both was calculated based on Williamson 2013. NMR spectra of the $\alpha\text{A}_{\text{ox}}$ looked mostly similar to that of the wild-type αA , though due to line-broadening a few peaks disappeared (mostly seen in lower contours, data not shown), indicating that the oligomer has a higher molecular weight than the wild-type protein. **Fig. 4.44A** shows a ^1H , ^{15}N HSQC overlay spectrum of the reduced and oxidized αA . $^1\text{H}^{\text{N}}$ and ^{15}N backbone resonances (for G149-S173 of the native sequence) have been assigned. In the ^1H , ^{15}N HSQC experiment, there were a few resonances that shifted in the oxidized compared to the reduced protein, such as A152, T153, H154, E156, S169 and A170. However, $^1\text{H}^{\text{N}}$ and ^{15}N assignments were transferred from the reduced to the oxidized form, as no additional peaks appeared in the spectrum. ^{15}N assignments for proline residues have not been obtained neither in reduced or oxidized αA .

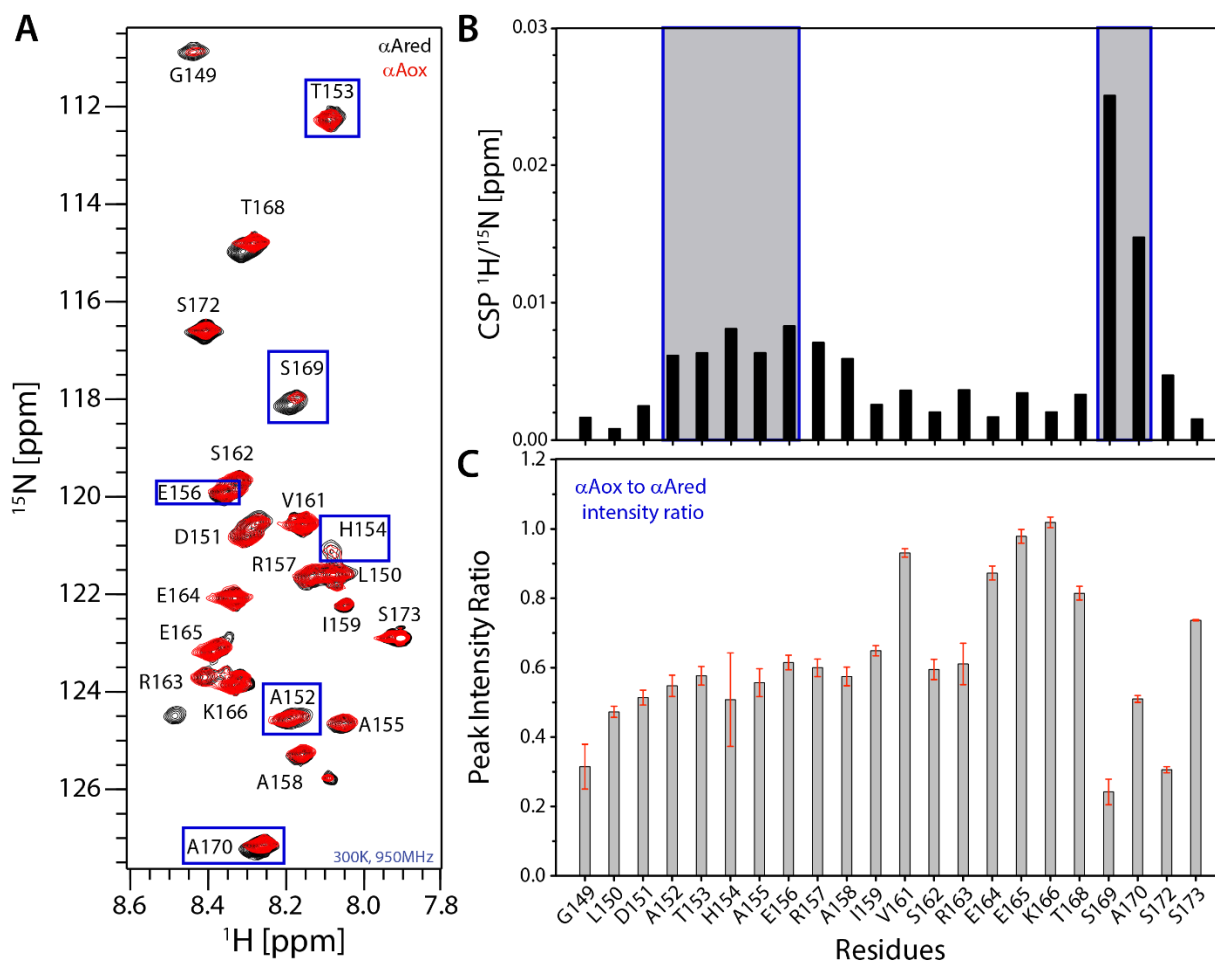


Fig. 4.44. Chemical Shift Perturbation Mapping of αA_{red} and αA_{ox} . (A) 1H , ^{15}N HSQC overlay of αA_{red} (black) and αA_{ox} (red) recorded at 300 K and 950 MHz. Peak assignments for backbone amides of residues G149-S173 of the native sequence are indicated. Peaks labeled with blue boxes indicate combined chemical shift difference observed between the two oxidation states. (B) Chemical shift perturbation changes observed between the reduced and the oxidized states of αA are plotted as a function of amino acid sequence. Regions with most shift changes are shown in grey-blue boxes. Chemical shift changes were small, with the most prominent changes at S169 and A170. (C) Peak intensity ratio of αA_{ox} to αA_{red} as a function of residues.

Next, we analyzed the CSPs introduced by oxidation to the spectra in order to investigate, which residues are affected by the disulphide bond formation. The combined chemical shift difference in 1H , ^{15}N dimensions is plotted as a function of sequence and displayed in **Fig. 4.44B**. Residues showing a chemical shift difference greater than 0.02 ppm involve residues S169 and A170, while negligible shifts are observed for A152 - E156 resonances (CSPs ~ 0.01 ppm) and the rest of the residues are not affected upon oxidation (with CSPs < 0.004 ppm) as suggested by the HSQC already. Additionally, although the CSPs for most residues were insignificant, the majority of the resonances have decreased peak intensity ratio (**Fig. 4.44C**) of about 40 %, with an exception of part of the C-terminal extension, i.e. residues E164-T168. This is associated with the disulphide bond and the signal dropping strongly suggest that changes in local protein conformation alter the magnetic shielding and/or that the residues might be in direct contact with the cysteine resonances.

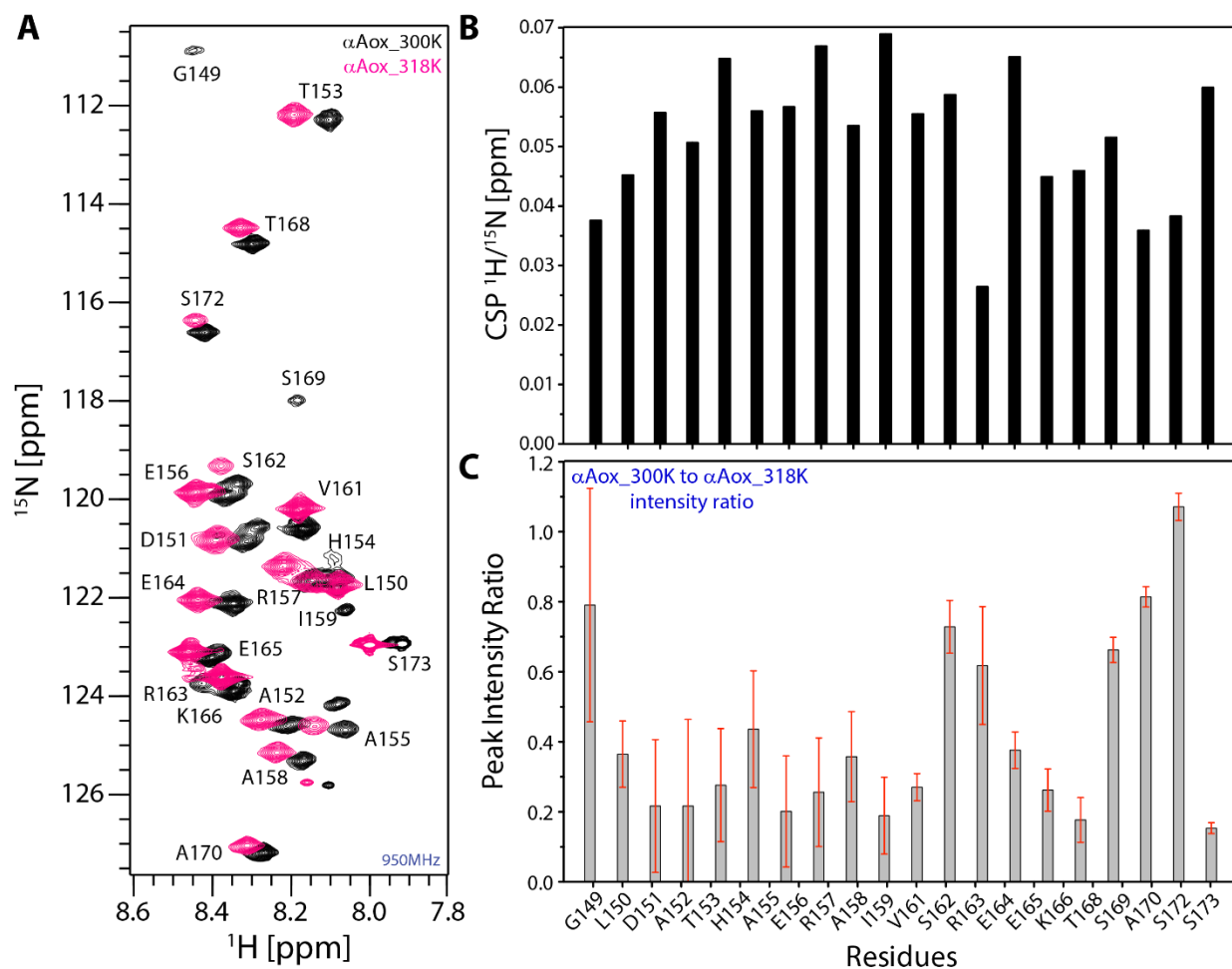


Fig. 4.45. αA_{ox} measured at 300 K and 318 K. (A) A 950 MHz 1H , ^{15}N HSQC overlay spectrum of αA_{ox} measured at 300 K (black) and 318 K (pink). Peak assignments for backbone amides of residues G149-S173 are indicated. (B) Chemical shift perturbation changes observed for the oxidized state of αA at two different temperatures are plotted as a function of amino acid sequence. (C) Peak intensity ratio of αA_{ox_300K} to αA_{ox_318K} as a function of residues.

When the oxidized sample was measured at a higher temperature a small number of peaks showed line-broadening due to exchange. However, the quality of the spectra were improved by increasing the temperature from 300 K to 318 K, and hence, shifting the binding kinetics from intermediate to fast-exchange (Fig. 4.45A). A large number of peaks arising from the 318 K spectrum, are exchange-broadened in the αA_{ox} measured at 300 K. CSPs in this case are associated with the temperature change (Fig. 4.45B). However, most resonances' signal decreased in the peak intensity ratio plot of the oxidized protein measured at 300 K to 318 K (Fig. 4.45C) suggesting that the oligomer at higher temperature becomes more flexible as expected and gives better resolution spectra. For comparison reduced αA was also measured at low (300 K) and higher (318 K) (Fig. 4.46A), and gave a similar motif for the peak intensity ratio in the two temperatures (Fig. 4.46C), however, the residues at the CTE appear to be less affected by the temperature increase compared to the oxidized form of αA . Additionally, chemical shift changes arising from the temperature change are observed (Fig. 4.46B), and R157 and A158 seem to be significant affected by this, which means that there can be a conformational change in the chaperone upon 318K that makes the residues solvent accessible and more flexible than in lower temperature.

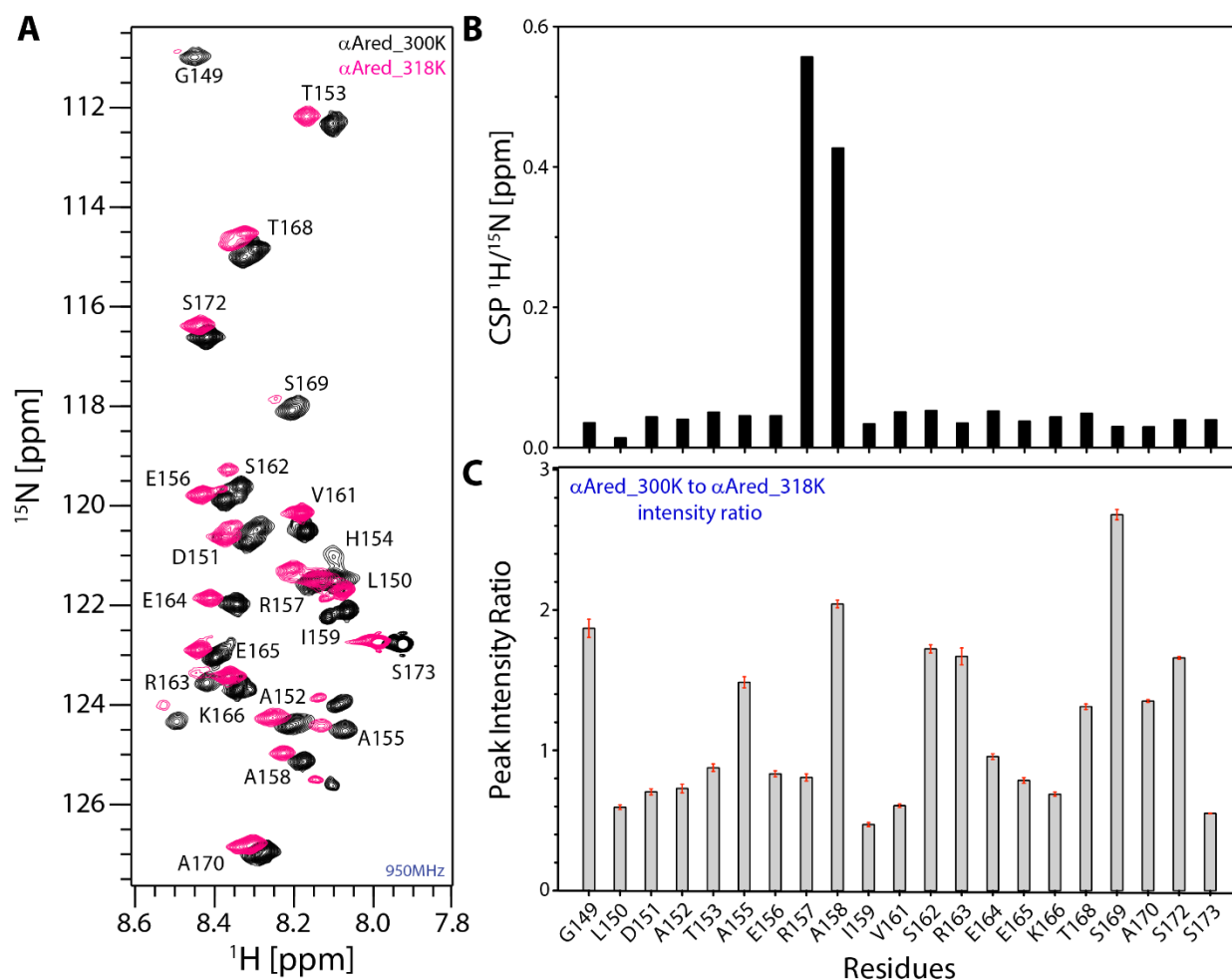


Fig. 4.46. αA_{red} measured at 300 K and 318 K. (A) A 950 MHz 1H , ^{15}N HSQC overlay spectrum of αA_{red} measured at 300 K (black) and 318 K (pink). Peak assignments for backbone amides of residues G149-S173 are indicated. (B) Chemical shift perturbation changes observed for the reduced state of αA at two different temperatures are plotted as a function of amino acid sequence. (C) Peak intensity ratio of αA_{red_300K} to αA_{red_318K} as a function of residues.

4.10.6. NMR Relaxation Analysis of αA_{red} , αA_{ox} and αB

In this study, uniform ^{15}N -labeling of wild-type αA_{red} , αA_{ox} and αB -crystallins allowed us to study the backbone dynamics and quantify the flexibility of the C-terminal regions of all samples via measuring the 1H , ^{15}N heteronuclear Nuclear Overhauser Effect (hetNOE), and the $R1$ and $R1_{Rho}$ relaxation times at 300 K and in two different fields. A low field, 500 MHz (Fig. 4.47) and a higher, 950 MHz (Fig. 4.48) spectrometer. Such NMR studies are a powerful tool for examining the backbone dynamics of proteins in solution (Redfield *et al.* 1992; Clore *et al.* 1990; Kay *et al.* 1989). Upon uniform ^{15}N -labeling of proteins, data can be obtained on the motion of the backbone amides (Clore *et al.* 1990). The set of three experiments described in this study (1H , ^{15}N T1 and $T1_{Rho}$ relaxation times and hetNOE) are routinely used to investigate the amplitude and range of local molecular motions of backbone amides (Cho *et al.* 1996; Barbato *et al.* 1992). T1 relaxation times and hetNOE, are sensitive to faster timescales and provide information on motions occurring with a pico- to nanosecond frequency, whereas $T1_{Rho}$ relaxation times are sensitive to slower motions occurring over micro- to milliseconds, and therefore they reflect molecular

motion over a large timescale (Kay *et al.* 1989). Having assigned the ^1H , ^{15}N cross-peaks in the C-terminal extension of ^{15}N -labeled αA - and αB -crystallin (Fig. 4.36), hetNOEs, $R1$ and $R1_{Rho}$ relaxation times were determined for each residue in this region. The $R1$ and $R1_{Rho}$ values were calculated as the $1/T1$ and $1/T1_{rho}$ fraction.

^1H , ^{15}N hetNOE measurements provide information on the motion of individual N-H bonds with their sign and magnitude being indicative of their mobility relative to the overall molecular tumbling rate of the protein and also to internal dynamics. Thus, positive hetNOE values occur for N-H bonds that are tumbling with a correlation time comparable to the overall protein, i.e. they are reflective of folded or structured regions within the protein. Large negative hetNOE values from the other side, are indicative of large amplitude motions for N-H bonds that occur on a faster timescale and arise from unstructured regions of the protein i.e., regions with correlation times that are much shorter than those from structured regions of proteins.

HetNOE values are field dependent and sensitive to the effects of the backbone motion, much more than $R1$ and $R1_{Rho}$ values, since dipolar interactions between attached ^1H and ^{15}N nuclei are being observed. In Fig. 4.47A and 4.48A, the hetNOE values were plotted against C-terminal residues. All three experiments show that the C-termini of the constructs are highly flexible as expected, and negative and large values are consistent to high mobility regions, i.e. large amplitude motions. Furthermore, it is apparent that the greatest degree of flexibility increases at the distal end of the C-terminal extension (i.e. S173 for αA and K175 for αB) indicating higher mobility the further the distance from the tethering point along with significant mobility in the region of I159 to E164 for αA and I159 to E165 for αB . Overall, the samples were measured at the same conditions, however, αA_{ox} appears to be slightly more dynamic than the rest, as it shows lower than the average hetNOE values, with αA_{red} following and αB being the last with less mobility. For example, the hetNOE value for S173 of αA_{ox} is -3.5 at 500 MHz and -0.87 at 950 MHz compared to the average value of -0.9 and 0.15 at 500 and 950 MHz, respectively for the entire C-terminal extension. Interestingly, S173 of αA_{red} has a higher hetNOE value of about -2.5 measured at 500 MHz in a average of -0.67 and the same hetNOE value (i.e. -0.87) compared though to an average of 0.09 at 950 MHz. On the other side, K175 of αB has a value of -1.7 and -0.3 at an average of -0.67 and 0.19 at 500 and 950 MHz, individually, with both values being higher than αA -crystallin, either reduced or oxidized.

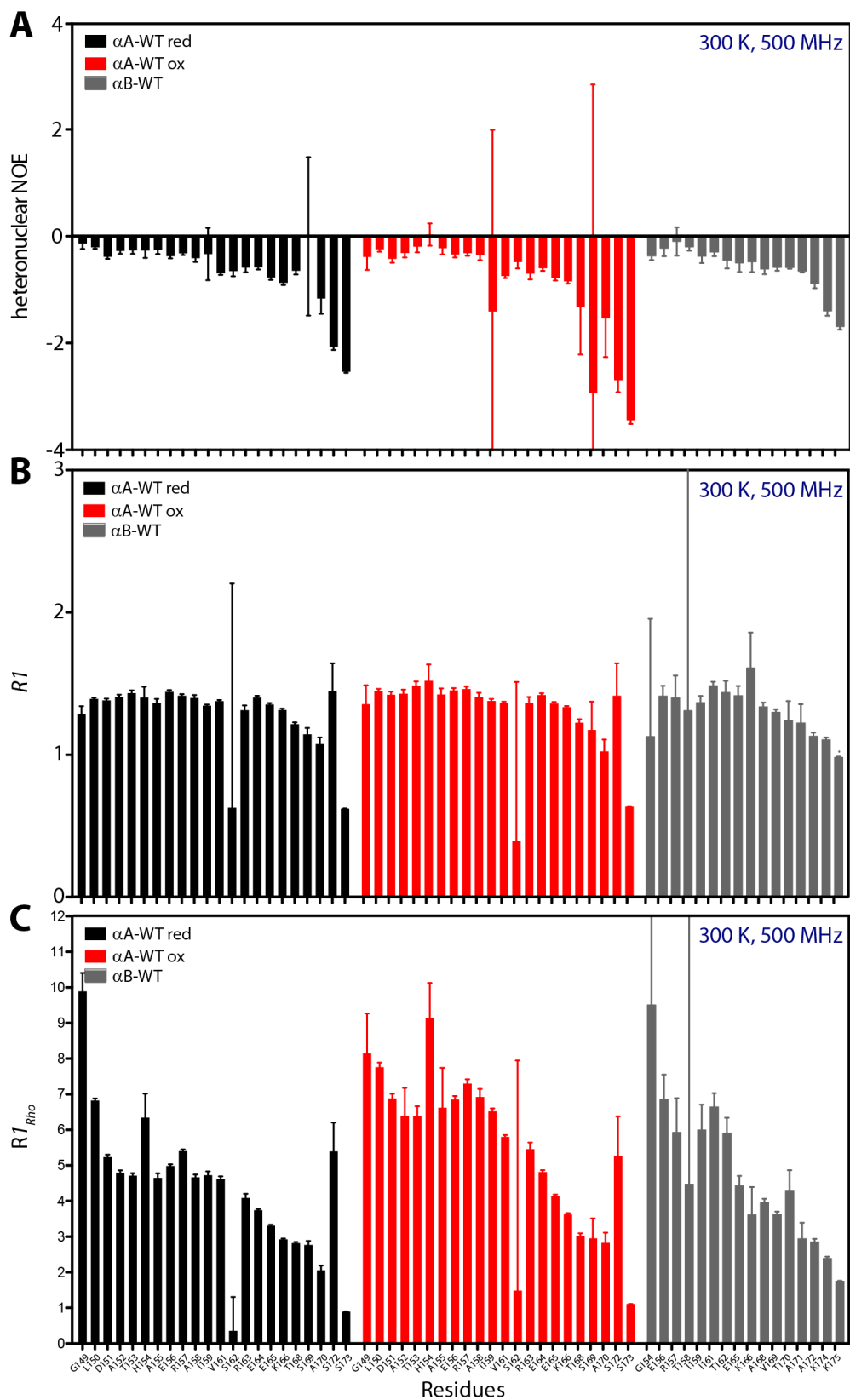


Fig. 4.47. ^{15}N relaxation analysis performed at 300 K and 500 MHz. (A) heteronuclear $-\text{NOE}$, (B) R_1 and (C) $R_{1\rho}$ for $\alpha\text{A}_{\text{red}}$, $\alpha\text{A}_{\text{ox}}$ and αB plotted as a function of the residue number.

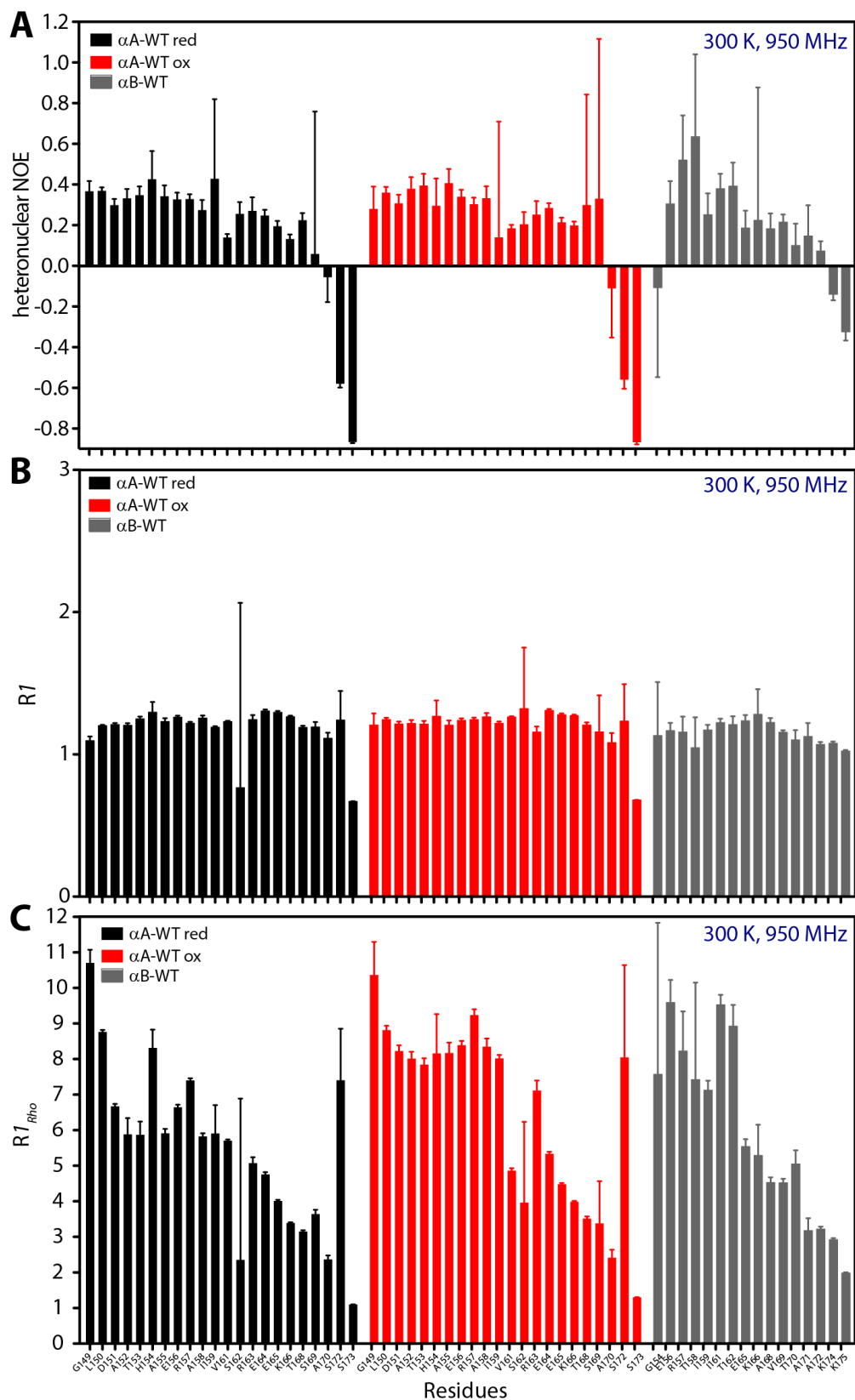


Fig. 4.48. ^{15}N relaxation analysis performed at 300 K and 950 MHz. (A) heteronuclear-NOE, (B) T_1 , and (C) $T_{1_{Rho}}$ for αA_{red} , αA_{ox} and αB plotted as a function of the residue number. The measurements were performed at 300 K and 950 MHz.

Experimentally determined $R1$ values for each residue in all samples were significantly larger than corresponding $R1_{rho}$ values in both fields (Fig. 4.44B,C; 4.45B,C), which is consistent with significant conformational flexibility in the C-terminal extension of αA and αB . The $R1$ values were generally similar throughout the extension with the exception of S162 and S173 for αA and K175 for αB . In general, $R1$ and $R1_{rho}$ values for each protein increased toward the extreme C-terminus indicating greater conformational mobility in this region, i.e. upon moving further away from the ‘tethering point’ to the structured, less conformationally mobile, domain core. In particular, relaxation times for the ultimate residue of αA , S173, but also for S162 were considerably longer than for the remaining residues in the C-terminal extension, indicating greater mobility of this residue compared to the remainder of the extension, which could be explained by the fact that it is structurally maybe more solvent accessible than its neighbouring resonances. In addition, there is an offset of the $R1_{rho}$ values dropping for the reduced form in both fields, indicating that the oxidized form appears to be in some part (i.e. around residues A158-T168) more rigid than the reduced. $T1$ and $T1_{rho}$ curves versus the recovery delay for representative residues (i.e. G149, I159, T168, A170 and S173) for αA_{red} and αA_{ox} are presented further in Fig. 4.49. As G149 and I159 are closer to the bulky and big protein core, cannot be therefore too flexible. On the other hand, A170 and S173 are much further away from the folded part and experience almost no steric hindrance, therefore they are more flexible than the rest of the residues. The overall tumbling correlation time (τ_c) or the order parameter were not estimated as the samples are too flexible and non-globular, facts that make it difficult to calculate the desired values.

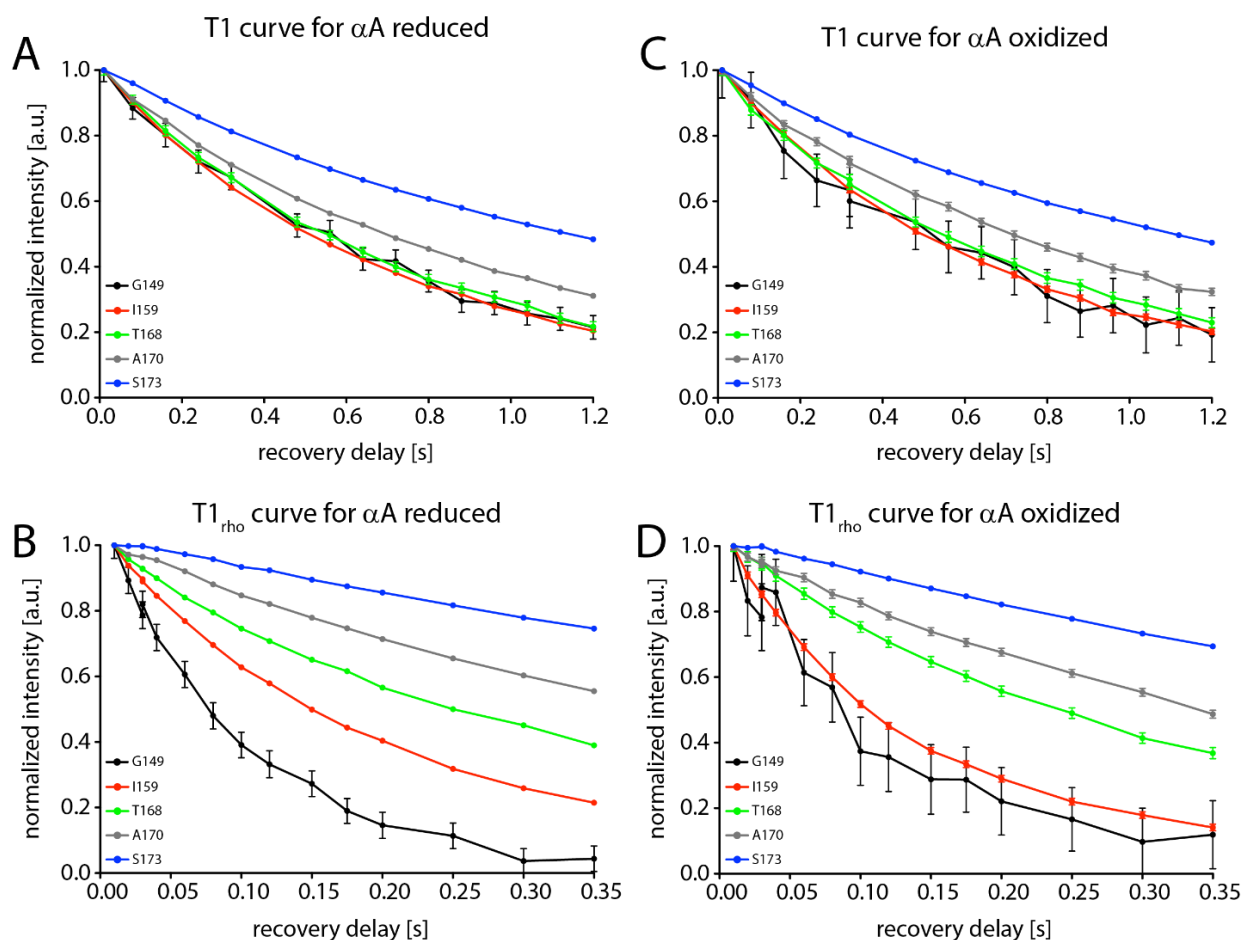


Fig. 4.49. $T1$ and $T1_{rho}$ intensity curves versus the recovery delay. (A, B) αA reduced and (C, D) αA oxidized. Representative C-terminal residues are shown (G149, I159, T168, A170 and S173). The experiments were recorded at 300 K and 500 MHz.

4.11. Solid – state NMR PDS D Spectra of α B-WT and α A-WT

The EM images revealed high-ordered oligomers for α A-crystallin. Additionally, in solution-state NMR only the flexible parts of α A are detectable, i.e. the C-terminal region (residues: G149-S173). Therefore, solid-state NMR could be the best technique to study the structure of this human protein at atomic resolution as crystallization of the wild-type protein was until now not successful. As outlined in the introductory part, MAS solid-state NMR requires rotationally immobilized biomolecules, as in the case of microcrystalline or precipitated protein samples. The preparation of homogeneous samples is thus, the essential step to yield high-quality spectra, but often fails. In this case, we performed MAS NMR experiments employing the FROSTY (Freezing Rotational diffusion Of protein Solutions at low Temperature and high viscosity) approach. In contrast to conventional solid-state MAS NMR, the protein was not precipitated, but investigated in solution.

As the project is at an early stage in order to access the nitrogen line widths of the full-length human α A, a NCA spectra was recorded (Fig. 4.50) on an about \sim 30 mg/ml concentration sample, packed into a 3.2 mm rotor. In this case, magnetization is transferred from ^1H to ^{15}N via cross polarization and then selectively to the $^{13}\text{C}\alpha$ using specific cross polarization. The chemical shift is evolved on the ^{15}N nuclei and detected on the ^{13}C nuclei. This experiment may also provide a means for assigning the nitrogen chemical shifts.

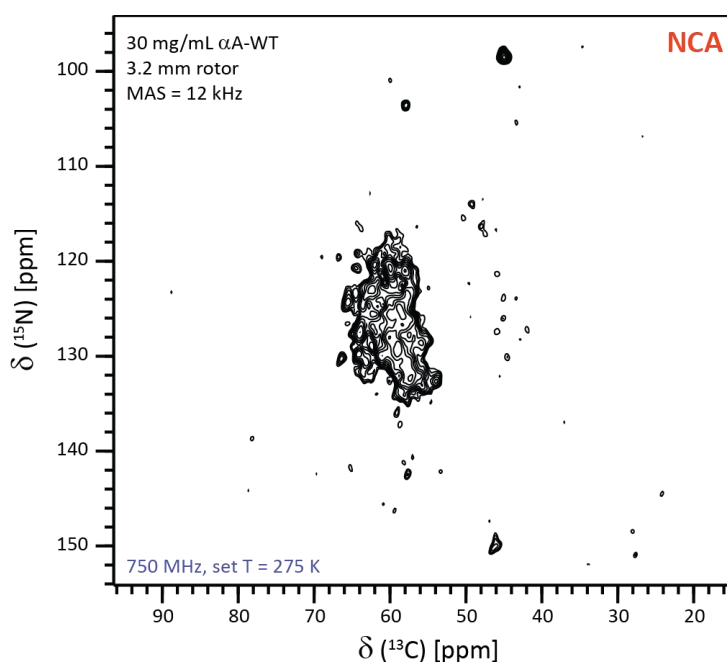


Fig. 4.50. 2D NCA spectra of the human α A-crystallin recorded at 0°C and 750 MHz.

As an additional model system, the large homo-oligomers of α B (\sim 600 kDa) were employed at high concentration (\sim 100 mg/ml). The pellet, which was obtained after centrifugation of the turbid solution, was subjected to a solid-state thin-wall 3.2 mm rotor. MAS NMR spectroscopy yielded high-quality ^{13}C - ^{13}C correlation spectra for the viscous protein solution at 0°C and 12 kHz spinning speed (Fig. 4.51A, shown is black). The 2D spectrum was obtained within four days. 2D ^{13}C - ^{13}C correlation spectra for α A-crystallin were also recorded and presented in an overlay with α B in Fig. 4.51A. The spectrum showed reasonable resolution indicating a sample possible to be assigned at higher concentration later on as the insufficient

amount of material hindered resonance assignment, which is required to further describe the structural state of α A-crystallin. Notably, the comparison of the spectra obtained in solution for α B and α A revealed many overlapping regions shown in a zoom-in in **Fig. 4.51B**. In particular, assignments of α B-crystallin for Ile, Thr and Ala are indicated.

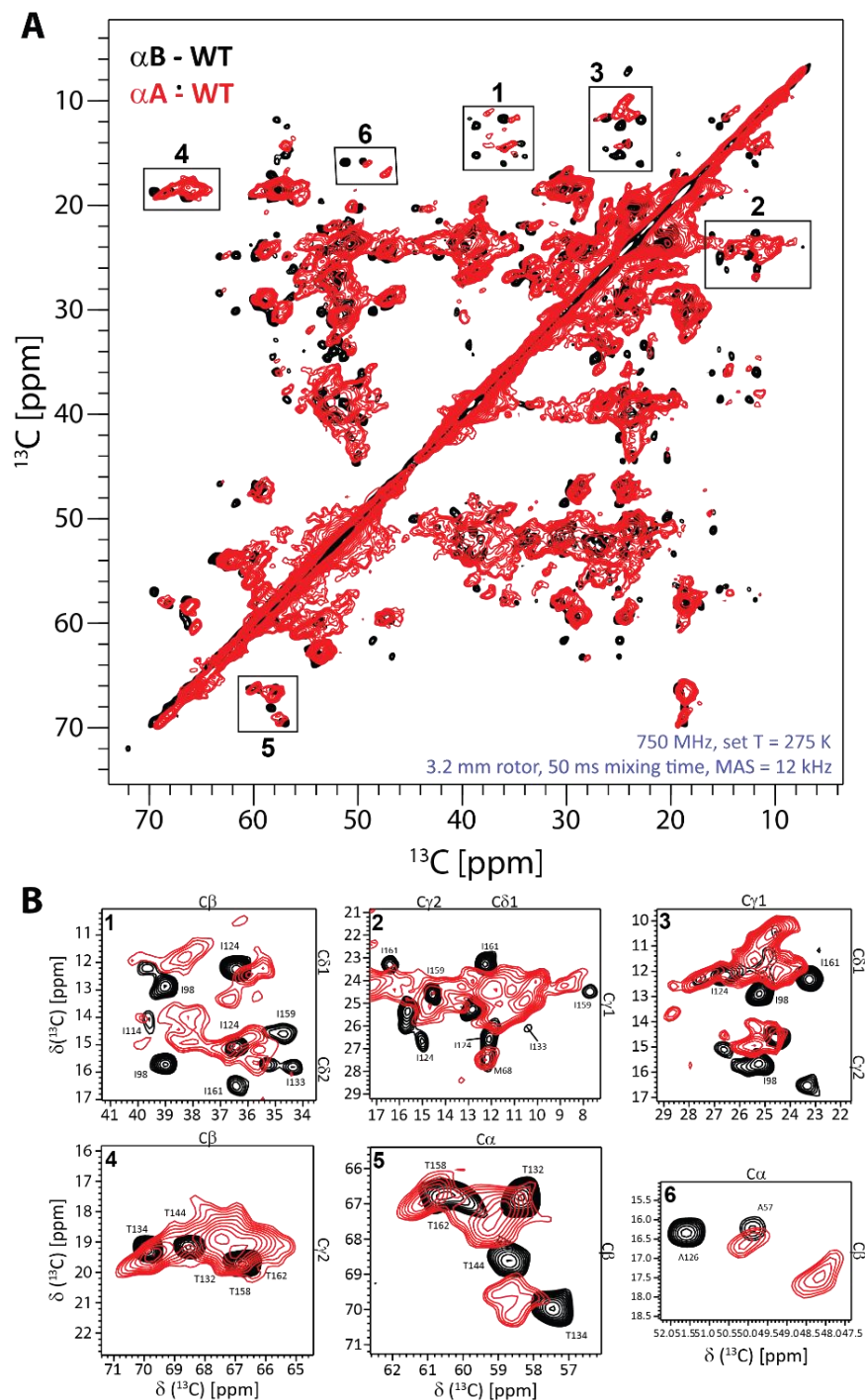


Fig. 4.51. MAS NMR on (A) α B (black) and α A (red) oligomers in solution. 2D PDSM spectrum obtained for full-length α B and α A at a concentration of 100 mg/mL (~ 6 mM) and 30 mg/ml (~ 2 mM), respectively in PBS buffer. The spectrum was recorded at 0 $^{\circ}\text{C}$ with a spinning frequency of 12 kHz. The PDSM mixing time was set to 50 ms. The aliphatic regions are shown. (B) Zoom into Ile, Thr and Ala regions. Assignments of α B are indicated.

4.12. ^{13}C , ^{13}C – Correlation Spectra of αA - and αB -crystallin in Solution-state NMR

Molecular size has limited solution NMR analyses of proteins. Here, in collaboration with Dr. Asami (TU Munich), we report an alternative and complementary approach, ^{13}C - ^{13}C NOESY experiments on a 580 kDa, αB and on a 320 kDa (as suggested by the cryo-EM model) protein, αA , respectively (Fig.4.52A,B, red). The ^{13}C - ^{13}C NOESY experiments were carried out on a 950 MHz spectrometer equipped with a triple-resonance probe optimised for ^{13}C direct detection experiments, at 300 K on samples that were about 2 mM in monomer concentration each, at pH 7.4. ^{13}C - ^{13}C NOESY maps were recorded at different mixing times (100 ms, 150 ms, 200 ms, 300 ms, 500 ms, 1 s) on the full spectral width and on the aliphatic region in order to increase resolution. At a mixing time of 200 ms, in the ^{13}C - ^{13}C NOESY map the maximum intensity for interresidue connectivities could be detected for most residues (Fig.4.52A,B, red). Experiments on a sample, 2 mM in monomer concentration, lasted 40 h each to achieve good signal-to-noise ratios.

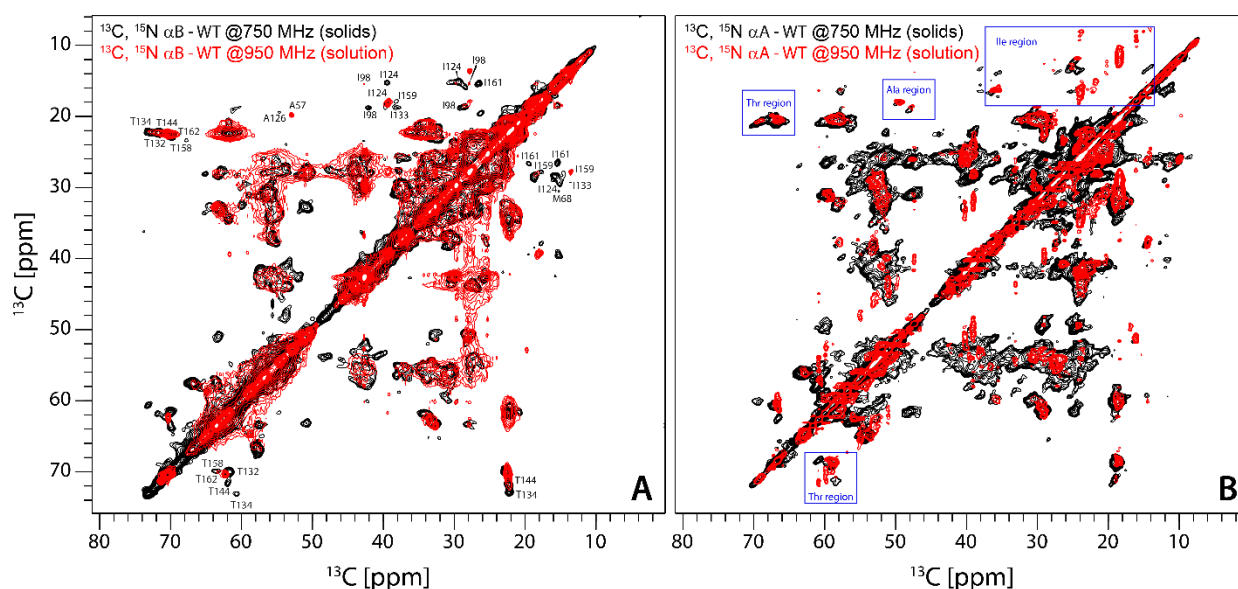


Fig. 4.52. Overlay of the aliphatic region of ^{13}C , ^{15}N (A) αB - and (B) αA -crystallin in solid- (black) and solution-state (red) NMR. The 2D PSDS solid-state spectra were recorded at 275 K and 750 MHz, while the ^{13}C - ^{13}C NOESY spectra at 300 K and 950 MHz with 200 ms mixing time.

These results show the potential of ^{13}C - ^{13}C NOESY for solution studies of molecular assemblies >100 kDa. In a large system such as αB -crystallin for example, the ^{13}C - ^{13}C NOESY solution spectra are rich in information, as emphasized by the large number of resolved peaks compared to the solid-state spectrum, where the sample concentration was three times higher (Fig.4.52A, black). Therefore, residues assigned in the solid spectrum could be transferred to the solution one, like resonances A57, I98, I124, T144, T158 or T162. Furthermore, αA -crystallin gives also high-resolution spectra when ^{13}C - ^{13}C NOESY experiments are superimposed to the solid-state spectrum (Fig.4.52B, black). Thr, Ile or Ala regions are overlapping nicely in the spectrum, indicating that for initial studies of a large system, before going for a solid-state sample, someone could try to test how it would looklike using solution NMR in order to save material and time. Additionally, a titration with different substrates is more feasible this way compared to a solid-state sample.

However, the quality of the ^{13}C , ^{13}C NOESY spectra in solution is very good and the resolution is now absolutely comparable to the solid spectrum, the spectral quality can be significantly improved by employing a deuterated instead of a protonated sample. The two kinds of spectra (^1H and ^2H) could not be superimposed due to the isotope effect of deuterium, as for each methyl- d_3 substitution the isotope effect on the β -carbons is around -0.0 till -0.3 ppm (Servis and Shue 1980). The sample used in this case was an αB sample of about 1.3 mM in concentration, that is almost half the protonated sample and the impact of deuterium in spectral resolution and sensitivity is presented in Fig. 4.53.

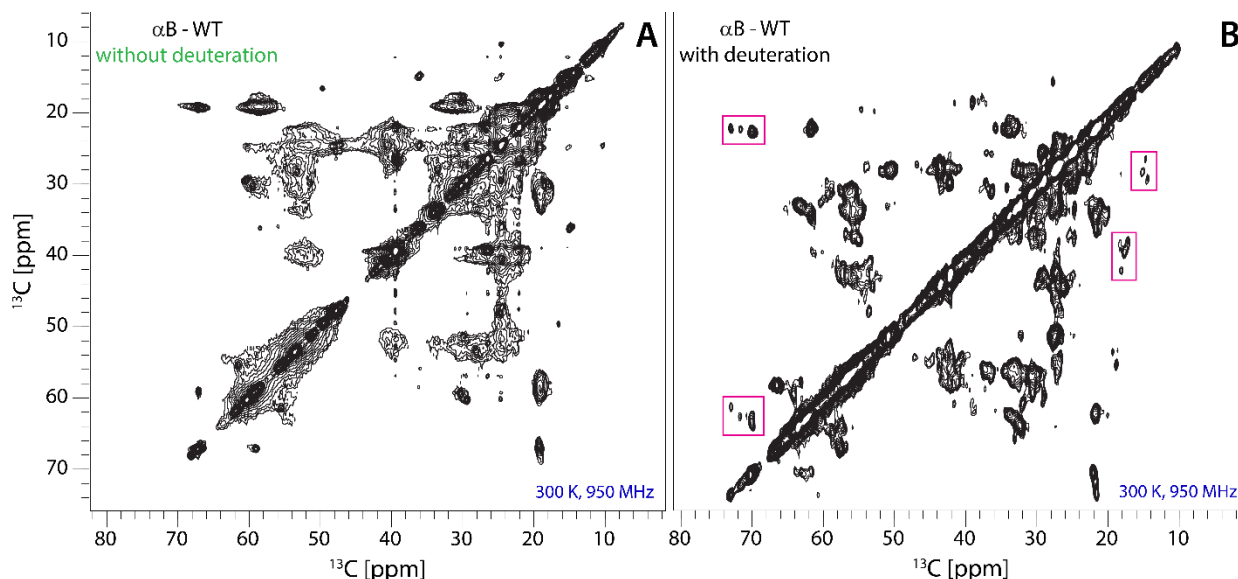


Fig. 4.53. ^{13}C , ^{13}C NOESY solution-state NMR spectra of the aliphatic region of ^{13}C , ^{15}N αB -crystallin (A) protonated and (B) deuterated. The spectra were recorded at 300 K and 950 MHz with 200 ms mixing time.

4.13. Solution-state NMR Investigations of the Truncated αA Construct

It was shown that X-ray crystallography, as well as solution-state NMR spectroscopy have been successful to study the central ACD of αB by using N- and C-terminally truncated αB variants, which adopts a β -sandwich structure and forms only dimers in solution (Mainz et al. 2012; Bagneris et al. 2009). Additionally, the structure of truncated human αA is so far not known, and only the crystal structures of truncated bovine (Laganowsky et al. 2010a) and zebrafish αA (Laganowsky et al. 2010b), lacking the NTR, but containing part of the C-terminal extension (CTE), have been solved.

Until now we focused on studying the CTR of αA in solution-state NMR. However, we carried out preliminary biochemical assays and solution-state NMR experiments to structurally characterize the truncated human αA . The first construct we tested, i.e. residues 62-166, contained as in the zebrafish and bovine studies, also part of the CTE. We measured both, truncated αA reduced ($\alpha\text{Ared}_{(62-166)}$) and truncated αA oxidized ($\alpha\text{Aox}_{(62-166)}$). HPLC data of the full-length and truncated samples show an important shift in the elution volume of the truncated variants (Fig. 4.54A). Full-length αAred elutes at about 11 ml, αAox at 8 ml, while $\alpha\text{Ared}_{(62-166)}$ 17ml and finally, $\alpha\text{Aox}_{(62-166)}$ at 16 and 14 ml, as two peaks are detected. The HPLC suggests that the oxidized αA forms higher molecular weight oligomeric ensembles in both wild-type and truncated αA than the reduced form. However, for the truncated αA , it is proposed, based on the column calibration with standard samples that the protein is dimeric in its reduced form

(corresponding to a molecular weight of 40 kDa), while it appears to have two different populations in the oxidized form, a dimeric, and a higher molecular weight one, possibly tetrameric (corresponding to a molecular weight of 80 kDa).

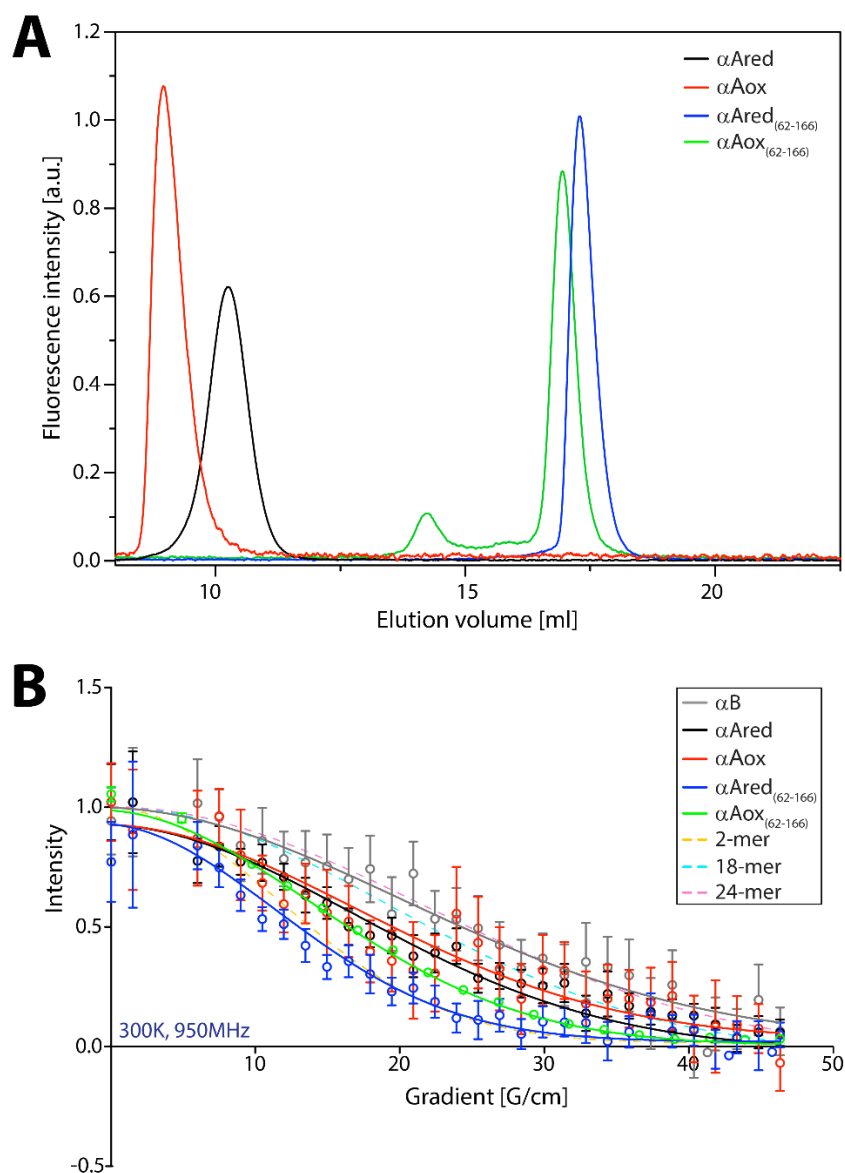


Fig. 4.54. HPLC and DOSY of the WT and truncated α A. (A) HPLC of the elution volumes of the full-length α A reduced (black) and oxidized (red) compared to the truncated α A reduced (blue) and oxidized (light green). (B) 1 H DOSY correlation curves of α B-WT (grey), α A-WT reduced (black) and oxidized (red), and truncated α A reduced (blue) and oxidized (light green). Simulation of attenuation profiles (dashed lines) for various α A n-mers are indicated in the legend: 2-mer (yellow), 18-mer (cyan) and 24-mer (pink). Samples had a concentration of 200 μ M and measured in a shigemi tube.

These results were further supported using 1 H diffusion ordered NMR spectroscopy (DOSY) experiments, which showed that both α Ared₍₆₂₋₁₆₆₎ and α Aox₍₆₂₋₁₆₆₎ consist of a smaller number of oligomers as compared to their wild-type proteins, and based on the simulated curves shown in the Fig. 4.54B with dashed lines, it is also hypothesized that the overall size of oxidized α A is increased compared to the reduced forms. In the DOSY experiments reduced and oxidized wild-type α A diffuse in a higher molecular weight than

corresponds to a 16-mer oligomer, whereas the truncated versions diffuse to smaller oligomeric states, either dimeric, tetrameric or hexameric, a results that is in agreement with the HPLC data.

The ^1H , ^{15}N HSQC spectra of $\alpha\text{Ared}_{(62-166)}$ give better resolved spectra (Fig. 4.55, blue) with narrower peaks than the wild-type protein, indicating a partially folded protein containing unstructured regions. Compared to $\alpha\text{Aox}_{(62-166)}$ (Fig. 4.55, light green), the signals are overlapping, proposing that it's a more heterogeneous sample, containing one or more different species as also seen by the HPLC data. Probably, in this case, the CTE folds to the ACD in a way that the protein obtains a different conformation. And based on our current hypothesis, $\alpha\text{Aox}_{(62-166)}$, can maybe form a tetramer by domain swapping of the CTE to neighboring dimer and therefore, its molecular weight is increased and the spectral resolution is decreased. Fig. 4.55 represents the overlay of the two samples in high and low contours for easier comparison.

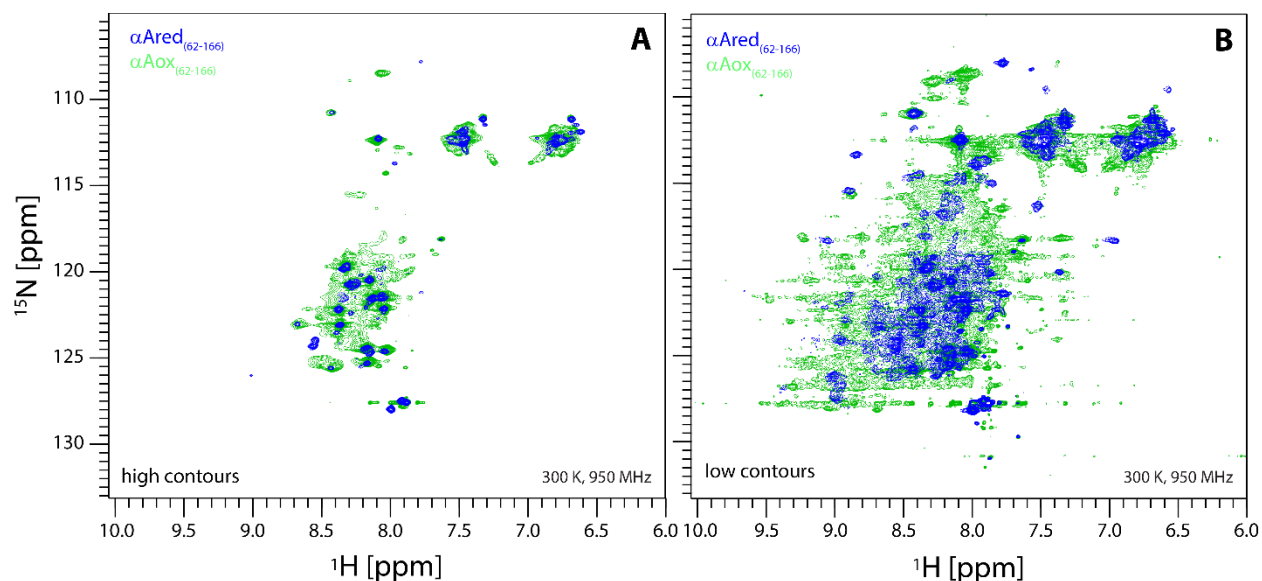


Fig. 4.55. Reduced versus oxidize αA . (A, B) ^1H , ^{15}N HSQC overlay spectra of the reduced (blue) and oxidized (light green) truncated αA , in low (A) and high (B) contours, showing that the oxidized state has a higher molecular weight than the reduced and it is more heterogeneous.

Due to the signal crowding in the presented spectra (and the existence of the CTE), assignment experiments for this sample were not feasible by now. As shown by the superposition of $\alpha\text{Ared}_{(62-166)}$ to the wild-type protein (Fig. 4.56A) only resonances arising from the CTE (L150 – K166) could be distinguished and assigned.

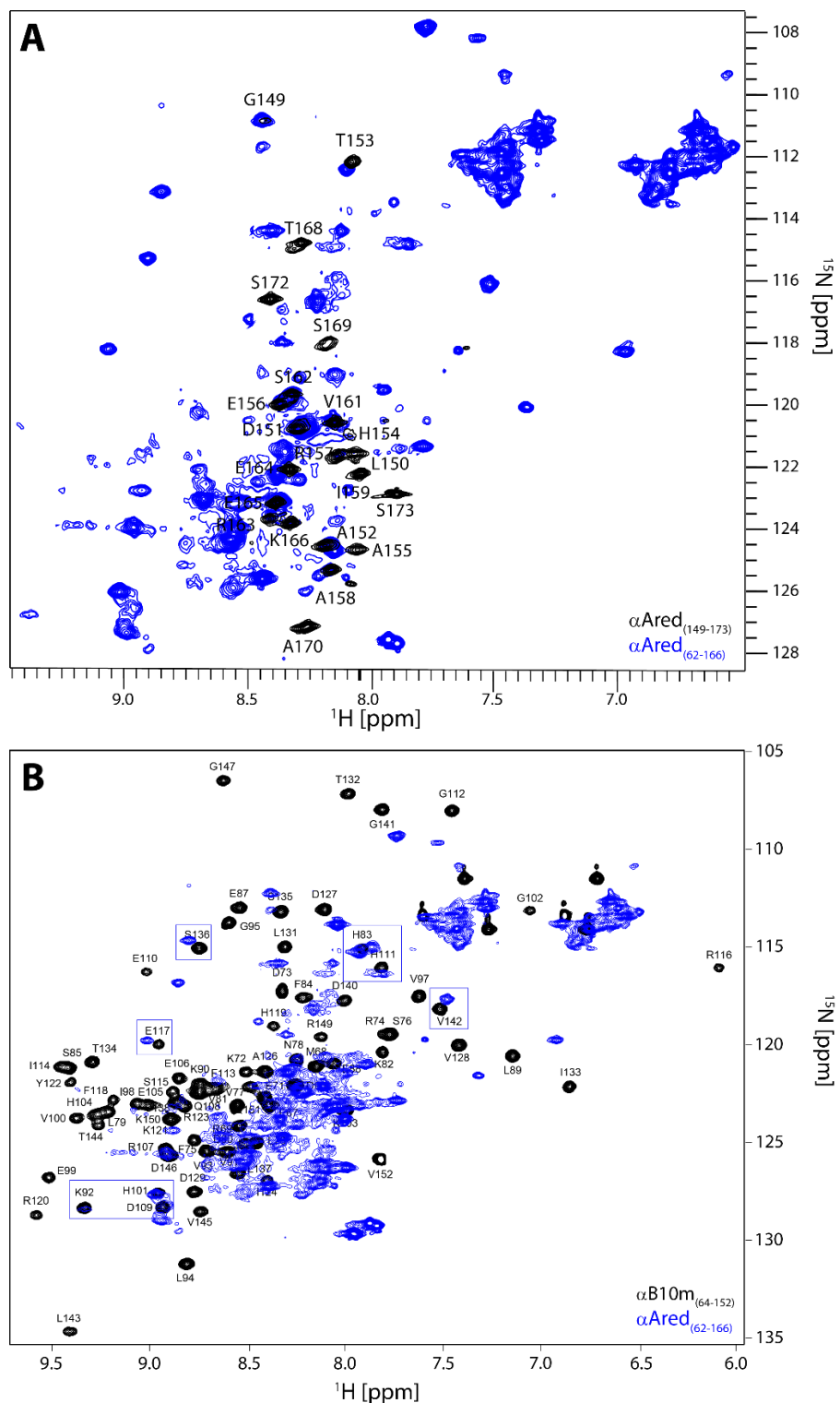


Fig. 4.56. Truncated α A versus α B-WT and truncated α B. (A) ^1H , ^{15}N HSQC superposition spectra of the reduced truncated α A (blue) and α A-WT (black) showing the overlapping residues contained in the truncated α A. The assignments of the flexible C-terminal region of the full-length protein are labeled in the spectra in black for residues G149-S173, while non-visible residues are presented in grey in the inset (top). (B) ^1H , ^{15}N HSQC overlay spectra of the reduced truncated α A (blue) and the truncated α B (black) (assignment for α B is taken from Mainz *et al.* 2012). Possible assignments transferred from α B to α A are labeled with blue boxes. In the figure full-length and truncated mutants of α A are labeled as α Ared (reduced form) and α Aox (oxidized form), and α Ared₍₆₂₋₁₆₆₎ and α Aox₍₆₂₋₁₆₆₎, respectively. All NMR related experiments were recorded at 300 K and 950 MHz.

The truncated α B mutant, containing residues 64-152 (**Fig. 4.56B**) was further plotted together with the truncated α A construct to show possible regions of overlap, as α A and α B have also a 58% sequence similarity. Possible overlapping assignments are indicated with boxes, covering a region between residues H83 till E117. Small chemical shifts in the overlay can be clarified by the different fields that the two samples were measured and the temperature. The ^1H , ^{15}N HSQC assignment spectrum of the truncated α B was kindly provided by Dr. A. Mainz (Mainz *et al.* 2012) and gives very well dispersed spectra, implicating a structured and folded α B core domain (**Fig. 4.56B**, black). In order to have a similar level of spectra for the truncated α A mutant, in the future plans, we would like to use another truncated construct, containing only the ACD resonances of α A (like the one used for α B by Mainz *et al.* 2012) in order to improve the spectral resolution and assignment, and be able to structurally characterize the possibly dimeric oligomer in both the reduced and oxidized state. For that reason a new truncated mutant of α A was cloned (containing residues 62-152) and its expression was already tested using ^{13}C , ^{15}N -labeled M9 medium. In the near future we will have the sample purified to use it for assignment experiments in solution-state NMR.

4.14. Prolines Isomerization of the C-terminal Region of α A

The CTR of α A, like other sHsps, is subdivided into the tail and the extension, which respectively include residues up to a well-conserved I-X-I/V-motif, and beyond (**Fig. 4.57**). Crystal structures of non-mammalian sHsps revealed that the I-X-I/V motif docks into a hydrophobic groove in the ACD of a neighbouring subunit (Haslbeck and Vierling 2015; Hilton *et al.* 2013b; Mchaourab *et al.* 2009), while crystal structures of mammalian truncated constructs suggested that docking of the CTR can occur bi-directionally (Laganowsky *et al.* 2010) and intra- or inter-monomer (Laganowsky and Eisenberg 2010). However, it was shown that the CTRs are overall being predominantly disordered in solution (Trewick *et al.* 2015; Hochberg and Benesch 2014; Delbecq and Kleivit 2013; Carver and Lindner 1998). Evidence for this flexibility of the CTR of α A has come primarily from solution-state NMR as shown in previous chapters, which is well-suited to studying unstructured regions within proteins. Disordered CTRs have been observed through different studies in human α A- and α B-crystallin (Carver *et al.* 1992), murine Hsp25 (Carver *et al.* 1995a), HSP27 (Carver and Lindner 1998), murine Hsp20 (van de Klundert *et al.* 1998) and *Saccharomyces cerevisiae* Hsp26 (Benesch *et al.* 2010).

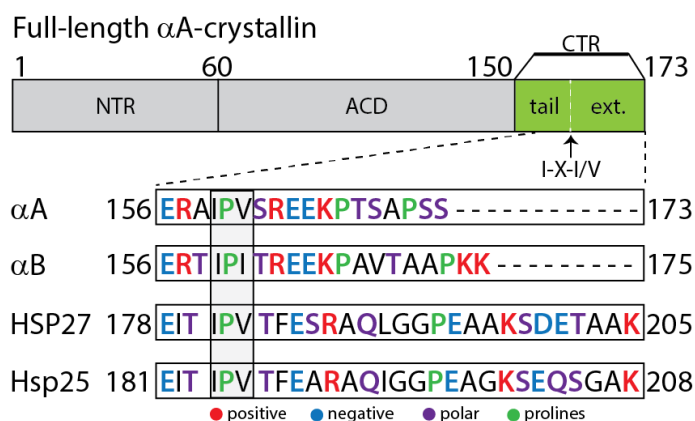


Fig. 4.57. The disordered C-terminal region of α A-crystallin contains an abundance of charged and proline residues. α A comprises three regions: the NTR, ACD and the CTR, which is further separated into the C-terminal tail and the C-terminal extension (ext., starting from end of the I-X-I/V motif through the C-terminus). The figure depicts an amino acid sequence alignment of CTRs from various mammalian sHsps. Shown here are human α A-crystallin (α A), human α B-crystallin (α B), human HSP27 and murine Hsp25. The I-X-I/V motif is boxed, while positively charged residues are coloured red, negative charged residues are blue, polar residues are purple and proline residues are green.

The CTR of α A contains an abundance of charged, polar and proline residues (Fig. 4.57), which are known to promote disordered backbone conformations in other sHsps (Theillet *et al.* 2014). Additionally, in crystal structures of α A, α B and HSP27 ACD-CTR complexes, the CTR forms an extended conformation, where the I-P peptide bond in the I-P-I/V motif adopts the trans-conformation, enabling penetration of the adjacent residues into the hydrophobic groove of the ACD. Here we report that the CTR of α A is predominantly disordered, and adopts distinct unfolded structural ensembles via cis-trans peptidylprolyl isomerization at its two proline residues, in both its reduced or oxidized state and the same implies to the CTD of α B at its three proline residues.

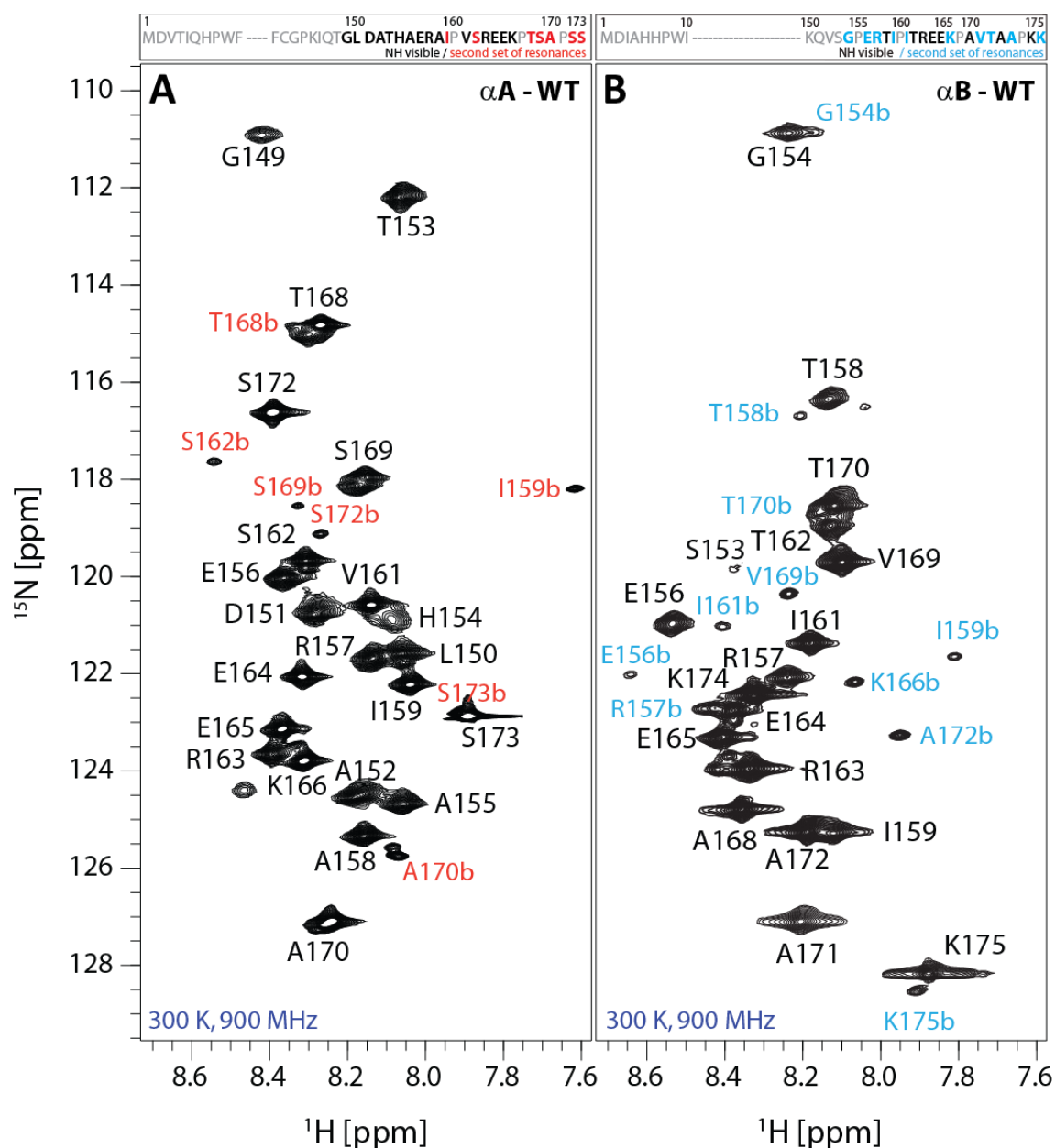


Fig. 4.58. Cis-trans proline isomerization in α A- and α B-crystallin. 2D ^1H , ^{15}N HSQC spectrum of $[\text{U-}^{13}\text{C}$, $^{15}\text{N}]$ - α A (A) and α B (B) at 300 K, 900 MHz and in 10 mM HEPES, 2 mM DTT, 1 mM EDTA pH 7.4 and 50 mM PBS, 100 mM NaCl pH 7.4 buffers, respectively. Each peak corresponds to an N-H bond and resonance assignments are listed next to each peak. The CTR sequence is shown at top. In the insets non-visible residues are shown in grey, NH visible residues in black and the doubled peaks in red (for α A) and blue (for α B) indicate the second set of peaks arising from the C-terminus for both proteins. Assignments for α B were obtained by Mainz *et al.* (2015).

Looking in our assignments of α A at lower contour levels, we noticed that a subset of CTR residues yielded two unique signals per residue, with appreciably different signal intensities. The same was observed for α B by Mainz *et al.* (2015), where 11 additional residues were observed for the entire C-terminal stretch S153-K175 (Fig. 4.58B). In case of α A, 6 additional CTR resonances were observed for residues I159, S162, T168, S169, A170 and S172, shown in Fig. 4.58A in red. Interestingly, the subset of residues with two NMR signals in α A are mostly clustered near a single proline residue, P171 (Fig. 4.58A, inset). This reveals two CTR conformational ensembles that interconvert with each other relatively slowly, on probably a timescale of seconds or longer. Importantly, this sequence also includes the conserved IPV motif, of which isoleucine methyl moieties have been reported to primarily populate a flexible, unbound state in case of α B-crystallin (Baldwin *et al.* 2012; Baldwin *et al.* 2011). Our results integrate and confirm previous solution-state and solid-state NMR data for α B (Baldwin *et al.* 2012; Baldwin *et al.* 2011; Jehle *et al.* 2010) and demonstrate that the IPI/V motif should exist for α A also in both a flexible and a rigid state. Furthermore, we can exclude the possibility that these doubled peaks are smaller oligomers or degradation products causing one of the two resonance sets for the CTR, because both conformational states possessed similar translational diffusion coefficients (Fig. 4.59).

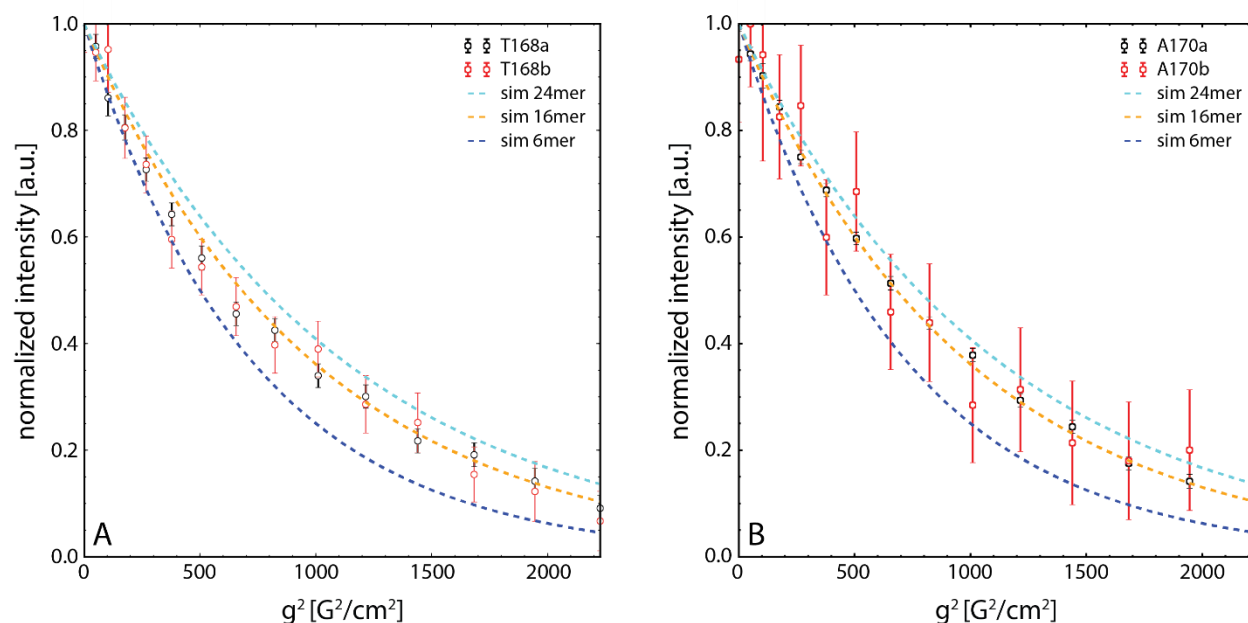


Fig. 4.59. Diffusion attenuation profiles. The major-a (black) and minor-b conformers (red) of the α A CTR are plotted for representative residues (T168 and A170). In all cases, both conformers decay equally. The average translational diffusion coefficient amounts to $5.43 \cdot 10^{-11} \text{ m}^2/\text{s}$ and it is the same within the error due to the spectral noise. The profiles were recorded at 300 K and an external magnetic field of 21.1 T. Simulation of attenuation profiles (dashed lines) for various α A n-mers as indicated in the legend.

In a disordered chain, the majority of the peptide bond conformations in protein structures are expected to predominantly adopt the *trans* conformation (>99.5%), while the *cis* conformation is about 0.5% for non-proline residues (X-non-Pro) (Ramachandran and Sasisekharan 1968) (Fig. 4.60A, right). For prolines, however, the situation is different. Peptide bonds involving proline residues (X-Pro) have an increased population of the *cis* conformation (5-15%) (Theillet *et al.* 2014; Weiss *et al.* 1998; MacArthur and Thornton 1991; Stewart *et al.* 1990) (Fig. 4.60, left). This rearrangement of the covalent bond is a very slow process, in a timescale of seconds or slower (Wedemeyer *et al.* 2002; Weiss *et al.* 1998; Grathwohl and Wüthrich 1981).

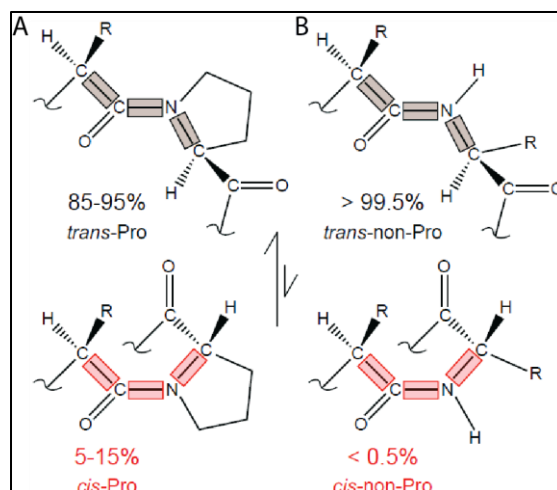


Fig. 4.60. Schematic depicting the propensity for X-Pro peptide bonds to form either *trans*- (black) or *cis*-proline (red) conformations. (A) An X-X-Pro peptide bond and (B) an X-X-non-Pro bond for comparison. Modified from Alderson *et al.* 2017.

Our observation of multiple resonances for residues in the vicinity of P171, hence alluded to potential *cis-trans* proline isomerization about the A170-P171 peptide bond. We directly assessed the possibility of a *cis*-Pro conformation in the A170-P171 peptide bond by analysing the ^{13}C side-chain chemical shifts in P171 (**Fig. 4.61A,B**). The difference in ^{13}C chemical shifts between Pro-C β and Pro-C γ nuclei is highly diagnostic of *cis* (~10 ppm) or *trans* (~5 ppm) peptide bond conformations (Shen and Bax 2010; Schubert *et al.* 2002). We correlated adjacent side-chain ^{13}C chemical shifts employing a 3D C(CO)NH experiment (Grzesiek *et al.* 1993), in order to show clear relations between resonances. Such an experiment reveals that the two resonances from S172 can be attributed to being directly adjacent to either the *cis* or *trans* form of P171. Similarly, additional minor peaks from other residues near P171, P167 and P160 arise from the formation of the *cis*-P171, *cis*-167 and *cis*-P160 bonds (**Fig. 4.61C-E**).

As there is a minor set of peaks existing for I159 and S162 in the ^1H , ^{15}N HSQC, which are in close proximity with P160, but no second set of peak is assigned to the *cis*-conformer for V161, and in order to address the likelihood of isomerization about the P160-V161 peptide bond, we therefore looked also at the ^1H , ^{13}C HSQC methyl region of αA . αA -crystallin contains only one Val in this region, and in the methyl region of the ^1H , ^{13}C HSQC of the peptide, we would actually expect only two peaks in absence of isomerization for V161. However, we observed more than two peaks arising from methyl-bearing residues (**Fig. 4.62A**, shown with red dashed boxes for V161 and I159). This indicates that there is *cis*-isomerization for P160 also, but the signal intensity of this minor population of V161 is maybe insufficient to be detected in a typical ^1H , ^{15}N HSQC spectrum. The appearance of additional resonances demonstrate that the peptide adopts multiple structural ensembles, with the most probable cause being proline isomerization. Given that the IPV motif is largely unbound in the oligomers, it is highly likely that P160 exists in both *cis* and *trans* forms. Together, these data clearly demonstrate that proline isomerization occurs for all proline residues of the CTR of αA .

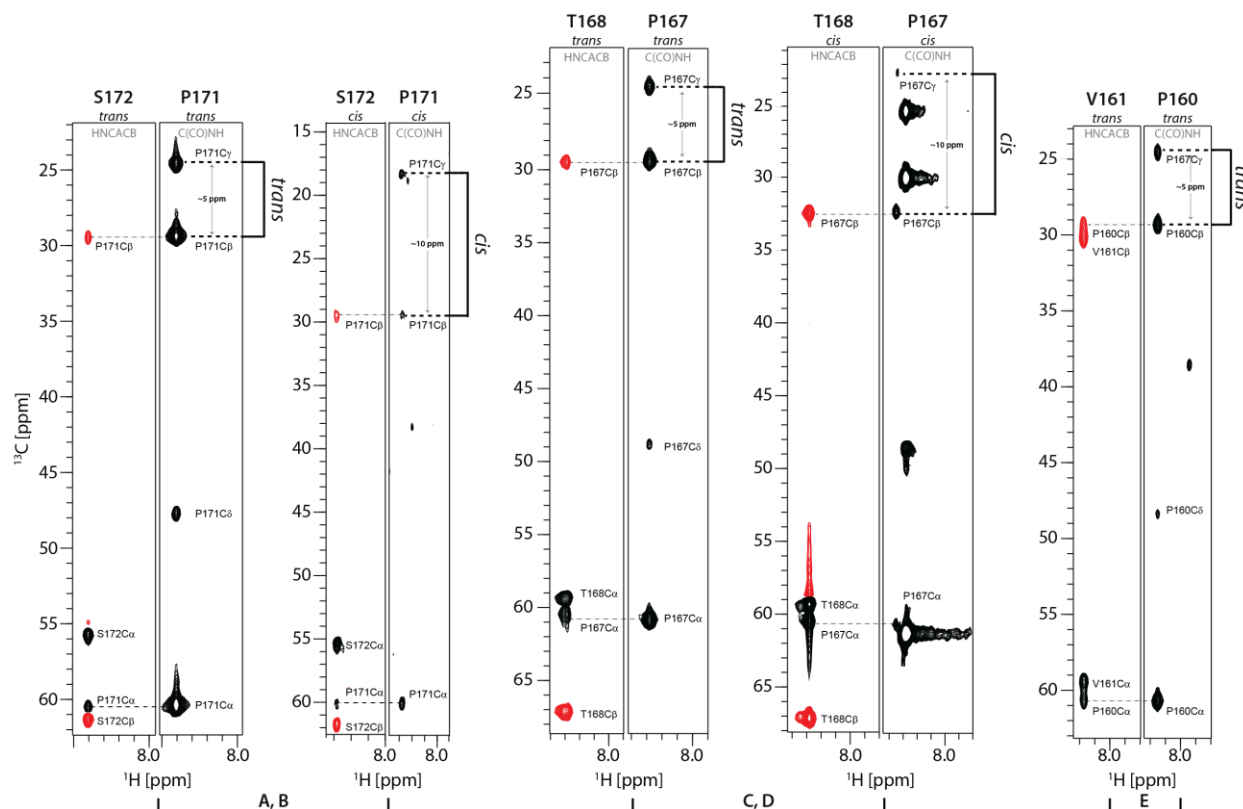


Fig. 4.61. 2D strip plots from 3D NMR spectra that were used to assign the *cis*- and *trans*-Pro conformations of the α A-crystallin C-terminal region. 2D strip plots from 3D HNCACB and 3D C(CO)NH spectra from [U - ^{13}C , ^{15}N]- α A. The 2D strips were taken at the ^{15}N frequency of the residue listed above the HNCACB strip. For the C(CO)NH strips, the ^{15}N frequency is at S172 (A,B), T168 (C,D) and V161 (E). (A, C, E) Strip plots from *trans*-P171, P167 and P160 showing the sequential assignment of residues that exist in the *trans*-P171, P167 and P160 conformation (B, D) Depicts the same strips as in (A, C), except that these resonances arise from *cis*-P171 and *cis*-P167. In the HNCACB, black peaks indicate the $^{13}\text{C}\alpha$ from the preceding and present amino acid and red peaks the $^{13}\text{C}\beta$. The C(CO)NH strip indicates the ^{13}C side-chain chemical shifts of each proline. The difference between $^{13}\text{C}\beta$ and $^{13}\text{C}\gamma$ chemical shifts in proline residues is diagnostic of *cis*- or *trans*-proline bonds. In the minor state, the $^{13}\text{C}\beta$ and $^{13}\text{C}\gamma$ chemical shift difference is ~ 10 ppm, indicative of a *cis*-conformation, whereas in the major state this difference is only ~ 5 ppm, indicative of a *trans*-conformation.

The NMR intensity signal is directly related to the nuclei resonating at a given chemical shift and reflects the population of a given conformation, provided that the two isoforms undergo similar dynamics. Using CCPN analysis software we extracted the peak intensities from both the *trans*- and *cis*-P171, P167 and P160 conformations, and calculated the population of the *cis* state in equimolar samples for both reduced or oxidized α A at 27 $^{\circ}\text{C}$ (Fig. 4.62B). The population for *cis*-P160 was about $\sim 6\%$, for *cis*-P167 about $\sim 15\%$ and for *cis*-P171 about $\sim 5\%$. Differences however, in *cis*-isomerization between the two kinds of samples are insignificant, as almost most of the peaks have a similar population percentage of the *cis*-state, except for A170, which is in about 17% in the reduced and around 14% in the oxidized form. Additionally, as the formation of *cis*-Pro can introduce β -hairpin conformations (Wedemeyer *et al.* 2002), and because NMR chemical shifts from backbone and side-chain nuclei can be highly sensitive to dihedral angles, hydrogen bonds and secondary structure, we further characterized the effect of the *cis*-isomerization on the backbone conformations in the CTR of α A (Fig. 4.62C). Therefore, we calculated the secondary chemical shift ($\Delta\delta$) difference between the observed chemical shift and the predicted chemical shift for a given residue in a random coil, and tested in either *trans* or *cis* form, if they adopt an entirely random coil conformation, or if they have a tendency to adopt residual local order. We observed relatively large $\Delta\delta$ values for residues in the vicinity of the conserved IXI/V motif, which we can attribute to their

adjacency to a proline residue (Shen and Bax 2010) and *cis*-P160 and P171 induced a small population of β -strand, whereas the *trans*-proline ensemble is more disordered in this region. For most residues in the *trans*-state, however, the $\Delta\delta$ values are near zero, indicating that both states remain dynamically disordered, but it is suggested for the residues in the *cis*-form that the $\Delta\delta$ values report on secondary structure, with significant deviations from zero over multiple residues reflecting mostly a tendency for β -strand conformation in the C-terminal extension. Furthermore, since the CTR is known to interact with the ACD in a β -strand conformation, the formation of residual β -strand structure in the CTR would be expected to influence binding to the hydrophobic β 4- β 8 groove (Hochberg *et al.* 2014; Laganowsky *et al.* 2010; Laganowsky and Eisenberg 2010).

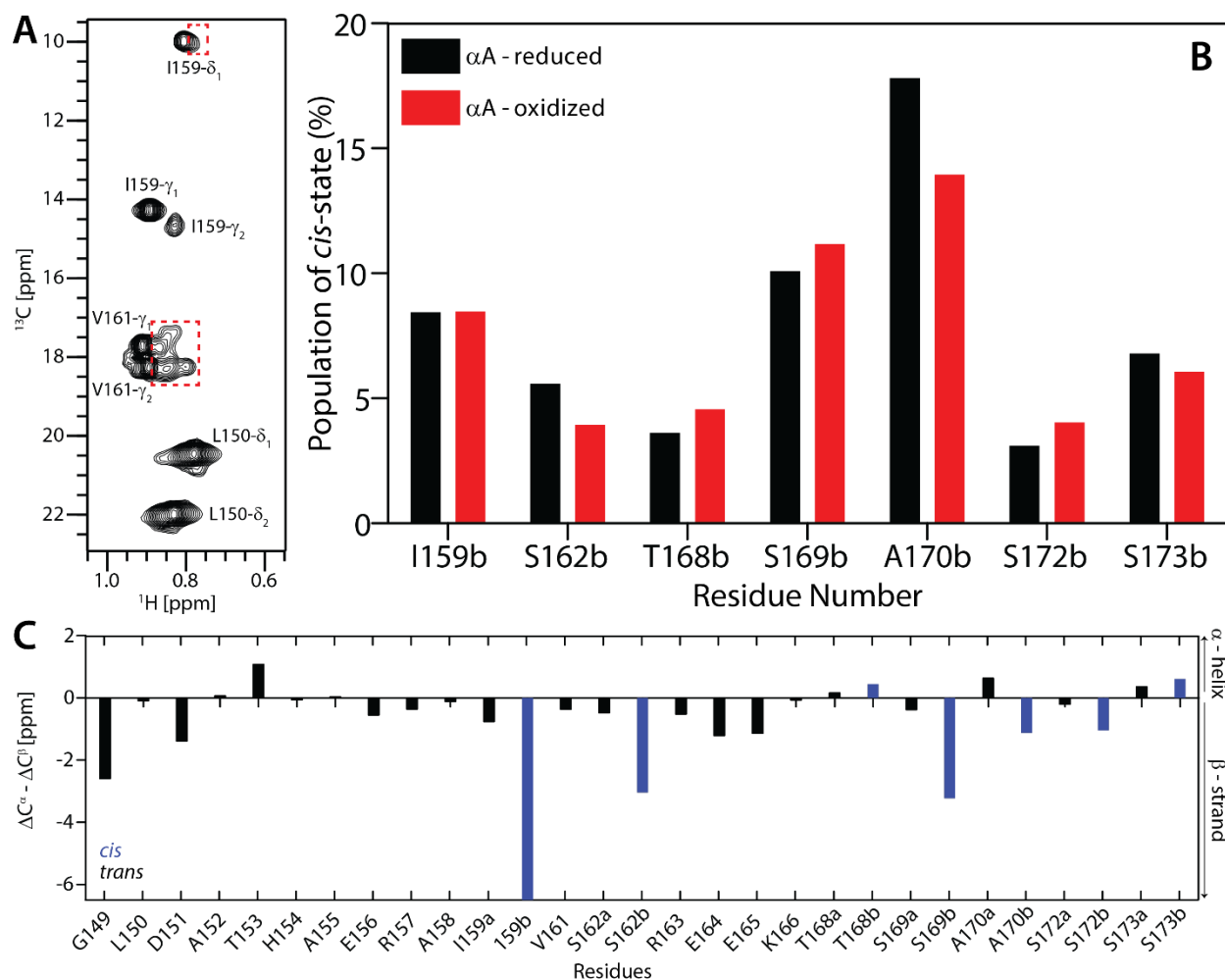


Fig. 4.62. Cis/trans isomerisation of reduced and oxidized α A. (A) Methyl region of the ^1H , ^{13}C HSQC spectrum of α A-crystallin. Red dashed boxes indicate additional Val and Ile peaks. (B) The population of *cis*-P171, P167 and P160 at 300 K is shown for each residue with well-resolved *cis* and *trans* peaks in the ^1H , ^{15}N HSQC spectrum for reduced (black) and oxidized (red) α A. (C) Carbon chemical shifts of the C-terminal region of α A plotted as a function of residue number for *cis*- (blue) and *trans*- (black) states. Difference of $\text{C}\alpha$ and $\text{C}\beta$ secondary chemical shifts ($\Delta^{13}\text{C}\alpha - \Delta^{13}\text{C}\beta$) for α A. A stretch, having negative values of $\Delta\text{C}\alpha - \Delta\text{C}\beta$, indicates β -strand sheet structure, whereas positive values indicate a regular α -helical regions.

To further characterize the potential impact of *cis*-proline formation on the internal dynamics of the CTR, we acquired ^{15}N spin relaxation data that probe motions on the picosecond timescale (Jarymowycz and Stone 2006). As the relaxation data of the reduced and oxidized form of α A are already presented in

Fig. 4.47, 4.48, here we plotted only the resonances that are affected by proline isomerization for both *trans*- and *cis*-states. For each residue in the CTR, we measured the hetNOE value, and R_1 and $R_{1,\rho}$ ^{15}N relaxation rates (**Fig. 4.63A**) at a 500 MHz spectrometer. For folded proteins, hetNOE values typically range from 0.65 to 0.85, while relatively flexible loops and regions with enhanced picosecond dynamics exhibit lower values. In the *cis*-state however, it is obvious that while for the reduced protein the two populations are similar, for oxidized αA the overall hetNOE values are significantly lower in the *cis*-state compared to the *trans*, a fact, which indicates that the minor population seems to be in a rigid state and not so flexible as the major one. The most important hetNOE value was obtained for I159, which reached near zero, and is the preceding residue of P160 (i.e. in the IPV motif)) and suggests that there is a conformational rearrangement of the protein structure upon *cis*-isomerization in oxidized αA . The overall resemblance of hetNOE values for both proline isomer states in the reduced αA demonstrates similar dynamical behavior, with picosecond-timescale motions throughout the CTR that increase toward the C-terminus for both conformations. This enhanced flexibility with increased distance from the ACD is similar to observations made in αB -crystallin (Mainz *et al.* 2015).

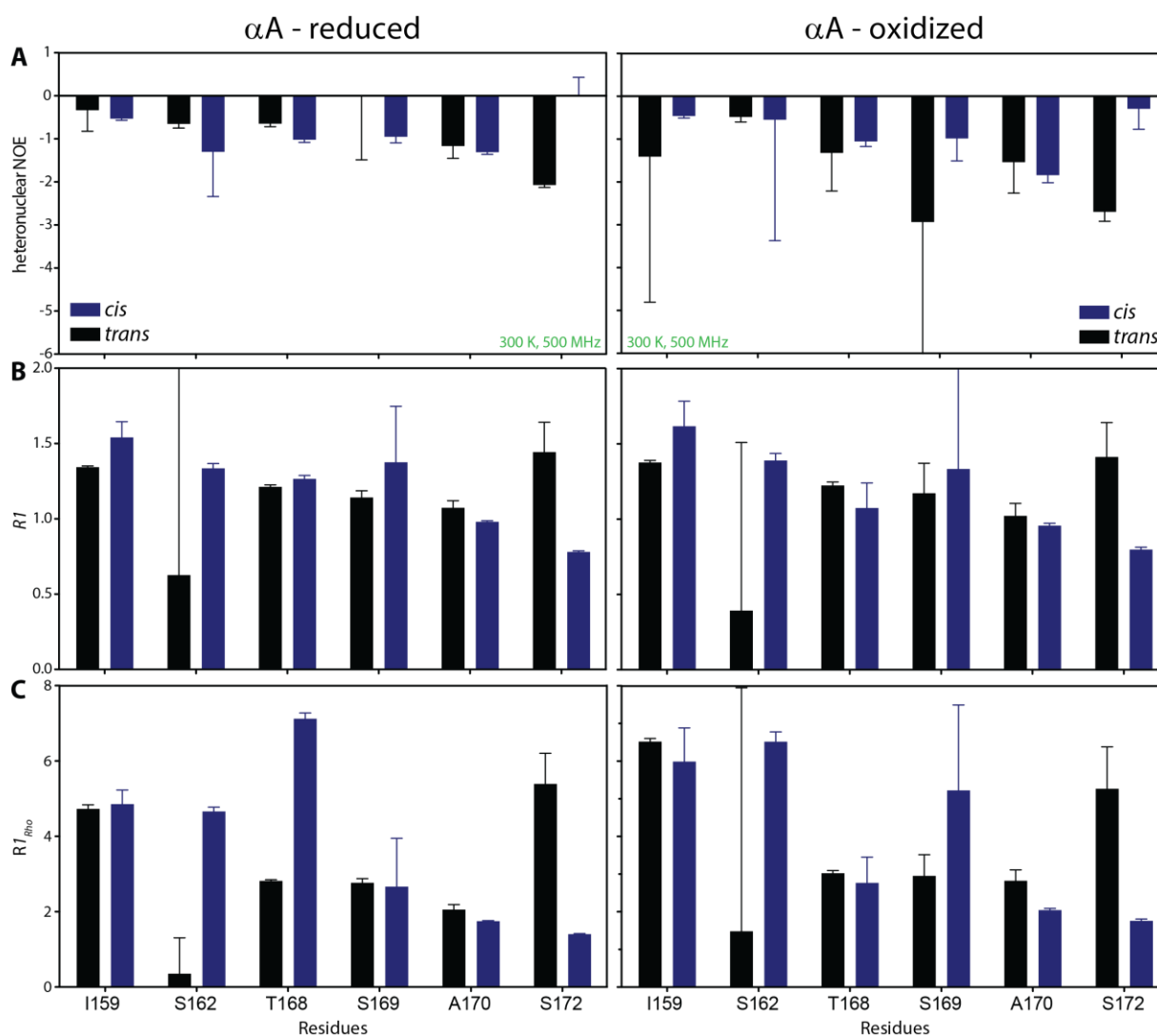


Fig. 4.63. Comparison of backbone motions for the *cis*- and *trans*-Pro conformations in the C-terminal region of αA -crystallin. ^{15}N relaxation data for the major state (black bars) and minor state (blue bars) of representative residues. Error bars were obtained from a monoexponential fit

of the experimental relaxation data. In panels (A) the ^1H , ^{15}N nuclear Overhauser enhancement (hetNOE), (B) ^{15}N longitudinal relaxation rate (R_1), and (C) the ^{15}N spin-lattice relaxation in the rotating frame ($T_{1\rho}$) are shown. All data were recorded at 500 MHz and 300 K.

^{15}N relaxation R_1 and $R_{1\rho}$ values obtained for the *cis*-P160 form show a significant increase compared to the *trans*, around the IPV motif (residues I159 - T168) (Fig. 4.63B,C), suggesting differential dynamics of the minor state for both reduced and oxidized αA . This observation was not however, prominent for the amide resonances of the C-terminal extension (i.e. residues S169 - S173). Taken together, our data have revealed that the CTR, including the IPV motif, is highly flexible and populates at least two different states that undergo very slow chemical exchange (on the picosecond-nanosecond timescale), with the magnitude of these motions increasing upon moving away from the ACD towards the C-terminus. Interestingly, amide resonances of N-terminal residues were not observed in the solution-state spectra, which underlines that the extreme N-terminus is fairly rigid. Given the importance of the CTRs of mammalian sHSPs in assembly and recognition (Treweek *et al.* 2015; Hochberg and Benesch 2014; Delbecq and Klevit 2013), we speculate that proline isomerization may play a role in regulating the assembly of sHsps.

5. Discussion

5.1. The Effect of Phosphorylation on α B Structure and Chaperone Function

The sHsp α B-crystallin is an important member of the cells network that aids in maintaining intracellular proteostasis under conditions of proteotoxic stress (Basha *et al.* 2012; Eyles *et al.* 2010; Haslbeck *et al.* 2005). The majority of sHsps, among them also human α B, show an unusual structural plasticity (Horwitz 2009). To understand the contribution of sHsps to the chaperone machinery of the cell, it is a prerequisite to uncover the mechanistic link between their structure, dynamics, and the regulation of substrate binding and chaperone activity. One key PTM that occurs in some human sHsps, including α B, is phosphorylation. Phosphorylation is often coupled to conformational changes and all major *in vivo* phosphorylation sites of α B are located within its NTD. This PTM changes the quaternary structure and dynamics of α B, whereby phosphorylation at either the three or six serine residues of the N-terminal region decreases the size of α B oligomers (Peschek *et al.* 2013), as it was also shown for other sHsps (McDonald *et al.* 2012; Hayes *et al.* 2009; Rogalla *et al.* 1999). However, there is no comprehensive survey performed on the specific effect(s) phosphorylation at each serine residue has on the oligomer size, oligomer distribution and chaperone function of α B. Consequently, the first aim of this thesis was to study the phosphomimicking α B-6E mutant with solution-state NMR.

In order to ascertain the role phosphorylation has on α B structure and chaperone function, a α B-6E mutant was produced, in which phosphorylatable serine residues were substituted with glutamates residues, i.e. S19E, S21E, S43E, S45E, S53E and S59E. The negative charges introduced by phosphorylation (mimetics) in the NTD do not seem to negatively influence client interactions. Hence, the existence of multiple sites, which undergo differential phosphorylation in response to diverse stress conditions, might allow tuning of the binding affinity of α B toward unfolded proteins according to the demands of the cell. To assess the effect of phosphorylation on α B quaternary structure, AUC experiments together with analytical SEC and SAXS were performed to examine how the PTM changes the oligomeric distribution of α B. This work showed that substitution at six serine residues had a significant impact on α B quaternary structure, reducing the size of α B oligomers, and led to dissociation of oligomers with the most predominant species composed of hexameric building blocks, i.e. 6-mers and 12-mers. When the α B-6D mutant was used, where serines residues were substituted by aspartic acid, i.e. S19D, S21D, S43D, S45D, S53D and S59D, the results were similar, but the stability of the protein was improved, as it was less aggregating compared to α B-6E mutant. This overall surface hydrophobicity of the phosphomimicking mutants, is the so-called order-to-disorder transition that has also been found in the context of client interactions for other chaperones (Reichmann *et al.* 2012; Chen *et al.* 2011; Tapley *et al.* 2009). In this case the proteins are more confined when engaged in intersubunit interactions in higher-order oligomers and more disordered when exposed to the solvent in smaller species.

Solution-state NMR was further employed to identify potential differences in the conformation of α B oligomers. However, due to sample heterogeneity, assignment of the observed resonances on the ^1H , ^{15}N HSQC spectra were not yet possible, but this study found that phosphorylation makes α B oligomers more unstructured (i.e. more flexible) in the N-terminal domain, less stable and concentration dependent. This may be favourable for the recognition of misfolded proteins since the lower molecular weight oligomers are more adaptable and flexible. The increase in flexibility of the NTD of the α B

dissociated oligomers observed may facilitate subunit-exchanging with the wild type protein and would therefore explain the observed promiscuity in adapting to multiple clients.

A strong correlation between oligomer dissociation and enhanced chaperone activity against amorphous and fibrillar client proteins was also observed using $A\beta_{40}$ as a substrate of αB -6E. The results of this work support a model whereby the lower oligomeric states are more effective chaperones than the larger oligomers. This enhanced function, combined with dissociation, suggests that the inter-dimer contacts maintained in oligomeric αB are disrupted by the negative charges introduced by phosphorylation. It appears that the large oligomers act as reservoirs of these chaperone-active smaller oligomers. As a result, it is proposed that phosphorylation acts as a molecular switch, activating αB under conditions of cellular stress in order to boost the overall protein quality control network in the cell.

Many studies have structurally and functionally characterised various point mutations of αB that have led to an apparent increase or decrease in chaperone function (Peschek *et al.* 2013; Santhoshkumar *et al.* 2009; Biswas *et al.* 2007; Sreelakshmi and Sharma 2006; Sreelakshmi and Sharma 2005; Bova *et al.* 1999; Horwitz *et al.* 1998a). The generally accepted mechanism of action by which sHsps become chaperone-active is by oligomeric dissociation and enhanced rate of subunit-exchange, whereby the population of smaller 'chaperone-active' species (i.e. monomers and dimers) are responsible for inhibiting protein aggregation. In contrast to Hsp27, where dimerization occurs via inter-molecular disulfide bonding of Cys137 that is located along the $\beta 6$ sheet of the ACD (Hochberg *et al.* 2014), αB dimer is mediated only by a charged network along the $\beta 6+7$ sheets (Hochberg *et al.* 2014; Bagneris *et al.* 2009). Previous studies of other human sHsps, have also shown that phosphorylated forms of Hsp27, are more efficient at inhibiting the amorphous and fibrillar aggregation of client proteins compared to Hsp27-WT (Jovcevski *et al.* 2015; McDonald *et al.* 2012; Hayes *et al.* 2009; Rogalla *et al.* 1999).

Future directions with this aspect of the project should focus on investigating the conformation of αB oligomers subunit-exchange using additional methods, except for solution- and solid-state NMR, such as FRET, native MS, SAXS or cryo-EM. This would help further to define whether the presence of dissociated species is either enhanced or diminished with mutation. In addition, chaperone activity assays to test the chaperone function of the N-terminal αB mutants against amorphous and fibrillar client proteins (such as κ -casein, $A\beta_{40/42}$, creatine phosphatase kinase, alcohol dehydrogenase and α -lactalbumin) should be performed to determine whether αB becomes 'hyperactive' across a range of client proteins. The chaperone system used in our study cannot completely mimic the sophisticated cellular folding machinery. However, such approaches may also provide information on role of the N-terminal domain in substrate binding and in order to find out whether N-terminal mutations significantly weaken/destabilize the inter-dimer contacts that maintain αB oligomers. Put together, these studies would reflect a greater physiological relevance in the cell as the population and abundance of all these potential protein species are likely to occur and interact *in vivo*. Overall, the results of the work presented in this chapter indicate that upon phosphorylation, the unstructured N-terminal domain of αB plays a key role in dictating oligomeric structure and dynamics of the protein and acts as a tunable conformational sensor in regulating αB activity against non-native proteins. It remains to be determined whether other triggers also activate the chaperone function of αB or sHsps according to this principle.

5.2. The Interaction of A β_{40} with α B and the Cu(II) Metal Ion

Despite more than a decade of intense studies, the roles of metal ions in the process of aggregation and amyloid formation by the amyloid- β peptide involved in Alzheimer's disease are still not well understood. However, A β was reported to be in affinity to Cu(II) in a micromolar range (Ghalebani *et al.* 2012). Given the proposed connection between metal ions and A β amyloid formation, metal chelation therapy has been tried and evaluated as a potential therapy against AD (Choi *et al.* 2010). However, the understanding is limited and the results are not conclusive, showing the need for further studies of the metal binding properties of the A β peptide. Additionally, solution- and solid-state NMR investigations have shown that α B also is able to coordinate Cu(II) with high affinity and that the potential binding site is between β -sheets 5 and 6+7 (Fig. 5.1), thereby suppressing the redox-chemistry and the cytotoxic effects of the transition metal (Ahmad *et al.* 2008).

In this study, we carried out titration experiments by adding Cu(II) to 15 N-labeled A β_{40} that suggested the major binding site, common for Cu(II) to be located within the N-terminus, close to positions H6, H13 and H14. We further added Cu(II) to the A β_{40} - α B complex and observed a competition in the copper binding between the two proteins. In the future, we would like to characterize this ternary complex consisting of A β_{40} - α B and Cu(II), using solid-state NMR experiments. The binding site of Cu(II) in the complex of both molecules could be used to determine the structure of A β_{40} in the bound state. In addition, solution-state titrations should be performed using labeled α B in combination with methyl-TROSY experiments to elucidate the effects of copper and A β_{40} (unlabeled) binding with respect to α B.

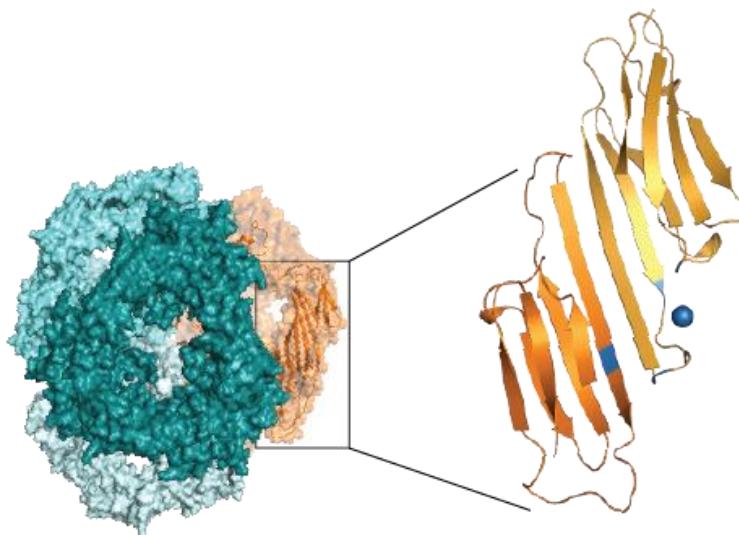


Fig. 5.1. Copper binding site between the β -sheets 5 and 6+7 in the ACD of α B-crystallin. The figure was designed using Adobe Illustrator CS6.

5.3. The Interaction of α B-Crystallin with Different Clients

The quaternary dynamics and high polydispersity of α B are considered to be essential for its chaperone function (Hochberg *et al.* 2014), but have hindered atomic-level structural analysis. The NMR data presented here show that monomers within the α B complex are not equivalent, supporting previous structural models in which an asymmetric dimer builds up the tetrahedral α B 24-mer (Braun *et al.* 2011;

Jehle *et al.* 2010). For example, peak doubling of I133 can be rationalized by its different chemical environment in the bent and extended conformer (**Fig. 1.8**). Structural heterogeneity is induced by the different arrangement of NTDs and CTDs in α B oligomers.

Solution-state NMR and detailed ^{13}C secondary chemical shift analysis demonstrated that the sequence $\text{Q}_{15}\text{KLVFFA}_{21}$ of monomeric $\text{A}\beta_{40}$ exhibits considerable propensity for β -strand conformation. Intriguingly, the region $\text{Q}_{15}\text{KLVFFAEDV}_{24}$ has been reported to be involved in intermolecular contacts $\text{A}\beta_{40}$ molecules in oligomeric assemblies of the peptide. In addition, the sequence $\text{Q}_{15}\text{KLVFFAEDV}_{24}$ was also identified as the major interaction site with the molecular chaperone α B (Narayanan *et al.* 2006).

Previous NMR studies have shown that α B competes for $\text{A}\beta_{40}$ monomer-monomer interactions by transiently binding to the hydrophobic core of $\text{A}\beta_{40}$ (Narayanan *et al.* 2006). Our NMR titration experiments yielded small CSP upon addition of α B to monomeric $\text{A}\beta_{40}$. These effects occurred in a defined region of the ACD and hence point towards the interaction site with the amyloid peptide. Accordingly, the β 4- β 8 groove of the ACD was unambiguously identified as the binding site for monomeric $\text{A}\beta_{40}$ (Mainz *et al.* 2015). This region is one of the reported candidate binding sites for client proteins (Ghosh *et al.* 2005). The β -sandwich of α B resembles the β -strand assembly of $\text{A}\beta_{40}$ fibrils and appeared to play an important role in molecular recognition of amyloid aggregates. In fact, the excised ACD inhibits fibril formation of $\text{A}\beta_{40}$, but also of other amyloid clients such as κ -casein and $\text{A}\beta_{42}$ (Hochberg *et al.* 2014). Likewise, α B- δ NTD was capable of inhibiting amyloid formation of $\text{A}\beta_{40}$ similarly to α B WT. This demonstrates that α B- δ NTD, despite its potentially altered oligomer architecture, retained chaperone function toward an amyloidogenic client, thus highlighting the importance of the ACD in this process. Binding of the ACD to these β -rich species might be governed by the accessibility of β -strand edges in the growing aggregate, so that α B can compete for fibril growth. Our results hint at an intervention of α B in both phases of amyloidogenesis: (i) transient interaction with amyloid building blocks, which may possibly be sufficient to hinder the slow fibril nucleation process (Cohen *et al.* 2015) and (ii) inhibition of fibril elongation through binding of α B to the termini of protofibrillar structures, as suggested previously (Shammas *et al.* 2011). At higher abundance, α B also adheres to the walls of $\text{A}\beta_{42}$ fibrils, thereby affecting their elongation (Shammas *et al.* 2011). In order to prove this protofibril capping of α B bound to $\text{A}\beta_{40}$, we recorded additionally negative stained EM images, with immunogold labeled α B and observed that the chaperone is mostly bound on at the edges of (capping) the amyloid client, but it was also found to be only at the one side of the fibril (**Fig. 4.33**) or all along the fibrils in different positions. Therefore, an additional statistical analysis of different ratios between the two interacting proteins is required in order to evaluate the results better.

In this work, EM images revealed that $\text{A}\beta_{40}$, which is co-incubated with α B, is impaired in generating mature amyloid fibrils. The presence of α B inhibits the propagation of large $\text{A}\beta_{40}$ aggregates and mature fibrils. It has been shown that the intervention of α B and the accompanying inhibition of fibril formation can increase the toxic effects of $\text{A}\beta_{40}$ in cultured neurons (Stege *et al.* 1999). Extending the incubation time finally leads to the formation of insoluble aggregates and protofibrillar structures. This observation might reflect the diagnostic finding of co-aggregated α B in amyloid plaques in the brains of AD patients (Wilhelms *et al.* 2006). These ' α B-mediated' aggregates of $\text{A}\beta_{40}$ were investigated using MAS solid-state NMR spectroscopy. The obtained spectra demonstrate that catalytic amounts of α B force $\text{A}\beta_{40}$ to follow a different aggregation pathway or to pause at an intermediate stage and multiple sets of resonances were observed, e.g. for residue S26. The structural state of $\text{A}\beta_{40}$ and its higher-order assemblies is thus altered by the chaperone. Further studies are envisaged to characterize the architecture of these assemblies in more detail and to understand the role of α B in their formation. Moreover, the addition of α B to fibril

seeds will be a key aspect for solid-state NMR investigations in the future. These experiments will allow to elucidate the chaperone mechanism of α B with respect to the inhibition of A β fibril elongation.

In contrast to binding of an amyloid client, binding of the amorphously aggregating lysozyme occurred at the partially disordered NTD of α B. Intervention of α B in amorphous aggregation of lysozyme and in fibril formation of A β ₄₀ has fundamentally different mechanisms. These findings may not be applicable for the entire interactome of α B, i.e., conformational ensembles of hundreds of misfolded proteins, but they may disclose some general principles in antiaggregation strategies of sHsps. The picture of a chaperone, which captures destabilized proteins by structurally mimicking their key conformational properties, appears to be intuitive, but needs to be validated in future experiments with a wider range of clients.

5.4. Dynamic Fluctuations of the C-terminal Region of the Human α A-crystallin

The number of solution structures determined by NMR has been growing rapidly since the first NMR protein structure determination in 1985 (Kaptein *et al.* 1985; Williamson *et al.* 1985). However, the structure of the human α A-crystallin is yet to be elucidated. α A-crystallin is a protein of 173-residues with a mass of 19.9 kDa (Groenen *et al.* 1994), containing two naturally occurring cysteines (Cys-131, Cys-142) responsible for its redox sensitivity. Here, we have probed the conformation and dynamics of the flexible and unstructured C-terminal region of α A by means of solution-state NMR spectroscopy using non-deuterated samples. In this study, we were able to observe and assign an additional 10 residues within the disordered CTR of α A over those described previously (Treweek *et al.* 2010), likely due to our usage of modern hardware, a higher magnetic field strength, and [¹³C, ¹⁵N]-labeled samples, and we could **thus probe the conformations and dynamics of the final 24 residues. Similarly, a recent NMR investigation** of the CTR in human α B and HSP27 was able to extend the number of observed residues to ~25 (Mainz *et al.* 2015) and to ~28 (Alderson *et al.* 2017), respectively. The extensions of the above mentioned sHsps are therefore predominantly disordered at physiological solution conditions. Interestingly, the IPI/V motifs in all cases are primarily detached from the oligomers, and therefore only make transient interactions with their own ACD or adjacent ACDs.

As the CTRs of α -crystallins are highly flexible, unstructured and solvent accessible, they give rise to well-resolved solution-state NMR spectra. The detailed analysis of chemical shifts and relaxation properties, reveals that the CTR of α A is also highly dynamic and that rapid motions take place on the picosecond timescale, as shown previously for α B (Treweek *et al.* 2010) and HSP25 (Esposito *et al.* 1998). Moreover, the presence of unassigned cross-peaks in the HSQC spectrum that arise from residues outside of the flexible C-terminal extension of α A is consistent with α -crystallins being highly dynamic and malleable species, and these conclusions are in agreement with previous NMR studies of the flexible CTRs of mammalian sHsps α A and α B (Mainz *et al.* 2015; Delbecq *et al.* 2015; Baldwin *et al.* 2012; Treweek *et al.* 2010; Carver and Lindner 1998; Smulders *et al.* 1996; Carver *et al.* 1995b; 1992), HSP27 (Carver and Lindner 1998), Hsp20 (van de Klundert *et al.* 1998), and Hsp25 (Lindner *et al.* 2000; Carver *et al.* 1995a), in which the final 10-15 residues were amenable to NMR investigation under non-heat-shock conditions.

Detailed interrogation of the CTR in α B has revealed that in solution and above 0 °C, the IPI/V motif is transiently bound to the ACD (Baldwin and Kay 2012; Baldwin *et al.* 2011a), and that the independent binding of two CTRs, either in an intra- or inter-molecular manner, triggers the dissociation of a monomer from an oligomer (Baldwin *et al.* 2012; 2011b). These interactions appear to be finely tuned to regulate

both sHsp assembly and hetero-oligomerization (Delbecq *et al.* 2015; Hochberg and Benesch 2014). In addition, mutations for example in the CTR of HSP27 are implicated in neuromuscular and neurodegenerative diseases including amyotrophic lateral sclerosis (Capponi *et al.* 2016) and Charcot-Marie-Tooth disease (Ylikallio *et al.* 2015; Chalova *et al.* 2014). The high density of PTMs and disease-associated mutations in the CTR of different sHsps allude to a significant functional role for this region in health, and malfunction in disease.

In this work as a first step towards the structural characterization of the human α A by NMR spectroscopy and in order to examine the backbone dynamics of α A in solution, we were able to assign the backbone of ^{15}N , ^{13}C -labeled α A, i.e. residues G149–S173, as well as the side chains, and additional NMR signals for residues in the vicinity of prolines 160, 167 and 171. We looked at both, its reduced and oxidized form. However, the oxidized form in our biochemical assays appears to be much bigger than the reduced, our NMR spectra have shown that there is no significant chemical shift alteration of resonances in the C-terminal extension between them. The highest observed chemical shift change arises particularly for residues A170 till S173, which show higher flexibility. Flexibility in the C-terminal extension plays a key role in maintaining the solubility of the α -crystallin oligomer itself, and also that of the chaperone complex (Carver 1999).

The considerable flexibility in the region from A158 to S173 of α A is evident with hetNOE values. The A158 to R163 region (that contains the IPV-motif) acts as a ‘hinge’ for the C-terminal extension and is critical for oligomeric assembly of wheat Hsp16.9 (van Montfort *et al.* 2001a). The IXI motif in α B (I159, P160 and I161) also interacts with residues towards the end of the ACD in adjacent subunits in the absence of a target protein (Pasta *et al.* 2004). The ^{15}N $T1/T1_{\text{rho}}$ ratio for I159, for instance, is about 3.52, which is consistent with respective ratios previously determined for highly mobile regions of other proteins, e.g. insulin-like growth factor-1 (Laajoki *et al.* 2000). The greatest degree of flexibility is seen in the ultimate C-terminal residue of α A, with a ^{15}N hetNOE value of -2.54 for the reduced and -3.44 for the oxidized α A. This value is significantly large when compared with studies on interleukin-4, where ^{15}N NOE value of approximately -0.4 was reported, for mobile regions of the protein (Redfield *et al.* 1992). Flexibility of the C-terminal extension of wild type α B is reduced compared to that of wild type α A (hetNOE value of K175 of about -1.69) and is only observed for E164 to K175, i.e. the preceding residues encompassing the IPI-motif, which is additionally confirmed by the detection of more residues for α A (G149-S173) than α B (G154-K175) in the NMR spectra. The greater flexibility and length of α A-crystallin’s C-terminal extension can be explained by its enhanced thermostability compared to α B (Abgar *et al.* 2000; Liang *et al.* 2000; Sun *et al.* 1997). These observations combined however, show that the motions at the end of several mammalian CTRs are effectively uncoupled from the slowly tumbling oligomers, and behave like an unstructured peptide.

5.5. *Cis-trans* Proline Isomerization in the CTR of α A-crystallin

Furthermore, we observed multiple NMR signals for residues in the vicinity of prolines 160, 167 and 171, and the CTRs of α A appeared non-equivalent and populated a minimum of one mobile, as well as one immobile conformer. This reflects a heterogeneous architecture of α A and the possible role of asymmetry in its dimeric building block. We determined that, while all observed forms are highly disordered, the extra resonances arise from *cis-trans* peptidyl-prolyl isomerization of the peptide bonds at the positions of the proline residues (about the I159-P160 (IPV motif), K166-P167 and A170-P171 peptide bonds). Similar results were also shown previously for α B-crystallin (Mainz *et al.* 2015) or recently for HSP27 (Alderson *et*

al. 2017). Regarding α B, the occurrence of multiple sets of resonances for the ACD and CTD in solid-state and solution-state NMR spectra of α B raised the question of whether these observations originate from the same structural feature. In the tetrahedral 24-mer model, the extreme N- and C-termini of the bent conformer (CTD_{bent}) are accessible for proteolytic degradation, whereas both termini of the extended conformer (CTD_{ext}) reside in the inner cavity of the complex. The observation of mobile and immobile states might thus reflect the variable flexibility of CTD_{bent} and CTD_{ext} (Mainz *et al.* 2015). In case of HSP27 the inter-conversion between *cis*- and *trans*-Pro conformations within the G193-P194 peptide bond was shown to be slow and the *cis*-P194 conformation is populated to ~15% at near-physiological solution conditions (Alderson *et al.* 2017).

The *cis*-Pro state is populated to near 6% at physiological temperatures, and, although both *cis*- and *trans*-P160 forms of the CTR are highly dynamic, we determined that the *cis*-Pro state of the CTR ensembles has the tendency adopt β -strand conformations between residues 159 and 162, encompassing the IPV motif. Formation of residual β -strand structure in residues 159-162 could facilitate both docking of the hydrophobic IPI/V motif and hydrogen bonding between the ACD and CTR. Alternatively, the residual structure could also enable inter-molecular interactions with another sHsp CTR, or a substrate protein in a similar conformation. In addition, we note that *cis*-P171 leads to a similar increase in β -strand propensity between residues 169 and 172, while P167 and residues around it have a small tendency to α -helical conformations.

For the proline residue in the CTR of α A situated within the highly conserved IPV motif, we cannot certainly conclude that *cis-trans* isomerization of P160 takes place since the chemical shifts near this residue are weak, rendering a lowly populated and unobservable *cis* conformation. However, looking at the methyl region of α A in the ^1H , ^{13}C HSQC spectra, we observed more NMR signals than would be expected from the amino acid sequence, which likely indicates *cis-trans* isomerization about the I159-P160-V161 peptide bonds. This is further supported for residues near P160 and P182 in the IXI motif of human α B (Mainz *et al.* 2015) and HSP27 (Alderson *et al.* 2017), respectively. This combined evidence suggests that α A, α B and HSP27 undergo *cis-trans* proline isomerization in the IPI/V motif. *Cis-trans* proline isomerization about the I159-P160 bond could play a significant role in α A oligomerization and based on other studies it is expected that the conformation of the CTR has a higher affinity to be bound in the hydrophobic groove of the ACD in its *trans*-P160 form (Hochberg *et al.* 2014; Hilton *et al.* 2013b).

5.6. Possible Roles for *Cis-trans* Proline Isomerization in the Cells

In the cells, *cis*-proline isomerization plays a fundamental role within a variety of biological implications (Sarkar *et al.* 2007) as it was found that it often regulates the rates with which proteins fold (Wedemeyer *et al.* 2002) or that can induce structural changes in membrane-embedded receptors (Lummi *et al.* 2005). For example, a *cis*-Pro bond in HSP70 has been proposed that regulates the allosteric transition between nucleotide- and substrate-bound states (Vogel *et al.* 2006; Alderson *et al.* 2016). Therefore considering the evidence of allosteric communication between the contact the CTR transiently makes with the ACD, and the dimer interface in HSP27 also (Delbecq *et al.* 2012; Hochberg and Benesch 2014), the *cis*-P182 and *cis*-P194 bonds affect the oligomerization and its interactions with cellular targets (Alderson *et al.* 2017).

Furthermore, changes between *cis* and *trans* conformations are found to be associated with the evolution of new functions facilitated by local structural changes. This is most frequent in enzymes, where new

calalytic activity emerges with local changes in the active site. *Cis-trans* changes are also seen to facilitate inter-domain and inter-protein interactions. As in the case of folding, *cis-trans* conversions have been used as an important driving factor in evolution (Pahlke et al. 2005). The possible biological role of the *cis/trans* isomerization, especially for prolines, in protein folding, splicing, active transport through membranes, and energy reservoir is still a matter of some debate (Andreotti 2003; Fischer and Aumuller 2003). Collectively, the existing data indicate a potential role for *cis-trans* proline isomerization in regulating the oligomerization of sHsps.

5.7. The Polydispersity of α A-crystallin

The crystallins are the major proteins of the eye lens, the refractive power of which is achieved by their enormously high protein concentration (human 400 mg/mL, rat 900 mg/mL, and blue eyed trevally fish 1100 mg/mL). Therefore, much study has been devoted to understanding how the lens remains transparent, despite its high protein concentrations, and on how crystallins prevent aggregation (Pierscionek and Augusteyn 1995; Benedek 1993; Delaye and Tardieu 1993; Veretout et al. 1989; Philipson 1969). Additionally, crystallization of proteins in the eye lenses destroys lens transparency and must be prevented in functional lenses. However, although pure substances readily crystallize from solutions at high concentrations, polydisperse and heterogeneous substances tend not to crystallize. Thus, evolution of molecular mechanisms to ensure polydispersity of the crystallins would be one type of protection against lens crystallization.

It was shown that X-ray crystallography, as well as solution-state NMR have been successful to study the central ACD of α B by using N- and C-terminally truncated α B variants (Mainz et al. 2012; Bagneris et al. 2009). Moreover, the structure of truncated human α A is so far not known, and only the crystal structures of truncated bovine (Laganowsky et al. 2010a) and zebrafish α A (Laganowsky et al. 2010b), lacking the NTR, but containing part of the C-terminal extension (CTE) that functions in chaperone action and oligomeric assembly, have been solved. In the bovine case, the crystal structure of the truncated form of bovine α A (residues: 59–163) was presented, where the CTE swaps into neighboring molecules, creating runaway domain swaps. This interface enables crystallin polydispersity because the CTE is palindromic and thereby allows the formation of equivalent residue interactions in both directions (Laganowsky et al. 2010a). In contrast to the bovine α A, the zebrafish crystal structure revealed that the CTEs are in a non three-dimensional (3D) domain swapped, “closed” state and the extension here is quasi-palindromic, bound within its own zebrafish core domain (Laganowsky et al. 2010b).

Regardless of whether the CTE of human α A is in a swapped or closed state, the C-terminal hinge loop maintains structural rigidity, while offering enough structural flexibility to enable various oligomeric interactions. In this work we carried out paramagnetic relaxation enhancement (PRE) experiments with the full-length protein, where we could confirm the cryo-EM hypothesis that a small amount of ca. 20% of the CTR of α A is in a domain swapping state, indicating that it can form both, transient intra- and inter-molecular interactions with adjacent oligomers. Our observation, together with the work of Eisenberg and co-workers (Laganowsky et al. 2010a; Laganowsky et al. 2010b) that the CTEs can be found in either a 3D domain swapped or closed state, and that the palindromic nine amino acid sequence centred around P160 enables equivalent inter-subunit interactions when aligned in opposite directions, provides another molecular mechanism by which α -crystallins facilitate polydisperse oligomeric assemblies. This evolved polydispersity is crucial for eye lens transparency.

Until now our focus was in studying the CTR of α A in solution-state NMR. In the future, our investigations should be extended on the structural characterization of the truncated human α A. Therefore, we already carried out preliminary biochemical assays and solution-state NMR experiments on a construct containing residues 62-166, which showed that the overall size of α A oxidized₍₆₂₋₁₆₆₎ is increased compared to α A reduced₍₆₂₋₁₆₆₎, and it forms higher molecular weight oligomeric ensembles that appear to possibly be in a tetrameric state (of about 80 kDa). Furthermore, ^1H , ^{15}N HSQC spectra indicate a partially folded protein, however the presence of the CTR makes the sample more heterogeneous and based on our PRE hypothesis, the CTE may be domain swapped to a neighboring α A oligomer. Due to the existence of the CTE, assignment experiments for this sample were not feasible till now. Therefore, we suggest to use later on another α A construct containing only the ACD resonances, i.e. residues 62-152, in order to simplify the spectral resolution and make the assignment of the NMR spectra possible. Finally, recording assignment experiments with PEG-precipitated sample on the full-length protein will allow us to contribute in the structural characterization of the wild-type α A-crystallin.

6. Conclusions and Future Remarks

Defining the structure-function relationship of sHsps is crucial to understanding the mechanisms involved in maintaining intracellular proteostasis. More importantly, delineating this relationship has the potential to inform therapeutic design, whereby the activation of sHsps is enhanced to combat neurodegenerative diseases that are associated with protein aggregation. For example, drugs could potentially be designed that trigger the dissociation of large sHsp oligomers into chaperone-active dimers, which would be ideal to inhibit and prevent protein aggregation.

There is much more work that needs to be done to further our understanding of the structure, function and interactions of sHsps within the cell. It is well-known that various sHsp family members undergo subunit-exchange *in vitro* and *in vivo* and form large hetero-oligomers. Some of these hetero-oligomers have been previously studied, predominantly Hsp27/ α B (Aquilina *et al.* 2013; Bova *et al.* 2000), α A/ α B (Morris and Aquilina 2010; Aquilina *et al.* 2005), Hsp16.9/Hsp18.1 (Sobott *et al.* 2002) and more recently Hsp27/Hsp20 (Heirbaut *et al.* 2016; Bukach *et al.* 2009). However, all of the above mentioned studies have only investigated the wild-type (WT) isoforms of each sHsp. The hetero-oligomerisation dynamics between WT and phosphorylated isoforms has not been addressed. It is very likely that there are distinct populations of sHsp oligomers in cells that contain both non-phosphorylated and phosphorylated forms of various sHsps. These likely form a wide range of oligomeric forms of sHsps in cells, much more complicated than the 'simple' oligomers that have been studied in most work to date.

Our current understanding of sHsps has been attained using purified recombinant proteins in relatively simple buffer systems. However, it remains to be determined whether the structure and dynamics of sHsps is similar in the presence of other non-interacting proteins and/or crowding agents that can mimic the intracellular environment. The optimal crowding agent or non-interacting protein would be the one that does not undergo subunit-exchange with sHsps, does not covalently attach to or modify sHsp residues, and does not directly contribute to aggregation. A great example for this would be polyethylene glycol (PEG). Previous studies have shown e.g. that the molecular crowding agent trimethylamine N-oxide (TMAO) induced oligomerisation of Hsp20-WT, but had no effect on the oligomerisation state of phosphorylated Hsp20 (Sluchanko *et al.* 2015). The presence of crowding agents (such as dextran, PEG, Ficoll and TMAO) lowered also the subunit-exchange rate and decreased chaperone activity (Roman *et al.* 2011; Ghahghaei *et al.* 2007). Investigating the effects of molecular crowding on sHsps could provide a more relevant picture of their structural characteristics and how changes that occur to structure translate to differences in chaperone activity.

The primary focus of this thesis was to study the quaternary structure and dynamics of the human sHsps, α B and α A-crystallin, and especially their disordered CTRs, in order to rationalise the effects these have on the capacity of these proteins to act as molecular chaperones by inhibiting protein aggregation. Due to the large and heterogeneous nature of these mammalian sHsps, this work primarily employed solution- and solid-state NMR spectroscopy to study the structure and dynamics of these molecular chaperones. A detailed analysis in solution NMR was undertaken on α A-crystallin, and in its reduced and oxidized form, as the human α A is not a well-studied protein and little data exist regarding its structure and function. The results of this work highlight the important role that sHsps have in regulating protein aggregation. Here we provided quantitative data on the backbone flexibility of individual residues in the C-terminal extensions of α A. In addition, the role of the C-terminal prolines in modulating the structure and function of α A was assessed and we found that the all proline residues (P160, P167, P171) within the CTR undergo *cis-trans* isomerization, but also that P160 leads to an increase in a β -strand structure in residues 159-162.

We speculate that *cis-trans* proline isomerization is a feature of those mammalian sHsp CTRs that are flexible, in particular α A, α B and HSP27 and given the fact that these human sHsps have the most widespread expression, are up-regulated during cell-stress conditions and have the largest number of interactors (Mymrikov *et al.* 2017; Kampinga *et al.* 2015), it is possible that the dynamic fluctuations of their CTRs play an important role in their canonical sHsp chaperone activity and oligomerization.

Overall, the results of the work presented here emphasise the key role the quaternary structure has on the function of these mammalian sHsps, both of which are crucial parts of the network that acts to maintain proteostasis in cells. A better understanding of the mechanisms involved in regulating the structure-function relationship of sHsps provides new targets for therapeutic development. Enhancing the ability of sHsps to inhibit and prevent protein aggregation may one day lead to the development of a drug to treat a range of devastating neurodegenerative diseases.

7. Appendix

7.1. Vector Maps

Supplementary Table S1. The vector maps and the multiple cloning site of the commercially available vector pET28a(+) and pET-30 Ek/LIC (Novagen), which were used in the scope of this thesis for expression and cloning purposes.

pET-28a(+) sequence landmarks	
T7 promoter	370-386
T7 transcription start	369
His•Tag coding sequence	270-287
T7•Tag coding sequence	207-239
Multiple cloning sites (<i>Bam</i> H I - <i>Xho</i> I)	158-203
His•Tag coding sequence	140-157
T7 terminator	26-72
<i>lacI</i> coding sequence	773-1852
pBR322 origin	3286
Kan coding sequence	3995-4807
f1 origin	4903-5358

The maps for pET-28b(+) and pET-28c(+) are the same as pET-28a(+) (shown) with the following exceptions: pET-28b(+) is a 5368bp plasmid; subtract 1bp from each site beyond *Bam*H I at 198. pET-28c(+) is a 5367bp plasmid; subtract 2bp from each site beyond *Bam*H I at 198.

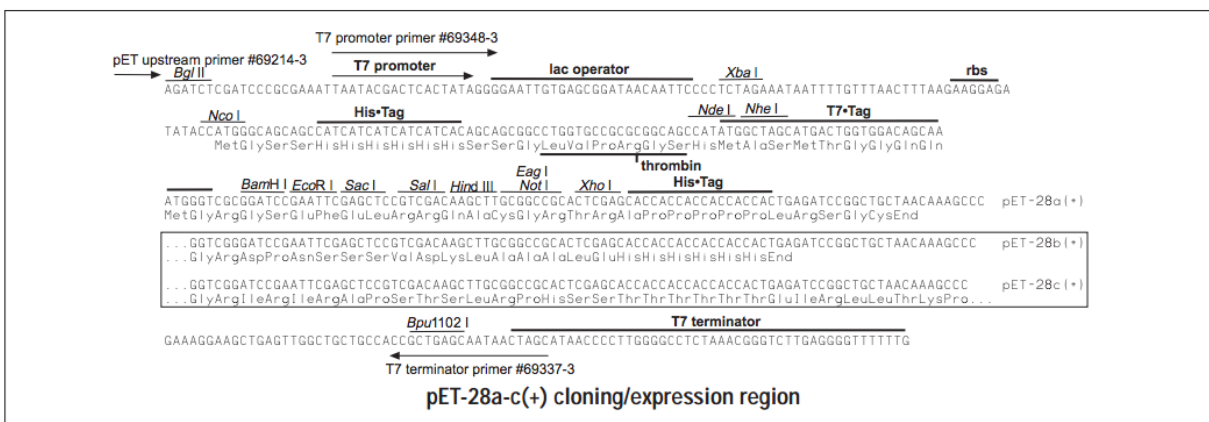
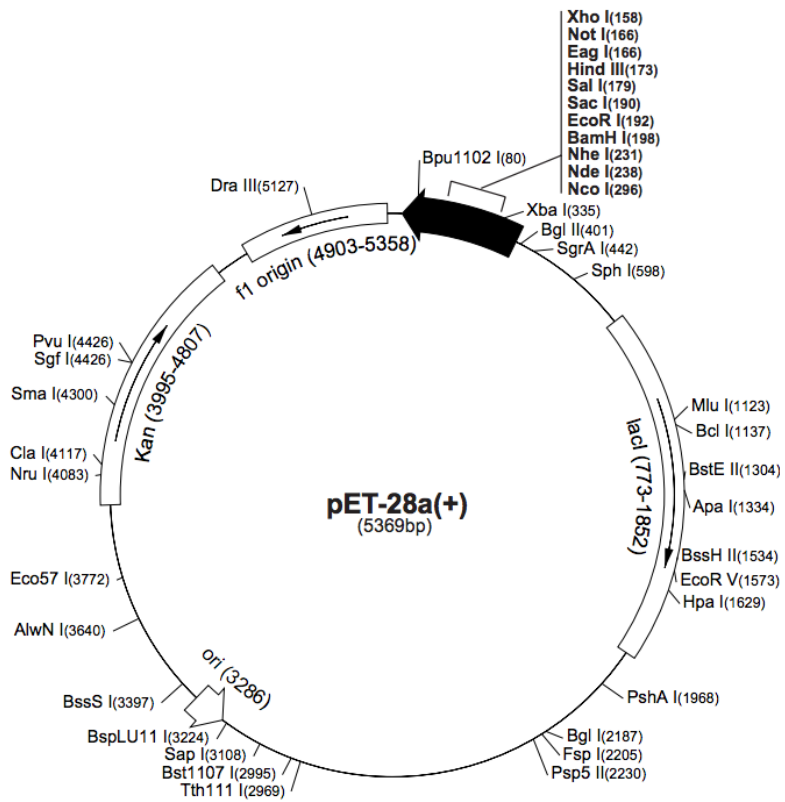
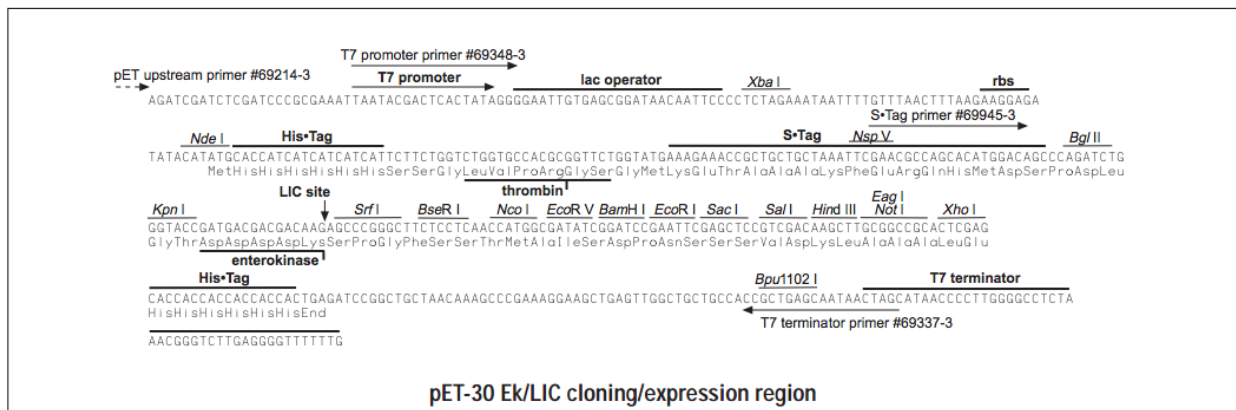
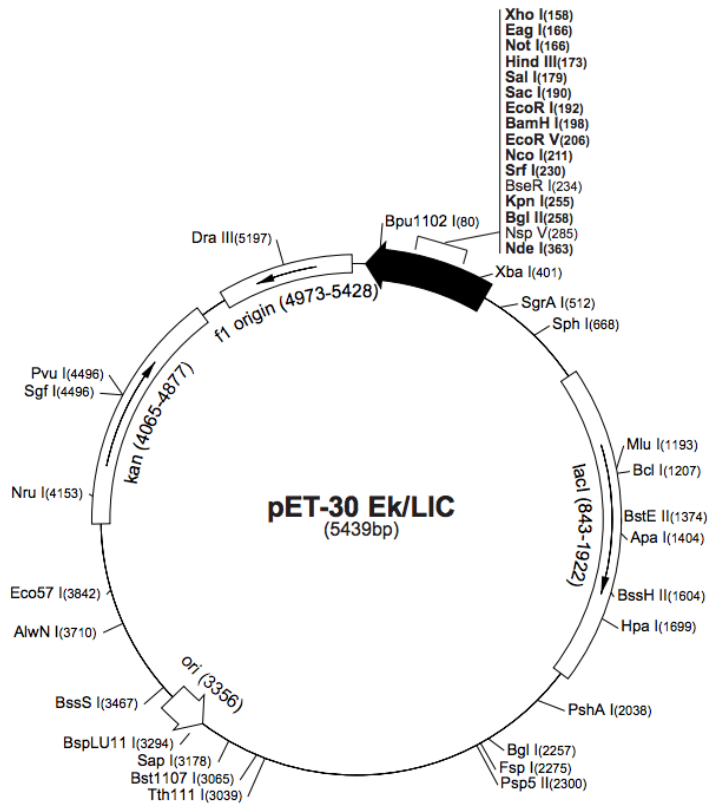
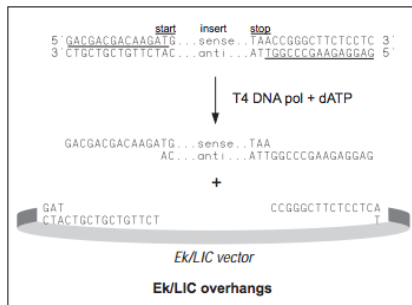


Table continued.

pET-30 Ek/LIC sequence landmarks	
T7 promoter	436-452
T7 transcription start	435
His•Tag coding sequence	344-361
S•Tag coding sequence	266-310
Multiple cloning sites (<i>Bse</i> I - <i>Xho</i> I)	158-224
His•Tag coding sequence	140-157
T7 terminator	26-72
<i>lac</i> I coding sequence	843-1922
pBR322 origin	3356
Kan coding sequence	4065-4877
f1 origin	4973-5428

Note: the *Srf*I site is destroyed during Ligation Independent Cloning. Primer sequence extensions required for LIC compatibility are underlined in the diagram below.



7.2. Primer Sequences for Site-directed Mutagenesis

Supplementary Table S2. Protein parameters given from ProtParam.

Protein Name	Primer Sequence (5' – 3')
Forward pET28 α B-6E_C-term_Histag	GTCACCGCAGCCCCAAGAAAGCGGCCGCACTCGAGCACCAC
Reverse pET28 α B-6E_C-term_Histag	GTGGTGCTCGAGTGC GGCCGCTTCTTGGGGGCTCGGGTGAC
Forward pET28 α B-E19D_E21D	GCCCCCTTTCTTTCCACGACCCCGACCGCCTCTTCGACCA
Reverse pET28 α B-E19D_E21D	TGGTGAAGAGGCGGTTCGGGGTCGTGGAAGGAAAGAAGGGGC
Forward pET28 α B-E43D_E45D	ATCTTTCCCGACGTCTACTGACCTGGACCCCTCTACCTTCG
Reverse pET28 α B-E43D_E45D	CGAAGGTAGAAGGGGTCCAGGTCACTAGACGTCCGGGAAAAGAT
Forward pET28 α B-E53D	CCTTCTACCTTCGGCCACCCGACTTCTGCGGGCACC CGACTG
Reverse pET28 α B-E53D	CAGTCGGGTGCCCGCAGGAAGTCGGGTGGCCGAAGGTAGAAGG
Forward pET28 α B-E59D	CCGACTTCTGCGGGCACC CGACTGTTTGACTGACTCTC
Reverse pET28 α B-E59D	GAGAGTCCAGTGTCAAACAGTCGGGTGCCCGCAGGAAGTCGG

7.3. Protein Sequences

Supplementary Table S3. Amino acid sequences of relevant proteins used in this work are listed here. The accession codes in the Uniprot database (Jain *et al.* 2009) are also given in brackets.

Protein Name	Number of Residues	Sequence (5' – 3')
$A\beta_{(1-40)}$ (P05067)	40	DAEFRHDSGY EVHHQKLVFF AEDVGSNKGA IIGLMVGGVV
α B-WT (P02511)	175	MDIAIHPWI RRPFFPFHSP SRLFDQFFGE HLESDFPT STLSPFYLR PPSFLRAPSW FDTGLSEMRL EKDRFSVNL DVKHFSPPEELK VKVLGDVIEV HGKHEERQDE HGFISREFHR KYRIPADVDP LTITSSLSSD GVLTVNGPRK QVSGPERTIP ITREEKPAVT AAPKK
α B- δ NTD	117	MWFDTGLSEM RLEKDRFSVN LDVVKHFSPEE LKVKVLGDVI EVHGKHEERQ DEHGFISREF HRKYRIPADV DPLTITSSLS SDGVLTVNGP RKQVSGPERT IPITREEKPA VTAAPKK
α B-10m	91	MFDTGLSEMR LEKDRFSVNL DVKHFSPPEEL KVKVLGDVIE VHGKHEERQD EHGFIREFHR RKYRIPADVDP PLTITSSLSS DGVLTVNGPR K
α B-6E	175	MDIAIHPWI RRPFFPFHSP ERLFDQFFGE HLESDFPT STELEPFYLR PPEFLRAPEW FDTGLSEMRL EKDRFSVNL DVKHFSPPEELK VKVLGDVIEV HGKHEERQDE HGFISREFHR KYRIPADVDP LTITSSLSSD GVLTVNGPRK QVSGPERTIP ITREEKPAVT AAPKK
α B-6E_C-term_Histag	186	MDIAIHPWI RRPFFPFHSP ERLFDQFFGE HLESDFPT STELEPFYLR PPEFLRAPEW FDTGLSEMRL EKDRFSVNL DVKHFSPPEELK VKVLGDVIEV HGKHEERQDE HGFISREFHR KYRIPADVDP LTITSSLSSD GVLTVNGPRK QVSGPERTIP ITREEKPAVT AAPKAAAAL HHHHHH
α B-6D	175	MDIAIHPWI RRPFFPFHDP DRLFDQFFGE HLESDFPT STDLDPFYLR PPDFLRAPDW FDTGLSEMRL EKDRFSVNL DVKHFSPPEELK VKVLGDVIEV HGKHEERQDE HGFISREFHR KYRIPADVDP LTITSSLSSD GVLTVNGPRK QVSGPERTIP ITREEKPAVT AAPKK
α A-WT (P02489)	173	MDVTIQHPWF KRTLGPFPYS RLFQDFGEG LFEYDLLPFL SSTISPPYRQ SLFRTVLDSD ISEVRSRDK FVIFLDVKHF SPEDLTVKVQ DDFVEIHGKH NERQDDHGYI SREFHRRYRL PSNVDQSALS CSLSADGMLT FCGPKIQTGL DATHAERAIP VSREEKPTSA PSS
α A-ACD_CTE	93	MSEVRSRDK FVIFLDVKHF SPEDLTVKVQ DDFVEIHGKH NERQDDHGYI SREFHRRYRL PSNVDQSALS CSLSADGMLT FCGPKIQTGL DAT
lysozyme	129	KV FGRCELAAM KRHGLDNYRG YSLGNWVCAA KFESNFNTQA TNRNTDGS TD YGILQINSRW WCNDGRTPGS RNLCNIPCSA LLSSDITASV NCAKKIVSDG NGMNAWVAWR NRCKGTDVQA WIRGCR L

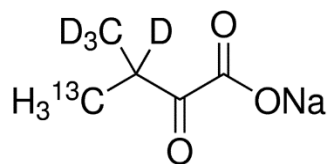
7.4. Protein Parameters

Supplementary Table S4. Molar extinction coefficients and molecular weights (Gasteiger *et al.* 2003) of relevant proteins are given in table. Molecular weights were calculated in consideration of the different isotopic labeling schemes (<http://protecalc.sourceforge.net/>). These parameters were used for the photometric determination of protein concentration.

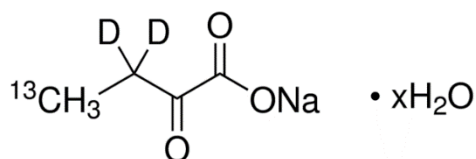
Protein Name	Number of Residues	Isoelectric Point (pI)	ϵ ($M^{-1} \text{ cm}^{-1}$)	M_w (Da)	Isotope labeling
$A\beta_{(1-40)}$ (P05067)	40	5.31	1490	4330 4515 4712	unlabeled ^{15}N $^{13}\text{C}, ^{15}\text{N}$
$\alpha\text{B-WT}$ (P02511)	175	6.76	13980	20159 20410 21318 22712	unlabeled ^{15}N $^{13}\text{C}, ^{15}\text{N}$ $^2\text{H}, ^{13}\text{C}, ^{15}\text{N}$
$\alpha\text{B-}\delta\text{NTD}$	117	6.52	6990	13320 13487	unlabeled ^{15}N
$\alpha\text{B-10m}$	91	5.92	1490	10448 10587	unlabeled ^{15}N
$\alpha\text{B-6E}$	175	5.72	13980	20411 20661 21582	unlabeled ^{15}N $^{13}\text{C}, ^{15}\text{N}$
$\alpha\text{B-6E_C-term_Histag}$	186	5.99	13980	21689 21962	unlabeled ^{15}N
$\alpha\text{B-6D}$	175	5.70	13980	20327 20577	unlabeled ^{15}N
$\alpha\text{A-WT}$ (P02489)	173	5.77	14565	19909 20150 21037	unlabeled ^{15}N $^{13}\text{C}, ^{15}\text{N}$
$\alpha\text{A-ACD_CTE}$	93	5.63	2980	10685 10819	unlabeled ^{15}N
lysozyme	129	9.32	37970	14313	unlabeled

7.5. Structure of Precursors for ILV Labeling

- 2-Keto-3-(methyl- d_3)-butyric acid-4- ^{13}C ,3-d sodium salt, 97 atom % D, 99 atom % ^{13}C , 97% (CP)



- 2-Ketobutyric acid-4- ^{13}C ,3,3- d_2 sodium salt hydrate, 99 atom % ^{13}C , 98 atom % D, 98% (CP)



7.6. Chemical Shifts of the CTR of the Wild-type α A-crystallin

Supplementary Table S5. ^1H , ^{13}C and ^{15}N chemical shifts (in p.p.m.) of α A-crystallin in 10mMHEPES/KOH pH 7.4 at 300 K as obtained by solution – state NMR spectroscopy.

Residue	H _N	N _H	C'	C α	C β	H α	miscellaneous
G149	8.42	110.80	171.59	42.79	-----	4.18	-----
L150	8.07	121.53	174.54	52.53	39.69	4.26	1.49 (H β 1), 1.54 (H β 2), 24.34 (C γ), 22.23 (C δ 1), 20.7 (C δ 2)
D151	8.30	120.73	173.54	51.51	38.45	4.48	2.57 (H β 1), 2.62 (H β 2)
A152	8.19	124.49	175.52	50.28	16.47	4.24	1.31 (H β)
T153	8.08	112.13	172.09	59.97	66.93	4.14	4.10 (H β), 1.08 (H γ), 18.82 (C γ)
H154	8.09	120.93	172.40	53.65	27.50	4.52	3.00 (H β 1), 3.12 (H β 2)
A155	8.06	124.63	175.07	50.10	16.53	4.20	1.29 (H β)
E156	8.37	119.92	173.85	54.06	27.41	4.16	1.89 (H β 1), 2.22 (H β 2), 33.5 (C γ)
R157	8.14	121.61	173.01	53.20	28.40	4.24	1.79 (H β 1), 1.55 (H β 2), 24.37 (C γ), 3.12 (H δ), 40.77 (C δ)
A158	8.16	125.28	174.56	49.55	16.51	4.25	1.27 (H β)
I159	8.05	122.17	171.96	55.90	35.91	4.36	1.77 (H β), 0.87 (H γ), 14.38 (C γ), 0.78 (H δ), 10.00 (C δ)
V161	8.15	120.52	173.58	59.52	30.18	4.02	1.98 (H β), 0.89 (H γ)1, 17.87 (C γ 1), 0.88 (H γ 2), 18.43 (C γ 2)
S162	8.32	119.61	171.71	55.36	61.31	4.40	3.77 (H β)
R163	8.41	123.63	173.25	53.50	28.21	4.30	1.67 (H β), 3.12 (H δ), 40.56 (C δ)
E164	8.33	122.03	173.50	53.64	27.74	4.21	1.83 (H β), 2.14 (H γ), 33.51 (C γ)
E165	8.38	123.11	173.41	53.52	27.74	4.21	1.94 (H β), 2.18 (H γ), 33.54 (C γ)
K166	8.33	123.77	171.67	51.33	29.92	4.55	1.64 (H β), (H β 1), 1.74 (H β 2), 1.37 (H γ), 21.81 (C γ)
T168	8.28	114.74	171.88	59.26	67.19	4.26	4.16 (H β), 1.17 (H γ), 18.76 (C γ)
S169	8.17	117.91	170.88	55.28	61.29	4.40	3.77 (H β)
A170	8.26	127.11	172.72	47.81	15.50	4.55	1.29 (H β)
S172	8.41	116.55	171.07	55.61	61.38	4.40	3.85 (H β)
S173	7.90	122.84	175.83	57.27	62.13	4.20	3.78 (H β)

8. References

- Adhikari, A. S., Sridhar Rao, K., Rangaraj, N., Parnaik, V. K., & Mohan Rao, Ch. (2004). Heat stress-induced localization of small heat shock proteins in mouse myoblasts: intranuclear lamin A/C speckles as target for alphaB-crystallin and Hsp25. *Exp Cell Res*, 299(2), 393-403.
- Ahmad, M. F., Raman, B., Ramakrishna, T., & Rao Ch, M. (2008). Effect of phosphorylation on alpha B-crystallin: differences in stability, subunit exchange and chaperone activity of homo and mixed oligomers of alpha B-crystallin and its phosphorylation-mimicking mutant. *J Mol Biol*, 375(4), 1040-1051.
- Alexander, N., Bortolus, M., Al-Mestarihi, A., McHaourab, H., & Meiler, J. (2008). De novo high-resolution protein structure determination from sparse spin-labeling EPR data. *Structure*, 16(2), 181-195.
- Amero, C., Schanda, P., Dura, M. A., Ayala, I., Marion, D., Franzetti, B., . . . Boisbouvier, J. (2009). Fast two-dimensional NMR spectroscopy of high molecular weight protein assemblies. *J Am Chem Soc*, 131(10), 3448-3449.
- Andley, U. P., Patel, H. C., & Xi, J. H. (2002). The R116C mutation in alphaA-crystallin diminishes its protective ability against stress-induced lens epithelial cell apoptosis. *J Biol Chem*, 277(12), 10178-10186.
- Andrew, E. R., Bradbury, A. and Eades, R.G. (1958). Nuclear Magnetic Resonance Spectra From A Crystal Rotated At High Speed. *Letters to Nature*.
- Aquilina, J. A., & Watt, S. J. (2007). The N-terminal domain of alphaB-crystallin is protected from proteolysis by bound substrate. *Biochem Biophys Res Commun*, 353(4), 1115-1120.
- Aquilina, J. A., Benesch, J. L., Bateman, O. A., Slingsby, C., & Robinson, C. V. (2003). Polydispersity of a mammalian chaperone: mass spectrometry reveals the population of oligomers in alphaB-crystallin. *Proc Natl Acad Sci U S A*, 100(19), 10611-10616.
- Aquilina, J. A., Benesch, J. L., Ding, L. L., Yaron, O., Horwitz, J., & Robinson, C. V. (2004). Phosphorylation of alphaB-crystallin alters chaperone function through loss of dimeric substructure. *J Biol Chem*, 279(27), 28675-28680.
- Atwood, C. S., Scarpa, R. C., Huang, X., Moir, R. D., Jones, W. D., Fairlie, D. P., . . . Bush, A. I. (2000). Characterization of copper interactions with alzheimer amyloid beta peptides: identification of an attomolar-affinity copper binding site on amyloid beta 1-42. *J Neurochem*, 75(3), 1219-1233.
- Ayala, I., Hamelin, O., Amero, C., Pessey, O., Plevin, M. J., Gans, P., & Boisbouvier, J. (2012). An optimized isotopic labelling strategy of isoleucine-gamma2 methyl groups for solution NMR studies of high molecular weight proteins. *Chem Commun (Camb)*, 48(10), 1434-1436.
- Ayala, I., Sounier, R., Use, N., Gans, P., & Boisbouvier, J. (2009). An efficient protocol for the complete incorporation of methyl-protonated alanine in perdeuterated protein. *J Biomol NMR*, 43(2), 111-119.
- Babu, M. M., van der Lee, R., de Groot, N. S., & Gsponer, J. (2011). Intrinsically disordered proteins: regulation and disease. *Curr Opin Struct Biol*, 21(3), 432-440.
- Badyaev, A. V. (2005). Stress-induced variation in evolution: from behavioural plasticity to genetic assimilation. *Proc Biol Sci*, 272(1566), 877-886.
- Bagneris, C., Bateman, O. A., Naylor, C. E., Cronin, N., Boelens, W. C., Keep, N. H., & Slingsby, C. (2009). Crystal structures of alpha-crystallin domain dimers of alphaB-crystallin and Hsp20. *J Mol Biol*, 392(5), 1242-1252.
- Baldus, M. (2006). Solid-state NMR spectroscopy: molecular structure and organization at the atomic level. *Angew Chem Int Ed Engl*, 45(8), 1186-1188.
- Baldwin, A. J., Hilton, G. R., Lioe, H., Bagneris, C., Benesch, J. L., & Kay, L. E. (2011c). Quaternary dynamics of alphaB-crystallin as a direct consequence of localised tertiary fluctuations in the C-terminus. *J Mol Biol*, 413(2), 310-320.
- Baldwin, A. J., Lioe, H., Hilton, G. R., Baker, L. A., Rubinstein, J. L., Kay, L. E., & Benesch, J. L. (2011a). The polydispersity of alphaB-crystallin is rationalized by an interconverting polyhedral architecture. *Structure*, 19(12), 1855-1863.
- Baldwin, A. J., Lioe, H., Robinson, C. V., Kay, L. E., & Benesch, J. L. (2011b). alphaB-crystallin polydispersity is a consequence of unbiased quaternary dynamics. *J Mol Biol*, 413(2), 297-309.
- Baldwin, A. J., Walsh, P., Hansen, D. F., Hilton, G. R., Benesch, J. L., Sharpe, S., & Kay, L. E. (2012). Probing dynamic conformations of the high-molecular-weight alphaB-crystallin heat shock protein ensemble by NMR spectroscopy. *J Am Chem Soc*, 134(37), 15343-15350.
- Barbato, G., Ikura, M., Kay, L. E., Pastor, R. W., & Bax, A. (1992). Backbone dynamics of calmodulin studied by 15N relaxation using inverse detected two-dimensional NMR spectroscopy: the central helix is flexible. *Biochemistry*, 31(23), 5269-5278.
- Bardwell, J. C., & Craig, E. A. (1984). Major heat shock gene of Drosophila and the Escherichia coli heat-inducible dnaK gene are homologous. *Proc Natl Acad Sci U S A*, 81(3), 848-852.
- Basha, E., O'Neill, H., & Vierling, E. (2012). Small heat shock proteins and alpha-crystallins: dynamic proteins with flexible functions. *Trends Biochem Sci*, 37(3), 106-117.
- Battiste, J. L., & Wagner, G. (2000). Utilization of site-directed spin labeling and high-resolution heteronuclear nuclear magnetic resonance for global fold determination of large proteins with limited nuclear overhauser effect data. *Biochemistry*, 39(18), 5355-5365.
- Beall, A., Bagwell, D., Woodrum, D., Stoming, T. A., Kato, K., Suzuki, A., Brophy, C. M. (1999). The small heat shock-related protein, HSP20, is phosphorylated on serine 16 during cyclic nucleotide-dependent relaxation. *J Biol Chem*, 274(16), 11344-11351.
- Beatty, E. J., Cox, M. C., Frenkiel, T. A., Tam, B. M., Mason, A. B., MacGillivray, R. T., . . . Woodworth, R. C. (1996). Interlobe communication in 13C-methionine-labeled human transferrin. *Biochemistry*, 35(24), 7635-7642.
- Becker, E. D. (1999). High Resolution NMR: Theory and Chemical Applications, Elsevier Science.
- Benedek G (1983) Why the eye lens is transparent. *Nature* 302:383-384.
- Berengian, A. R., Bova, M. P., & McHaourab, H. S. (1997). Structure and function of the conserved domain in alphaA-crystallin. Site-directed spin labeling identifies a beta-strand located near a subunit interface. *Biochemistry*, 36(33), 9951-9957.
- Berry, V., Francis, P., Reddy, M. A., Collyer, D., Vithana, E., MacKay, I., Quinlan, R. A. (2001). Alpha-B crystallin gene (CRYAB) mutation causes dominant congenital posterior polar cataract in humans. *Am J Hum Genet*, 69(5), 1141-1145.
- Bertini, I., Engelke, F., Gonnelli, L., Knott, B., Luchinat, C., Osen, D., & Ravera, E. (2012). On the use of ultracentrifugal devices for sedimented solute NMR. *J Biomol NMR*, 54(2), 123-127.
- Bertini, I., Gonnelli, L., Luchinat, C., Mao, J., & Nesi, A. (2011). A new structural model of Abeta40 fibrils. *J Am Chem Soc*, 133(40), 16013-16022.
- Biswas, A., Goshe, J., Miller, A., Santhoshkumar, P., Luckey, C., Bhat, M. B., & Nagaraj, R. H. (2007). Paradoxical effects of substitution and deletion mutation of Arg56 on the structure and chaperone function of human alphaB-crystallin. *Biochemistry*, 46(5), 1117-1127.
- Blake, C. C., Koenig, D. F., Mair, G. A., North, A. C., Phillips, D. C., & Sarma, V. R. (1965). Structure of hen egg-white lysozyme. A three-dimensional Fourier synthesis at 2 Angstrom resolution. *Nature*, 206(4986), 757-761.
- Blakytyn, R., Carver, J. A., Harding, J. J., Kilby, G. W., & Sheil, M. M. (1997). A spectroscopic study of glycosylated bovine alpha-crystallin: investigation of flexibility of the C-terminal extension, chaperone activity and evidence for diglycation. *Biochim Biophys Acta*, 1343(2), 299-315.
- Bloembergen, N. (1949). On the interaction of nuclear spins in a crystalline lattice. *Physica*, 15: 386-426.
- Bloemendal, H., de Jong, W., Jaenicke, R., Lubsen, N. H., Slingsby, C., & Tardieu, A. (2004). Ageing and vision: structure, stability and function of lens crystallins. *Prog Biophys Mol Biol*, 86(3), 407-485.

- Bosl, B., Grimminger, V., & Walter, S. (2006). The molecular chaperone Hsp104—a molecular machine for protein disaggregation. *J Struct Biol*, *156*(1), 139–148.
- Bova, M. P., Yaron, O., Huang, Q., Ding, L., Haley, D. A., Stewart, P. L., & Horwitz, J. (1999). Mutation R120G in alphaB-crystallin, which is linked to a desmin-related myopathy, results in an irregular structure and defective chaperone-like function. *Proc Natl Acad Sci U S A*, *96*(11), 6137–6142.
- Brady, J. P., Garland, D., Douglas-Tabor, Y., Robison, W. G., Jr., Groome, A., & Wawrousek, E. F. (1997). Targeted disruption of the mouse alphaA-crystallin gene induces cataract and cytoplasmic inclusion bodies containing the small heat shock protein alpha B-crystallin. *Proc Natl Acad Sci U S A*, *94*(3), 884–889.
- Braun, N., Zacharias, M., Peschek, J., Kastenmuller, A., Zou, J., Hanzlik, M., Weinkauff, S. (2011). Multiple molecular architectures of the eye lens chaperone alphaB-crystallin elucidated by a triple hybrid approach. *Proc Natl Acad Sci U S A*, *108*(51), 20491–20496.
- Braun, W., Wider, G., Lee, K. H., & Wuthrich, K. (1983). Conformation of glucagon in a lipid-water interphase by 1H nuclear magnetic resonance. *J Mol Biol*, *169*(4), 921–948.
- Bryantsev, A. L., Chechenova, M. B., & Shelden, E. A. (2007). Recruitment of phosphorylated small heat shock protein Hsp27 to nuclear speckles without stress. *Exp Cell Res*, *313*(1), 195–209.
- Buchner, J. (1996). Supervising the fold: functional principles of molecular chaperones. *FASEB J*, *10*(1), 10–19.
- Bukau, B., Weissman, J., & Horwich, A. (2006). Molecular chaperones and protein quality control. *Cell*, *125*(3), 443–451.
- Burdon, R. H. (1986). Heat shock and the heat shock proteins. *Biochem J*, *240*(2), 313–324.
- Carr, H. Y., & Purcell, E. M. (1954). Effects of Diffusion on Free Precession in Nuclear Magnetic Resonance Experiments. *Physical Review*, *94*(3), 630–638.
- Carra, S., Rusmini, P., Crippa, V., Giorgetti, E., Boncoraglio, A., Cristofani, R., Poletti, A. (2013). Different anti-aggregation and pro-degradative functions of the members of the mammalian sHSP family in neurological disorders. *Philos Trans R Soc Lond B Biol Sci*, *368*(1617), 20110409.
- Carver, J. A., & Lindner, R. A. (1998). NMR spectroscopy of alpha-crystallin. Insights into the structure, interactions and chaperone action of small heat-shock proteins. *Int J Biol Macromol*, *22*(3–4), 197–209.
- Carver, J. A., Aquilina, J. A., Truscott, R. J., & Ralston, G. B. (1992). Identification by 1H NMR spectroscopy of flexible C-terminal extensions in bovine lens alpha-crystallin. *FEBS Lett*, *311*(2), 143–149.
- Cavanagh, J., Fairbrother, W. J., Palmer, A. G., Skelton, N. J. & Rance, M. (2010). Protein NMR Spectroscopy: Principles and Practice, 2nd Ed., *Academic Press*
- Chaves, J. M., Srivastava, K., Gupta, R., & Srivastava, O. P. (2008). Structural and functional roles of deamidation and/or truncation of N- or C-termini in human alpha A-crystallin. *Biochemistry*, *47*(38), 10069–10083.
- Chayen, N. E., & Saridakis, E. (2008). Protein crystallization: from purified protein to diffraction-quality crystal. *Nat Methods*, *5*(2), 147–153.
- Chen L, et al. (2011) Structural instability tuning as a regulatory mechanism in protein-protein interactions. *Mol Cell* *44*(5):734–744.
- Chiou, S. H., Huang, C. H., Lee, I. L., Wang, Y. T., Liu, N. Y., Tsay, Y. G., & Chen, Y. J. (2010). Identification of in vivo phosphorylation sites of lens proteins from porcine eye lenses by a gel-free phosphoproteomics approach. *Mol Vis*, *16*, 294–302.
- Cho, H. S., Liu, C. W., Damberger, F. F., Pelton, J. G., Nelson, H. C., & Wemmer, D. E. (1996). Yeast heat shock transcription factor N-terminal activation domains are unstructured as probed by heteronuclear NMR spectroscopy. *Protein Sci*, *5*(2), 262–269.
- Choi, J. S., Braymer, J. J., Nanga, R. P., Ramamoorthy, A., & Lim, M. H. (2010). Design of small molecules that target metal-A{beta} species and regulate metal-induced A{beta} aggregation and neurotoxicity. *Proc Natl Acad Sci U S A*, *107*(51), 21990–21995.
- Christodoulou, J., Larsson, G., Fucini, P., Connell, S. R., Pertinhez, T. A., Hanson, C. L., . . . Dobson, C. M. (2004). Heteronuclear NMR investigations of dynamic regions of intact Escherichia coli ribosomes. *Proc Natl Acad Sci U S A*, *101*(30), 10949–10954.
- Claridge T. D. W. (2009). High-Resolution NMR Techniques in Organic Chemistry. Volume 2, 2nd Edition, *Elsevier Science*.
- Clark, J. I., & Muchowski, P. J. (2000). Small heat-shock proteins and their potential role in human disease. *Curr Opin Struct Biol*, *10*(1), 52–59.
- Clore, G. M., & Iwahara, J. (2009). Theory, practice, and applications of paramagnetic relaxation enhancement for the characterization of transient low-population states of biological macromolecules and their complexes. *Chem Rev*, *109*(9), 4108–4139.
- Clore, G. M., Driscoll, P. C., Wingfield, P. T., & Gronenborn, A. M. (1990). Analysis of the backbone dynamics of interleukin-1 beta using two-dimensional inverse detected heteronuclear 15N-1H NMR spectroscopy. *Biochemistry*, *29*(32), 7387–7401.
- Clore, G. M., Gronenborn, A. M., Brunger, A. T., & Karplus, M. (1985). Solution conformation of a heptadecapeptide comprising the DNA binding helix F of the cyclic AMP receptor protein of Escherichia coli. Combined use of 1H nuclear magnetic resonance and restrained molecular dynamics. *J Mol Biol*, *186*(2), 435–455.
- Clubb, R. T., Thanabal, V. & Wagner, G. (1992). A constant-time 3-dimensional tripleresonance pulse scheme to correlate intrasidue H-1(N), N-15, and C-13(') chemical shifts in N-15-C-13-labeled protein. *J Magn Reson* *97*: 213–217.
- Cohen, S. I. A., Arosio, P., Presto, J., Kurudenkandy, F. R., Biverstal, H., Dolfe, L., . . . Linse, S. (2015). A molecular chaperone breaks the catalytic cycle that generates toxic A-beta oligomers. *Nat Struct Mol Biol*, *22*(3), 207–213.
- Colvin, M. T., Silvers, R., Ni, Q. Z., Can, T. V., Sergeev, I., Rosay, M., . . . Griffin, R. G. (2016). Atomic Resolution Structure of Monomeric A-beta42 Amyloid Fibrils. *J Am Chem Soc*, *138*(30), 9663–9674.
- Costanzo, M., & Zurzolo, C. (2013). The cell biology of prion-like spread of protein aggregates: mechanisms and implication in neurodegeneration. *Biochem J*, *452*(1), 1–17.
- Cox, D., Selig, E., Griffin, M. D., Carver, J. A., & Ecroyd, H. (2016). Small Heat-shock Proteins Prevent alpha-Synuclein Aggregation via Transient Interactions and Their Efficacy Is Affected by the Rate of Aggregation. *J Biol Chem*, *291*(43), 22618–22629.
- Crublet, E., Kerfah, R., Mas, G., Noirclerc-Savoye, M., Lantze, V., Vernet, T., & Boisbouvier, J. (2014). A cost-effective protocol for the parallel production of libraries of 13CH3-specifically labeled mutants for NMR studies of high molecular weight proteins. *Methods Mol Biol*, *1091*, 229–244.
- Danielsson, J., Pierattelli, R., Banci, L., & Graslund, A. (2007). High-resolution NMR studies of the zinc-binding site of the Alzheimer's amyloid beta-peptide. *FEBS J*, *274*(1), 46–59.
- Dasari, M. (2011). Expression purification and structural studies of Alzheimer's disease amyloid b peptides. PhD thesis.
- Dasari, M., Espargaro, A., Sabate, R., Lopez del Amo, J. M., Fink, U., Grelle, G., . . . Reif, B. (2011). Bacterial inclusion bodies of Alzheimer's disease beta-amyloid peptides can be employed to study native-like aggregation intermediate states. *Chembiochem*, *12*(3), 407–423.
- d'Auvergne, E. J., & Gooley, P. R. (2003). The use of model selection in the model-free analysis of protein dynamics. *J Biomol NMR*, *25*(1), 25–39.
- de Jong, W. W., Leunissen, J. A., & Voorter, C. E. (1993). Evolution of the alpha-crystallin/small heat-shock protein family. *Mol Biol Evol*, *10*(1), 103–126.
- Dehle, F. C., Ecroyd, H., Musgrave, I. F., & Carver, J. A. (2010). AlphaB-Crystallin inhibits the cell toxicity associated with amyloid fibril formation by kappa-casein and the amyloid-beta peptide. *Cell Stress Chaperones*, *15*(6), 1013–1026.
- Delano, W. L. (2002). The PyMOL molecular graphics system.
- Delaye, M., & Tardieu, A. (1983). Short-range order of crystallin proteins accounts for eye lens transparency. *Nature*, *302*(5907), 415–417.
- Delbecq, S. P., & Klevit, R. E. (2013). One size does not fit all: the oligomeric states of alphaB crystallin. *FEBS Lett*, *587*(8), 1073–1080.

- DellaVecchia, M. J., Merritt, W. K., Peng, Y., Kirby, T. W., DeRose, E. F., Mueller, G. A., . . . London, R. E. (2007). NMR analysis of [methyl-¹³C]methionine UvrB from *Bacillus caldoteanax* reveals UvrB-domain 4 heterodimer formation in solution. *J Mol Biol*, *373*(2), 282-295.
- den Engelsman, J., Gerrits, D., de Jong, W. W., Robbins, J., Kato, K., & Boelens, W. C. (2005). Nuclear import of {alpha}B-crystallin is phosphorylation-dependent and hampered by hyperphosphorylation of the myopathy-related mutant R120G. *J Biol Chem*, *280*(44), 37139-37148.
- Devi, R. R., Yao, W., Vijayalakshmi, P., Sergeev, Y. V., Sundaresan, P., & Hejtmancik, J. F. (2008). Crystallin gene mutation in Indian families with inherited pediatric cataract. *Mol Vis*, *14*, 1157-1170.
- Diaz-Villanueva, J. F., Diaz-Molina, R., & Garcia-Gonzalez, V. (2015). Protein Folding and Mechanisms of Proteostasis. *Int J Mol Sci*, *16*(8), 17193-17230.
- Dinner, A. R., Sali, A., Smith, L. J., Dobson, C. M., & Karplus, M. (2000). Understanding protein folding via free-energy surfaces from theory and experiment. *Trends Biochem Sci*, *25*(7), 331-339.
- Dobson, C. M., & Karplus, M. (1999). The fundamentals of protein folding: bringing together theory and experiment. *Curr Opin Struct Biol*, *9*(1), 92-101.
- Douglas, N. R., Reissmann, S., Zhang, J., Chen, B., Jakana, J., Kumar, R., Frydman, J. (2011). Dual action of ATP hydrolysis couples lid closure to substrate release into the group II chaperonin chamber. *Cell*, *144*(2), 240-252.
- Duer, M. J. (2008). Solid state NMR spectroscopy: principles and applications. *John Wiley & Sons*.
- Durbin, S. D., & Feher, G. (1996). Protein crystallization. *Annu Rev Phys Chem*, *47*, 171-204.
- Ecroyd, H., & Carver, J. A. (2008). Unraveling the mysteries of protein folding and misfolding. *IUBMB Life*, *60*(12), 769-774.
- Ecroyd, H., & Carver, J. A. (2009). Crystallin proteins and amyloid fibrils. *Cell Mol Life Sci*, *66*(1), 62-81.
- Ecroyd, H., Meehan, S., Horwitz, J., Aquilina, J. A., Benesch, J. L., Robinson, C. V., Carver, J. A. (2007). Mimicking phosphorylation of alphaB-crystallin affects its chaperone activity. *Biochem J*, *401*(1), 129-141.
- Edwards, H. V., Scott, J. D., & Baillie, G. S. (2012). PKA phosphorylation of the small heat-shock protein Hsp20 enhances its cardioprotective effects. *Biochem Soc Trans*, *40*(1), 210-214.
- El-Agnaf, O. M., Mahil, D. S., Patel, B. P., & Austen, B. M. (2000). Oligomerization and toxicity of beta -amyloid-42 implicated in Alzheimer's disease. *Biochem Biophys Res Commun*, *273*(3), 1003-1007.
- Ellis, R. J. (1996). Discovery of molecular chaperones. *Cell Stress Chaperones*, *1*(3), 155-160.
- Ellis, R. J., & Minton, A. P. (2006). Protein aggregation in crowded environments. *Biol Chem*, *387*(5), 485-497.
- Encyclopedia Britanica, <https://www.britannica.com/science/bacteria/Growth-of-bacterial-populations>
- Erllich, H. A. (1989). "Polymerase chain reaction." *Journal of Clinical Immunology* *9*: 437-447.
- Ernst, R. R., Bodenhausen, G., and Wokaun, A. (1990). Principles of Nuclear Magnetic Resonance in One and Two Dimensions, *Clarendon Press*
- Eyles, S. J., & Gierasch, L. M. (2010). Nature's molecular sponges: small heat shock proteins grow into their chaperone roles. *Proc Natl Acad Sci USA*, *107*(7), 2727-2728.
- Fan, Q., Huang, L. Z., Zhu, X. J., Zhang, K. K., Ye, H. F., Luo, Y., Lu, Y. (2014). Identification of proteins that interact with alpha A-crystallin using a human proteome microarray. *Mol Vis*, *20*, 117-124.
- Fandrich, M., Meinhardt, J., & Grigorieff, N. (2009). Structural polymorphism of Alzheimer Abeta and other amyloid fibrils. *Prion*, *3*(2), 89-93.
- Fandrich, M., Schmidt, M., & Grigorieff, N. (2011). Recent progress in understanding Alzheimer's beta-amyloid structures. *Trends Biochem Sci*, *36*(6), 338-345.
- Farrow, N. A., Muhandiram, R., Singer, A. U., Pascal, S. M., Kay, C. M., Gish, G., . . . Kay, L. E. (1994). Backbone dynamics of a free and phosphopeptide-complexed Src homology 2 domain studied by 15N NMR relaxation. *Biochemistry*, *33*(19), 5984-6003.
- Fernandez, C., & Wider, G. (2003). TROSY in NMR studies of the structure and function of large biological macromolecules. *Curr Opin Struct Biol*, *13*(5), 570-580.
- Fesik, S. W. & Zuiderweg, E. R. (1988). Heteronuclear three-dimensional NMR spectroscopy. A strategy for the simplification of homonuclear two-dimensional NMR spectra. *J Magn Reson* *78*: 588-593.
- Fiaux, J., Bertelsen, E. B., Horwich, A. L., & Wuthrich, K. (2002). NMR analysis of a 900K GroEL GroES complex. *Nature*, *418*(6894), 207-211.
- Findeis, M. A. (2007). The role of amyloid beta peptide 42 in Alzheimer's disease. *Pharmacol Ther*, *116*(2), 266-286.
- Fischer, M., Kloiber, K., Hausler, J., Ledolter, K., Konrat, R., & Schmid, W. (2007). Synthesis of a ¹³C-methyl-group-labeled methionine precursor as a useful tool for simplifying protein structural analysis by NMR spectroscopy. *Chembiochem*, *8*(6), 610-612.
- Frydman, J. (2001). Folding of newly translated proteins in vivo: the role of molecular chaperones. *Annu Rev Biochem*, *70*, 603-647.
- Fujii, N., Awakura, M., Takemoto, L., Inomata, M., Takata, T., Fujii, N., & Saito, T. (2003). Characterization of alphaA-crystallin from high molecular weight aggregates in the normal human lens. *Mol Vis*, *9*, 315-322.
- Gans, P., Hamelin, O., Sounier, R., Ayala, I., Dura, M. A., Amero, C. D., . . . Boisbouvier, J. (2010). Stereospecific isotopic labeling of methyl groups for NMR spectroscopic studies of high-molecular-weight proteins. *Angew Chem Int Ed Engl*, *49*(11), 1958-1962.
- Gardner, K. H., & Kay, L. E. (1998). The use of ²H, ¹³C, ¹⁵N multidimensional NMR to study the structure and dynamics of proteins. *Annu Rev Biophys Biomol Struct*, *27*, 357-406.
- Garrido, C., Paul, C., Seigneuric, R., & Kampinga, H. H. (2012). The small heat shock proteins family: the long forgotten chaperones. *Int J Biochem Cell Biol*, *44*(10), 1588-1592.
- Gasteiger, E., Gattiker, A., Hoogland, C., Ivanyi, I., Appel, R. D., and Bairoch, A. (2003). *Nucleic Acids Res*. **31**, 3784-3788.
- Ghahghaei, A., Rekas, A., Carver, J. A., & Augusteyn, R. C. (2009). Structure/function studies of dogfish alpha-crystallin, comparison with bovine alpha-crystallin. *Mol Vis*, *15*, 2411-2420.
- Ghosh, J. G., Estrada, M. R., & Clark, J. I. (2005). Interactive domains for chaperone activity in the small heat shock protein, human alphaB crystallin. *Biochemistry*, *44*(45), 14854-14869.
- Gillespie, J. R., & Shortle, D. (1997). Characterization of long-range structure in the denatured state of staphylococcal nuclease. I. Paramagnetic relaxation enhancement by nitroxide spin labels. *J Mol Biol*, *268*(1), 158-169.
- Glennner, G. G., & Wong, C. W. (1984). Alzheimer's disease and Down's syndrome: sharing of a unique cerebrovascular amyloid fibril protein. *Biochem Biophys Res Commun*, *122*(3), 1131-1135.
- Goldstein, L. E., Muffat, J. A., Cherny, R. A., Moir, R. D., Ericsson, M. H., Huang, X., . . . Bush, A. I. (2003). Cytosolic beta-amyloid deposition and supranuclear cataracts in lenses from people with Alzheimer's disease. *Lancet*, *361*(9365), 1258-1265.
- Golenhofen, N., Ness, W., Koob, R., Htun, P., Schaper, W., & Drenckhahn, D. (1998). Ischemia-induced phosphorylation and translocation of stress protein alpha B-crystallin to Z lines of myocardium. *Am J Physiol*, *274*(5 Pt 2), H1457-1464.
- Goloubinoff, P., Christeller, J. T., Gatenby, A. A., & Lorimer, G. H. (1989). Reconstitution of active dimeric ribulose bisphosphate carboxylase from an unfolded state depends on two chaperonin proteins and Mg-ATP. *Nature*, *342*(6252), 884-889.
- Gravina, S. A., Ho, L., Eckman, C. B., Long, K. E., Otvos, L., Jr., Younkin, L. H., . . . Younkin, S. G. (1995). Amyloid beta protein (A beta) in Alzheimer's disease brain. Biochemical and immunocytochemical analysis with antibodies specific for forms ending at A beta 40 or A beta 42(43). *J Biol Chem*, *270*(13), 7013-7016.

- Graw, J., Klopp, N., Illig, T., Preising, M. N., & Lorenz, B. (2006). Congenital cataract and macular hypoplasia in humans associated with a de novo mutation in CRYAA and compound heterozygous mutations in P. *Graefes Arch Clin Exp Ophthalmol*, 244(8), 912-919.
- Gray, K.A., Seal, R.L., Tweedie, S., Wright, M.W. & Bruford, E.A. (2016). A review of the new HGNC gene family resource. *Hum Genomics*, 10(1):6.
- Grommek, A., Meier, B. and Ernst, M. (2006). Distance information from proton-driven spin diffusion under MAS. *Chemical physics letters*, 427(4):404-409.
- Grzesiek, S. & Bax, A. (1992). Correlating backbone amide and side chain resonances in larger proteins by multiple relayed triple resonance NMR. *J. Am. Chem. Soc.* 114: 6291-6293.
- Gu, F., Luo, W., Li, X., Wang, Z., Lu, S., Zhang, M., Ma, X. (2008). A novel mutation in AlphaA-crystallin (CRYAA) caused an autosomal dominant congenital cataract in a large Chinese family. *Hum Mutat*, 29(5), 769.
- Haass, C., & Selkoe, D. J. (2007). Soluble protein oligomers in neurodegeneration: lessons from the Alzheimer's amyloid beta-peptide. *Nat Rev Mol Cell Biol*, 8(2), 101-112.
- Hains, P. G., & Truscott, R. J. (2010). Age-dependent deamidation of lifelong proteins in the human lens. *Invest Ophthalmol Vis Sci*, 51(6), 3107-3114.
- Haley, D. A., Horwitz, J., & Stewart, P. L. (1998). The small heat-shock protein, alphaB-crystallin, has a variable quaternary structure. *J Mol Biol*, 277(1), 27-35.
- Hansen, D. F., Vallurupalli, P., & Kay, L. E. (2008). An improved 15N relaxation dispersion experiment for the measurement of millisecond time-scale dynamics in proteins. *J Phys Chem B*, 112(19), 5898-5904.
- Hansen, L., Yao, W., Eiberg, H., Kjaer, K. W., Baggesen, K., Hejtmancik, J. F., & Rosenberg, T. (2007). Genetic heterogeneity in microcornea-ataract: five novel mutations in CRYAA, CRYGD, and GJA8. *Invest Ophthalmol Vis Sci*, 48(9), 3937-3944.
- Hardy, J. (1997). The Alzheimer family of diseases: many etiologies, one pathogenesis? *Proc Natl Acad Sci U S A*, 94(6), 2095-2097.
- Hartl, F. U. (1996). Molecular chaperones in cellular protein folding. *Nature*, 381(6583), 571-579.
- Hartl, F. U., & Hayer-Hartl, M. (2002). Molecular chaperones in the cytosol: from nascent chain to folded protein. *Science*, 295(5561), 1852-1858.
- Hartl, F. U., & Hayer-Hartl, M. (2009). Converging concepts of protein folding in vitro and in vivo. *Nat Struct Mol Biol*, 16(6), 574-581.
- Hartl, F. U., Bracher, A., & Hayer-Hartl, M. (2011). Molecular chaperones in protein folding and proteostasis. *Nature*, 475(7356), 324-332.
- Hartmann, R. & Hahn, E. L. (1962). Nuclear double resonance in rotating frame. *Phys. Rev.*, 128(5):2042-2053.
- Haslbeck, M., Franzmann, T., Weinfurter, D., & Buchner, J. (2005). Some like it hot: the structure and function of small heat-shock proteins. *Nat Struct Mol Biol*, 12(10), 842-846.
- Haslbeck, M., Peschek, J., Buchner, J., & Weinkauff, S. (2016). Structure and function of alpha-crystallins: Traversing from in vitro to in vivo. *Biochim Biophys Acta*, 1860(1 Pt B), 149-166.
- Hemmingsen, S. M., Woolford, C., van der Vies, S. M., Tilly, K., Dennis, D. T., Georgopoulos, C. P., Ellis, R. J. (1988). Homologous plant and bacterial proteins chaperone oligomeric protein assembly. *Nature*, 333(6171), 330-334.
- Hendrick, J. P., & Hartl, F. U. (1995). The role of molecular chaperones in protein folding. *FASEB J*, 9(15), 1559-1569.
- Henzler-Wildman, K. A., Lei, M., Thai, V., Kerns, S. J., Karplus, M., & Kern, D. (2007). A hierarchy of timescales in protein dynamics is linked to enzyme catalysis. *Nature*, 450(7171), 913-916.
- Henzler-Wildman, K., & Kern, D. (2007). Dynamic personalities of proteins. *Nature*, 450(7172), 964-972.
- Herzfeld, J. and Berger, A. E. (1980). Sideband intensities in nmr-spectra of samples spinning at the magic angle. *J. Chem. Phys.*, 73 (12):6021-6030.
- Hilton, G. R., & Benesch, J. L. (2012). Two decades of studying non-covalent biomolecular assemblies by means of electrospray ionization mass spectrometry. *J R Soc Interface*, 9(70), 801-816.
- Hilton, G. R., Hochberg, G. K., Laganowsky, A., McGinnigle, S. I., Baldwin, A. J., & Benesch, J. L. (2013b). C-terminal interactions mediate the quaternary dynamics of alphaB-crystallin. *Philos Trans R Soc Lond B Biol Sci*, 368(1617), 20110405.
- Hilton, G. R., Lioe, H., Stengel, F., Baldwin, A. J., & Benesch, J. L. (2013a). Small heat-shock proteins: paramedics of the cell. *Top Curr Chem*, 328, 69-98.
- Hochberg, G. K., Ecroyd, H., Liu, C., Cox, D., Cascio, D., Sawaya, M. R., Laganowsky, A. (2014). The structured core domain of alphaB-crystallin can prevent amyloid fibrillation and associated toxicity. *Proc Natl Acad Sci U S A*, 111(16), E1562-1570.
- Hoffmann, J. H., Linke, K., Graf, P. C., Lilie, H., & Jakob, U. (2004). Identification of a redox-regulated chaperone network. *EMBO J*, 23(1), 160-168.
- Horwitz J (2009) Alpha crystallin: The quest for a homogeneous quaternary structure. *Exp Eye Res* 88(2):190-194.
- Horwitz, J. (1992). Alpha-crystallin can function as a molecular chaperone. *Proc Natl Acad Sci U S A*, 89(21), 10449-10453.
- Horwitz, J. (2003). Alpha-crystallin. *Exp Eye Res*, 76(2), 145-153.
- Horwitz, J., Bova, M. P., Ding, L. L., Haley, D. A., & Stewart, P. L. (1999). Lens alpha-crystallin: function and structure. *Eye (Lond)*, 13 (Pt 3b), 403-408.
- Hsu, A. L., Murphy, C. T., & Kenyon, C. (2003). Regulation of aging and age-related disease by DAF-16 and heat-shock factor. *Science*, 300(5622), 1142-1145.
- Huang, X., Atwood, C. S., Hartshorn, M. A., Multhaup, G., Goldstein, L. E., Scarpa, R. C., . . . Bush, A. I. (1999). The A beta peptide of Alzheimer's disease directly produces hydrogen peroxide through metal ion reduction. *Biochemistry*, 38(24), 7609-7616.
- Hutanu, D.; Frishberg, MD.; Guo, L.; Darie, C. C. (2014). Recent Applications of Polyethylene Glycols (PEGs) and PEG Derivatives. *Mod. Chem. Appl.* 2, 132.
- Inagaki, N., Hayashi, T., Arimura, T., Koga, Y., Takahashi, M., Shibata, H., Kimura, A. (2006). Alpha B-crystallin mutation in dilated cardiomyopathy. *Biochem Biophys Res Commun*, 342(2), 379-386.
- Isaacson, R. L., Simpson, P. J., Liu, M., Cota, E., Zhang, X., Freemont, P., & Matthews, S. (2007). A new labeling method for methyl transverse relaxation-optimized spectroscopy NMR spectra of alanine residues. *J Am Chem Soc*, 129(50), 15428-15429.
- Ishima, R., & Torchia, D. A. (2006). Accuracy of optimized chemical-exchange parameters derived by fitting CPMGR2 dispersion profiles when R2(0a) not = R2(0b). *J Biomol NMR*, 34(4), 209-219.
- Ito, H., Iida, K., Kamei, K., Iwamoto, I., Inaguma, Y., & Kato, K. (1999). AlphaB-crystallin in the rat lens is phosphorylated at an early post-natal age. *FEBS Lett*, 446(2-3), 269-272.
- Ito, H., Okamoto, K., Nakayama, H., Isobe, T., & Kato, K. (1997). Phosphorylation of alphaB-crystallin in response to various types of stress. *J Biol Chem*, 272(47), 29934-29941.
- Iwahara, J., & Clore, G. M. (2006). Detecting transient intermediates in macromolecular binding by paramagnetic NMR. *Nature*, 440(7088), 1227-1230.
- Iwaki, T., Wisniewski, T., Iwaki, A., Corbin, E., Tomokane, N., Tateishi, J., & Goldman, J. E. (1992). Accumulation of alpha B-crystallin in central nervous system glia and neurons in pathologic conditions. *Am J Pathol*, 140(2), 345-356.
- Iwatsubo, T., Odaka, A., Suzuki, N., Mizusawa, H., Nukina, N., & Ihara, Y. (1994). Visualization of A beta 42(43) and A beta 40 in senile plaques with end-specific A beta monoclonals: evidence that an initially deposited species is A beta 42(43). *Neuron*, 13(1), 45-53.
- Jain, E., Bairoch, A., Duvaud, S., Phan, I., Redaschi, N., Suzek, B. E., . . . Gasteiger, E. (2009). Infrastructure for the life sciences: design and implementation of the UniProt website. *BMC Bioinformatics*, 10, 136.

- Jankowsky, J. L., Fadale, D. J., Anderson, J., Xu, G. M., Gonzales, V., Jenkins, N. A., . . . Borchelt, D. R. (2004). Mutant presenilins specifically elevate the levels of the 42 residue beta-amyloid peptide in vivo: evidence for an augmentation of a 42-specific gamma secretase. *Hum Mol Genet*, *13*(2), 159-170.
- Jarrett, J. T., Berger, E. P., & Lansbury, P. T., Jr. (1993a). The carboxy terminus of the beta amyloid protein is critical for the seeding of amyloid formation: implications for the pathogenesis of Alzheimer's disease. *Biochemistry*, *32*(18), 4693-4697.
- Jarrett, J. T., Berger, E. P., & Lansbury, P. T., Jr. (1993b). The C-terminus of the beta protein is critical in amyloidogenesis. *Ann N Y Acad Sci*, *695*, 144-148.
- Jehle, S., Rajagopal, P., Bardiaux, B., Markovic, S., Kuhne, R., Stout, J. R., Oschkinat, H. (2010). Solid-state NMR and SAXS studies provide a structural basis for the activation of alphaB-crystallin oligomers. *Nat Struct Mol Biol*, *17*(9), 1037-1042.
- Jehle, S., van Rossum, B., Stout, J. R., Noguchi, S. M., Falber, K., Rehbein, K., Rajagopal, P. (2009). alphaB-crystallin: a hybrid solid-state/solution-state NMR investigation reveals structural aspects of the heterogeneous oligomer. *J Mol Biol*, *385*(5), 1481-1497.
- Jehle, S., Vollmar, B. S., Bardiaux, B., Dove, K. K., Rajagopal, P., Gonen, T., Klevit, R. E. (2011). N-terminal domain of alphaB-crystallin provides a conformational switch for multimerization and structural heterogeneity. *Proc Natl Acad Sci U S A*, *108*(16), 6409-6414.
- Jomova, K., Vondrakova, D., Lawson, M., & Valko, M. (2010). Metals, oxidative stress and neurodegenerative disorders. *Mol Cell Biochem*, *345*(1-2), 91-104.
- Jones, W. C., Rothgeb, T. M., & Gurd, F. R. (1976). Nuclear magnetic resonance studies of sperm whale myoglobin specifically enriched with ¹³C in the methionine methyl groups. *J Biol Chem*, *251*(23), 7452-7460.
- Kainosho, M., Torizawa, T., Iwashita, Y., Terauchi, T., Mei Ono, A., & Guntert, P. (2006). Optimal isotope labelling for NMR protein structure determinations. *Nature*, *440*(7080), 52-57.
- Kamei, A., Hamaguchi, T., Matsuura, N., Iwase, H., & Masuda, K. (2000). Post-translational modification of alphaB-crystallin of normal human lens. *Biol Pharm Bull*, *23*(2), 226-230.
- Kampinga, H. H., & Craig, E. A. (2010). The HSP70 chaperone machinery: J proteins as drivers of functional specificity. *Nat Rev Mol Cell Biol*, *11*(8), 579-592.
- Kampinga, H. H., & Garrido, C. (2012). HSPBs: small proteins with big implications in human disease. *Int J Biochem Cell Biol*, *44*(10), 1706-1710.
- Kappe, G., Franck, E., Verschuure, P., Boelens, W. C., Leunissen, J. A., & de Jong, W. W. (2003). The human genome encodes 10 alpha-crystallin-related small heat shock proteins: HspB1-10. *Cell Stress Chaperones*, *8*(1), 53-61.
- Kappe, G., Leunissen, J. A., & de Jong, W. W. (2002). Evolution and diversity of prokaryotic small heat shock proteins. *Prog Mol Subcell Biol*, *28*, 1-17.
- Kaptein, R., Zuiderweg, E. R., Scheek, R. M., Boelens, R., & van Gunsteren, W. F. (1985). A protein structure from nuclear magnetic resonance data. lac repressor headpiece. *J Mol Biol*, *182*(1), 179-182.
- Karplus, M., & Petsko, G. A. (1990). Molecular dynamics simulations in biology. *Nature*, *347*(6294), 631-639.
- Kase, S., He, S., Sonoda, S., Kitamura, M., Spee, C., Wawrousek, E., Hinton, D. R. (2010). alphaB-crystallin regulation of angiogenesis by modulation of VEGF. *Blood*, *115*(16), 3398-3406.
- Kato, K., Goto, S., Inaguma, Y., Hasegawa, K., Morishita, R., & Asano, T. (1994). Purification and characterization of a 20-kDa protein that is highly homologous to alpha B crystallin. *J Biol Chem*, *269*(21), 15302-15309.
- Kato, K., Ito, H., Kamei, K., Inaguma, Y., Iwamoto, I., & Saga, S. (1998). Phosphorylation of alphaB-crystallin in mitotic cells and identification of enzymatic activities responsible for phosphorylation. *J Biol Chem*, *273*(43), 28346-28354.
- Kato, K., Shinohara, H., Kurobe, N., Inaguma, Y., Shimizu, K., & Ohshima, K. (1991). Tissue distribution and developmental profiles of immunoreactive alpha B crystallin in the rat determined with a sensitive immunoassay system. *Biochim Biophys Acta*, *1074*(1), 201-208.
- Kay, L. E., & Gardner, K. H. (1997). Solution NMR spectroscopy beyond 25 kDa. *Curr Opin Struct Biol*, *7*(5), 722-731.
- Kay, L. E., Ikura, M., Tschudin, R. and Bax, A. (1990). Three-dimensional triple-resonance NMR Spectroscopy of isotopically enriched proteins. *J Magn Reson* *89*: 496-514.
- Kay, L. E., Torchia, D. A., & Bax, A. (1989). Backbone dynamics of proteins as studied by ¹⁵N inverse detected heteronuclear NMR spectroscopy: application to staphylococcal nuclease. *Biochemistry*, *28*(23), 8972-8979.
- Keeler, J. (2011). Understanding NMR spectroscopy. *John Wiley & Sons*.
- Kelley, M. J., David, L. L., Iwasaki, N., Wright, J., & Shearer, T. R. (1993). alpha-Crystallin chaperone activity is reduced by calpain II in vitro and in senile cataract. *J Biol Chem*, *268*(25), 18844-18849.
- Kendrew, J. C., Bodo, G., Dintzis, H. M., Parrish, R. G., Wyckoff, H., & Phillips, D. C. (1958). A three-dimensional model of the myoglobin molecule obtained by x-ray analysis. *Nature*, *181*(4610), 662-666.
- Kerner, M. J., Naylor, D. J., Ishihama, Y., Maier, T., Chang, H. C., Stines, A. P., Hartl, F. U. (2005). Proteome-wide analysis of chaperonin-dependent protein folding in Escherichia coli. *Cell*, *122*(2), 209-220.
- Kim, K. K., Kim, R., & Kim, S. H. (1998). Crystal structure of a small heat-shock protein. *Nature*, *394*(6693), 595-599. doi: 10.1038/29106
- Kim, Y. E., Hipp, M. S., Bracher, A., Hayer-Hartl, M., & Hartl, F. U. (2013). Molecular chaperone functions in protein folding and proteostasis. *Annu Rev Biochem*, *82*, 323-355.
- Kleckner, I. R., & Foster, M. P. (2011). An introduction to NMR-based approaches for measuring protein dynamics. *Biochim Biophys Acta*, *1814*(8), 942-968.
- Knowles, T. P., Waudby, C. A., Devlin, G. L., Cohen, S. I., Aguzzi, A., Vendruscolo, M., . . . Dobson, C. M. (2009). An analytical solution to the kinetics of breakable filament assembly. *Science*, *326*(5959), 1533-1537.
- Kosen, P. A. (1989). *Methods Enzymol.*, *177*, 86.
- Koteiche, H. A., & McHaourab, H. S. (1999). Folding pattern of the alpha-crystallin domain in alphaA-crystallin determined by site-directed spin labeling. *J Mol Biol*, *294*(2), 561-577.
- Kriehuber, T., Rattei, T., Weinmaier, T., Bepperling, A., Haslbeck, M., & Buchner, J. (2010). Independent evolution of the core domain and its flanking sequences in small heat shock proteins. *FASEB J*, *24*(10), 3633-3642.
- Kumar, P. A., Kumar, M. S., & Reddy, G. B. (2007). Effect of glycation on alpha-crystallin structure and chaperone-like function. *Biochem J*, *408*(2), 251-258.
- Kumar, S.M., et al. (2004). Enhanced degradation and decreased stability of eye lens alphacrystallin upon methylglyoxal modification. *Exp Eye Res*. *79*(4): 577-83.
- Laajoki, L. G., Francis, G. L., Wallace, J. C., Carver, J. A., & Keniry, M. A. (2000). Solution structure and backbone dynamics of long-[Arg(3)]insulin-like growth factor-I. *J Biol Chem*, *275*(14), 10009-10015.
- Laemmli, U. K. (1970). "Cleavage of structural proteins during the assembly of the head of bacteriophage T4." *Nature* **227**: 680-685.
- Laganowsky, A., & Eisenberg, D. (2010b). Non-3D domain swapped crystal structure of truncated zebrafish alphaA crystallin. *Protein Sci*, *19*(10), 1978-1984.

- Laganowsky, A., Benesch, J. L., Landau, M., Ding, L., Sawaya, M. R., Cascio, D., Eisenberg, D. (2010a). Crystal structures of truncated alphaA and alphaB crystallins reveal structural mechanisms of polydispersity important for eye lens function. *Protein Sci*, *19*(5), 1031-1043.
- Landry, J., Chretien, P., Laszlo, A., & Lambert, H. (1991). Phosphorylation of HSP27 during development and decay of thermotolerance in Chinese hamster cells. *J Cell Physiol*, *147*(1), 93-101.
- Landry, J., Lambert, H., Zhou, M., Lavoie, J. N., Hickey, E., Weber, L. A., & Anderson, C. W. (1992). Human HSP27 is phosphorylated at serines 78 and 82 by heat shock and mitogen-activated kinases that recognize the same amino acid motif as S6 kinase II. *J Biol Chem*, *267*(2), 794-803.
- Larkin, M. A., Blackshields, G., Brown, N. P., Chenna, R., McGettigan, P. A., McWilliam, H., . . . Higgins, D. G. (2007). Clustal W and Clustal X version 2.0. *Bioinformatics*, *23*(21), 2947-2948.
- Laskey, R. A., Honda, B. M., Mills, A. D., & Finch, J. T. (1978). Nucleosomes are assembled by an acidic protein which binds histones and transfers them to DNA. *Nature*, *275*(5679), 416-420.
- Latchman, D. S. (2002). Protection of neuronal and cardiac cells by HSP27. *Prog Mol Subcell Biol*, *28*, 253-265.
- Launay, N., Goudeau, B., Kato, K., Vicart, P., & Lilienbaum, A. (2006). Cell signaling pathways to alphaB-crystallin following stresses of the cytoskeleton. *Exp Cell Res*, *312*(18), 3570-3584.
- Levitt, M. (2013). Spin Dynamics: Basics of Nuclear Magnetic Resonance, 2nd Ed., John Wiley & Sons.
- Levy, M., Karplus, M., & McCammon, J. A. (1981). Increase of τ -13 nmr relaxation-times in proteins due to picosecond motional averaging. *J. Am. Chem. Soc.*, *103*(4):994-996.
- Li, H., Li, C., Lu, Q., Su, T., Ke, T., Li, D. W., Liu, M. (2008). Cataract mutation P20S of alphaB-crystallin impairs chaperone activity of alphaA-crystallin and induces apoptosis of human lens epithelial cells. *Biochim Biophys Acta*, *1782*(5), 303-309.
- Liang, J. J. (2000). Interaction between beta-amyloid and lens alphaB-crystallin. *FEBS Lett*, *484*(2), 98-101.
- Lichtenecker, R. J., Coudeville, N., Konrat, R., & Schmid, W. (2013). Selective isotope labelling of leucine residues by using alpha-ketoacid precursor compounds. *Chembiochem*, *14*(7), 818-821.
- Lichtenthaler, S. F., Haass, C., & Steiner, H. (2011). Regulated intramembrane proteolysis—lessons from amyloid precursor protein processing. *J Neurochem*, *117*(5), 779-796.
- Lin, P. P., Barry, R. C., Smith, D. L., & Smith, J. B. (1998). In vivo acetylation identified at lysine 70 of human lens alphaA-crystallin. *Protein Sci*, *7*(6), 1451-1457.
- Litt, M., Kramer, P., LaMorticella, D. M., Murphey, W., Lovrien, E. W., & Weleber, R. G. (1998). Autosomal dominant congenital cataract associated with a missense mutation in the human alpha crystallin gene CRYAA. *Hum Mol Genet*, *7*(3), 471-474.
- Liu, M. et al. (1998). Improved WATERGATE Pulse Sequences for Solvent Suppression in NMR Spectroscopy. *J. Magn. Reson.* **132**, 125-129.
- Liu, Y., Zhang, X., Luo, L., Wu, M., Zeng, R., Cheng, G., Shang, F. (2006). A novel alphaB-crystallin mutation associated with autosomal dominant congenital lamellar cataract. *Invest Ophthalmol Vis Sci*, *47*(3), 1069-1075.
- Lomakin, A., Teplow, D. B., Kirschner, D. A., & Benedek, G. B. (1997). Kinetic theory of fibrillogenesis of amyloid beta-protein. *Proc Natl Acad Sci U S A*, *94*(15), 7942-7947.
- Lowe, I. J. (1959). Free Induction Decays of Rotating Solids. *Physical Review Letters*, *2*(7):285.
- Lu, J. X., Qiang, W., Yau, W. M., Schwieters, C. D., Meredith, S. C., & Tycko, R. (2013). Molecular structure of beta-amyloid fibrils in Alzheimer's disease brain tissue. *Cell*, *154*(6), 1257-1268.
- Lund, A. L., Smith, J. B., & Smith, D. L. (1996). Modifications of the water-insoluble human lens alpha-crystallins. *Exp Eye Res*, *63*(6), 661-672.
- Macario, A. J., & Conway de Macario, E. (2005). Sick chaperones, cellular stress, and disease. *N Engl J Med*, *353*(14), 1489-1501.
- MacCoss, M. J., McDonald, W. H., Saraf, A., Sadygov, R., Clark, J. M., Tasto, J. J., Yates, J. R., 3rd. (2002). Shotgun identification of protein modifications from protein complexes and lens tissue. *Proc Natl Acad Sci U S A*, *99*(12), 7900-7905.
- Mackay, D. S., Andley, U. P., & Shiels, A. (2003). Cell death triggered by a novel mutation in the alphaA-crystallin gene underlies an autosomal dominant cataract linked to chromosome 21q. *Eur J Hum Genet*, *11*(10), 784-793.
- MacRae, T. H. (2000). Structure and function of small heat shock/alpha-crystallin proteins: established concepts and emerging ideas. *Cell Mol Life Sci*, *57*(6), 899-913.
- Mainz, A., Bardiaux, B., Kuppler, F., Multhaupt, G., Felli, I. C., Pierattelli, R., & Reif, B. (2012). Structural and mechanistic implications of metal binding in the small heat-shock protein alphaB-crystallin. *J Biol Chem*, *287*(2), 1128-1138.
- Mainz, A., Peschek, J., Stavropoulou, M., Back, K. C., Bardiaux, B., Asami, S., Reif, B. (2015). The chaperone alphaB-crystallin uses different interfaces to capture an amorphous and an amyloid client. *Nat Struct Mol Biol*, *22*(11), 898-905.
- Maloy, S. (2002). Codon usage in E. coli. <http://www.sci.sdsu.edu/smaloy/MicrobialGenetics/topics/in-vitro-genetics/codon-usage.html>.
- Manolikas, T., Herrmann, T., & Meier, B. H. (2008). Protein structure determination from 13C spin-diffusion solid-state NMR spectroscopy. *J Am Chem Soc*, *130*(12), 3959-3966.
- Mao, P., & Reddy, P. H. (2011). Aging and amyloid beta-induced oxidative DNA damage and mitochondrial dysfunction in Alzheimer's disease: implications for early intervention and therapeutics. *Biochim Biophys Acta*, *1812*(11), 1359-1370.
- Marchetti, A., Jehle, S., Felletti, M., Knight, M. J., Wang, Y., Xu, Z. Q., . . . Pintacuda, G. (2012). Backbone assignment of fully protonated solid proteins by 1H detection and ultrafast magic-angle-spinning NMR spectroscopy. *Angew Chem Int Ed Engl*, *51*(43), 10756-10759.
- Marion, D., Driscoll, P. C., Kay, L. E., Wingfield, P. T., Bax, A., Gronenborn, A. M. and Clore, G. M. (1989). Overcoming the overlap problem in the assignment of 1H NMR spectra of larger proteins by use of three-dimensional heteronuclear 1H-15N Hartmann-Hahn-multiple quantum coherence and nuclear Overhauser-multiple quantum coherence spectroscopy: application to interleukin 1 beta. *Biochemistry* *28*: 6150-6156.
- Markwick, P. R., Malliavin, T., & Nilges, M. (2008). Structural biology by NMR: structure, dynamics, and interactions. *PLoS Comput Biol*, *4*(9), e1000168.
- Mas, G., Crublet, E., Hamelin, O., Gans, P., & Boisbouvier, J. (2013). Specific labeling and assignment strategies of valine methyl groups for NMR studies of high molecular weight proteins. *J Biomol NMR*, *57*(3), 251-262.
- Mayer, M. P. (2010). Gymnastics of molecular chaperones. *Mol Cell*, *39*(3), 321-331.
- McClellan, A. J., Xia, Y., Deutschbauer, A. M., Davis, R. W., Gerstein, M., & Frydman, J. (2007). Diverse cellular functions of the Hsp90 molecular chaperone uncovered using systems approaches. *Cell*, *131*(1), 121-135.
- McHaourab, H. S., Berengian, A. R., & Koteiche, H. A. (1997). Site-directed spin-labeling study of the structure and subunit interactions along a conserved sequence in the alpha-crystallin domain of heat-shock protein 27. Evidence of a conserved subunit interface. *Biochemistry*, *36*(48), 14627-14634.
- McIntosh, P. L. (2013). CPMG. In G. C. K. Roberts (Ed.), *Encyclopedia of Biophysics* (pp. 386-386). Berlin, Heidelberg: Springer Berlin Heidelberg.
- Meiboom, S. & Gill, D. (1958). Modified Spin-Echo Method for Measuring Nuclear Relaxation Times. *Review of Scientific Instruments*, *29*, 688-691.
- Merril, C. R. (1990). "Silver staining of proteins and DNA." *Nature* **343**: 779-780.

- Miyanoiri, Y., Takeda, M., Okuma, K., Ono, A. M., Terauchi, T., & Kainosho, M. (2013). Differential isotope-labeling for Leu and Val residues in a protein by E. coli cellular expression using stereo-specifically methyl labeled amino acids. *J Biomol NMR*, 57(3), 237-249.
- Morimoto, R. I., & Cuervo, A. M. (2009). Protein homeostasis and aging: taking care of proteins from the cradle to the grave. *J Gerontol A Biol Sci Med Sci*, 64(2), 167-170.
- Morimoto, R. I., Selkoe, D. J., & Kelly, J. W. (2012). Protein Homeostasis 1st edition, Cold Spring Harbor Laboratory Press, Cold Spring Harbor, New York.
- Muchowski, P. J., & Wacker, J. L. (2005). Modulation of neurodegeneration by molecular chaperones. *Nat Rev Neurosci*, 6(1), 11-22.
- Muirhead, H., & Perutz, M. F. (1963). Structure of Haemoglobin. A Three-Dimensional Fourier Synthesis of Reduced Human Haemoglobin at 5.5 Å Resolution. *Nature*, 199, 633-638.
- Mulder, F. A., Mittelman, A., Hon, B., Dahlquist, F. W., & Kay, L. E. (2001). Studying excited states of proteins by NMR spectroscopy. *Nat Struct Biol*, 8(11), 932-935.
- Mund, M., Overbeck, J. H., Ullmann, J., & Sprangers, R. (2013). LEGO-NMR spectroscopy: a method to visualize individual subunits in large heteromeric complexes. *Angew Chem Int Ed Engl*, 52(43), 11401-11405.
- Munoz, I. G., Yebenes, H., Zhou, M., Mesa, P., Serna, M., Park, A. Y., Montoya, G. (2011). Crystal structure of the open conformation of the mammalian chaperonin CCT in complex with tubulin. *Nat Struct Mol Biol*, 18(1), 14-19.
- Nagaraj, R. H., Nahomi, R. B., Shanthakumar, S., Linetsky, M., Padmanabha, S., Pasupuleti, N., Biswas, A. (2012). Acetylation of alphaA-crystallin in the human lens: effects on structure and chaperone function. *Biochim Biophys Acta*, 1822(2), 120-129.
- Nakamoto, H., & Vigh, L. (2007). The small heat shock proteins and their clients. *Cell Mol Life Sci*, 64(3), 294-306.
- Narayanan, S., Kamps, B., Boelens, W. C., & Reif, B. (2006). alphaB-crystallin competes with Alzheimer's disease beta-amyloid peptide for peptide-peptide interactions and induces oxidation of Abeta-Met35. *FEBS Lett*, 580(25), 5941-5946.
- Narberhaus, F. (2002). Alpha-crystallin-type heat shock proteins: socializing minichaperones in the context of a multichaperone network. *Microbiol Mol Biol Rev*, 66(1), 64-93; table of contents.
- Ngo, J. T., Klisak, I., Dubin, R. A., Piatigorsky, J., Mohandas, T., Sparkes, R. S., & Bateman, J. B. (1989). Assignment of the alpha B-crystallin gene to human chromosome 11. *Genomics*, 5(4), 665-669.
- Numoto, N., Kita, A., Fujii, N., & Miki, K. (2012). A P39R mutation at the N-terminal domain of human alphaB-crystallin regulates its oligomeric state and chaperone-like activity. *Biochem Biophys Res Commun*, 425(3), 601-606.
- Ollerenshaw, J. E., Tugarinov, V. and Kay, L. E. (2003), Methyl TROSY: explanation and experimental verification. *Magn. Reson. Chem.*, 41: 843-852. One-way ANOVA followed by Dunnett's multiple comparisons test was performed using GraphPad Prism version 7.00 for Windows, GraphPad Software, La Jolla California USA, www.graphpad.com.
- Paravastu, A. K., Leapman, R. D., Yau, W. M., & Tycko, R. (2008). Molecular structural basis for polymorphism in Alzheimer's beta-amyloid fibrils. *Proc Natl Acad Sci U S A*, 105(47), 18349-18354.
- Pervushin, K., Riek, R., Wider, G., & Wuthrich, K. (1997). Attenuated T2 relaxation by mutual cancellation of dipole-dipole coupling and chemical shift anisotropy indicates an avenue to NMR structures of very large biological macromolecules in solution. *Proc Natl Acad Sci U S A*, 94(23), 12366-12371.
- Peschek, J., Braun, N., Franzmann, T. M., Georgalis, Y., Haslbeck, M., Weinkauff, S., & Buchner, J. (2009). The eye lens chaperone alpha-crystallin forms defined globular assemblies. *Proc Natl Acad Sci U S A*, 106(32), 13272-13277.
- Peschek, J., Braun, N., Rohrbeg, J., Back, K. C., Kriehuber, T., Kastenmuller, A., Buchner, J. (2013). Regulated structural transitions unleash the chaperone activity of alphaB-crystallin. *Proc Natl Acad Sci U S A*, 110(40), E3780-3789.
- Petkova, A. T., Ishii, Y., Balbach, J. J., Antzutkin, O. N., Leapman, R. D., Delaglio, F., & Tycko, R. (2002). A structural model for Alzheimer's beta-amyloid fibrils based on experimental constraints from solid state NMR. *Proc Natl Acad Sci U S A*, 99(26), 16742-16747.
- Petkova, A. T., Yau, W. M., & Tycko, R. (2006). Experimental constraints on quaternary structure in Alzheimer's beta-amyloid fibrils. *Biochemistry*, 45(2), 498-512.
- Philipson B (1969) Distribution of protein within the normal rat lens. *Invest Ophthalmol* 8:258-270.
- Pierscionek BK, Augusteyn RC (1995) The refractive index and protein distribution in the blue eye trevally lens. *J Am Optom Assoc* 66:739-743.
- Pilotto, A., Marziliano, N., Pasotti, M., Grasso, M., Costante, A. M., & Arbustini, E. (2006). alphaB-crystallin mutation in dilated cardiomyopathies: low prevalence in a consecutive series of 200 unrelated probands. *Biochem Biophys Res Commun*, 346(4), 1115-1117.
- Pines, A., Gibby, M. G., and Waugh, J. S. (1973). Proton-enhanced NMR of dilute spins in solids. *J. Chem. Phys.* 59, 569-590.
- Posner, M., Hawke, M., Lacava, C., Prince, C. J., Bellanco, N. R., & Corbin, R. W. (2008). A proteome map of the zebrafish (Danio rerio) lens reveals similarities between zebrafish and mammalian crystallin expression. *Mol Vis*, 14, 806-814.
- Quax-Jeuken, Y., Quax, W., van Rens, G., Khan, P. M., & Bloemendal, H. (1985). Complete structure of the alpha B-crystallin gene: conservation of the exon-intron distribution in the two nonlinked alpha-crystallin genes. *Proc Natl Acad Sci U S A*, 82(17), 5819-5823.
- Raman, B., Ban, T., Sakai, M., Pasta, S. Y., Ramakrishna, T., Naiki, H., . . . Rao Ch, M. (2005). AlphaB-crystallin, a small heat-shock protein, prevents the amyloid fibril growth of an amyloid beta-peptide and beta2-microglobulin. *Biochem J*, 392(Pt 3), 573-581.
- Redfield, C., Boyd, J., Smith, L. J., Smith, R. A., & Dobson, C. M. (1992). Loop mobility in a four-helix-bundle protein: 15N NMR relaxation measurements on human interleukin-4. *Biochemistry*, 31(43), 10431-10437.
- Reichmann D, et al. (2012) Order out of disorder: Working cycle of an intrinsically unfolded chaperone. *Cell* 148(5):947-957.
- Rekas, A., Adda, C. G., Andrew Aquilina, J., Barnham, K. J., Sunde, M., Galatis, D., Carver, J. A. (2004). Interaction of the molecular chaperone alphaB-crystallin with alpha-synuclein: effects on amyloid fibril formation and chaperone activity. *J Mol Biol*, 340(5), 1167-1183.
- Religa, T. L., Sprangers, R., & Kay, L. E. (2010). Dynamic regulation of archaeal proteasome gate opening as studied by TROSY NMR. *Science*, 328(5974), 98-102.
- Renkawek, K., Voorter, C. E., Bosman, G. J., van Workum, F. P., & de Jong, W. W. (1994). Expression of alpha B-crystallin in Alzheimer's disease. *Acta Neuropathol*, 87(2), 155-160.
- Richter, K., Haslbeck, M., & Buchner, J. (2010). The heat shock response: life on the verge of death. *Mol Cell*, 40(2), 253-266.
- Richter, L., Flodman, P., Barria von-Bischhoffshausen, F., Burch, D., Brown, S., Nguyen, L., . . . Bateman, J. B. (2008). Clinical variability of autosomal dominant cataract, microcornea and corneal opacity and novel mutation in the alpha A crystallin gene (CRYAA). *Am J Med Genet A*, 146A(7), 833-842.
- Riek, R., Guntert, P., Dobeli, H., Wipf, B., & Wuthrich, K. (2001). NMR studies in aqueous solution fail to identify significant conformational differences between the monomeric forms of two Alzheimer peptides with widely different plaque-competence, A beta(1-40)(ox) and A beta(1-42)(ox). *Eur J Biochem*, 268(22), 5930-5936.
- Ritossa, F. (1962). A new puffing pattern induced by temperature shock and DNP in drosophila. *Experientia*, 18(12), 571-573.
- Roher, A. E., Lowenson, J. D., Clarke, S., Woods, A. S., Cotter, R. J., Gowing, E., & Ball, M. J. (1993). beta-Amyloid-(1-42) is a major component of cerebrovascular amyloid deposits: implications for the pathology of Alzheimer disease. *Proc Natl Acad Sci U S A*, 90(22), 10836-10840.

- Rudiger, S., Freund, S. M., Vepintsev, D. B., & Fersht, A. R. (2002). CRINEPT-TROSY NMR reveals p53 core domain bound in an unfolded form to the chaperone Hsp90. *Proc Natl Acad Sci U S A*, *99*(17), 11085-11090.
- Ruschak, A. M., Velyvis, A., & Kay, L. E. (2010). A simple strategy for (1)3C, (1)H labeling at the Ile-gamma2 methyl position in highly deuterated proteins. *J Biomol NMR*, *48*(3), 129-135.
- Sacchettini, J. C., & Kelly, J. W. (2002). Therapeutic strategies for human amyloid diseases. *Nat Rev Drug Discov*, *1*(4), 267-275.
- Sachse, C., Fandrich, M., & Grigorieff, N. (2008). Paired beta-sheet structure of an Abeta(1-40) amyloid fibril revealed by electron microscopy. *Proc Natl Acad Sci U S A*, *105*(21), 7462-7466.
- Safieh, L. A., Khan, A. O., & Alkuraya, F. S. (2009). Identification of a novel CRYAB mutation associated with autosomal recessive juvenile cataract in a Saudi family. *Mol Vis*, *15*, 980-984.
- Samoson, A., Tuhem, T., & Gan, Z. (2001). High-field high-speed MAS resolution enhancement in 1H NMR spectroscopy of solids. *Solid State Nucl Magn Reson*, *20*(3-4), 130-136.
- Santhiya, S. T., Soker, T., Klopp, N., Illig, T., Prakash, M. V., Selvaraj, B., Graw, J. (2006). Identification of a novel, putative cataract-causing allele in CRYAA (G98R) in an Indian family. *Mol Vis*, *12*, 768-773.
- Santhoshkumar, P., & Sharma, K. K. (2004). Inhibition of amyloid fibrillogenesis and toxicity by a peptide chaperone. *Mol Cell Biochem*, *267*(1-2), 147-155.
- Santhoshkumar, P., Murugesan, R., & Sharma, K. K. (2009). Deletion of (54)FLRAPSWF(61) residues decreases the oligomeric size and enhances the chaperone function of alphaB-crystallin. *Biochemistry*, *48*(23), 5066-5073.
- Santoro, M. G. (2000). Heat shock factors and the control of the stress response. *Biochem Pharmacol*, *59*(1), 55-63.
- Sattler, M., & Fesik, S. W. (1996). Use of deuterium labeling in NMR: overcoming a sizeable problem. *Structure*, *4*(11), 1245-1249.
- Sattler, Michael, Schleucher, Jürgen, & Griesinger, Christian. (1999). Heteronuclear multidimensional NMR experiments for the structure determination of proteins in solution employing pulsed field gradients. *Progress in Nuclear Magnetic Resonance Spectroscopy*, *34*(2), 93-158.
- Schaefer, H., Chamrad, D. C., Herrmann, M., Stuwe, J., Becker, G., Klose, J., Marcus, K. (2006). Study of posttranslational modifications in lenticular alphaA-Crystallin of mice using proteomic analysis techniques. *Biochim Biophys Acta*, *1764*(12), 1948-1962.
- Schagger, H. (2006). Tricine-SDS-PAGE. *Nat Protoc*, *1*(1), 16-22.
- Schanda, P., & Brutscher, B. (2005). Very fast two-dimensional NMR spectroscopy for real-time investigation of dynamic events in proteins on the time scale of seconds. *J Am Chem Soc*, *127*(22), 8014-8015.
- Schlesinger, M. J. (1990). Heat shock proteins. *J Biol Chem*, *265*(21), 12111-12114.
- Schutz, A. K., Vagt, T., Huber, M., Ovchinnikova, O. Y., Cadalbert, R., Wall, J., . . . Meier, B. H. (2015). Atomic-resolution three-dimensional structure of amyloid beta fibrils bearing the Osaka mutation. *Angew Chem Int Ed Engl*, *54*(1), 331-335.
- Selcen, D., & Engel, A. G. (2003). Myofibrillar myopathy caused by novel dominant negative alpha B-crystallin mutations. *Ann Neurol*, *54*(6), 804-810.
- Selkoe, D. J. (1994a). Alzheimer's disease: a central role for amyloid. *J Neuropathol Exp Neurol*, *53*(5), 438-447.
- Selkoe, D. J. (1994b). Cell biology of the amyloid beta-protein precursor and the mechanism of Alzheimer's disease. *Annu Rev Cell Biol*, *10*, 373-403.
- Selkoe, D. J. (2001). Alzheimer's disease: genes, proteins, and therapy. *Physiol Rev*, *81*(2), 741-766.
- Selkoe, D. J., & Hardy, J. (2016). The amyloid hypothesis of Alzheimer's disease at 25 years. *EMBO Mol Med*, *8*(6), 595-608.
- Servis, K. L., & Shue, F. F. (1980). Deuterium Isotope Effects on the Carbon-13 Chemical Shifts of Carbocations. *J Am Chem Soc*, *102*(24), 1233-1240.
- Sgourakis, N. G., Yau, W. M., & Qiang, W. (2015). Modeling an in-register, parallel "iowa" beta fibril structure using solid-state NMR data from labeled samples with rosetta. *Structure*, *23*(1), 216-227.
- Shammas, S. L., Waudby, C. A., Wang, S., Buell, A. K., Knowles, T. P., Ecroyd, H., . . . Meehan, S. (2011). Binding of the molecular chaperone alphaB-crystallin to Abeta amyloid fibrils inhibits fibril elongation. *Biophys J*, *101*(7), 1681-1689.
- Sharma, S. K., De los Rios, P., Christen, P., Lustig, A., & Goloubinoff, P. (2010). The kinetic parameters and energy cost of the Hsp70 chaperone as a polypeptide unfoldase. *Nat Chem Biol*, *6*(12), 914-920.
- Sharp, S., & Workman, P. (2006). Inhibitors of the HSP90 molecular chaperone: current status. *Adv Cancer Res*, *95*, 323-348.
- Shen, Y., Delaglio, F., Cornilescu, G., & Bax, A. (2009). TALOS+: a hybrid method for predicting protein backbone torsion angles from NMR chemical shifts. *J Biomol NMR*, *44*(4), 213-223.
- Shen, Y., Lange, O., Delaglio, F., Rossi, P., Aramini, J. M., Liu, G., . . . Bax, A. (2008). Consistent blind protein structure generation from NMR chemical shift data. *Proc Natl Acad Sci U S A*, *105*(12), 4685-4690.
- Simon, B., Madl, T., Mackereth, C. D., Nilges, M., & Sattler, M. (2010). An efficient protocol for NMR-spectroscopy-based structure determination of protein complexes in solution. *Angew Chem Int Ed Engl*, *49*(11), 1967-1970.
- Sinha, K., Jen-Jacobson, L., & Rule, G. S. (2011). Specific labeling of threonine methyl groups for NMR studies of protein-nucleic acid complexes. *Biochemistry*, *50*(47), 10189-10191.
- Sipe, J. D. (1992). Amyloidosis. *Annu Rev Biochem*, *61*, 947-975.
- Slepenkov, S. V., & Witt, S. N. (2002). The unfolding story of the Escherichia coli Hsp70 DnaK: is DnaK a holdase or an unfoldase? *Mol Microbiol*, *45*(5), 1197-1206.
- Smith, D. G., Cappai, R., & Barnham, K. J. (2007). The redox chemistry of the Alzheimer's disease amyloid beta peptide. *Biochim Biophys Acta*, *1768*(8), 1976-1990.
- Smith, J. B., Sun, Y., Smith, D. L., & Green, B. (1992). Identification of the posttranslational modifications of bovine lens alpha B-crystallins by mass spectrometry. *Protein Sci*, *1*(5), 601-608.
- Smulders, Rph, Carver, J. A., Lindner, R. A., van Boekel, M. A., Bloemendal, H., & de Jong, W. W. (1996). Immobilization of the C-terminal extension of bovine alphaA-crystallin reduces chaperone-like activity. *J Biol Chem*, *271*(46), 29060-29066.
- Spector, A., Chiesa, R., Sredy, J., & Garner, W. (1985). cAMP-dependent phosphorylation of bovine lens alpha-crystallin. *Proc Natl Acad Sci U S A*, *82*(14), 4712-4716.
- Sprangers, R., & Kay, L. E. (2007). Quantitative dynamics and binding studies of the 20S proteasome by NMR. *Nature*, *445*(7128), 618-622.
- Sprangers, R., Gribun, A., Hwang, P. M., Houry, W. A., & Kay, L. E. (2005). Quantitative NMR spectroscopy of supramolecular complexes: dynamic side pores in ClpP are important for product release. *Proc Natl Acad Sci U S A*, *102*(46), 16678-16683.
- Sreelakshmi, Y., & Sharma, K. K. (2006). The interaction between alphaA- and alphaB-crystallin is sequence-specific. *Mol Vis*, *12*, 581-587.
- Sreelakshmi, Y., Santhoshkumar, P., Bhattacharyya, J., & Sharma, K. K. (2004). AlphaA-crystallin interacting regions in the small heat shock protein, alphaB-crystallin. *Biochemistry*, *43*(50), 15785-15795.
- Srinivas, P., Narahari, A., Petrash, J. M., Swamy, M. J., & Reddy, G. B. (2010). Importance of eye lens alpha-crystallin heteropolymer with 3:1 alphaA to alphaB ratio: stability, aggregation, and modifications. *IUBMB Life*, *62*(9), 693-702.
- Stege, G. J., Renkawek, K., Overkamp, P. S., Verschuure, P., van Rijk, A. F., Reijnen-Aalbers, A., . . . de Jong, W. W. (1999). The molecular chaperone alphaB-crystallin enhances amyloid beta neurotoxicity. *Biochem Biophys Res Commun*, *262*(1), 152-156.

- Steinman, L. (2009). A molecular trio in relapse and remission in multiple sclerosis. *Nat Rev Immunol*, 9(6), 440-447.
- Stengel, F., Baldwin, A. J., Painter, A. J., Jaya, N., Basha, E., Kay, L. E., . . . Benesch, J. L. (2010). Quaternary dynamics and plasticity underlie small heat shock protein chaperone function. *Proc Natl Acad Sci USA*, 107(5), 2007-2012.
- Stevens, V. J., Rouzer, C. A., Monnier, V. M., & Cerami, A. (1978). Diabetic cataract formation: potential role of glycosylation of lens crystallins. *Proc Natl Acad Sci USA*, 75(6), 2918-2922.
- Straub, J. E., & Thirumalai, D. (2011). Toward a molecular theory of early and late events in monomer to amyloid fibril formation. *Annu Rev Phys Chem*, 62, 437-463.
- Suh, J. Y., Tang, C., & Clore, G. M. (2007). Role of electrostatic interactions in transient encounter complexes in protein-protein association investigated by paramagnetic relaxation enhancement. *J Am Chem Soc*, 129(43), 12954-12955.
- Sun, Y., & MacRae, T. H. (2005). Small heat shock proteins: molecular structure and chaperone function. *Cell Mol Life Sci*, 62(21), 2460-2476.
- Suzuki, N., Cheung, T. T., Cai, X. D., Odaka, A., Otvos, L., Jr., Eckman, C., . . . Younkin, S. G. (1994). An increased percentage of long amyloid beta protein secreted by familial amyloid beta protein precursor (beta APP717) mutants. *Science*, 264(5163), 1336-1340.
- Szeverenyi, N. M., Sullivan, M. J., and Maciel, G. E. (1982). Observation of spin exchange by two-dimensional fourier transform ¹³C cross polarization-magic-angle spinning. *J Magn. Reson.* 47, 462-475.
- Szymczyna, B. R., Gan, L., Johnson, J. E., & Williamson, J. R. (2007). Solution NMR studies of the maturation intermediates of a 13 MDa viral capsid. *J Am Chem Soc*, 129(25), 7867-7876.
- Tabner, B. J., Turnbull, S., El-Agnaf, O. M., & Allsop, D. (2002). Formation of hydrogen peroxide and hydroxyl radicals from A(beta) and alpha-synuclein as a possible mechanism of cell death in Alzheimer's disease and Parkinson's disease. *Free Radic Biol Med*, 32(11), 1076-1083.
- Taipale, M., Jarosz, D. F., & Lindquist, S. (2010). HSP90 at the hub of protein homeostasis: emerging mechanistic insights. *Nat Rev Mol Cell Biol*, 11(7), 515-528.
- Takemoto, L. J. (1996). Differential phosphorylation of alpha-A crystallin in human lens of different age. *Exp Eye Res*, 62(5), 499-504.
- Takemoto, L. J. (1998). Quantitation of asparagine-101 deamidation from alpha-A crystallin during aging of the human lens. *Curr Eye Res*, 17(3), 247-250.
- Takemoto, L., Emmons, T., & Horwitz, J. (1993). The C-terminal region of alpha-crystallin: involvement in protection against heat-induced denaturation. *Biochem J*, 294 (Pt 2), 435-438.
- Tang, C., Iwahara, J., & Clore, G. M. (2006). Visualization of transient encounter complexes in protein-protein association. *Nature*, 444(7117), 383-386.
- Tapley TL, et al. (2009) Structural plasticity of an acid-activated chaperone allows promiscuous substrate binding. *Proc Natl Acad Sci USA* 106(14):5557-5562.
- Thompson, J. D., Higgins, D. G., & Gibson, T. J. (1994). CLUSTAL W: improving the sensitivity of progressive multiple sequence alignment through sequence weighting, position-specific gap penalties and weight matrix choice. *Nucleic Acids Res*, 22(22), 4673-4680.
- Tikhomirova, T. S., Selivanova, O. M., & Galzitskaya, O. V. (2017). alpha-Crystallins Are Small Heat Shock Proteins: Functional and Structural Properties. *Biochemistry (Mosc)*, 82(2), 106-121.
- Tilley, L., Morgan, K., & Kalsheker, N. (1998). Genetic risk factors in Alzheimer's disease. *Mol Pathol*, 51(6), 293-304.
- Tissieres, A., Mitchell, H. K., & Tracy, U. M. (1974). Protein synthesis in salivary glands of *Drosophila melanogaster*: relation to chromosome puffs. *J Mol Biol*, 84(3), 389-398.
- Tkáčová, J. & Angelovičová, M. (2012). Heat shock proteins (HSPs): a review. *Scientific Papers: Animal Scienc. and Biotechnol.*, 45(1), 349-353.
- Tollinger, M., Skrynnikov, N. R., Mulder, F. A., Forman-Kay, J. D., & Kay, L. E. (2001). Slow dynamics in folded and unfolded states of an SH3 domain. *J Am Chem Soc*, 123(46), 11341-11352.
- Tomita, T., Maruyama, K., Saido, T. C., Kume, H., Shinozaki, K., Tokuhiro, S., . . . Obata, K. (1997). The presenilin 2 mutation (N141I) linked to familial Alzheimer disease (Volga German families) increases the secretion of amyloid beta protein ending at the 42nd (or 43rd) residue. *Proc Natl Acad Sci USA*, 94(5), 2025-2030.
- Treweek, T. M., Ecroyd, H., Williams, D. M., Meehan, S., Carver, J. A., & Walker, M. J. (2007). Site-directed mutations in the C-terminal extension of human alphaB-crystallin affect chaperone function and block amyloid fibril formation. *PLoS One*, 2(10), e1046.
- Treweek, T. M., Meehan, S., Ecroyd, H., & Carver, J. A. (2015). Small heat-shock proteins: important players in regulating cellular proteostasis. *Cell Mol Life Sci*, 72(3), 429-451.
- Tugarinov, V., & Kay, L. E. (2003). Ile, Leu, and Val methyl assignments of the 723-residue malate synthase G using a new labeling strategy and novel NMR methods. *J Am Chem Soc*, 125(45), 13868-13878.
- Tugarinov, V., & Kay, L. E. (2005). Methyl groups as probes of structure and dynamics in NMR studies of high-molecular-weight proteins. *ChemBiochem*, 6(9), 1567-1577.
- Tugarinov, V., Hwang, P. M., Ollershaw, J. E., & Kay, L. E. (2003). Cross-correlated relaxation enhanced ¹H[¹³C]NMR spectroscopy of methyl groups in very high molecular weight proteins and protein complexes. *J Am Chem Soc*, 125(34), 10420-10428.
- Tycko, R. (2006). Molecular structure of amyloid fibrils: insights from solid-state NMR. *Q Rev Biophys*, 39(1), 1-55.
- Tycko, R. (2011). Solid-state NMR studies of amyloid fibril structure. *Annu Rev Phys Chem*, 62, 279-299.
- Tycko, R. (2016). Molecular Structure of Aggregated Amyloid-beta: Insights from Solid-State Nuclear Magnetic Resonance. *Cold Spring Harb Perspect Med*, 6(8).
- Udgaonkar, J. B. (2008). Multiple routes and structural heterogeneity in protein folding. *Annu Rev Biophys*, 37, 489-510.
- Ulrich, E. L., Akutsu, H., Doreleijers, J. F., Harano, Y., Ioannidis, Y. E., Lin, J., . . . Markley, J. L. (2008). BioMagResBank. *Nucleic Acids Res*, 36(Database issue), D402-408.
- Uversky, V. N. (2009). Intrinsic disorder in proteins associated with neurodegenerative diseases. *Front Biosci (Landmark Ed)*, 14, 5188-5238.
- Vabulas, R. M., Raychaudhuri, S., Hayer-Hartl, M., & Hartl, F. U. (2010). Protein folding in the cytoplasm and the heat shock response. *Cold Spring Harb Perspect Biol*, 2(12), a004390.
- van den, IJssel P. R., Overkamp, P., Bloemendal, H., & de Jong, W. W. (1998). Phosphorylation of alphaB-crystallin and HSP27 is induced by similar stressors in HeLa cells. *Biochem Biophys Res Commun*, 247(2), 518-523.
- van den, IJssel P., Wheelock, R., Prescott, A., Russell, P., & Quinlan, R. A. (2003). Nuclear speckle localisation of the small heat shock protein alpha B-crystallin and its inhibition by the R120G cardiomyopathy-linked mutation. *Exp Cell Res*, 287(2), 249-261.
- van der Ouderaa, F. J., de Jong, W. W., Groenendijk, G. W., & Bloemendal, H. (1974). Sequence of the first 68 residues of the alpha B2 chain of bovine alpha-crystallin. *Biochem Biophys Res Commun*, 57(1), 112-119.
- van Montfort, R. L., Basha, E., Friedrich, K. L., Slingsby, C., & Vierling, E. (2001). Crystal structure and assembly of a eukaryotic small heat shock protein. *Nat Struct Biol*, 8(12), 1025-1030.
- Van Montfort, R., Slingsby, C., & Vierling, E. (2001). Structure and function of the small heat shock protein/alpha-crystallin family of molecular chaperones. *Adv Protein Chem*, 59, 105-156.

- Velyvis, A., Ruschak, A. M., & Kay, L. E. (2012). An economical method for production of (2)H, (13)CH₃-threonine for solution NMR studies of large protein complexes: application to the 670 kDa proteasome. *PLoS One*, *7*(9), e43725.
- Veretout F, Delaye M, Tardieu A (1989) Molecular basis of eye lens transparency. Osmotic pressure and X-ray analysis of alpha-crystallin solutions. *J Mol Biol* 205: 713–728.
- Vicart, P., Caron, A., Guichenev, P., Li, Z., Prevost, M. C., Faure, A., Fardeau, M. (1998). A missense mutation in the alpha B-crystallin chaperone gene causes a desmin-related myopathy. *Nat Genet*, *20*(1), 92–95.
- Volkov, A. N., Worrall, J. A., Holtzmann, E., & Ubbink, M. (2006). Solution structure and dynamics of the complex between cytochrome c and cytochrome c peroxidase determined by paramagnetic NMR. *Proc Natl Acad Sci USA*, *103*(50), 18945–18950.
- Voorter, C. E., de Haard-Hoekman, W. A., Roersma, E. S., Meyer, H. E., Bloemendal, H., & de Jong, W. W. (1989). The in vivo phosphorylation sites of bovine alpha B-crystallin. *FEBS Lett*, *259*(1), 50–52.
- Voorter, C. E., Wintjes, L., Bloemendal, H., & de Jong, W. W. (1992). Relocalization of alpha B-crystallin by heat shock in ovarian carcinoma cells. *FEBS Lett*, *309*(2), 111–114.
- Vranken, W. F., Boucher, W., Stevens, T. J., Fogh, R. H., Pajon, A., Llinas, M., . . . Laue, E. D. (2005). The CCPN data model for NMR spectroscopy: development of a software pipeline. *Proteins*, *59*(4), 687–696.
- Wagner, G., Braun, W., Havel, T. F., Schaumann, T., Go, N., & Wuthrich, K. (1987). Protein structures in solution by nuclear magnetic resonance and distance geometry. The polypeptide fold of the basic pancreatic trypsin inhibitor determined using two different algorithms, DISGEO and DISMAN. *J Mol Biol*, *196*(3), 611–639.
- Wagner, G., Hyberts, S. G., & Havel, T. F. (1992). NMR structure determination in solution: a critique and comparison with X-ray crystallography. *Annu Rev Biophys Biomol Struct*, *21*, 167–198.
- Walsh, D. M., Thulin, E., Minogue, A. M., Gustavsson, N., Pang, E., Teplow, D. B., & Linse, S. (2009). A facile method for expression and purification of the Alzheimer's disease-associated amyloid beta-peptide. *FEBS J*, *276*(5), 1266–1281.
- Walter, S., & Buchner, J. (2002). Molecular chaperones—cellular machines for protein folding. *Angew Chem Int Ed Engl*, *41*(7), 1098–1113.
- Wälti, M. A., Ravotti, F., Arai, H., Glabe, C. G., Wall, J. S., Bockmann, A., Riek, R. (2016). Atomic-resolution structure of a disease-relevant Abeta(1–42) amyloid fibril. *Proc Natl Acad Sci USA*, *113*(34), E4976–4984.
- Wandinger, S. K., Richter, K., & Buchner, J. (2008). The Hsp90 chaperone machinery. *J Biol Chem*, *283*(27), 18473–18477.
- Waterhouse, A. M., Procter, J. B., Martin, D. M., Clamp, M., & Barton, G. J. (2009). Jalview Version 2—a multiple sequence alignment editor and analysis workbench. *Bioinformatics*, *25*(9), 1189–1191.
- Wei, J., Dobnikar, J., Curk, T., & Song, F. (2016). The Effect of Attractive Interactions and Macromolecular Crowding on Crystallins Association. *PLoS One*, *11*(3), e0151159.
- Wider, G., & Wuthrich, K. (1999). NMR spectroscopy of large molecules and multimolecular assemblies in solution. *Curr Opin Struct Biol*, *9*(5), 594–601.
- Wilhelmus, M. M., Otte-Holler, I., Wesseling, P., de Waal, R. M., Boelens, W. C., & Verbeek, M. M. (2006). Specific association of small heat shock proteins with the pathological hallmarks of Alzheimer's disease brains. *Neuropathol Appl Neurobiol*, *32*(2), 119–130.
- Williamson, M. P. (2013). Using chemical shift perturbation to characterise ligand binding. *Progress in nuclear magnetic resonance spectroscopy*, 73:1–16.
- Williamson, M. P., Havel, T. F., & Wuthrich, K. (1985). Solution conformation of proteinase inhibitor IIA from bull seminal plasma by ¹H nuclear magnetic resonance and distance geometry. *J Mol Biol*, *182*(2), 295–315.
- Wilmarth, P. A., Tanner, S., Dasari, S., Nagalla, S. R., Riviere, M. A., Bafna, V., David, L. L. (2006). Age-related changes in human crystallins determined from comparative analysis of post-translational modifications in young and aged lens: does deamidation contribute to crystallin insolubility? *J Proteome Res*, *5*(10), 2554–2566.
- Wittekind, M. & Mueller, L. (1993). HNCACB, a High-Sensitivity 3D NMR Experiment to Correlate Amide-Proton and Nitrogen Resonances with the Alpha- and Beta-Carbon Resonances in Proteins. *J Magn Reson B* 101: 201–205.
- Wu, C., & Shea, J. E. (2011). Coarse-grained models for protein aggregation. *Curr Opin Struct Biol*, *21*(2), 209–220.
- Xi, J., Farjo, R., Yoshida, S., Kern, T. S., Swaroop, A., & Andley, U. P. (2003). A comprehensive analysis of the expression of crystallins in mouse retina. *Mol Vis*, *9*, 410–419.
- Xia, C. H., Liu, H., Chang, B., Cheng, C., Cheung, D., Wang, M., Gong, X. (2006). Arginine 54 and Tyrosine 118 residues of alphaA-crystallin are crucial for lens formation and transparency. *Invest Ophthalmol Vis Sci*, *47*(7), 3004–3010.
- Xiao, X., & Benjamin, I. J. (1999). Stress-response proteins in cardiovascular disease. *Am J Hum Genet*, *64*(3), 685–690.
- Xiao, Y., Ma, B., McElheny, D., Parthasarathy, S., Long, F., Hoshi, M., Ishii, Y. (2015). Abeta(1–42) fibril structure illuminates self-recognition and replication of amyloid in Alzheimer's disease. *Nat Struct Mol Biol*, *22*(6), 499–505.
- Xu, X., Reinle, W., Hannemann, F., Konarev, P. V., Svergun, D. I., Bernhardt, R., & Ubbink, M. (2008). Dynamics in a pure encounter complex of two proteins studied by solution scattering and paramagnetic NMR spectroscopy. *J Am Chem Soc*, *130*(20), 6395–6403.
- Xu, Z., Horwich, A. L., & Sigler, P. B. (1997). The crystal structure of the asymmetric GroEL-GroES-(ADP)₇ chaperonin complex. *Nature*, *388*(6644), 741–750.
- Younkin, S. G. (1998). The role of A beta 42 in Alzheimer's disease. *J Physiol Paris*, *92*(3–4), 289–292.
- Zhang, S., Iwata, K., Lachenmann, M. J., Peng, J. W., Li, S., Stimson, E. R., . . . Lee, J. P. (2000). The Alzheimer's peptide A beta adopts a collapsed coil structure in water. *J Struct Biol*, *130*(2–3), 130–141.
- Zheng, X., Mueller, G. A., DeRose, E. F., & London, R. E. (2009). Solution characterization of [methyl-(13)C]methionine HIV-1 reverse transcriptase by NMR spectroscopy. *Antiviral Res*, *84*(3), 205–214.
- Zimmerman, S. B., & Trach, S. O. (1991). Estimation of macromolecule concentrations and excluded volume effects for the cytoplasm of Escherichia coli. *J Mol Biol*, *222*(3), 599–620.

9. Curriculum Vitae

Maria Stavropoulou

Festkörper-NMR-Spektroskopie, Dept. Chemie
Technischen Universität München
Lichtenbergstr. 4
85747 Garching, Germany
maria.stavropoulou@tum.de

EDUCATION

- Oct 2012 – Sept 2017** **Department of Chemistry, Technical University of Munich (TUM)**
Ph.D Student at the Chair of Solid – state NMR Spectroscopy
- Sept 2009 – March 2012** **Department of Medicine, University of Patras**
Master of Science in “*Basic Sciences in Medicine*” with Specialization in Pathobiochemistry
- Sept 2004 – Sept 2009** **Department of Biology, University of Patras**
Diplom in *Biology* with Specialization in “*Genetic, Cellular & Molecular Biology and Physiology*”
- Sept 2001 – Sept 2004** **5th High School of Volos, Volos-Magnesia, Greece**

RESEARCH EXPERIENCE

- Oct 2012 – Sept 2017** **Department of Chemistry, Technical University of Munich**
Laboratory of Solid – state NMR Spectroscopy
Research Project: “*NMR Spectroscopic Investigations of α B- and α A-crystallin*”
Supervisor: Professor Bernd Reif
- Sept 2009 – March 2012** **Department of Medicine, University of Patras**
Laboratory of Biological Chemistry
Research Project: “*Mode of action of new fluoroketolides, strong inhibitors of protein synthesis*”
Supervisor: Associate Professor George Dinos
- Feb 2011 – May 2011** **Gene Center, Ludwig-Maximilians University of Munich (LMU)**
Laboratory of Chemistry and Biochemistry
Research Project: “*Elongation Factor EF-P and its Role in Environmental Stress Adaptation*”
Supervisor: Professor Daniel Wilson
- Sept 2007 – Sept 2008** **Department of Medicine, University of Patras**
Laboratory of Biological Chemistry
Research Project: “*Studies of New Ketolides on Mutant Ribosomes*”
Supervisor: Associate Professor George Dinos

10. List of Publications

1. Mainz A, Peschek J, Stavropoulou M, Back K, Bardiaux B, Asami S, Prade E, Peters C, Weinkauff S, Buchner J and Reif B (2015) The chaperone α B-crystallin uses different interfaces to capture an amorphous and an amyloid client *NSMB* 22: 898-905.
2. Krokidis, M., Bougas, A., Stavropoulou, M., Kalpaxis, D., Dinos, G.P., 2015, 'The slow dissociation rate of K-1602 contributes to the enhanced inhibitory activity of this novel alkyl-aryl-bearing fluoroketolide', *J. Enzyme Inhib. Med. Chem.*, 31: 1-6.

The following manuscripts are submitted or in preparation:

1. Asami, S., Kallies, W., Günther, J., Stavropoulou, M., Glaser, S., Sattler, M. «Ultrashort broadband cooperative pulses for multidimensional bio-molecular NMR experiments», *submitted to JACS*
2. Kaiser, C., Carstens, P., Stavropoulou, M, Haberl, B., Mymrikov, E., Rockel, B., Schmid, P., Zou, J., Asami, S., Rappsilber, J., Haslbeck, M., Zacharias, M., Reif, B., Buchner, J. and Weinkauff, S., «C-terminal domain swapping and cysteine oxidation control the oligomerization of the eye lens chaperone α A-crystallin», *in preparation*
3. Stavropoulou, M, Asami, S., Kaiser, C., Haslbeck, M., Buchner, J., Weinkauff, S. and Reif, B. «Dynamic Aspects of the C-terminal Region of the redox-sensitive human small heat shock protein α A-crystallin», *in preparation*